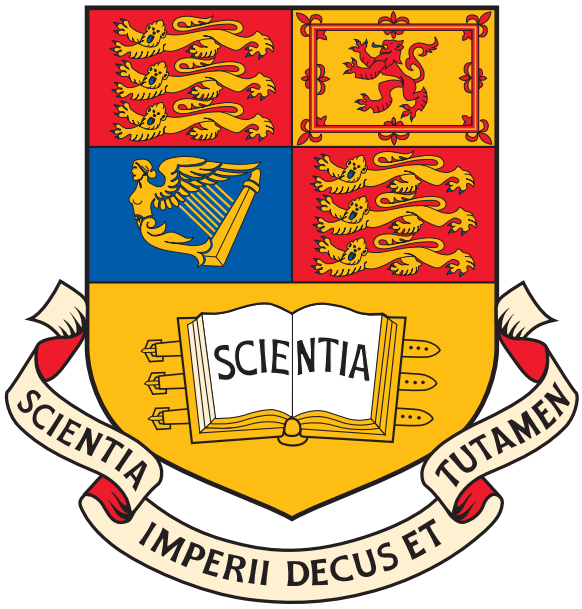
Imperial College London

Probing molecular structure and dynamics with coherent extreme ultraviolet and X-ray pulses

Richard James Squibb

February 2013



Thesis submitted in partial fulfilment of the requirements for the degree of

Doctor of Philosophy of Imperial College London and the Diploma of Imperial College

Laser Consortium
Quantum Optics and Laser Science Group
Physics Department
Imperial College London
Prince Consort Road, London SW7 2BW
United Kingdom

Abstract

This thesis presents how sources of coherent sources extreme ultraviolet (XUV) and soft X-ray wavelengths can be generated and how these sources may be used to study both the dynamics and structure of molecular systems.

Developmental work on a beam line designed to generate XUV radiation using high harmonic generation is presented. In addition to commissioning experimental work using both a flat-field XUV spectrometer and magnetic bottle electron spectrometer, software development work towards building a scalable and future proof acquisition framework for future experiments is presented.

The remainder of the thesis presents results obtained from experiments performed at the Linac Coherent Light Source (LCLS) X-ray free electron laser (FEL). We demonstrate that by using a UV femtosecond pulse and a weakly focused X-ray pulse of duration 70 fs, the evolution of UV induced photoisomerisation of 1-3 cyclohexadiene can be tracked. Over timescales of ≈1 ps after UV excitation, the ion yields of the H^+ and C^+ species were observed to increase by 10% and the observed kinetic energy of all fragments is observed to increase over the same time scale, which can be explained by the structural change of the molecule into the hexatriene isomers.

There has been a recent focus in FEL science in using tightly focused X-rays to generate so called hollow atoms, with a completely empty inner shell. Study of the products of the creation of these states ideally requires a measurement in coincidence of multiple particles. We demonstrate that by using the technique of partial covariance mapping (PCM) in conjunction with a high efficiency electron time-of-flight spectrometer, multiple processes in the core ionisation of neon can be resolved. We also use the scheme to successfully measure single site double-core hole states in the hydrocarbons of acetylene and ethane. We discuss how this technique will be a powerful tool in future experiments designed for chemical analysis of the core hole states of systems.

Declaration

I hereby certify that the material of this thesis, which I now submit for the award of Doctor of Philosophy of Imperial College London, is entirely my own work unless otherwise cited or acknowledged within the body of the text.

Richard James Squibb

Contents

Abstract **3**

List of Figures **9**

List of Tables **12**

1 Introduction **15**

1.1 Light as a probe of molecular dynamics 15

1.2 Recent progress in XUV/X-ray sources 16

1.3 Structure of the thesis 17

1.4 Author's contribution 18

2 The interaction of light and matter **20**

2.1 Selected aspects of nonlinear optics and short optical pulses 20

2.1.1 Short optical pulses 20

2.1.2 Dispersion 21

2.1.3 Nonlinear optics 22

2.2 Photo-ionisation and excitation processes 24

2.2.1 Qualitative description of molecular orbitals and energy levels 24

2.2.2 Photoionisation as a probe of matter 26

2.2.3 Direct ionisation 26

2.2.4 Multi-photon and above threshold ionisation 29

2.2.5 Field induced ionisation 30

2.3 Strong Field Laser Physics 31

2.3.1 Keldysh parameter 31

2.3.2 High harmonic generation 32

2.3.3 Attosecond pulse generation 38

3 Laser technology for coherent XUV/X-ray radiation 39

3.1 Femtosecond optical lasers . . . 39

3.1.1 Short pulse generation - femtosecond oscillators . . . 40

3.1.2 Chirped pulse amplification . . . 43

3.2 Diagnostics and pulse measurement techniques . . . 46

3.2.1 Intensity autocorrelator and FROG . . . 47

3.2.2 SPIDER . . . 49

3.3 Soft/Hard X-ray free electron lasers . . . 51

3.3.1 Undulator radiation . . . 51

3.3.2 Self-amplified spontaneous emission . . . 53

3.3.3 Electron Accelerator . . . 56

3.4 Linac Coherent Light Source free electron laser . . . 58

3.4.1 Specifications . . . 59

3.4.2 Characterisation of Free Electron Laser pulses . . . 60

3.4.3 Pump-probe experiments using X-rays . . . 61

4 Review of experimental techniques and technology 65

4.1 High vacuum technology . . . 65

4.2 X-ray/XUV optics and diagnostics . . . 67

4.2.1 Flat-field spectrometry . . . 68

4.3 Time-of-flight spectrometry . . . 68

4.3.1 Basic operation - the ion mass spectrometer . . . 69

4.3.2 Electron time-of-flight - the energy spectrometer . . . 72

4.3.3 Energy resolution and Collection Efficiency . . . 72

4.3.4 Velocity map imaging . . . 73

4.4 Sample delivery systems . . . 76

4.4.1 Gas samples . . . 76

4.4.2 Solid and liquid sources . . . 77

4.5 Detectors . . . 78

4.5.1 Microchannel plates . . . 78

4.5.2 Cameras . . . 80

4.5.3 X-ray cameras . . . 80

5 Development towards XUV beamline components 82
5.1 Scientific motivation . . . 82
5.2 Experimental apparatus . . . 85
5.2.1 Beamline . . . 85
5.2.2 XUV flat-field spectrometer . . . 87
5.2.3 Magnetic bottle electron spectrometer . . . 88
5.3 High harmonic optimisation . . . 92
5.4 Electron spectroscopy measurements . . . 95
5.4.1 Future work . . . 98
5.5 Software development . . . 98
5.6 Summary and Outlook . . . 101

6 Molecular isomerization probed with soft X-rays 102
6.1 The AMO experimental station . . . 102
6.1.1 High field physics chamber . . . 103
6.1.2 Data acquisition and processing . . . 104
6.2 Time resolved studies of molecular isomerisation in 1,3-cyclohexadiene . . . 106
6.2.1 X-ray induced fragmentation as a probe for large molecules . . . 107
6.2.2 The ring opening of 1,3-Cyclohexadiene . . . 108
6.2.3 Experimental setup . . . 110
6.2.4 Data analysis methods . . . 114
6.2.5 Simion simulations and VMI calibration . . . 115
6.2.6 Results . . . 121
6.2.7 Discussion . . . 124
6.3 Conclusions . . . 126

7 Multi-particle X-ray processes explored using partial covariance mapping 128
7.1 Software development for data conversion . . . 128
7.1.1 CASS based converter . . . 129
7.1.2 Pyana based converter . . . 131
7.2 Chemical shifts in molecules probed using double-core-hole photoelectron spectroscopy . . . 133
7.2.1 Double-core-hole spectroscopy for chemical analysis . . . 134
7.2.2 Two-dimensional spectroscopy . . . 135
7.2.3 Covariance mapping . . . 136
7.2.4 Experimental setup . . . 140
7.2.5 Neon . . . 146
7.2.6 Discussion . . . 157
7.2.7 Hydrocarbons . . . 158
7.3 Conclusions . . . 166

8 Conclusions **168**

8.1 Future directions 170

A LCLS Data Handling **172**

A.1 Server information 172

A.2 Data storage format 173

A.3 An overview of the Pyana analysis framework 174

A.3.1 An example pyana module 174

A.3.2 Creating a pyana user release 180

A.4 CASS HDF to Matlab converter 181

A.4.1 Generating an HDF5 file using CASS 181

A.4.2 Example ini file for configuring CASS 182

A.4.3 CASS_hdf5parser conversion script 183

A.4.4 Source Code 184

A.5 Pyana converter 191

A.5.1 MatConverter.py 191

A.5.2 Example .ini configuration file 192

A.5.3 Source Code 192

Bibliography **205**

List of Figures

1.1 The timescales involved in the dynamics of matter 16

2.1 Schematic of bonding and anti bonding orbitals and the consequent energy curves for a diatomic molecule 25

2.2 Photoelectric cross-sections over the XUV and soft-Xray regimes 27

2.3 Core hole creation and decay processes in neon 28

2.4 Photoionisation mechanisms 30

2.5 Schematic of a typical high harmonic spectrum 33

2.6 Three step model of high harmonic generation 33

2.7 Classical electron trajectories in a CW electric field 34

2.8 Schematic representation of the Gouy and atomic dipole wavevectors for a focused Gaussian beam 37

3.1 Schematic of grating pair and prism pair compressors 42

3.2 Schematic of the Micra-6 Oscillator 42

3.3 Schematic overview of the Chirped Pulse Amplification method 44

3.4 Schematic of the Legend-HE-USP-1K regnerative amplifier 45

3.5 Schematic of a multiple shot Intensity autocorrelator and Frequency Resolved Optical Gating 47

3.6 Schematic of a generic SPIDER 49

3.7 Example spectra and SPIDER trace from the Coherent Legend laser system 50

3.8 Principle of Operation of an Undulator 52

3.9 Overview of microbunching in an SASE FEL 54

3.10 Simulated pulses for the LCLS accelerator for nominal pulse durations of 75 and 175 fs 55

3.11 Magnetic chicane bunch compressor 57

3.12 Schematic of the LCLS accelerator 58

3.13 Shot to shot variability of LCLS electron beam and X-ray parameters . . . 62

3.14 Principle of the emittance spoiler method 63

4.1 Reflectivity of a 50 nm layer of C_4B on a SiO_2 substrate with surface roughness 1 nm σ 67

4.2 Principle of operation of a single acceleration region linear time-of-flight spectrometer 70

4.3 Layout and electric fields of a velocity map imaging spectrometer 74

4.4 (a) A channel electron multiplier (b) structure of a single microchannel plate. A potential difference applied across the length of the channels will result in electron gain. 79

4.5 Quantum efficiency in the XUV/ Soft X-ray region for CCD detectors . . . 80

5.1 Principle of the RABITT technique 83

5.2 Schematic of the High Harmonic and Recombination chambers 86

5.3 Schematic of the tube target used for generation of the harmonics. 87

5.4 Schematic of the Flat-field spectrometer 88

5.5 Calibration curve of the flat-field spectrometer 89

5.6 Single-photon ionisation cross-sections for the noble gases. 89

5.7 Principle of operation of the Magnetic Bottle electron spectrometer 90

5.8 Magnetic bottle Electron spectrometer schematic 91

5.9 Transmission of 200 nm thick filters of various materials 93

5.10 Harmonic signal as captured with the flat field spectrometer 94

5.11 Effect of the position of the tube target and pressure on the harmonic signal 95

5.12 Principle of rebinning time-of-flight traces into equal width energy bins . . 96

5.13 Electron time of flight signal acquired using magnetic bottle for neon ionised with high harmonics 97

5.14 Calibration of the electron time of flight signal as produced by high harmonics 97

5.15 Normalised high harmonic signal recorded using the magnetic bottle. 98

5.16 GUIs coded in Matlab for control of both the Piezo stage and the Andor camera 100

6.1 Schematic of the high-field physics chamber in standard configuration . . . 103

6.2 Schematic of the Hemmers electon TOF design in single and multi electrode modes 104

6.3 Energy level diagram of CHD ring opening 109

6.4 UV-IR delay 1,3 cyclohexadiene TOF delay scans for H and C6Hn ions . . . 112

6.5 Dependence of the X-ray - IR delay on the kinetic energy distribution of the N^+/N_2^{2+} fragments. 113

6.6 Decoupled ion time-of-flight spectrum of X-ray fragmentation of CHD and Nitrogen 113

6.7 Imaging microchannel plate dark counts 115

6.8 Potential array used for the Simion calculations for the VMI calibration . . 116

6.9 Simulated projected velocity spheres for ion kinetic energies 0 24 eV 117

6.10 Dependence of the MCP voltage on the simulated velocity spheres 118

6.11 VMI detection radius as a function of the Z position of the source 119

6.12 VMI detection radius as a function of the Y position of the source 120

6.13 Kinetic energy and ion counts as a function of the UV - X-ray delay as measured using the VMI 122

6.14 Pressure and pulse energy statistics for the ion time-of-flight delay scan . . 123

6.15 Ion time-of-flight signal as a function of UV - X-ray delay for the H^+ and C^+ ion species 125

6.16 Branching ratios of Auger decay of 1,3-cyclohexadiene and Hexatriene . . . 126

7.1 Outputs for the HDF5 and Matlab for a test XTC which contains 2498 shots. 130

7.2 Carbon 1s binding energies for the Ethyl Trifluoroacetate molecule 133

7.3 Coincidence map of the fragmentation of CO from heavy ion bombardment 135

7.4 Covariance map of multi-photon ionisation of CO 138

7.5 LCLS magnetic bottle electron spectrometer used for the correlation experiments. 141

7.6 Neon ion time-of-flight spectra at optimal focusing conditions. 142

7.7 Correlation plots and Pearson coefficients for the four different gas detectors 144

7.8 Electron counts as a function of measured pulse energy for selected runs. . . 145

7.9 Single shot time-of-flight data for neon irradiated with 1065 eV 146

7.10 Electron time-of-flight to energy conversion coefficients for neon runs 147

7.11 Neon electron energy spectra for kinetic energies 0-1200 eV irradiated with a 1065 eV FEL pulse 148

7.12 Covariance map of neon electrons of energy 4-1200 eV 150

7.13 Covariance map of neon electrons of energy 10-220 eV 152

7.14 Covariance map of neon electrons for the core-valence and core-Auger correlation region. 154

7.15 Average line outs of the core-Auger region of the neon covariance map . . . 156

7.16 Covariance maps for C_2H_2 for electron energies of 110 - 560 eV 159

7.17 Covariance maps for C_2H_6 for electron energies of 110 - 560 eV 160

7.18 Covariance maps for C_2H_2 for electron energies of 160 - 500 eV for 100 and 150 V retardations 162

7.19 Comparison of the average kinetic energy spectrum with the integrated covariance of the P_1 correlations 163

7.20 Covariance maps for C_2H_2 for electron energies of 160 - 500 eV for 100 and 150 V retardations 164

7.21 Comparison of the average kinetic energy spectrum with the integrated covariance of the P_1 correlations 165

List of Tables

2.1 Important nonlinear optical processes 23

3.1 Key parameters of LCLS accelerator 59

5.1 Operating voltages and currents at optimal operating conditions for the magnetic bottle. 96

7.1 Experimental settings for the magnetic bottle and detectors. 142

7.2 Pearson Correlation Coefficients for a selection of different experimental runs. 143

7.3 Electron TOF calibration coefficients used for the hydrocarbon runs 158

A.1 LCLS server names and purposes 172

A.2 Pyana module functions and workflow 174

A.3 CASS arguments 181

A.4 List of CASS Postproccessors relevant to HDF5 file creation. 182

A.5 List of parameters for the CASS_hdf5parser matlab function 183

A.6 List of configuration parameters for the MatConverter.py pyana module . . 191

Acknowledgements

I would first and foremost like to extend my thanks to my supervisor, Leszek Frasinski, for his continued support and guidance for the last few years, and for providing me the opportunity to explore these new areas of physics and research. I would also like to extend my gratitude to Jon Marangos for his leadership and assistance both in and out the lab, and the other professors in the group, John Tisch, Roland Smith and Misha Ivanov for their assistance both in and out the lab.

Next I would like to extend my thanks to everyone in the laser consortium making me feel so welcome to the group and being such good friends and co-workers. Special thanks really have to go to Amelle for the huge amount of support you gave me both in the lab and outside, Gavin, for your help when I was starting out, Thomas for your help in the lab and being instrumental in dragging the group to the pub every week, Marco for putting up with me being opposite you in the office for 3 years and for making the LCLS trips so productive and fun, and Simon for his efforts when we were working together. I would also like to extend thanks to everyone else who worked in the Red Dragon lab during my time here: Ann, Chris, Malte, Rashid, Seb, Eva, Leo, Delphine and Sarah. Thanks also go to the attoboys, Chris, Felix, Tobi, Will and Jarlath, even if you did steal the stuff from 005 far too often, and the Glass Lab guys, Hugo, Sid, Stefan and Damien for sticking around with us low power laser folk. Thanks also go to the theorists, Luke, Davids (both), Narges, Bridgette and Ryan. I would also like to extend my gratitude to the newest members of our group: Davide, Felicity, Zara, Pricey, Hazel, and the really new members, Daniel, Emma, Martin and Nick. While I didnt spend much time working with you, you did make the writing up stage much more enjoyable. Last but not least, I would like to extend my thanks to the people behind the scenes, Judith, Sanja and Marcia in the optics office, and Peter and Andy in the workshop for their support. Thank you all (and any I forgot) for making my time here so enjoyable.

Portions of this research were carried out at the Linac Coherent Light Source (LCLS) at the SLAC National Accelerator Laboratory. LCLS is an Office of Science User Facility operated for the U.S. Department of Energy Office of Science by Stanford University. I would also like to extend sincere gratitude to the principle investigators of the LCLS experiments I took part in: Vladmir Petrovic, Raimund Feifel, Ryan Coffee, Mike Glownia and Norah Berrah for their support and leadership during those experimental runs and everyone else who took part in the LCLS runs who are too numerous to mention by name.

Finally I would like to extend my love and thanks to my family: Mum, Dad, Rebecca and Mike for the love and support they have shown me during this long journey from simple fresher up until submission of this thesis. I really could not have done this without you, and I will be eternally grateful.

I would also thank the love of my life, as is traditional in these acknowledgements, but she didn't turn up in time for the end of the PhD.

Chapter 1

Introduction

1.1 Light as a probe of molecular dynamics

The absorption and emission of electromagnetic radiation by matter has long been used as a probe of the internal structure and properties of matter. Since the invention of the laser in 1960, the technology has developed such that experimenters now have access to both short duration and tunable wavelength sources of coherent light, which can be used in a number of different spectroscopic techniques. A particular strength of laser driven experiments is their ability to perform time resolved measurements of the evolution of a system using pump-probe techniques [1, 2]. This technique uses two time delayed pulses to first pump a system into an excited or ionised state of interest, and then probed using another pulse to probe the system though either absorption, emitted particles or other such measurable. By varying the delay of the two pulses it is possible to build up a time-resolved measurement of the system. Study of nuclear dynamics on the femtosecond (1 fs = 10^{-15} s) timescale was driven by a generation of broad bandwidth femtosecond laser systems and these techniques have been able to measure wavepacket evolution and structural changes in molecular systems on the femtosecond timescales.

Similarly, radiation spanning the extreme ultraviolet (XUV), soft and hard X-ray regimes * have proven to be the workhorse for the study of structure. First studied in depth by Rontgen in 1895 [3], X-ray sources have been used extensively in research into the structure of bulk materials and biological samples, and the internal electronic structure of atoms and molecules. Kai Siegbahn's work pioneering x-ray photoelectron spectroscopy (XPS) demonstrated that X-rays can be used to measure inner shell electron binding energies in atoms, enabling the derivation of both the energy shifts of the binding energies due to the chemical environment of the atoms in molecules, and yielding efficient methods

*There are no well defined boundaries for where XUV and Soft/Hard X-rays start and end. For the purposes of the thesis we will be using the definition XUV = 10 to 300 eV, Soft X-rays = 300 to 2000 eV and Hard X-rays > 2000 eV

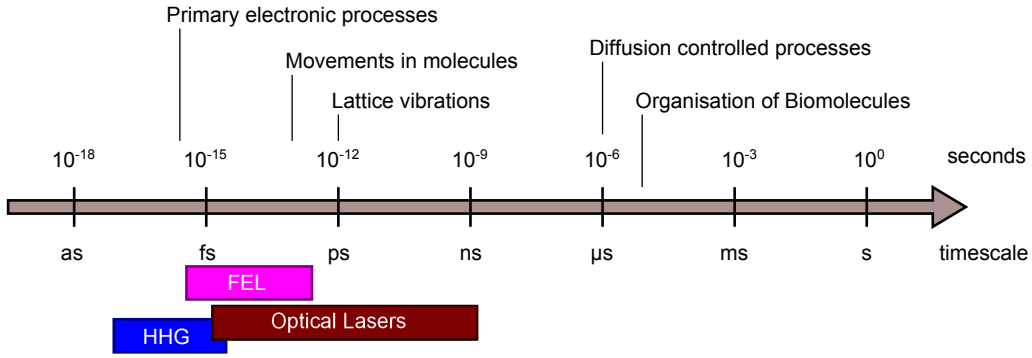


Figure 1.1: Schematic presentation of timescales involved in the dynamics of matter. Adapted from Rev. Accel. Sci. Tech. **03** 13 [8].

of deriving the surface composition of materials through their distinctive absorption and photoionisation spectra [4, 5]. Storage ring based synchrotron light sources have been used since the late 1960s to using the methods of X-ray scattering and diffraction [6, 7].

1.2 Recent progress in XUV/X-ray sources

In the last decade there have been two large advances in technology that have allowed for the first time a light source that has the potential to combine the high coherence and short pulse durations of optical laser systems with the high photon energies and short wavelengths available to X-ray sources. The first is the the generation of coherent XUV pulses using the process of high harmonic generation (HHG), achieved using a high intensity femtosecond optical source focused into a gas target[9, 10]. HHG is capable of generating spectra of coherent radiation spanning photon energies of hundreds of electron Volts (eV) [11] with recent results exceeding keV energies [12]. With the technique being based on some fairly simple experimental techniques, any lab with access to a reasonably high power, femtosecond duration laser can in principle access such a source with relative ease. There are two main methodologies which can utilise such harmonics. Firstly, since the harmonic spectral structure is heavily dependent on both the structural and electronic properties of the generating medium, HHG spectroscopy has been demonstrated as as powerful tool in probing the structure of molecules [13–16]. Secondly, the broad bandwidth afforded by the spectra allow the possibility of the generation of coherent pulses with durations of the order of hundreds or tens of attoseconds (as) [17, 18] with the current record holders having demonstrated pulses of 80 and 67 as. As such there has been a great deal of research in the last few years focused on electron dynamics in atoms, molecules and condensed matter systems [19, 20].

The other major development has been the development and construction of a new generation of national scale facilities capable of generating high energy, femtosecond duration X-ray pulses using free electron laser (FEL) technology [21]. These new facilities com-

bine the high field strengths, pulse durations, pulse energies and high coherence properties available using conventional optical laser systems with high photon energy and tunability available using a synchrotron radiation based source. The high degree of transverse coherence, combined with the high brightness also allows the possibility of using diffraction imaging techniques capable of high resolution reconstructions of nanocrystals, or even single micro-organisms and viruses [22–25]. Additionally, the high photon energies allow excitation and ionisation of the inner shell electrons through single photon absorption, allowing the creation of both core ionised states and high energy core excited states. The high intensities of FELs, which can be in excess of 10^{18} Wcm^{-2}, allow for the first time multi-photon X-ray processes to be created and measured with a reasonable probability. The study of such processes hold the promise of high resolution measurements of the core states of molecules using two-photon double core hole (DCH) spectroscopy [26–28]. Both of these methods can be combined with the above mentioned pump-probe techniques for time resolved imaging of structural and electronic changes [29].

1.3 Structure of the thesis

The overarching theme of the work presented in this thesis is applying these new sources of coherent XUV and X-ray radiation to studies in probing the chemical structure and dynamics of molecules. This is represented by my work in two complementary areas of research: the continued development of an infra-red (IR)/XUV pump-probe experimental apparatus at the Blackett Laboratory, and experiments using the Linac Coherent Light Source (LCLS) atomic-molecular-optical (AMO) end station to probe both structural dynamics and internal electronic structure by using coherent soft X-rays. The thesis also attempts to present the research in the broader context of research applied in this area of research.

The thesis has been written primarily from an experimental viewpoint and aims to inform the reader of the general techniques used during the course of the experiments. Rather than being a purely chronological account of work completed, the thesis groups work completed into the overarching concepts of HHG generation and application, pump-probe experiments using the LCLS X-ray source, and the application of covariance mapping techniques to the study of correlated X-ray driven photoionisation processes. The structure of the thesis is therefore as such: Chapter 2 briefs the reader on the theoretical background necessary for descriptions of the experiments described in the chapter, including strong field physics, an introduction to molecular structure and ionisation processes that can be driven using coherent, intense light sources. Chapter 3 describes the theoretical and practical considerations in building/using a source of coherent XUV or X-ray source, beginning with a description of high peak power, femtosecond laser system suitable for driving HHG based sources, and the methods required to diagnose such systems, be-

fore concluding by describing the fundamentals of an X-ray FEL and discussing the LCLS user facility's specifications and capabilities. Chapter 4 describes the various experimental techniques common to the experiments described in the thesis, including creating sample sources, detection methods, X-ray and XUV optical methods and time-of-flight energy and mass spectrometry of charged particles. Chapter 5 discusses efforts and considerations of building an HHG beam line, and presents results of tests of the different experimental rigs that can be attached to the system, and software development towards a a unified acquisition framework.. Chapter 6 describes the LCLS AMO experimental station, before describing work performed during an experimental run at the LCLS FEL facility to explore ring opening dynamics in 1,3-cyclohexadiene (CHD). Chapter 7 discusses an experiment designed to probe DCH states in atoms and molecules using the partial covariance mapping technique. The work completed is then summarised and discussed in chapter 8. Further supplementary information on how to utilise the LCLS computing systems and analysis frameworks is presented in appendix A.

1.4 Author's contribution

During the course of my PhD I have gained a working knowledge of the operation, alignment and maintenance of CPA based, femtosecond laser systems, and was responsible for running and maintaining the Coherent Legend laser system. I have gained practical knowledge in the operation and maintenance of vacuum technology including chamber construction, vacuum pumps and detection. I have operated and analysed the output from a number of different time-of-flight (TOF) systems including linear systems, magnetic bottle electron spectrometers, and velocity mapping spectrometers.

Working with Gavin Waters and Marco Siano, we performed the completed commissioning of the beamline and testing of the elements of the beamline including both the magnetic bottle and the flat field spectrometer. I further contributed towards development of the rig through software development of control software for the Andor X-ray camera and the delay stages for use in future experiments, and trained a new student, Simon Hutchinson in the use of the experimental apparatus to prepare for his future experiments in HHG in XUV excited systems.

During the course of the CHD experiment I contributed to simulating and calibrating the velocity map imaging (VMI) spectrometer used during the experiment. In post analysis I performed analysis of the time-of-flight data in addition to supporting my colleague Marco Siano in his efforts towards the VMI analysis.

For the DCH experiments I was directly responsible for the development of code used to convert the data sets into format that could be quickly utilised by other members of the experimental team, and during the course of the run I held sole responsibility in running

the conversion code in addition to preliminary analysis of the data. After the experimental run was completed I was responsible for performing data analysis of the time of flight data using both my own code and that derived from my supervisor Leszek Frasinski, and had responsibility for performing investigations into the electron beam data to evaluate both the gas detector values reliability and potential damage of the XTC files.

Further experiments and work which I have participated in during the course of my PhD, which are not covered by this thesis, have included work at the Rutherford Appleton laboratory on an experiment to explore electron diffraction from aligned molecules using mid-IR sources, and collaborative efforts with TU Wein university in assisting them with the measurements of Harmonics from low wavelength fields. I have also assisted in additional experiments at LCLS to study the molecules of O_2 and I_2.

Work described in this thesis has been reported in the following papers:

Petrovic et al., **Transient X-Ray Fragmentation: Probing a Prototypical Photoinduced Ring Opening**, *Phys. Rev. Lett.* **108** pp. 253006 [30]

Additional papers covering the double core hole experiments are currently in preparation and are expected to be published in the next few months following submission of this thesis.

Chapter 2

The interaction of light and matter

This chapter serves as an introduction to the relevant theory and background behind the experimental schemes and methods described later in the thesis. Some introductory optical theory is then presented, outlining the mathematical treatment of ultrashort optical pulses and how the properties of these pulses can be modified by their interaction with bulk materials. The bulk of the chapter discusses processes of photon initiated ionisation with a focus on how these processes can be used to both generate XUV pulses and probe molecular structure.

2.1 Selected aspects of nonlinear optics and short optical pulses

This section gives a brief introduction to the mathematical treatment of short duration, large bandwidth optical pulses, how the propagation of the pulses will be affected by the propagation medium and how the intense fields can be used to produce non-linear optic effects in materials.

2.1.1 Short optical pulses

For optical pulses of duration approaching the limit of a few optical cycles, the electric field can be described by the product of a sinusoidal carrier wave and a pulse envelope which describes the shape of the pulse. The electric field as a function of time t and space for an optical pulse travelling in the z direction is given by:

$$E(z,t) = A(z,t)\exp\left[i(\omega_0 t - \frac{n(\omega_0)\omega_0}{c}z + \phi_0)\right] = A(z,t)\exp\left(i\Phi(z,t)\right), \qquad (2.1)$$

where $A(z,t)$ is an envelope function, that vary slowly on the timescale of a single cycle, ω_0 is the angular frequency of the carrier, c is the speed of light, $n(\omega_0)$ is the refractive index of the propagation medium at the carrier frequency, and ϕ_0 is the carrier-envelope phase (CEP), and describes where the maximum of the electric field lies with respect to the maximum of the envelope. The quantity $\Phi(z,t)$ is the temporal phase, and the instantaneous frequency is given by the time derivative of $\Phi(z,t)$.

The electric field can also be described in frequency space and we can switch between the two through a simple Fourier transform:

$$E(z,t) = \frac{1}{\sqrt{2\pi}} \int \tilde{E}(z,\omega) \exp(-i\omega t)\, \mathrm{d}\omega \tag{2.2}$$

$$\tilde{E}(z,\omega) = \frac{1}{\sqrt{2\pi}} \int E(z,t) \exp(i\omega t)\, \mathrm{d}t \tag{2.3}$$

where $\tilde{E}(z,\omega) = A(z,\omega)\exp(i\phi(\omega))$ is the electric field in frequency space and $A(z,\omega)$ and $\phi(\omega)$ are the spectral amplitude and phase respectively. Since time and frequency are linked Fourier pairs, a short time requires a large bandwidth and they must both satisfy the time-bandwidth inequality:

$$\Delta\nu\Delta t \geq \mathrm{TBP} \tag{2.4}$$

where $\Delta\nu$ and Δt are the full-width half-maximum (FWHM) bandwidth and pulse durations respectively. The time-bandwidth product (TBP), is a constant that depends on the form of the envelope function. For example, a Gaussian pulse has a TBP equal to 0.44. A pulse where $\Delta\nu\Delta t = \mathrm{TBP}$ is the shortest possible pulse for the given bandwidth, and in this case is said to be a transform limited pulse.

2.1.2 Dispersion

Satisfying the case for a transform limited pulse requires that all spectral components have the same phase. Since all materials exhibit a frequency dependent refractive index, propagation of a pulse through a material will lead to dispersion and therefore broadening of the pulse as the different frequency components travel at different phase velocities. The dispersion can be represented by a Taylor expansion of the spectral phase, around the carrier frequency:

$$\phi(\omega-\omega_0) = \overbrace{\phi_0}^{\text{CEP}} + \overbrace{\phi_1(\omega-\omega_0)}^{\text{Group delay}} + \overbrace{\phi_2\frac{(\omega-\omega_0)^2}{2!}}^{\text{Group delay dispersion}} + \overbrace{\phi_3\frac{(\omega-\omega_0)^3}{3!}}^{\text{Third order dispersion}} + \cdots \tag{2.5}$$

The first two terms of the expansion are the CEP and the group delay, and do not affect the shape of the pulse, only delaying it in time. The third term is the most important

term when it comes to ultra-short pulses, and is called the group delay dispersion (GDD). This term leads to the pulse being stretched in time due to a frequency dependent delay of the spectral components, creating what is called a chirped pulse. Positive GDD creates a positively chirped pulse where the longer frequency components lead the shorter ones, and negative GDD creates the opposite case, a negatively chirped pulse.

Propagation through any material will cause the accumulation of GDD, with the effect being more pronounced as you move to shorter (i.e. larger bandwidth) pulses. The refractive index of a material as a function of wavelength can be calculated using either a Sellmeier or a Laurent series equation. The Sellmeier series is given by:

$$n(\lambda) = \sqrt{1 + \sum_i \frac{B_i \lambda^2}{\lambda^2 - C_i}} \tag{2.6}$$

where B_i and C_i are ith order Sellmeier coefficients of a given material. Using this formula in conjunction with equation 2.5 allows the calculation of the GDD in a given material as a function of wavelength, and the total dispersion is simply the product of the GDD with the length of propagation.

2.1.3 Nonlinear optics

Nonlinear optics is the study of optics in the regime where the optical field is intense enough that the optical properties of the material start to be modified by the light propagating through it. This section presents a selective treatment of nonlinear optics, mainly to both introduce the concepts of phase matching, which become important when considering HHG later in the chapter, and to introduce some processes which will be utilised by experimental techniques described later in the thesis. The field is covered in depth by multiple sources which go into both the theoretical treatment and practical implementations of using these nonlinear effects [31].

The polarisation in the nonlinear regime can not be treated as simply being proportional to the electric field as in the case of classical optics and instead is usually expressed as a power series. If we assume that the polarization depends only on the instantaneous electric field, the polarisation, $\mathbf{P}$ as a function of the electric field $\mathbf{E}$ is given by:

$$\mathbf{P} = \epsilon_0 \left[\chi^{(1)}\mathbf{E} + \chi^{(2)}\mathbf{E}^2 + \chi^{(3)}\mathbf{E}^3 + \cdots \right] \tag{2.7}$$

where ϵ_0 is the vacuum permittivity, $\chi^{(n)}$ is the nth order susceptibility*. For simplicity's sake let us only consider the first 2 terms of equation (2.7) and consider the problem as purely scalar. If we were to apply an electric field of the form $E = E_0 \cos(\omega t)$, then,

*The susceptibility is an nth rank tensor. For our purposes we will largely ignore its vectorial nature.

Name	Susceptibility	Effect
Second Harmonic Generation	$\chi^{(2)}$	Generates light at twice fundamental frequency
Sum Frequency Generation	$\chi^{(2)}$	Generates light at frequency equal to the difference of two fields
Parametric Amplification	$\chi^{(2)}$	Amplification of field through frequency mixing processes
Self-phase modulation	$\chi^{(3)}$	Spectral broadening due to time dependant refractive index
Kerr Lensing	$\chi^{(3)}$	Modifies refractive index proportional to the intensity of the applied field

Table 2.1: The names of important nonlinear optical processes, the relevant susceptibility and the effect of the process.

ignoring propagation effects, equation (2.7) becomes:

$$P = \epsilon_0 \left[\chi^{(1)} E_0 \cos(\omega t) + \chi^{(2)} E_0^2 (1 - \sin(2\omega t)) \right]. \tag{2.8}$$

It can be seen that the $\chi^{(2)}$ expansion yields a harmonic term at twice the fundamental frequency. In practical terms this can lead to the generation of light at twice the fundamental frequency for sufficiently high intensities. This effect, second harmonic generation (SHG), was discovered only one year after the invention of the laser by Franken et al. [32]. Similarly the $\chi^{(3)}$ term yields a third harmonic term, leading to third harmonic generation (THG) [33]. In addition to the frequency mixing processes, a number of other effects leading to the modification of the light frequency or the properties of the nonlinear medium such as refractive index can occur. A summary of the important processes for the $\chi^{(2)}$ and $\chi^{(3)}$ susceptibilities are shown in table 2.1.

In SHG, the direction of the transfer of energy from the fundamental and the second harmonic is given by the complex phase of the product $E_1^2 E_2^*$ where E_1 and E_2 are the complex representations of the electric field for the fundamental and the second harmonic respectively. This is constant along the propagation direction only in the case when the wavevectors for the fundamental and harmonic are equal, or mathematically, that $\mathbf{k}_2 = 2\mathbf{k}_1$ is satisfied. In this case the harmonic power will, to the first approximation, increase with the square of the length of the nonlinear medium. However, due to chromatic dispersion in the nonlinear medium, in general there will be a non-zero mismatch between the wavevectors, $\Delta\mathbf{k} = \mathbf{k}_2 - 2\mathbf{k}_1$ which leads to a periodic change in the energy transfer direction as a function of crystal length. Using the mismatch $\Delta\mathbf{k}$ we can define the coherence length L_C:

$$L_C = \frac{\pi}{|\Delta\mathbf{k}|}. \tag{2.9}$$

After this distance the harmonic power reaches a maximum and increasing the interaction length yields no benefit. Thus efficient harmonic generation requires that this mismatch is minimised. It is possible to achieve the condition $\Delta\mathbf{k} = 0$ under some conditions, such as using birefringent phase matching for a single frequency, but this is next to impossible for broadband sources, where instead a compromise of phase matching across the bandwidth of the pulse must be reached.

2.2 Photo-ionisation and excitation processes

Any atom or molecule interacting with an electromagnetic field has the possibility of absorbing one or more photons of energy $\hbar\omega$. A bound-bound transition occurs when the photon(s) energy absorbed by the system is equal to the energy difference between two bound states, with energy E_i and E_f respectively. This leads to an electron being excited to a higher energy state in the system, leaving the system in an excited state. Absorption occurs around a small finite energy interval, called the spectral line width, centred around the energy difference of the two states. The line width, from the Heisenberg uncertainty principle $\Delta E \Delta t \geq \hbar/2$, also determines the lifetime of the state, which will then decay via multiple possible processes, including spontaneous and stimulated emission of radiation, the emission of a particle from the system, or through a change in the geometry or composition of a molecular system. Since these line widths are small, such transitions are also referred to as resonances. If instead the energy delivered to the system is sufficiently large that an electron is liberated to the continuum, the atom/molecule becomes ionised in a so-called photoionisation process.

2.2.1 Qualitative description of molecular orbitals and energy levels

Compared to atoms, which have only electronic energy levels, the internal energy of a molecule is spread across a number of rotational and vibrational modes. While in principle we would like to solve the Schrödinger equation for the molecular system, even the simplest conceivable molecule, H_2^+ already consists of three particles which makes it practically impossible to solve analytically, as the Hamiltonian already contains 6 interdependent terms, and the number of terms will increase rapidly with increasing complexity of the molecule. The starting point for all molecular physics is the Born-Oppenheimer approximation, which splits the full wavefunction Ψ into an electronic part ψ_e and a nuclear part ψ_N so that $\Psi = \psi_e\psi_N$ [34]. The approximation assumes that since the nuclei are far more massive than the electrons their motion can be neglected, allowing the electronic wavefunction to be solved for the Coulomb potentials created from nuclei fixed in space (the so called 'clamped nuclei' approximation).

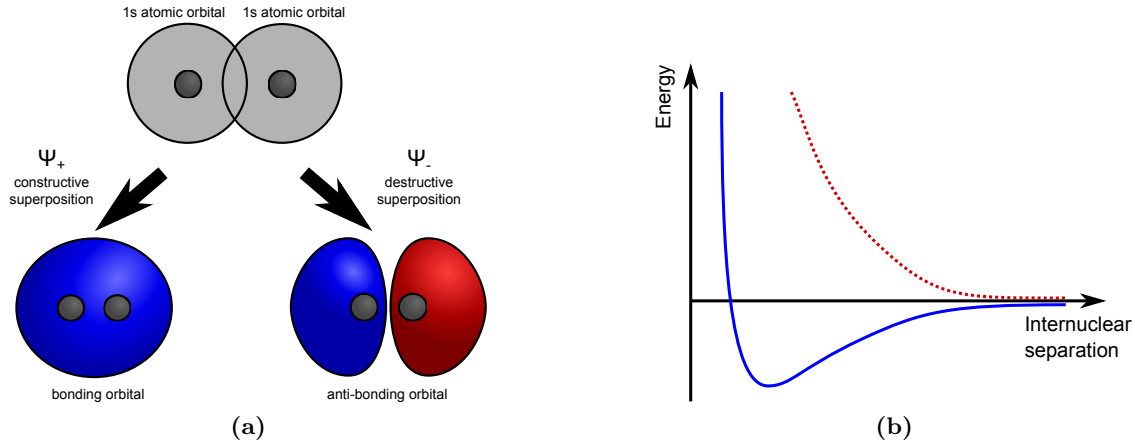


Figure 2.1: (a) Constructive and destructive superposition of two 1s atomic orbitals, leading to the formation of a bonding and anti-bonding molecular orbital respectively. The red and blue areas represent 3D surfaces with constant modulus of the wavefunction, with negative and positive values respectively. (b) Schematic of the energy curves for a bonding (blue solid line) and anti-bonding (red dashed line) orbital. The bonding orbital will lead to a stable molecule with an equilibrium internuclear separation, whereas the anti-bonding curve will lead to dissociation of the molecule.

In 1929, Lennard-Jones proposed that the molecular orbitals could be approximated through a superposition of the individual atomic orbitals [35], which qualitatively remains one of the most direct and easy to understand methods of describing molecular orbitals. As an example of this method, named linear combination of atomic orbitals (LCAO), let us consider a simple diatomic molecule with atoms we label a and b which have wavefunctions Ψ_a and Ψ_b respectively. These can be summed either constructively or destructively to form wavefunctions $\Psi_+ = C_1\Psi_a + C_2\Psi_a$ and $\Psi_- = C_1\Psi_a - C_2\Psi_a$ where the Cs are constants. The Ψ_+ wavefunction leads to surplus of electron density located between the atoms, which in turn shields the positive charges from both nuclei. The energy of the two atom system as a function of separation will therefore reach a minimum around a particular distance, or in other words a covalent bond is formed. This type is therefore referred to as a bonding orbital. The Ψ_- wavefunction on the other hand leads to charge depletion between the atoms, and they will therefore want to separate due to Coulomb repulsion of the nuclei, only reaching minimum energy at infinite separation. This type of orbital is therefore referred to as an anti-bonding orbital. A schematic of these two orbitals created from the combination of two 1s atomic orbitals is shown in figure 2.1a, and the corresponding energy curves are shown in figure 2.1b.

In molecules formed from larger atoms we must consider a larger number of orbitals, leading to a number of different types of molecular orbital. Orbitals are usually labelled according to their symmetry; p orbitals can form two different types of bond, σ bonds, which are formed from p orbitals in the axis of the molecular bond, and π bonds, which are formed from the p orbitals perpendicular to this axis. A * superscript denotes that the orbital is an anti bonding type, and a g/u suffix denotes whether the orbital is gerade

or ungerade, where gerade orbitals are ones that reverse in phase when you pass through the plane of symmetry. While this notation only strictly applies to homonuclear molecules the notation is convenient enough that it is used in literature to describe bonds in larger molecules as well.

2.2.2 Photoionisation as a probe of matter

A photoionisation event is a particularly good probe of matter since the kinetic energy of the resultant particles depends on the internal energy levels of the system being studied. By studying the energies of the products of the photoionisation process, information about the internal state of the system at the time of ionisation can be measured. The potential for the technique of photoelectron spectroscopy was first demonstrated by Einstein's seminal paper explaining the the photo-electric effect [36]; by using a photon with a well defined energy, the resulting kinetic energy of the ejected particles can be used to derive the work function of the bulk system. From these humble beginnings, photo-ion and photo-electron spectroscopy has extended well beyond being used only for fundamental science, with applications ranging from medicine to quality control of surfaces in industry.

A generic photoionisation process is any process in which the interaction of one or more photons with an atomic/molecular system results in the ejection of an electron e^- from the system. Considering a generic molecule AB, composed of two fragments A and B, the photoionisation can be expressed in the generalised form:

$$AB + n\hbar\omega_0 \rightarrow AB^{*+} + e^- + U. \tag{2.10}$$

Here, n is the number of photons with frequency ω_0 involved in the process, $\hbar = \frac{h}{2\pi}$ is Dirac's constant [†] and U is the total kinetic energy distributed between the fragments. The $+/-$ and the * superscripts denote the charge state of the products, and that the product is in an excited state respectively. A molecule or molecular ion AB^{*+} left in an excited state can decay via multiple channels, including radiative decay or fluorescence ($AB^{*+} \rightarrow AB^+ + \gamma$), dissociation of the molecule ($AB^{*+} \rightarrow A^+ + B + U$), or the ejection of an electron ($AB^{*+} \rightarrow AB^{2+} + e^-$), as well as more exotic combinations of multiple processes. If the final energy of the system after excitation and ionisation is higher than for the case where two or more fragments of the molecule were separated, the molecule will fragment or dissociate.

2.2.3 Direct ionisation

Direct ionisation by a single photon can occur when $\hbar\omega_0$ is equal or larger than the ionisation potential (IP) of the atom/molecule. This process can occur for any laser intensity,

[†] Also called the reduced Planck's constant

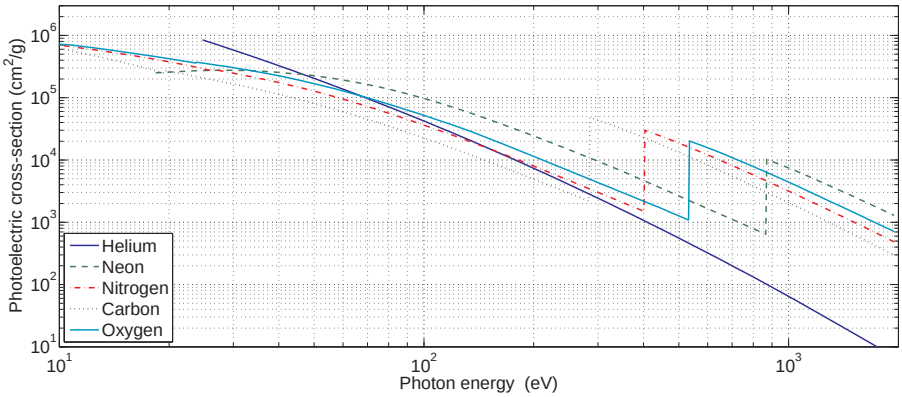


Figure 2.2: Log-log plot of the photoelectric cross-sections as a function of photon energy over the XUV and soft X-ray regimes for atomic species common to the experiments described later in the thesis. The sudden jumps in cross section correspond to the K-edge for the given atom, located just after the core-ionisation potential of the atom. Data retrieved from NIST database [37].

but is only possible using radiation in the XUV or X-ray region of the spectrum since even the most weakly bound valence electron has a binding energy of the order of 10 eV. For example neon, with a first IP of 21.6 eV, requires radiation with a wavelength equal or less than 57.4 nm for direct ionisation. The energy of the ejected electron is in this case simply the difference between the photon energy $\hbar\omega$ and the binding energy of the electron for the given state (figure 2.4 (a)).

X-ray sources such as storage ring synchrotron (SRS)s and FELs, with their much higher photon energies can directly ionise from even the K (1s) shell, and preferentially ionise from the largest energetically allowed sub-shell. The ability of X-rays to probe even the core states of samples has allowed XPS to be a powerful tool in measuring the binding energies or composition of a sample target [4, 5, 38]. Figure 2.2 shows the photoelectric cross sections for helium and a number of common, low Z atomic species relevant to experiments described later in the text. For a hydrogenic atom, the photoelectric cross section decreases smoothly with increasing photon energy, and increases with atomic number Z [39, pp. 313], and indeed this is the pattern that is observed in 2.2. In addition to this overall trend, there also exist a number of 'edges' located at photon energies just above the ionisation potential for a given shell, where a sharp increase in the cross section is observed as the shell becomes energetically accessible. Helium, with only one full shell, lacks such an edge.

The existence of the absorption edges has the distinct advantage of enabling site specific ionisation through careful selection of the photon energy. Taking carbon and oxygen as an example, at a photon energies $284.2 \geq \hbar\omega \leq 543.1eV$, the absorption cross section of carbon is approximately an order of magnitude larger than oxygen[‡]. Therefore by choosing

[‡]This region of the spectrum, called the 'water window' in literature, is of particular interest as water is therefore relatively transparent to these energies, allowing for studies of biological samples in the condensed phase.

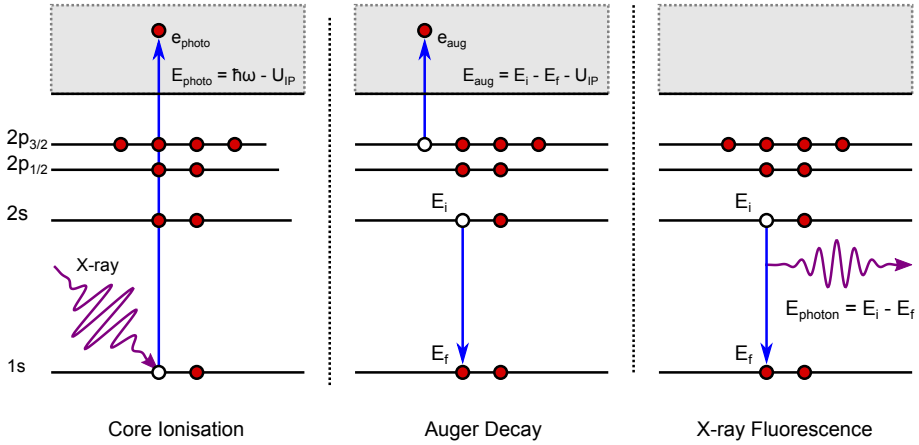


Figure 2.3: Schematic of core-hole creation and decay in neon. An incoming X-ray liberates a core (K shell electron), e_p. An electron from the L shell (in this case a 2s) decays into the core hole, and the excess energy leads to the emission of an Auger electron, e_{aug}, or an X-ray photon. The energy of the photoelectron E_{photo} depends on the energy of the incoming ionising photon, whereas both the Auger electron and the X-ray fluorescence energies depend only on the energy levels of the relevant electrons. Energy levels are schematic: the absolute values will depend on the electronic configuration at each step.

the right molecule and photon energy, you can preferentially ionise a specific site of the molecule.

A core ionised atom/molecule is left in a highly excited, unstable state, and the hole will be filled by an electron from a higher shell/sub-shell within a few tens of femtoseconds, and the excess energy from the decay yields either an X-ray fluorescence (a radiative decay), or the ejection of one or more electrons in an Auger process, named for Pierre Auger who first observed the process in 1929 [40]. Figure 2.3 shows a possible single electron Auger process in neon after core ionisation, and an equivalent fluorescence process involving the same sub-shells. Auger processes are labelled in a three letter format according to the shell transitions involved. For example the process depicted in figure 2.3 is a $KL_1L_{2,3}$ process, as it involves K-shell ionisation, followed by an L_1 sub-shell electron filling the hole, and finally a single electron being emitted from the $L_{2,3}$ sub-shell.

Auger and X-ray fluorescence are competing processes, and the ratio of the two processes is given by the fluorescence yield w_k, and depends strongly on the atomic number Z. R. Santra [41] presents a hydrogenic model of the core hole decay process, and the key findings are summarised thus. Whereas the Auger decay rate is to first approximation independent of the atomic number Z, the fluorescence rate scales with Z^4. As such, in the low Z limit, Auger processes are dominant with ω_i less or equal to 1% up to $Z = 18$ [42] with fluorescence becoming increasingly dominant in the limit of high Z. While the model applies only to hydrogenic like atoms, the results are similar for molecules. If we consider diatomics like N_2 and O_2, and hydrocarbon species, all the constituent atoms are still of low Z and as such Auger decay is the still the predominant mode of decay. Additionally, since the Auger electron and the X-ray fluorescence photon energies are independent of the

energy of the initial photon, and as such X-ray fluorescence spectroscopy and Auger electron spectroscopy (AES) have been widely used in studying both the structure of atoms and molecules, and the material composition of bulk systems [43].

In addition to this simple picture, there are also a number of other processes which can lead to a variation in the number of electrons being emitted. A valence electron may either be excited or liberated from the system as a result of the core electron ionisation, either through collisions of the core electron, or by the sudden change in the charge state of the molecule leading to the valence electron waveform collapsing to an ionised eigenstate. The excitation or ionisation of a valence electron is referred to as a 'shake-up' and 'shake-off' process respectively. In both of these processes the kinetic energy of the photoelectron is reduced and either deposited into the atom in the case of shake-up, or into the kinetic energy of the ionised valence electron in the case of shake-off. A shake up process will manifest in the photoelectron spectrum as a so called 'satellite' peak, shifted to lower kinetic energy compared to the main line. In the high intensity regime that an FEL is capable of creating, additional multi-photon effects will also be introduced, with the possibility of multiple routes of decay, depending on the timescales of absorption and decay.

To simplify labelling these processes, each step of the process can be labelled according to the electron type, with labels of P, A and V corresponding to photoelectrons, Auger and valence electrons respectively. So for example, a P_1A process would be the simple 1-photon core-ionisation followed by Auger decay shown in figure 2.3, whereas P_1VA would be a shake off process in which both a valence and core electron are removed before the Auger decay occurs. This notation will be used in the later sections of the thesis.

2.2.4 Multi-photon and above threshold ionisation

For lasers in the visible-IR region different mechanisms of ionisation have to be considered, which in the photon picture must all involve multiple photons. If an atom/molecule absorbs a single photon which is lower in energy than the IP of the system, it will initially be elevated to a virtual excited state which quickly decays back to the ground state. If the laser intensity is sufficiently high, the atom/molecule will absorb another photon before decay, and this process can be repeated multiple times. Multi-photon ionisation occurs when the total number of photons absorbed has sufficient total energy to overcome the IP of the system [44]. The rate at which ionisation occurs for N photons, R_N is related to the intensity I by the power relation:

$$R_N = \sigma_N I^N, \tag{2.11}$$

where σ_N is the N-photon absorption cross section for the system, which decreases rapidly with increasing N. The intensity dependence also increases dramatically for increasing N.

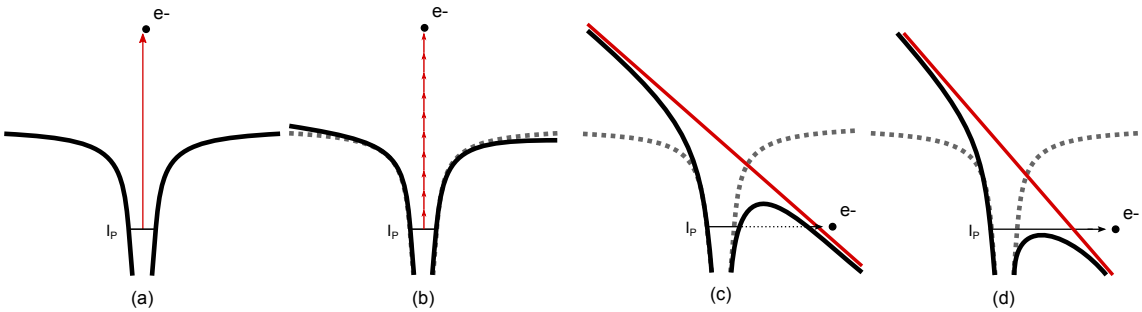


Figure 2.4: Different photoionisation mechanisms: (a) Direct ionisation (b) Multi-photon/Above-threshold ionisation (c) Tunnel ionisation (d) Over the barrier ionisation. The red line is the laser potential, the grey dashed line is the Coulomb potential, the black line is the combined potential the electron sees. Red arrows are photons or the laser field.

Above-threshold ionisation (ATI) can be considered an extension of multi photon ionisation (MPI) where the system absorbs additional photons/energy beyond the IP of the system [45], which will result in the kinetic energy of the emitted electrons being increased, with an energy U_k:

$$U_k = N\hbar\omega_0 - U_{IP}. \tag{2.12}$$

If we were to observe the photoelectron energy spectrum, we would observe a series of peaks separated by the photon energy $\hbar\omega_0$, rapidly falling off in intensity due to the decreasing cross section as n increases. These two mechanisms are demonstrated schematically in figure 2.4 (b).

2.2.5 Field induced ionisation

Beyond intensities in excess of 10^{13} W/cm^2, the distortion of the electric potential can no longer be viewed as a simple perturbation of the system, since the laser electric field can contribute to a significant distortion of the atomic/molecular potential. Considering the problem in only the x dimension for a single atom, the combined Coulomb and laser potential, $V(x,t)$ is given by:

$$V(x,t) = \frac{-Ze^2}{4\pi\epsilon_0 x} - eE_0 x \tag{2.13}$$

where Z is the charge state of the ion, E_0 is the electric field from the laser and e the elementary charge. If this distortion is large enough, one side of the potential can be suppressed to the point where the bound electron sees a finite potential, allowing ionisation via the mechanism of quantum tunnelling. This process, first report by Augst et al. in 1989 [46], and referred to as tunnel ionisation, is shown schematically in figure 2.4 (c).

For even higher intensities it is possible for the potential barrier to be suppressed below

the ground state energy of atom/molecule, in which case the electron is simply freed into the continuum, a process known as over-the-barrier ionisation, and is shown schematically in figure 2.4 (d). We can calculate the electric field required for the onset of over-the-barrier ionisation by taking the differential with respect to x of equation 2.13. By setting the differential to equal zero, we can find local maximum:

$$x_{max} = \sqrt{\frac{Ze}{4\pi\epsilon_0}E_0}. \tag{2.14}$$

By substituting 2.14 into 2.13 and using $I = \frac{c\epsilon_0}{2}E_0^2$ we can find the critical intensity required for over-the-barrier ionisation:

$$I_{\text{OTBI}} = \frac{U_{IP}^4\pi^2 c\epsilon_0^3}{2Z^2e^6}. \tag{2.15}$$

2.3 Strong Field Laser Physics

While multi-photon ionisation and low order ATI can be described quite adequately using low-order perturbation theory, it struggles to explain the spectra for higher orders of ATI and will completely break down for tunnel ionisation and beyond where the laser field contributes a significant distortion of the atomic/molecular potential. The regime in which perturbation theory is inadequate is referred to as the strong field regime.

2.3.1 Keldysh parameter

There is no sudden transition from the perturbative to the non-perturbative regime, and it is possible to have processes characteristic of both regimes occurring simultaneously. However in most experimental circumstances one will be the dominant process, and a useful measure of which is dominant for a given intensity is the Keldysh parameter, Γ, defined as the ratio between the tunnelling rate ω_t and the laser frequency ω_0 so that $\Gamma = \omega_0/\omega_t$. In the case of $\gamma < 1$, tunnelling is the dominant process, whereas for $\gamma >> 1$ MPI is dominant.

When the atom is ionised by a laser, the free electron is subjected to strong, oscillating electric field. The particle's motion in this case is given by the Lorentz force:

$$\mathbf{F} = q\left[\mathbf{E} + v \times \mathbf{B}\right] \tag{2.16}$$

where $\mathbf{F}$ is the force experienced by the particle, q the particle's charge, $\mathbf{v}$ its velocity, $\mathbf{E}$ the electric field and $\mathbf{B}$ the magnetic field. Assuming the non relativistic case, ie. $v \times \mathbf{B} \approx 0$, if we consider an electric field linearly polarised field in the x axis, where $E = E_0\cos(\omega_0 t - \phi)$,

the electron motion can be described classically by the equation:

$$m_e \frac{\partial^2 x}{\partial t^2} = E_0 \cos(\omega_0 t - \phi) \tag{2.17}$$

where m_e is the electron mass, t is time and ϕ the phase of the field. It can be seen from this equation that an electron released into the continuum will also undergo an oscillating motion. If we assume zero initial kinetic energy, and the slowly varying envelope approximation, we can find the cycle averaged energy the electron gains in the continuum. This is called the ponderomotive energy, U_p, and is given by the equation:

$$U_p = \frac{e^2 |E_0|^2}{4 m_e \omega_0^2}. \tag{2.18}$$

If we reformulate equation 2.18 by using $I = \frac{1}{2} c \epsilon_0 E_0^2$ and condense all the constants, we can express U_p in terms of intensity I and laser wavelength λ, yielding:

$$U_p[\text{eV}] = 9 \times 10^{-20} I[\text{Wcm}^{-2}] \lambda^2[\text{nm}]. \tag{2.19}$$

The Keldysh parameter can also be restated in terms of U_p, yielding:

$$\Gamma = \sqrt{\frac{U_{IP}}{2U_p}}. \tag{2.20}$$

The key consequence of equation 2.19 is that the ponderomotive potential increases linearly with intensity and quadratically with wavelength. For experiments where a high U_P is preferred, there is a great advantage to moving over to longer wavelength sources, and this is discussed in more detail in the next subsection. Conversely, for sources in the X-ray regime, U_P is essentially negligible as it can be assumed that the dominant ionisation routes are single or multi-photon processes as opposed to field induced processes.

2.3.2 High harmonic generation

HHG is a strong field process in which light is converted into integer multiples of its fundamental frequency ω_0. Compared to perturbative harmonic generation. HHG is capable of producing an extended spectrum of harmonics extending well into the XUV and recently even as far as the soft-X-ray region of the spectrum. A schematic view of a typical HHG spectrum is shown in figure 2.5. The primary features to note are that after the first few harmonics, which decrease rapidly in signal as one might expect from a perturbative model, there then follows an extended plateau of harmonics of approximately equal intensity until one reaches a sharp 'cut-off'.

As a broadband, coherent source, HHG has many potential applications, including the production of sub-femtosecond pulses, opening up a whole new range of pump probe

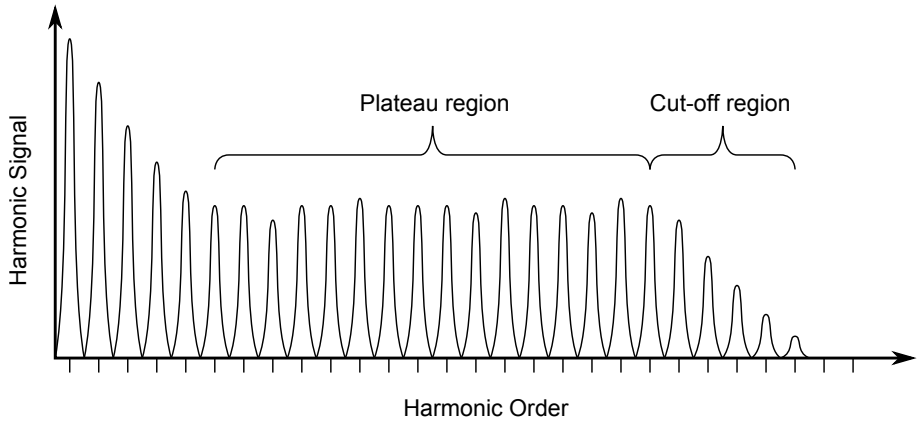


Figure 2.5: Schematic of a typical HHG spectrum. The first few harmonics display decreasing signal as one would expect of perturbative harmonics, followed by an extended plateau of harmonics with approximately equal intensity. The plateau is followed by a sharp cut-off.

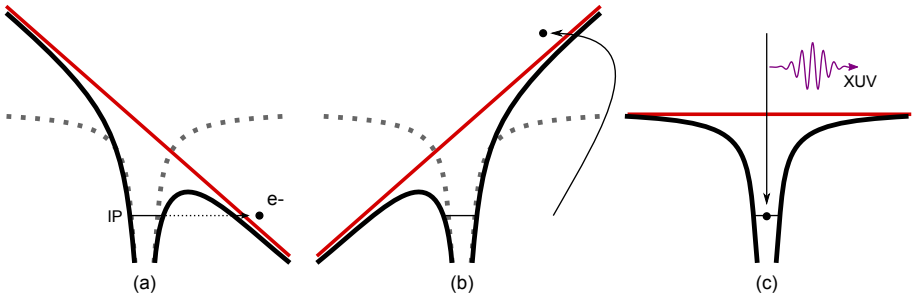


Figure 2.6: Three step model of HHG: (a) tunnel ionisation into the continuum, (b) acceleration of the free electron by the laser field and (c) recombination and emission of a photon. The red line is the laser potential, the grey dashed line is the Coulomb potential, the black line is the combined potential the electron sees.

experiments. Additionally, as a coherent source, it preserves structural information about the system that generated the harmonics within the spectra, providing a new tool for probing structural dynamics. The theoretical description of the HHG process can be split into two parts: the single atom/molecule response, and the macroscopic response of multiple emitters.

2.3.2.1 Single atom response

The physics behind HHG is well described both in a semi-classical model developed by P. Corkum [9], and a fully quantum mechanical model developed by M. Lewenstein [10]. According to Corkum, the process can be broken down into a simple three-step model, which is summarised in figure 2.6. Firstly the laser field depresses the potential of the atom/molecule such that tunnel ionisation can occur, and the electron will enter into the continuum. It is assumed that the electron has zero kinetic energy at this point. As the laser field changes direction over a half cycle of the laser field, the electron will be

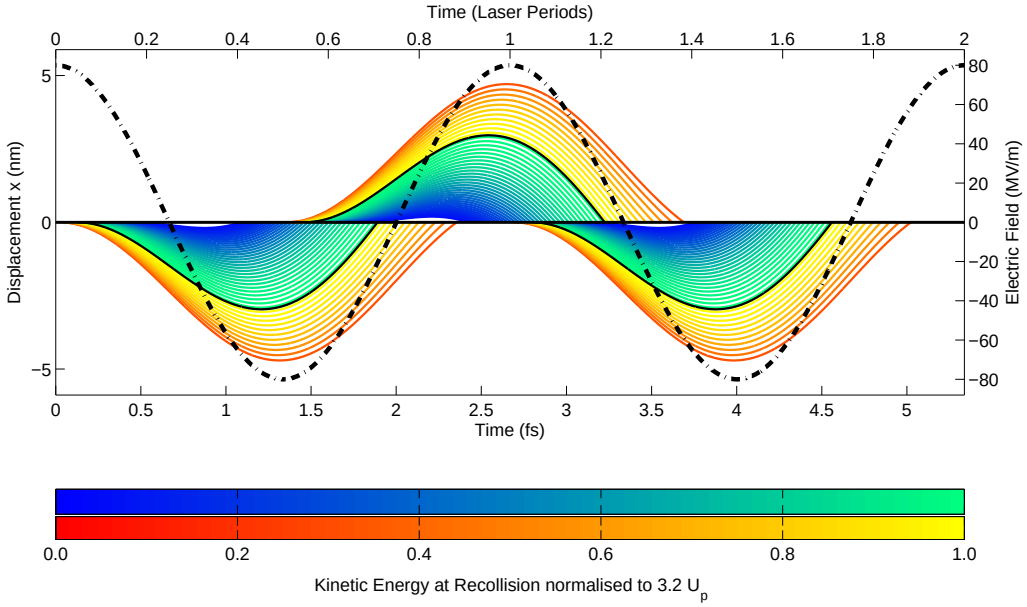


Figure 2.7: Classical electron trajectories in a CW electric field of maximum strength 8×10^{10} V/m. The blue lines correspond to short trajectories, the red lines correspond to the long trajectories. The solid black line corresponds to the trajectory with maximum recollision energy. The black dashed line is the electric field.

accelerated by the field, gaining kinetic energy and will be accelerated back towards the parent ion. This electron can then recombine with the ion, and will emit a photon equal in energy to the IP plus the kinetic energy gained in the continuum.

Let us first consider the classical trajectories of the electrons; these provide the most intuitive treatment while providing some meaningful results. If we consider an electron produced by by ionisation at time t_0, by integrating equation 2.17 with respect to t under the assumption that the electron initially starts at rest at $x = 0$, the velocity of the electron is given by:

$$v(t) = \frac{\partial x}{\partial t} = \frac{eE_0}{\omega_0 m_e} \left[\sin(\omega_0 t) - \sin(\omega_0 t_0)\right] \tag{2.21}$$

and the position $x(t)$ is given by:

$$x(t) = \frac{eE_0}{\omega_0^2 m_e} \left[\cos(\omega_0 t) - \cos(\omega_0 t_0) - \omega(t - t_0)\sin(\omega_0 t_0)\right]. \tag{2.22}$$

The kinetic energy can be calculated from $U_k = \frac{1}{2}mv(t)^2$, which yields:

$$U_k(t) = 2U_p \left[\sin(\omega_0 t) - \sin(\omega_0 t_0)\right]. \tag{2.23}$$

From analysis of these equations it can be seen that the recollision time and therefore energy depends on the time of birth. Not every ionisation time will lead to the electron

recolliding with the atom, those that do come after the crest of the electric field. Solving numerically we find the the maximum kinetic energy at recollision is approximately equal to $3.17U_P$. The maximum photon energy, $\hbar\omega_{\text{cutoff}}$, is therefore:

$$\hbar\omega_{cutoff} = U_{IP} + 3.17U_P. \tag{2.24}$$

We can therefore increase ω_{cutoff} in two ways, by using a higher U_{IP} target, or by increasing the U_P; when it comes to experiments we can either increase the intensity (through higher energy or tighter focusing), or go to longer wavelengths. For all other energies there are two possible electron trajectories that yield the same energy, a short and long trajectory. Figure 2.7 shows the electron trajectories for 2 cycles of an 800 nm continuous-wave (CW) electric field and their respective kinetic energies at re-collision.

The limitation of this semi-classical model is that it cannot predict the periodic structure of the harmonics nor more subtle effects on the harmonic yield from interference effects. The quantum mechanical models views the process a small part of the ground state electron wavefunction tunnelling out such that we are left with a bound wavefunction ψ_B and an accelerated wavefunction ψ_A. Practically, the solutions are generally computed using either a full time-dependent Schrödinger equation (TDSE) calculation or using the strong field approximation (SFA). Discussion of the mathematics of these methods is outside the scope of this thesis, and therefore the reader is directed to the following sources for comprehensive descriptions of these methods [47, 48]. In summary for the quantum treatment of the process, the probability of recombination is negligible for any state except the ground state since HHG stems from interference of ψ_A with ψ_B and the latter will be almost completely in the ground state.

HHG spectroscopy can therefore be used as a powerful probe of the structure and dynamics of atoms/molecules since the spectral structure will depend on the geometry of the generating state [49, 50]. Additionally, since a particular emission time (and therefore photon energy) maps to a specific recollision time allows the harmonics themselves to be used as a time resolved probe of the system producing the harmonics. Such techniques allow time-resolved measurements of molecular dynamics to be obtained purely in the spectral domain, with attosecond precision, and have successfully been demonstrated by Baker et al., who were able to observe structural rearrangement of CH_4 with a resolution of 100 as using only a 7 fs drive laser [51].

2.3.2.2 Collective response

When generating harmonics in the lab, one of course has to consider the contribution from a large ensemble of atoms/molecules. When considering propagation effects, it is convenient to switch from the photon picture back to the Maxwell wave picture. As in the case in perturbative nonlinear optics, phase matching between the fundamental and the

harmonics is essential to ensure a reasonable conversion efficiency, i.e. we wish to minimise $\Delta\mathbf{k} = q\mathbf{k}_L - \mathbf{k}_q$ where q is the harmonic order, $\mathbf{k}_1$ the fundamental wavevector and $\mathbf{k}_q$ the harmonic wavevector, and we need to achieve this for a broad range of harmonics. There are multiple sources of phase mismatch in the HHG process, including the Gouy shift, the wavelength and pressure dependent refractive index of the gas medium, free electron dispersion and the atomic phase shifts caused by different emission times [52]. We will consider each of these in turn, and how to optimise the experimental parameters to achieve a reasonable conversion efficiency in the laboratory.

We will first consider the Gouy phase shift and the atomic phase as these two effects are responsible for some key properties of an experimental HHG spectra. The Gouy phase shift is a purely geometrical effect caused by the focusing of the beam, where the phase fronts undergo a π phase shift as they propagate through the focus. If we consider the shift in the propagation axis, z, for a Gaussian beam, the geometric mismatch is given by the equation:

$$\mathbf{k}_{gouy}(r,z) = \frac{\omega_0}{c} - \nabla \arg\left[\frac{1}{2(z_R + iz)} \exp\left(\frac{\omega_0 r^2}{2c(z_R + iz)}\right)\right] \tag{2.25}$$

where $z_R = \pi w_0/\lambda$ is the Rayleigh range for a beam of minimum waist diameter w_0 and wavelength λ. It can be seen from this equation that this phase shift becomes much steeper for tighter focusing conditions. The atomic phase is the phase accumulated by electron as it spends time in the continuum, and is equal to :

$$\mathbf{k}_{at} = \nabla\left(q\omega_0 t_f - \frac{1}{\hbar}S\right), \tag{2.26}$$

where t_f is the recombination time, and S is the semi-classical action. In the long pulse limit, this can be approximated to [53]:

$$\mathbf{k}_{at} = \nabla\left(\frac{\alpha_j U_p}{\omega_0}\right). \tag{2.27}$$

The total phase mismatch from these contributions to the wavevector of the harmonic $\mathbf{k}_q$ is therefore:

$$\Delta\mathbf{k} = q\mathbf{k}_{gouy} + \mathbf{k}_{at} - \mathbf{k}_q, \tag{2.28}$$

or put another way, for most efficient phase matching we require the wavevectors $q\mathbf{k}_{gouy}$ and $\mathbf{k}_{at}$ to be approximately equal to the harmonic wavevector.

A schematic view of the wavevectors $\mathbf{k}_{gouy}$ and $\mathbf{k}_{at}$ as a function of both radius and z are given in figures 2.8a and 2.8b respectively. Note that while the wavevectors from the Gouy contribution are always nominally in the propagation direction, the atomic contribution reverses sign when travelling through the focus, and at the focus is zero. Given the phase

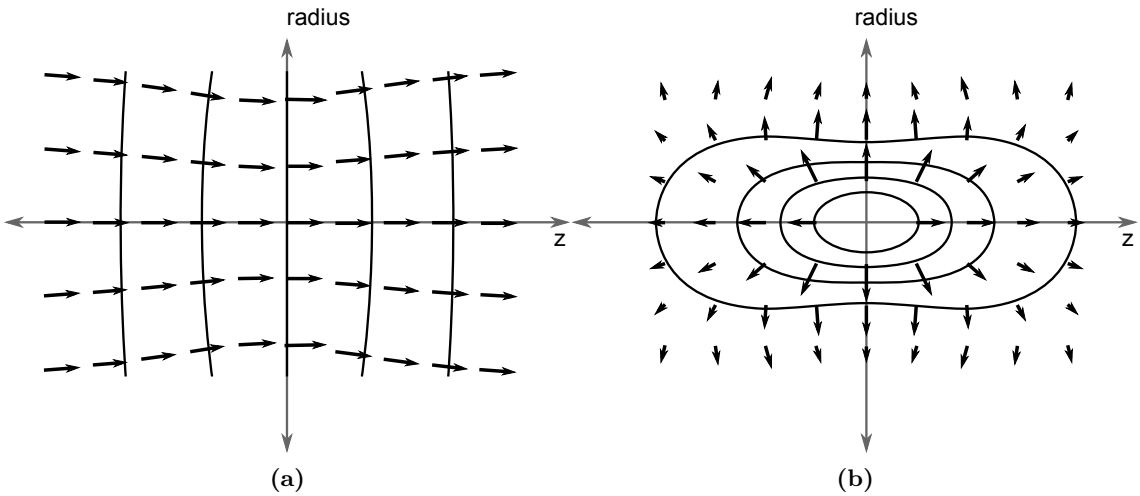


Figure 2.8: Wave vector maps for (a) the Gouy phase and (b) the atomic dipole phase for a focused Gaussian beam. Adapted from Phys. Rev. Lett. 55 pp. 3204-10 [54].

matching condition in equation 2.28, collinear (on-axis) phase matching is only possible by focusing before the gas jet. On the other hand by placing the gas jet before the focus, we can phase match off-axis emission. These two conditions also correspond to favouring phase matching of the short and long trajectories respectively [55]. Generally, if you want to use the XUV as a pump for another kind of experiment (ie using HHG as a source rather than a probe) you will primarily want on axis emission and so will therefore focus before the jet, whereas in spectroscopic experiments for which the the interference between the two trajectories becomes important, you will generally want to observe effects from both long and short trajectories and will focus after the jet [56, 57].

The above treatment neglects the effects of propagation through the medium. The refractive index of a gas n at pressure P for wavelength λ can be approximated by $n(\lambda) = 1 + \delta(\lambda)P$ where $\delta(\lambda) = n(\lambda)_{P=1bar} - 1$. Considering the effect on axis only, the phase mismatch due to the gas pressure can be approximated as:

$$\Delta k_{\text{disp}} = \frac{2\pi}{\lambda_L} qP \left[\delta(\lambda_L) - \delta(\lambda_q)\right] \tag{2.29}$$

where $\delta(\lambda) = (n(\omega)_{P=1bar} - 1)$. It can be seen that pressure differentials, as one might find in a typical gas jet, can cause this term to get very complicated, so we typically try to limit the process to a small interaction region where these effects are minimal. Additionally, since Δk_{disp} scales linearly with P, working with lower gas densities will also reduce this effect. If one has an atomic system where no cooling is required, it is also possible to use either a tube target or gas cell which has an approximately constant pressure over the interaction region.

The last things we need to consider are dispersion from free electrons and attenuation

of the X-rays by the generating medium. As the pulse propagates through the medium, it will ionise the medium and create free electrons. The creation of free electrons due to ionisation of the medium will cause defocusing as the electrons act as a negative lens. Similarly the further the X-rays propagate in the interaction medium, the higher the probability of absorption by the generating medium. Both can be minimised by limiting the density in the interaction region. Since these effects are quite difficult to model for real gas sources, generally the harmonics are optimised by performing a scan as a function of the pressure in the interaction region.

In summary, HHG requires careful consideration of the phase matching conditions, and considerable effort optimising the experimental conditions to ensure a reasonable conversion efficiency and photon flux.

2.3.3 Attosecond pulse generation

The structure of an HHG spectrum is a comb of harmonics separated by $2\hbar\omega_0$, which in the time domain will correspond to a train of pulses emitted every half laser-period. The broad bandwidth that the HHG spectrum covers is capable of producing pulses with sub-fs duration [17]. The possibility of HHG providing a sub-fs source was first proposed in 1992 [58], but it took almost a decade for the possibility to be demonstrated [59], with the first measurement of an attosecond pulse train performed by Paul et al. in 2001 [60] and the first measurement of an isolated pulse a few months after [18].

Isolated attosecond pulses, where only a single attosecond burst of XUV per driving pulse is produced, are of great interest as these are ideal for use in pump-probe experimental schemes. These are more complicated to produce than trains of pulses, with the general idea being to restrict the harmonic emission time to less than a single half cycle of the driving laser. Conceptually, the simplest way to achieve this is with a CEP stabilised, few cycle drive pulse ($\approx$5 fs). In this case the largest peak of electric field can be as much 40% larger than the adjacent peaks, and the highest energy harmonics will therefore only be emitted during this one intense half cycle, leading to the generation of a continuum in the cut-off region of the HHG spectrum and by filtering the HHG spectrum so that only this region is allowed to pass through, a single isolated pulse is yielded.

It is also possible to achieve isolated pulses using long pulse lasers by using other methods such as polarisation gating [61]. In this method a time dependent ellipticity is introduced to the laser. The HHG process is extremely sensitive to the laser ellipticity, as an elliptical field will drive the electron away from the atom preventing recombination. Thus, the HHG process will only occur for the short time where the laser is linearly polarised, restricting the emission to a short, well defined time.

Chapter 3

Laser technology for coherent XUV/X-ray radiation

The chapter begins with laboratory based tabletop sources of radiation, providing a brief introduction to the fundamentals of the lasing process, before focusing on the technology in building a high repetition rate, broadband, femtosecond duration source suitable for driving a XUV source using the process of HHG, and for use in ultrafast pump/probe experiments. The history and progress of these lasers will be described in parallel with a description of a Coherent Legend, a laser system I was responsible for running and maintaining over the course of my PhD. The section concludes with descriptions and discussion of common methods by which the systems can be diagnosed and characterised. The second half of the chapter details the operation of a FEL, and how a relativistic beam of electrons may produce coherent X-ray pulses under the right conditions, before concluding with a description of the LCLS FEL facility and its capabilities and specifications from a laser user's perspective.

3.1 Femtosecond optical lasers

A laser amplifies light through the process of stimulated emission. Most conventional laser systems start with some type of oscillator: a pair of mirrors enclosing a suitable gain medium, creating a laser cavity. Energy is initially supplied to the gain medium using a suitable pump centred around the absorption band of the medium. Initially, spontaneous emission will occur, with a small proportion limited to the axis of the cavity, which will be reflected back into the gain medium. These photons can then induce stimulated emission, which produces more coherent photons, and the process will repeat resulting in an intense beam. If one of the mirrors is then made to be only partially reflective (the output coupler), a small portion of the light will be allowed to escape. This light is the output of our laser.

Since their invention in 1962 [62], lasers have permeated every aspect of modern civilisation, from the microscopic diode lasers which power modern electronics to the football field sized lasers powering inertial confinement fusion experiments [63]. The requirements of a laser system being suitable for pump-probe experiments and a laser suitable for driving an HHG source are largely the same, requiring the laser pulses to be of the order of 10s of femtoseconds in duration, and thus broad bandwidth, ≈mJ pulse energies to reach the high intensities or fluxes, and ideally must also have a high pulse repetition rate so that experiments can be performed on a reasonable time frame. This section describes the theory and practical implementations behind building a laser system capable of meeting these requirements, with the focus on high power, femtosecond systems based on chirped pulse amplification (CPA) schemes. This will be supplemented by a description of the Coherent Legend-HE system which I was responsible for aligning, maintaining and operating over the course of my PhD.

3.1.1 Short pulse generation - femtosecond oscillators

Lasers can either be CW, where the laser output is approximately constant over time, and pulsed, where the output is confined to a train of pulses emitted at a constant repetition rate. These pulses can range in duration from microseconds to as small as only a few femtoseconds. By concentrating the laser power to this short amount of time allows lasers with reasonably modest average powers (≈1-10 W) to reach peak intensities in excess of 10^{14} Wcm^{-2}.

There are two common methods for generating short pulses: Q-switching and mode locking. In Q-switching, the losses in the cavity are modulated so that efficient lasing only occurs for a short time [62, 64]. Initially the cavity is held at a high loss state; as the system cannot lase efficiently, population inversion in the gain medium will increase quickly. The losses will then be reduced suddenly, allowing the start of lasing action, and the laser energy will increase extremely quickly. While this method cannot be used for the generation of femtosecond pulses as the loss modulation is limited to the electronic response of the modulator, it is still commonly used for nanosecond systems with reasonably high average powers due to its simplicity and robustness.

Femtosecond oscillators are based around the method of mode locking. Any laser cavity of length L_c is capable of supporting any longitudinal mode whose wavelength λ_n satisfies $L_c = 2L_c/n$ where n is any integer. The output intensity I will the be the result of the superposition of all of these modes:

$$I = \left| E_n e^{(i\omega_f t - \phi_n)} \right|^2 \tag{3.1}$$

where En and ϕ_n is the electric field and phase associated with the nth mode, ω_f is the fundamental frequency of the cavity and t is time. As the modes will typically vary in

phase, they will contribute to fluctuations in the output intensity. If however all modes can be made to oscillate in phase with each other, then all the modes will interfere constructively to form a single intense, short pulse at a repetition rate equal to the round trip time of the cavity. This is the principle behind the technique of mode locking. While the cavity can theoretically support an infinite number of modes, the modes that will be amplified will depend on the gain profile of the medium. This can be as small as supporting only 2-3 modes for something like a He:Ne laser, to upwards of tens of thousands for state of the art femtosecond systems.

Mode locking can be achieved either actively, where losses are modulated using an electro-optic or acousto-optic device such as a Pockels Cell, or passively in which a saturable, intensity dependent absorber is used. Only passive systems are capable of generating femtosecond pulses, as the response of the saturable absorber is much faster than any electronic response in active systems. Of particular relevance to the field of femtosecond systems is the method of Kerr lens mode-locking (KLM). First observed in 1991, KLM initially baffled scientists as it first appears to require no saturable absorber at all [65]. In summary, if light of sufficient intensity propagates through a crystal or other medium, the refractive index of the medium can be modified depending on the intensity of the light. This effect, the optical/AC Kerr effect*, will yield a refractive index n that is a function of both the normal (linear) refractive index n_0 and the intensity I:

$$n = n_0 + n_2 I \tag{3.2}$$

where n_2 is the nonlinear refractive index [31]. As a pulse will have a radially dependent intensity profile, the more intense centre of the beam will experience a larger refractive index than the edges, and the beam will undergo self-focusing within the medium. If an aperture is then introduced to the system, the low intensity modes will tend to be blocked by the aperture while the more intense modes will be free to propagate [66]. In the systems described later, the aperture is not a physical object but the lensing instead results in a better overlap with the pump laser, so called soft aperture KLM. The main disadvantage of this method is that the process is not self starting. An initial intensity perturbation is required to initiate the process, which is usually achieved by vibrating one of the cavity optics; once operating the process is usually stable.

The gain medium chosen for the laser is perhaps the most critical decision as the absorption/fluorescence spectra as well as the material properties define key properties such as wavelength, stability, bandwidth and resistance to damage. In the last two decades, the titanium doped sapphire (Ti^{3+}:Al_2O_3) or Ti:Sapph gain medium has proven to be the work-horse of the area of femtosecond science. The absorption band is centred at around 500 nm, making it ideal for pumping with frequency doubled Nd:YAG or Nd:YLF

*In literature it is often simply referred to as the Kerr effect, the label here is to ensure it is not confused with the DC Kerr effect which is observed through the application of an applied external field.

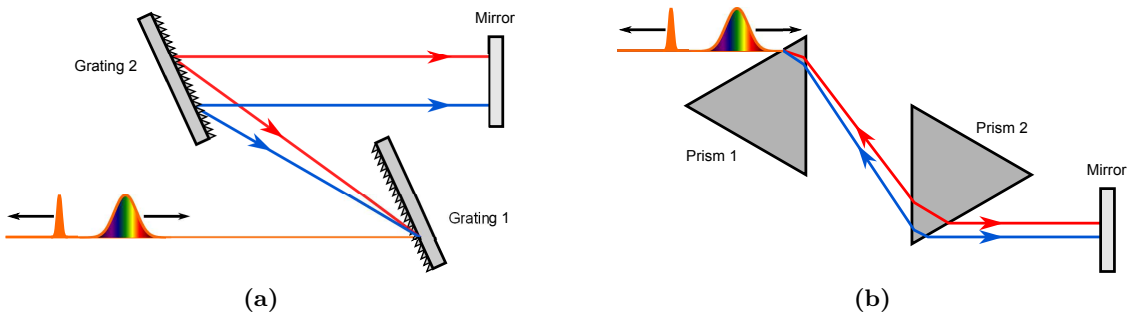


Figure 3.1: Schematic for a (a) grating pair compressor and (b) prism pair compressor. In both cases the longer wavelength components of the incoming chirped pulse are subjected to a longer optical path compared to the short wavelength components, leading to a compression of the outgoing pulse.

lasers and the gain bandwidth stretches from 600 nm to 1050nm, allowing for both high bandwidth (i.e. short) pulses with a large degree of tunability of the central wavelength [67].

Propagation of the optical pulses produced by such oscillators will introduce dispersion as discussed in section 2.1.2. In order to compensate for this we require a method of compressing the pulses back down, or in other words, we need to propagate the pulse through a system that has a negative GDD. The two common compression techniques used in laser systems are prism and grating compressors. These two methods are shown in figures 3.1a and 3.1b respectively. Prism compressors use a pair of identical prisms in combination with a mirror [68]. Grating compressors use a pair of anti-parallel gratings [69]. Comparing the two techniques, gratings will exhibit greater losses compared to prism compressors (which can be in excess of 35%) whereas prism compressors are limited in the pulse fluence since they are transmissive rather than reflective optics.

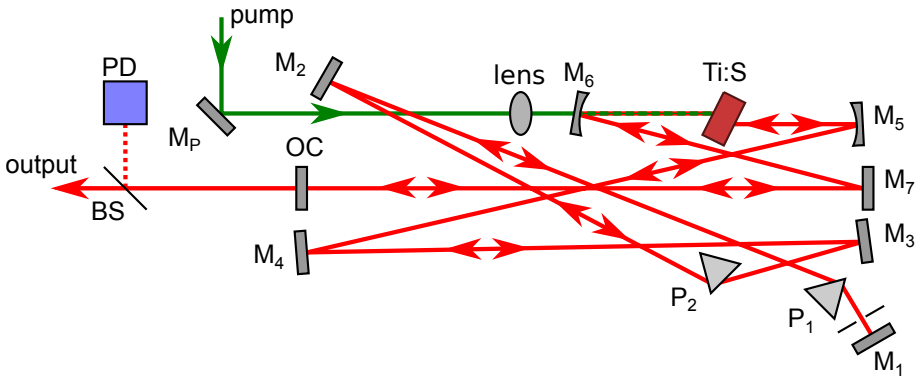


Figure 3.2: Schematic of the Micra-6 Oscillator. M = Mirror, PD = Photodiode, OC = Output coupler, BS = Beamsplitter, P = Prism. M5 and M6 are focusing spherical mirrors.

Figure 3.2 shows the optical layout for the Coherent Micra-6, the oscillator for the Legend-HE system, and a fairly typical commercial Ti:Sapphire oscillator. The Micra-6 is a Ti:Sapphire oscillator with a pulse repetition rate of 79 MHz. The crystal is pumped

by Coherent Verdi-V5 a CW, frequency doubled Nd-doped Yttrium Vanadate (Nd:YVO4) with a final central wavelength of 532 nm, and 4.5 W of pump power. It is focused using a lens and the overlap of the pump and IR was maintained with a piezo driven mirror in the pump laser which uses the photodiode to optimise for best power. The cavity is defined by mirrors M1 and the partially reflective output coupler OC, and the beam is focused through the crystal by two curved mirrors M5 and M6. The M4 mirror jiggles automatically to start modelocking, and the other mirrors exist to make the system more compact in space. The pulse compression is achieved with a prism pair, and the amount of compensation was tweaked by translating the prisms P1 and P2 in and out of the beam to vary the glass length in the beam. The Micra is capable of delivering 400 mW average power with pulse duration of ≈30 fs.

During day to day operation of the system, minimal if any tweaking was required as the piezo controlled mirror generally had enough travel to optimise the power, and the laser was usually stable within half hour of being turned on. Maintenance generally had to be performed every couple of weeks. The cavity mirrors were cleaned and then if required the end cavity mirrors were optimised by iterating between them for best CW power with the piezo mirror locked into its central travel position. Final wavelength and bandwidth adjustments were performed by iterating the prism distances for best bandwidth and central wavelength.

3.1.2 Chirped pulse amplification

Amplification of a laser pulse is performed in much the same way as they are initially generated: the pulse is propagated through a medium with a high population inversion. Stimulated emission will lead to an increase in energy of the pulse. Amplification of high fluence pulses, however, presents a challenge. As discussed in section 3.1.1, very intense pulses will undergo self focusing, and as we increase the energy of the pulse through amplification, this focusing effect will increase, eventually to the point where the fluence exceeds the damage threshold of the amplifying crystal. A useful quantity that can quantify the degree of focusing for is the B integral:

$$B = \frac{2\pi}{\lambda} \int n_2 I(z) \mathrm{d}z \tag{3.3}$$

where λ is the laser wavelength, n_2 is the nonlinear refractive index and $I(z)$ is the intensity as a function of the propagation distance z. In general any B integral over 2 will cause destructive self focusing. It can be seen from equation 3.3 that the only way to reduce this integral is to reduce the intensity. The method of CPA, first demonstrated by Strickland et al. in 1985 [70] and first applied to the amplification of femtosecond pulses by Pessot et al. in 1987 [71], proved to be a key technology in the development of a new generation of high power femtosecond systems. The principle of the method is shown in figure 3.3. In

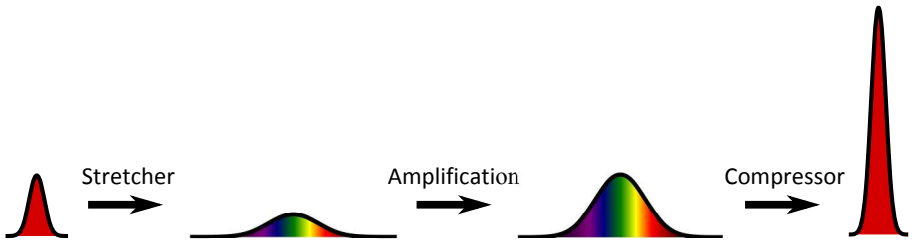


Figure 3.3: Schematic overview of the Chirped Pulse Amplification method

the same way that we can compensate for dispersion using a grating pair as described in previously, we can also use the inherent bandwidth of the short oscillator pulse to introduce dispersion via device called a stretcher, which will have the consequence of stretching the pulse in time. In a typical stretcher configuration, two gratings and a focusing optic are used to stretch the pulse to several hundred picoseconds with a much lower peak intensity, allowing it to be sent through an amplifying medium without damaging the medium. For the systems used in this thesis, the oscillator pulse typically needs in excess of 50 nm of bandwidth FWHM to provide sufficient stretching to avoid optical damage.

The stretched pulse is then sent through a Pockels cell, which selects only a small number of the oscillator pulses at a reduced repetition rate, thus reducing the MHz repetition rate of the oscillator down to that matching the pump laser for the amplifier, which depending on the type of system can be as low as 10 Hz up to several tens of kHz. The pulse is then allowed to propagate through the amplifying medium, gaining energy. Since, more often than not, not all of the energy in the gain medium is extracted in a single pass of the medium, the beam generally undergoes multiple passes through the medium to extract the maximum possible energy. There are two methods for achieving this: a multipass amplifier, and a regenerative amplifier. A multipass amplifier refers to any beam geometry in which the multiple passes through the amplifying medium are separated geometrically. The number of passes is limited by the geometrical complexity of the beam layout. As adding additional passes is not a trivial exercise the gain of the system must be kept high and generally requires the crystal to be pumped very close to the damage threshold. The beam can also be quite tedious to align. Regenerative amplifiers differ in that the multiple passes are formed using a cavity. A pulse is initially injected into the cavity using a waveplate and Pockels cell. Eventually after a number of round trips, the output pulse will be switched out with a second Pockels cell. As the number of round trips can be changed arbitrarily, it is quite easy to ensure that the gain is saturated by changing the number of round trips which is as simple as changing the timing of the second Pockels cell, which makes maintenance/optimisation far easier compared to a multipass system. Properties of the output beam such as spatial profile and the pointing stability will also be better as they are determined by the regenerative cavity rather than the properties of the seed.

After the amplification step we are left with a picosecond pulse with energy of the order of several millijoules. In the final step, the pulse is sent to a compressor, which

performs the inverse operation of the stretcher, plus compensates any additional dispersion introduced by the gain medium to achieve a short pulse. Typically the pulse duration will be longer than the input pulse due to the effects of gain narrowing. The gain profile will not be constant across all frequencies which means that some spectral components will experience a high gain than others, having the overall effect of squeezing the spectrum, lowering the FWHM bandwidth and thus increasing the transform limited pulse duration.

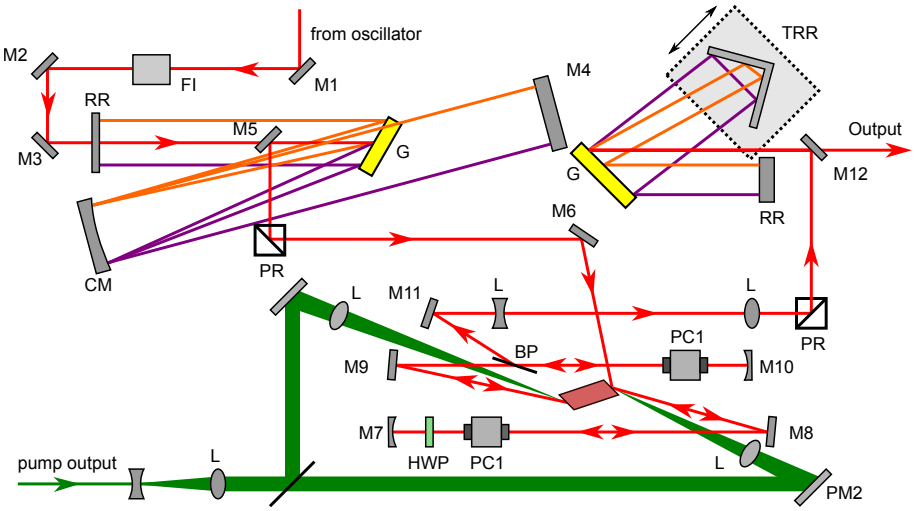


Figure 3.4: Schematic of the Legend-HE-USP-1K amplifier system. M = Mirror, L = Lens, RR = retroreflector, FI = Faraday isolator, G = Grating, PR = Periscope, BP = brewster plate, PC = Pockel's cell, HWP = halfwaveplate.

Figure 3.4 show the optical layout of the Legend-HE-USP-1K amplifier. The seed pulse from the Micra passes through a Faraday isolator before being routed into the stretcher. The stretcher uses a combination of grating and a curved focusing mirror. The pulse undergoes 4 passes of the grating and stretches the pulse from 30 fs to 200 ps, before being sent to the regenerative amplifier. The amplifier is a regenerative amplifier that is pumped using a 20 W Coherent Evolution, a 1 kHz, acousto-optically Q-switched Nd:YLF laser with pulse length of ≈300 ns. The amplifier cavity is made using mirrors M7 and M10, with a round trip time of approximately 10 ns. The Ti:Sapphire crystal is house in a temperature controlled perspex housing, with Brewster window entrances. The Pockels cell acts as a quarter wave plate, so that when the first cell is fired, the S-polarisation seed is switched to P-polarisation, and allowed to enter the crystal housing. After ≈20 passes, the second Pockels cell fires to switch out the pulse by reflecting it off the Brewster plate BP, before sending the beam to the compressor. The compressor again uses a single grating, 4 pass design to compress the pulse back to ≈45 fs. Since the amount of dispersion compensation required depends on the number of round trips in the amplifier cavity, there is a translatable retroreflector so that the final compression can be optimised by varying the grating-retroreflector distance.

Optimisation on a day to day basis was achieved by simply varying the Pockels cells timing to achieve the best pulse energy and optimising the compressor for best pulse length.

The regen cavity was tuned on a less regular basis by moving the half-waveplate to after the second Pockels cell. This bypasses the Pockels cell and makes the laser run CW. The end cavity mirrors M7 and M11 and the pump mirrors PM1 and PM2 are then iterated to optimise for best output power. The waveplate is then replaced and then the seed is allowed into the amplifier so that the pump-seed overlap can be optimised by iterating mirrors M5 and M6. Final adjustments are then performed using M7 and M11 to optimise for the best compromise in power and mode quality. Figure 3.7a shows example spectra taken from both the Micra and the Legend for a well optimised system.

3.2 Diagnostics and pulse measurement techniques

Strong field processes are very sensitive to the peak intensity at the interaction region, which for a Gaussian pulse focused to a $1/e^2$ beam diameter of w_0 is given by the equation:

$$I_{max} = 0.94 \times \left(\frac{2E_p}{\tau_p \pi w_0^2} \right) \tag{3.4}$$

Where E_p is the energy per pulse and τ_p is the FWHM pulse duration. It is therefore important to be able to characterise the laser system being used in order to have an accurate idea of what intensity regime you are in.

Average power can be measured using a power meter and the jitter/stability of the energy using a photodiode, and knowing the repetition rate of the laser it is then trivial to calculate the energy per pulse. The focal spot/beam profile measurements can be performed by simply focusing the beam onto a charge-coupled device (CCD) to obtain both intensity profile information from the pixel value and the size of the focus from the CCD number of pixels illuminated assuming one knows the pixel dimensions. The laser will need to be attenuated by several orders of magnitude using a neutral density filter to avoid damaging the CCD. Wincam and Spiricon produce commercial solutions which include an extensive software suite that will automatically calculate key parameters such as FWHM and $1/e^2$ profile sizes. The spectrum can be easily measured using a commercial CCD fibre optic spectrometer.

The measurement of pulse durations and the pulse structure present a more complicated problem. With long pulse lasers the pulse duration can be measured relatively directly by using either a photodiode or a streak camera, however once you reach the femtosecond regime, the pulse duration is far lower than the response time of any electronics (10s of picoseconds at the very best). Achieving an accurate measurement of the pulse duration is usually achieved by referencing the pulse against a time delayed replica of itself. Three of the most commonly used methods are intensity autocorrelation, frequency resolved optical gating (FROG) and spectral phase interferometry for direct electric-field reconstruction (SPIDER).

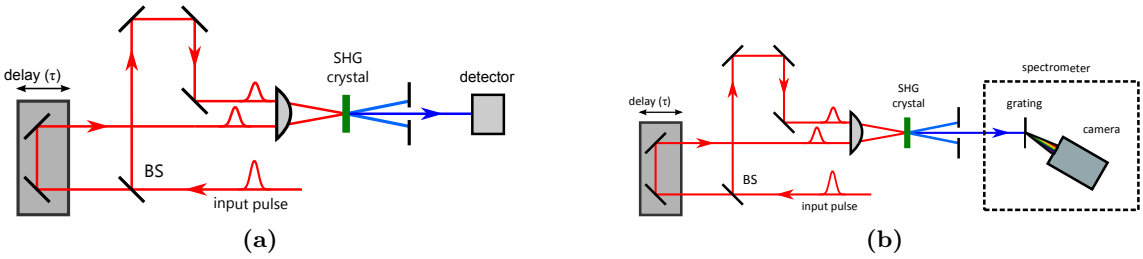


Figure 3.5: Schematic of a (a) multiple shot Intensity autocorrelator (b) SHG FROG. The main difference between the two is the addition of a spectrally resolved detector. BS = beamsplitter. Grey box = Delay stage.. BS = beamsplitter. Grey box = Delay stage

3.2.1 Intensity autocorrelator and FROG

Intensity autocorrelation remains the simplest way of measuring a laser pulse of 10s of femtoseconds. While it is not an apparatus I have used in any great depth, it serves as a good introduction to the principles ultrafast pulse measurement and also introduces concepts in common with the more complicated methods of FROG and SPIDER.

Two non-collinear pulse replicas are created using a beamsplitter, and these are both focused into a suitable SHG crystal such that they overlap in both space and time. If we then delay one of the pulses using a delay stage by a time τ the overlap of the two pulses will be reduced. The SHG signal as a function of τ is given by:

$$S_{AC}(\tau) = \int_{-\infty}^{\infty} I(t)I(t-\tau)\,\mathrm{d}t \tag{3.5}$$

By scanning the delay stage we obtain an auto correlation trace by observing the detected signal as a function of delay. The pulse duration is then found by multiplying the autocorrelation signal width by a deconvolution factor that depends on the pulse shape you assume. For a Gaussian this factor is $1/\sqrt{2} \approx 0.71$ and for a sech^2 pulse it is 0.64. If instead you use a 1D detector such as a CCD, the autocorrelation signal is instead mapped to a spatial intensity profile on the CCD array. This is then calibrated by introducing a known delay to one arm (for example by using a piece of glass).

This method has a significant limitation in that the autocorrelation trace depends only on the intensity. This becomes a problem for very short pulses, or pulses with significant structure, as very different pulse structures or chirps can yield similar autocorrelation traces, and you can lose a significant amount of information using this method. For pulses that exhibit a complicated structure or are below approximately 30 fs in duration, an accurate reconstruction requires a method that is able to retrieve the spectral phase profile in addition to the intensity profile. The FROG technique was first demonstrated by Trebino et al. [72] and since that time a large number of derivative techniques have been developed, including those that are capable of measuring attosecond pulses. A generic

FROG device can be described mathematically using the equation:

$$\Sigma_E(\omega,\tau) \equiv \left| \int_{\infty}^{\infty} E(t)g(t-\tau)e^{-i\omega t}dt \right| \tag{3.6}$$

where E is the electric field of the pulse, ω the frequency, t the time, τ is the delay and $g(t-\tau)$ is a gating function that can be varied in delay. The gating function produces a temporal 'slice' of the electric field, and integrating over all slices yields a spectrogram, a 2D dataset that is a function of both the frequency and delay. The gating function can be created by using a suitable nonlinear optical process.

There are a large number of different FROG designs all based on a different process such as THG [73] and interferometric techniques [74], though the focus will be on the SHG FROG. In design it is extremely similar to an intensity autocorrelator except that the detector replaced by either a 1D spectrometer or in the case of a single shot FROG, grating plus camera. The layout of the SHG FROG is shown in figure 3.5b. This design utilises the SHG process as the gating function, with the FROG signal taking the form:

$$\Sigma S_{SHG}(\omega,\tau) \equiv \left| \int_{\infty}^{\infty} E(t)E(t-\tau)exp(-i\omega t)dt \right|^2 . \tag{3.7}$$

The principle advantage of the SHG FROG besides its simplicity is that it is also the most sensitive type of frog. Because SHG is a $\chi^{(2)}$ process, compared to other geometries that use $\chi^{(3)}$ processes, the SHG FROG will yield more signal for a given pulse energy, and consequently can also measure pulses with far lower energies compared to the other beam geometries. The disadvantage of this type is that due to the symmetry of the SHG process, there is an ambiguity in the FROG trace, though this can be resolved by simply introducing a known dispersion to the beam. Once a FROG trace has been acquired, the data is processed with a retrieval algorithm to retrieve the pulse shape. The retrieval algorithm functions by first guessing an electric field E for the pulse, and calculating a theoretical FROG trace for that field. This trace is compared to the experimental trace, producing a matrix of the error function between the two traces. This error function is then used to refine the initial guess of the electric field. By going through multiple iterations of this algorithm the two FROG traces should eventually converge to the true electric field.

In addition to its ease of setup, the other principle advantage FROG has is its intrinsic error checking, as the algorithm can easily check to see if the pulse shape is physically possible. The disadvantage of this scheme is that due to its iterative retrieval algorithm, it can take some considerable time for it to converge, especially with very complicated pulse structures. This can however be improved though more efficient algorithms, and increases in computational power have served to make the reconstruction much quicker in the last decade.

3.2.2 SPIDER

SPIDER is an implementation of the more general technique of spectral shearing interferometry, and relies on producing two pulse replicas with different frequencies and observing the interference between the two beams [75]. A typical SPIDER setup is shown in figure 3.6. The input pulse is split into three different pulses. One of these pulse replicas is delayed with respect to the first by a delay τ, and propagated down the same optical path. The third pulse is propagated through a dispersive element to generate a stretched version of the other two pulses. The two legs are then focused into a nonlinear crystal. Assuming that both arms are overlapped in space and time, the two pulse replicas undergo sum frequency generation (SFG) with different, almost monochromatic parts of the stretched replica. The two pulses are up-converted to a frequency that is approximately double that of the input pulse, and separated by a constant frequency, Ω.

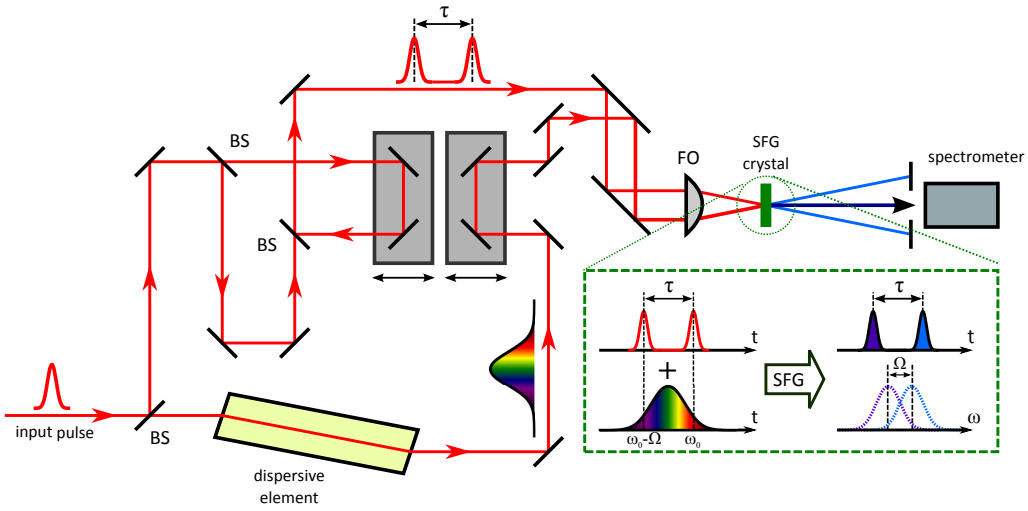
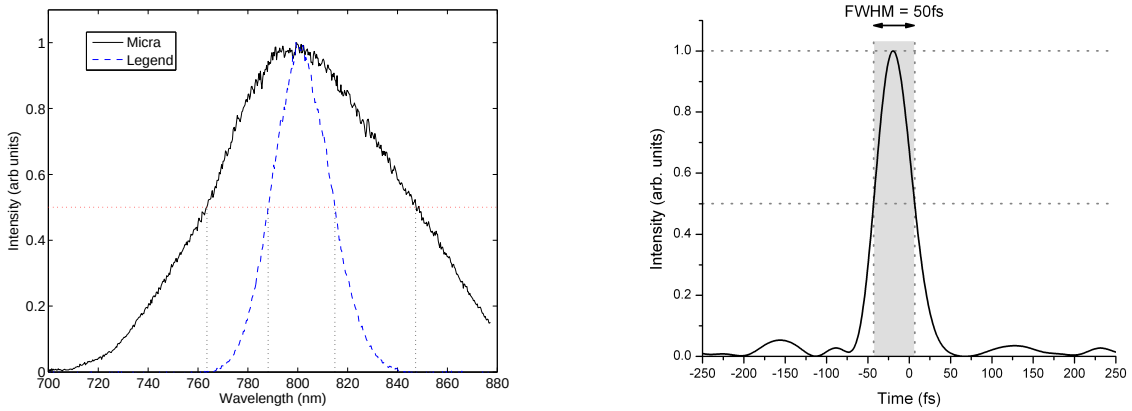


Figure 3.6: Schematic of a generic SPIDER. Three pulse replicas are created. Two are separated by a delay τ and sent down one arm, the remaining pulse is stretched and sent down another arm. The two arms are focused into a nonlinear crystal where SFG creates two spectrally sheared replicas of the original pulse, separated by a frequency Ω. The interference of the two pulses, resolved using a spectrometer allows retrieval of the spectral phase of the original pulse. BS = beam splitter, FO = focusing optic

The electric field of these two pulses are defined as $E_1(\omega) = E(\omega + \omega_0)$ and $E_1(\omega) = E(\omega+\omega_0+\Omega)$ respectively, where ω is the laser frequency, ω_0 is the frequency component of the stretched pulse that is mixed with the first replica, and Ω is the difference in frequency between the two pulses. If these two pulses are then interfered with each other they yield an interferogram that can be resolved using a standard CCD spectrometer. The signal of this interferogram, S_{INT} is then given by:

$$S_{INT}(\omega) = |E_1(\omega)|^2 + |E_2(\omega)|^2 + 2|E_1(\omega)||E_2(\omega)|\cos(\Delta\phi(\omega) - \omega\tau) \tag{3.8}$$

where $\Delta\phi(\omega)$ is the difference in the spectral phase of the two up-converted pulses. By



(a) **(b)**

Figure 3.7: Example of (a) spectra and (b) SPIDER trace from the Coherent Legend laser system.

letting $A_{DC} = |E_1(\omega)|^2 + |E_2(\omega)|^2$ and substituting the exponential form of the cosine into equation (3.8), so that $A_{AC}(\omega)e^{i\omega\tau} = |E(\omega_1)|\,|E(\omega_2)|\,e^{i\delta\phi(\omega)}$ allows us to rewrite it in the form:

$$S_{INT}(\omega) = A_{DC}(\omega) + A_{AC}(\omega)e^{i\omega\tau} + A^*_{AC}(\omega)e^{-i\omega\tau}. \tag{3.9}$$

By taking the Fourier transform of equation (3.9) we yield:

$$S_{INT}(t) = A_{DC}(t) + A_{AC}(t-\tau) + A_{AC}(t+\tau). \tag{3.10}$$

This will yield a trace that has three peaks: one large peak centred at $t = 0$ and two smaller sidebands at $t = \pm\tau$. These sidebands contain our phase information, which can be extracted by filtering out the other peaks and the performing an inverse Fourier transform back to frequency space, we are left with the spectral phase of the original pulse. By combining the measured phase and the spectral intensity the full electric field of the original pulse can be reconstructed.

SPIDER has an advantage over FROG in that the reconstruction is entirely non-iterative. This allows for real-time observation of the pulse duration and phase of the pulse, with minimal computational overhead. The SPIDER is thus ideal for tasks such as optimising the compressor as it is exceptionally easy to observe and optimise the temporal chirp in real-time. A commercial SPIDER made by APE GmbH was the apparatus used on a day to day basis to measure the pulse duration of the Legend and Red Dragon systems. This system was similar to the setup shown in figure 3.6 except that it used an etalon to create the time delayed pulse replicas, and a grating pair as the dispersive element. Figure 3.7b shows an example SPIDER trace acquired using this system for the Coherent Legend.

3.3 Soft/Hard X-ray free electron lasers

The femtosecond, high repetition rate optical systems described above take up a few 10s of metres squared at the largest, and any group with reasonable budget and available lab space can access a commercial system capable of delivering of delivering mJ pulses in 10s of femtoseconds or less, and using such lasers may gain access to the XUV wavelengths through a suitably engineered HHG source. X-ray FELs on the other hand are on a completely different scale: these are national scale facilities based around a particle accelerator, many hundreds or even thousands of metres in length, with construction and operating costs to match their huge scale. However in return, they offer a truly unique source of radiation that no other source is currently capable of delivering: high brightness, coherent X-ray pulses with a tunable photon energy/wavelength capable of spanning all the way from the XUV to the hard X-ray regime.

Free electron lasers were first conceptualised in 1970 by Madley et al. [76] and first demonstrated in practice by Deacon et al. in 1977 [77]. However it is only in the last decade that technological advancements in accelerator design have allowed the construction of a generation of XUV to hard X-ray sources with femtosecond pulse durations and in excess of microjoules of energy per pulse. As of writing there are 3 operating user facilities operating in these regimes: Free-electron Laser Hamburg (FLASH), operated by the DESY group in Hamburg [78], LCLS, operated by SLAC, based in Palo Alto California [79], and SACLA, operated by RIKEN in Japan [80]. Additionally, another hard X-ray laser, the XFEL project, is under construction by DESY, and LCLS-II, a source that will operate alongside the current LCLS facility is in the planning and design stages.

An FEL transforms the kinetic energy of a relativistic electron beam into coherent optical radiation and as such has completely different physics behind its operation compared to a typical optical laser. This section describes the operation of an FEL and the particular requirements necessary for operation in the X-ray region of the spectrum, before describing the capabilities of the LCLS user facility, where the experiments described later in the thesis were performed and analysed. The following description will be presented primarily from a user's perspective, covering in general only the basic principles of the FEL accelerator operation and design. Subtleties and nuances of the accelerator design will be largely ignored, and focus will be on what an end user can utilise from a scientific perspective. I will go into more detail on a few key aspects of the accelerator design where it is directly relevant to the experimental techniques described.

3.3.1 Undulator radiation

At their most basic, all free electron lasers have two essential components: a source of relativistic electrons from which the energy can be extracted, and a periodic magnet assembly

called an undulator, or 'wiggler' to generate the radiation. An undulator is constructed from a sequence of magnets with alternating polarity to create magnetic field that is periodic in space. If an electron is allowed to propagate through the undulator, it will undergo an oscillatory motion transverse to its nominal propagation axis. Two common forms of undulator exist: planar undulators, which have a periodic field in only one axis, and helical undulators in which has components in both axes. In this thesis we will be exclusively concerned with the former type.

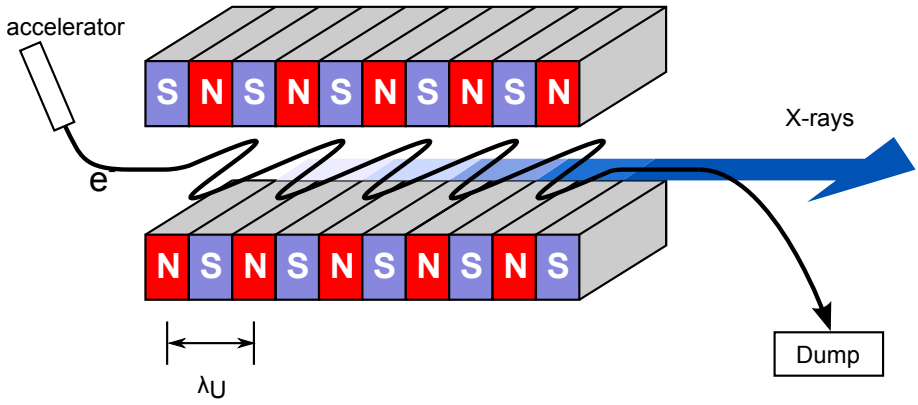


Figure 3.8: Principle of operation of an undulator. The periodic magnet field causes the electron to "wiggle" in a periodic motion, and therefore emits synchrotron radiation.

A generalised form of a planar undulator and the basic principle of its operation is shown in figure 3.8. As the electron beam propagates through the planar undulator, it will follow an approximately sinusoidal path as it is accelerated by the magnetic field, and will consequently emit synchrotron radiation. The path of the electron through the undulator can therefore be described by the following equations [81]:

$$x = -\frac{K}{\gamma}\cos(k_U s)/k_U \tag{3.11}$$

$$x\prime = \frac{K}{\gamma}\sin(k_U s) \tag{3.12}$$

where $k_U = 2\pi/\lambda_U$, where λ_U is the undulator period, s is the coordinate along the beam axis, γ is the Lorentz factor $\sqrt{(1-\beta^2)^{-1}}$ where $\beta = v/c$, and K is the dimensionless undulator strength parameter:

$$K = \frac{e\lambda_U B_0}{2\pi m_e c} \tag{3.13}$$

where B_0 is the peak on-axis magnetic field, e and m_e are the electron charge and mass respectively. For an electron with an initial velocity βc, the sinusoidal motion of the particle has the effect of reducing its velocity along the beam axis, $\dot{s}$ according to the

equation:

$$\dot{s} = \left[(\beta c)^2 - \dot{x}^2\right] \tag{3.14}$$

$$\approx c\left[1 - \frac{1}{2\gamma^2} - \frac{\dot{x}^2}{2c^2}\right]. \tag{3.15}$$

By substituting $\dot{x} = \beta c x'$, and using the definition of x' as stated in equation 3.12, and using the trigonometric identity $\sin^2(x) = \frac{1}{2}[1 - \cos(2x)]$ we yield:

$$\dot{s} \approx \overbrace{c\left[1 - \frac{1}{2\gamma^2}\left(1 - \frac{K^2\beta^2}{2}\right)\right]}^{\text{Average velocity}} + \overbrace{c\frac{K^2\beta^2}{4\gamma^2}\cos(2k_U s)}^{\text{Deviation from average}}. \tag{3.16}$$

For the undulator to emit radiation at reasonably high powers we require that the radiation emitted for each oscillation to add constructively. Since the on axis light will always be faster than $\dot{s}$, constructive addition requires that the electron falls behind the radiation by exactly one radiation wavelength λ_{rad} every undulator period, or mathematically:

$$\frac{\lambda_U}{c} = \frac{\lambda_U - \lambda_{\text{rad}}}{\langle \dot{s} \rangle}. \tag{3.17}$$

By using $\langle \dot{s} \rangle$ as defined in the first term of equation 3.16 and rearranging for λ_{rad} we find the resonance condition of the undulator:

$$\lambda_{fel} = \frac{\lambda_U}{2\gamma^2}\left(1 + \frac{K^2}{2}\right). \tag{3.18}$$

This is the fundamental wavelength a FEL will lase at. In addition to the fundamental frequency, the phase matching condition is also satisfied for the odd harmonics of the laser, allowing the potential to utilise higher frequency sources for a given system. In practical terms we have two possible 'dials' with which we can tune the photon energy: the electron energy and the undulator magnetic field B_0, however since undulators are typically constructed from permanent magnets for stability reasons, in practice the photon energy is tuned using the electron beam energy.

3.3.2 Self-amplified spontaneous emission

There are a considerable number of technical challenges to creating an FEL in the X-ray region, the first of which is getting coherent emission in the first place. For coherent, high gain emission we ideally want a large number of electrons to be constrained to a region far smaller than the radiation wavelength. Under these conditions all electrons would act a macroscopic point source, resulting in constructive addition of the radiation from all electrons, and the the coherent part of the radiation would surpass the incoherent component by a factor of the number of electrons N_e. In reality it essentially impossible

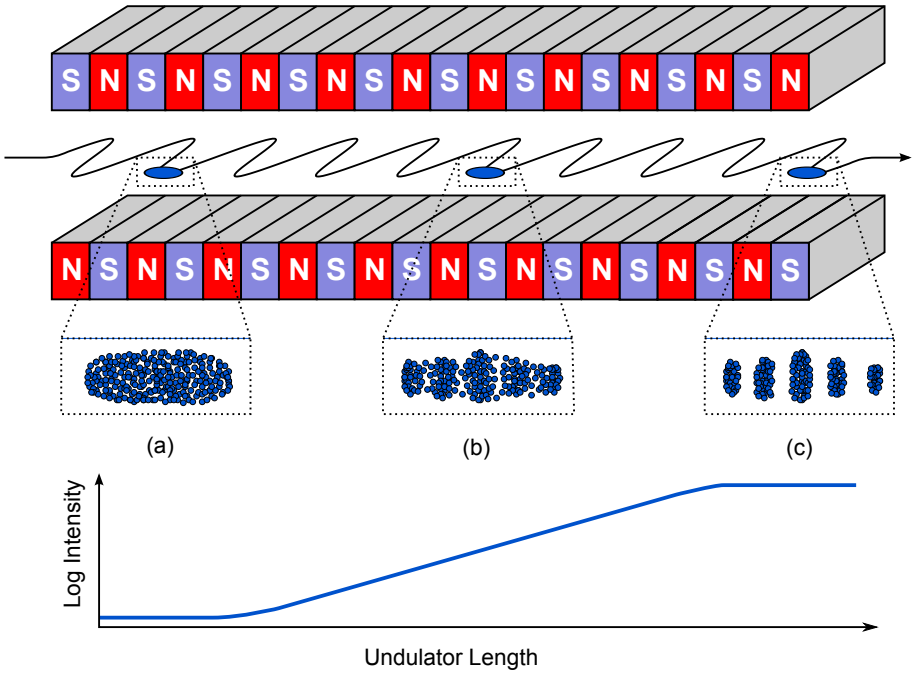
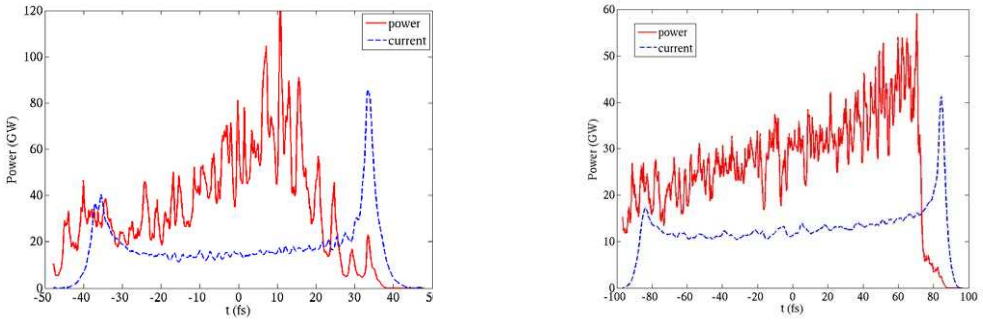


Figure 3.9: Overview of the microbunching process in an SASE FEL. (a) Initially the electron bunch emits incoherently as it is spread out over multiple laser wavelengths (b) The microbunches start to form through interaction with the initial radiation, resulting in more coherent emission and an exponential growth in radiation intensity (c) The microbunching is maximised and the FEL process reaches saturation.

to achieve an electron bunch this small; space charge effects would quickly destroy the bunch, and therefore typical bunches are many tens of wavelengths in length. Any emitted radiation will be, at least initially, incoherent [82, 83]. The second challenge is achieving a high gain. A conventional FEL design, operated in the visible or sub-visible frequencies typically operate with a low gain for a single pass of the undulator and high powers are achieved by enclosing the undulator in an optical cavity and using multiple, synchronised electron bunches to build up the radiation intensity. For an X-ray FEL, we are once again limited by the lack of suitable high reflectivity, normal incidence optics in the X-ray region, making a cavity design unsuitable. An X-ray undulator must therefore have sufficiently small gain length so as to produce its output over a single pass.

Even in the absence of an initial seed, the initial non-uniformity of the spatial electron distribution ensures that a small part of the initial spontaneous radiation will be at the undulator's resonant frequency, creating an initially weak radiation field. As mentioned previously, the basis of the FEL process is the transfer of energy between the electrons and the radiation field, and so the electrons will begin to interact with this spontaneous radiation, and will either gain or lose energy depending on their position relative to the field. Electrons that lose energy to the radiation will lose momentum, and will, according to equation 3.11, undergo a sinusoidal motion with a higher amplitude (and therefore a longer path length). These lower energy electrons will therefore lag behind the other



(a) **(b)**

Figure 3.10: Simulated pulses for the LCLS accelerator for nominal pulse durations of (a) 75 and (b) 175 fs. The red line indicates the pulse power as a function of time, the blue line the bunch current. Both were calculated using the GENESIS package. While the width of the pulse envelope follows the current, the structure of the pulse is quite erratic. Figure taken from N. J. Phys **13** 093024 [84].

electrons that instead gain energy from the field. This has the effect of increasing the local electron density and so the coherent emission increases and the radiation field starts to grow. This process repeats in a self sustaining way with the electron bunch eventually self-organising into small 'microbunches', each separated by a distance of λ_U, and with a length considerably smaller than λ_U. Each bunch then acts as a macroscopic point source, and the radiation of all bunches will add coherently since they're separated by one radiation wavelength, resulting in exponential gain of the coherent part of the radiation. This entire process of starting from noise and eventual high gain is termed self-amplified stimulated emission (SASE) and is shown schematically in figure 3.9. The gain length L_g, the length over which the FEL power grows by a factor of e, for a SASE FEL is given by the equation:

$$L_g = \frac{1}{3^{1/3}} \left(\frac{2\gamma^3 m_e}{\pi \mu_0 K^2 e^2 n_e} \right). \tag{3.19}$$

The gain length of the FEL can be used to define a parameter called, conveniently enough, the FEL parameter, which is given by the equation:

$$\rho = \frac{\lambda_U}{4\pi\sqrt{3}L_g}. \tag{3.20}$$

This parameter can be used to define a few useful properties of the system (see below). After approximately 20 gain lengths, the gain process will eventually saturate and may even reverse as the electron bunch is distorted due to continued interactions with the field.

While the SASE process allows the creation of high energy, short wavelength pulse, there are a few drawbacks of this technique that stem from the stochastic nature of the start of the process, with the effect that the properties of the pulses will vary significantly from shot to shot when compared to a traditional optical or seeded FEL. The pulse length will

be approximately the same as the length of the electron bunch, but the pulses themselves exhibit a varying sub-structure comprised of a large number of random individual spikes. Figure 3.10 shows some simulated pulses calculated using the GENESIS package (a 3D SASE FEL code). The spectral bandwidth of a pulse in terms of the FEL parameter is given by:

$$\Delta\omega = \rho\omega. \tag{3.21}$$

This can be compared to the width of a single spike, which is given by:

$$\Delta\omega_{spike} = \frac{1}{T} \tag{3.22}$$

where T is the bunch length [85, pp. 97]. The number of spikes for a pulse can be estimated by dividing equation 3.21 by equation 3.22, yielding:

$$n_{spike} = \rho\omega T. \tag{3.23}$$

Improvements to the FEL longitudinal structure can be attained by seeding the undulator with a coherent X-ray source, such as a filtered, monochromatic part of radiation created using a small undulator placed before the main undulator (so called self seeding schemes)[86] or through the use of a suitably intense HHG source [87]. These schemes largely remain in the planning stage of development at the time of writing, but is being considered for the next generation of FEL sources such as XFEL and LCLS-II,and the self seeding scheme has been demonstrated experimentally very recently using the LCLS [88].

Conversely, the transverse coherence of the FEL is generally excellent as the fundamental mode has the highest intensity on the electron beam axis, and will for normal operation be the dominant amplified mode. This has been demonstrated through experiments such as the classic Young's double slit experiment at both FLASH [89] and LCLS [90]. The spatial coherence in addition to the high flux makes the FEL an ideal source for coherent diffraction experiments, and there is currently a large focus on experiments in this area [25].

3.3.3 Electron Accelerator

It can be seen from previous discussions that in order to achieve lasing in the X-ray regime under high gain conditions, stringent requirements are placed on the properties of electron beam. Let us consider an undulator that has a period λ_U of 50 mm and a K of 1. To achieve lasing at a modest photon energy of 500 eV ($\lambda = 2.48$ nm) requires, according to the resonance condition (equation 3.18), that $\gamma \approx 3888$, or an electron kinetic energy of 1.986 GeV. Higher photon energies of course need higher electron energies so for X-ray operation we are looking at an electron source that can deliver electron kinetic energies in

excess of several GeV. Secondly, from equation 3.19 we can see that the gain length L_g will decrease with increasing electron count, or in other terms, the peak current of the electron bunch. A typical FEL requires a peak current in excess of 1000 A for a practical gain length. Lastly, the bunch must also be low emittance. The emittance of a beam can be thought of as the volume of the bunch in position and momentum space, and is required to be equal or less than 1 mm.mrad for SASE FELs to ensure a good overlap of the bunch with the radiation.

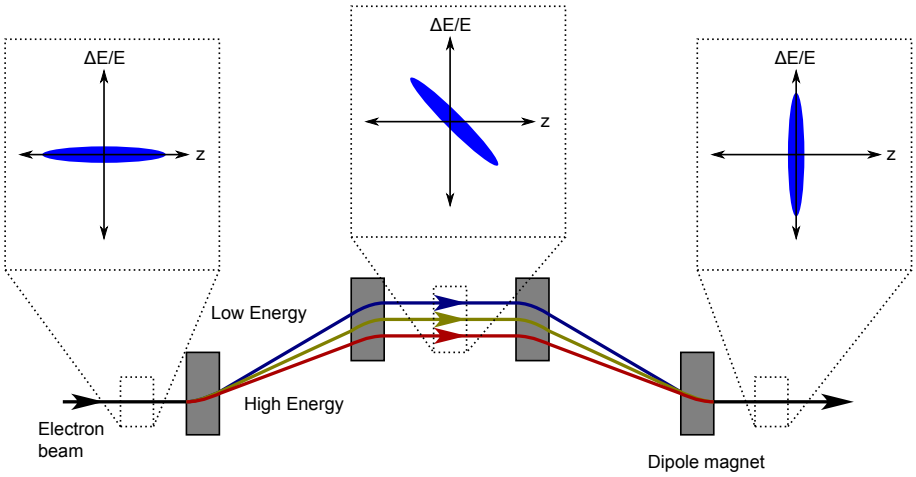


Figure 3.11: Magnetic chicane bunch compressor. The graphs represent the energy as a function of the distance in the propagation axis z.

The creation of an electron bunch with such properties is no simple task, and the only practical solution currently available is a large scale particle accelerator, and since an electron beam from a synchrotron source would not easily preserve the low emittance and short duration/high current bunches required due to the actions of the multiple bending magnets and subsequent losses to synchrotron radiation, all currently operating X-ray FELs use a linear accelerator (linac) electron acceleration based on radio frequency (RF) cavity technology [91]. The significant costs in both building and maintaining such accelerator sources, in addition to the large sizes of the systems mean that such sources are currently limited to national scale facilities. A promising alternative may eventually be found in laser wakefield technology, which uses a tightly focused optical laser to generate a plasma which then accelerates the electrons [92, 93]. These schemes show considerable promise, being able to generate both GeV electron beams and low emittance beams (albeit not simultaneously), and with the added advantage of being able to reach these energies over the order of centimetres rather than kilometres, but for the moment are no more than conceptual when it comes to FEL technology.

For all three currently operating XUV/X-ray FELs, an electron bunch is initially created using a laser driven photocathode, with a initially small peak current (a few tens of amperes) in order to limit Coulomb repulsion between particles, which at low energies is the dominant process for emittance growth [81]. The cathode is embedded in an RF

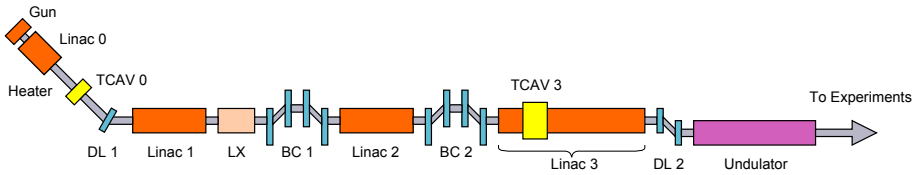


Figure 3.12: Schematic of the LCLS accelerator. Items labelled LX BC, DL and TCAV are an X band Linac, Bunch Compressors, dog legs and transverse mounted RF deflectors respectively.

accelerating cavity, which allows the bunch to be quickly accelerated to relativistic speeds. The electron bunch can then be compressed down to a high peak current using a device called a magnetic chicane. This device, which is displayed schematically in figure 3.11, which is conceptually similar to that of an optical compressor, and uses four dipole magnets to divert the electron beam in a trapezoidal path. By tailoring the parameters of the accelerator such that the bunch is accelerated 'off-crest', a longitudinal energy chirp is introduced to the electron bunch, with higher energy electrons arriving later compared to lower energy electrons. This energy chirp leads to an energy dependant path difference when travelling through the chicane, which is approximately given by:

$$\Delta l = L\theta^2 \frac{\Delta E}{E} \tag{3.24}$$

where L is the overall length of the chicane and θ is the angle of deflection. Thus through the actions of the chicane, the later, higher energy electrons travel a smaller path the earlier, lower energy electrons, and the bunch is compressed. Actual accelerators use multiple bunch compressors for practical reasons, primarily that performing the compression in a single step has deterimental effects of the emmittance properties of the beam at the high electron energies required for X-ray operation.

3.4 Linac Coherent Light Source free electron laser

The LCLS user facility is a soft-hard X-ray FEL operated by the SLAC National Accelerator Laboratory in Menlo Park, California. It is a SASE FEL which has an accelerator that is based on the old 3 km long linac that was originally built in the 1960s to be used for particle physics experiments. The LCLS utilises a significant amount of the last 1 km of the accelerator to seed a next generation light source that is as of writing capable of delivering pulses from a few hundred to less than 10 femtoseconds in duration, across a broad range of soft and hard X-ray wavelengths.

A schematic of the accelerator elements is shown in figure 3.12 and each section is described comprehensively in the Conceptual Design Report published by SLAC [94]. To summarise: at the 2 km point of the old accelerator a new beam line consisting of an RF coupled photocathode based electron gun and a small injection accelerator has been

Parameter	Hard (Long)	Soft (Long)	Unit
FEL gain length	3.0	1.5	m
Wavelength	1.5	6-22	Å
Photons per Pulse	1.0-2.3	10-20	10^{12}
Energy per Pulse	1.5-3.0	1.0-2.5	mJ
Peak Power	15-40	3-35	GW
Pulse Duration (FWHM)	70-100	70-500	fs
Bandwidth (FWHM)	0.2-0.5	0.2-1.0	%
Peak Brightness	20	0.3	10^{32}
Wavelength Stability (r.m.s)	0.1	0.2	%
Power Stability (r.m.s)	5-12	3-10	%

Table 3.1: Key parameters of the LCLS accelerator for both soft (500-2000 eV) and hard (8000 eV) X-rays for long pulse duration operation. Lower pulse durations can be achived at the expense of photons and energy per pulse due to the lower number of electrons in the bunch. Table adapted from Nat. Photon. Volume 4 pp. 641-7 [79].

installed. The electron gun is seeded by a 3 ps ultraviolet (UV) laser source which operates at a maximum rate of 120 Hz, and defines the repetition rate of the FEL. The electron bunch is injected in the main accelerator, composed of 3 different RF accelerator sections, a short X-band accelerator section and two bunch compressors. At certain sections along the accelerator are transverse mounted RF deflectors, which deflect the electron bunch onto an imager so that the bunch properties may be measured absolutely. All the accelerator sections together are approximately 1 km long, and are capable of accelerating electrons to energies between 3.5 and 14 GeV by the time they reach the undulator. The undulator is 132 m long, constructed from 33 individual segments with a 3 cm effective undulator period and an effective undulator parameter K of 3.71.

After the undulator the electron beam diverted to an RF phase cavity, which is used to coarsely measure the arrival time of the electron bunch before it is dumped, and the X-rays continue propagating to a diagnostics section called the front end enclosure (FEE), which houses devices for measuring and attenuating the pulse energy. Beyond the FEE lies two experimental halls (the near and far hall) where the user facilities and experimental chambers are located. Each experimental hall contains three different end stations, each with a unique set of instruments designed for a particular area of study, ranging from simple atoms to surfaces/condensed matter and warm dense matter/plasma experiments and allowing techniques ranging from time of flight to coherent diffraction imaging.

3.4.1 Specifications

As of October 2012, the fundamental photon energy of the LCLS can be varied from a minimum of 290 eV up to 10 keV. LCLS is capable of operating in a number of bunch charge regimes. For soft X-ray generation the charge is generally varied from ≈250 pC

with a pulse duration ≈70 fs down to as low as 10 pC and pulse durations low as 5 fs. The pulse energy can be as high as 3 mJ, but typically closer to 1-2 mJ, with the pulse energy decreasing with the bunch charge due to the decreased number of electrons in the bunch. A summary of pulse specifications for operation in the 250 pC bunch charge mode are presented in table 3.1.The pulse energy can be attenuated continuously by up to a factor of 10^4 using a combination of both solid beryllium attenuators, and a high pressure N_2 gas attenuator.

3.4.2 Characterisation of Free Electron Laser pulses

Because the shot to shot variability of pulse properties is much higher than one would expect with a traditional optical source, due to the stochastic nature of the SASE process, a series of diagnostics capable of measuring the properties of each pulse on a shot to shot basis is crucial to allow the necessary postproccessing of the acquired data. The pulse energy is perhaps the most visible manifestation of this variability: whereas typical optical lasers might have pulse energy variation of less than 1%, SASE FELs can vary shot to shot by essentially 100% of the peak value. The energy jitter has origins in the sensitivity of the bunch compression ratio (and therefore the electron bunch peak current) to the jitter of the RF accelerator parameters [95, 96]. The pulse energy is monitored on a shot-by-shot basis using a series of gas detectors that measure fluorescence in X-ray exposed nitrogen [97–99]. The X-ray beam is allowed to propagate through a tube containing approximately 10^{-1} mbar of molecular nitrogen. A small percentage of the photons will be absorbed (see figure 2.2), causing core ionisation and Auger decay, emitting a number of electrons. By confining these electrons with an axial magnetic field, these electrons will deposit almost all of their energy into the surrounding molecules, which are excited and then radiatively decay primarily over the 300-400 nm wavelength range. This light is detected by a photo-multiplier tube (PMT) with a UV filter, and the amplified signal is proportional to the pulse energy. An absolute energy calibration is then found by through a destructive measurement of the electron energy beam loss. There are a total of four detectors, two located before and two located after the solid and gas attenuators, which in this thesis are labelled 1/2 and 3/4 respectively.

The measurement of the pulse duration presents a greater problem, because in addition to the problems inherent in femtosecond precision measurement as discussed in section 3.2, we have the added difficulty in the lack of suitable X-ray optics. Nevertheless, direct measurements of the pulse duration have been demonstrated, such as autocorrelators based around ionisation in helium, where the two-photon ionisation process acts as the nonlinear process [100, 101]. However these measurements are technically challenging to achieve at the same time as an actual experiment, so shot to shot statistics are instead calculated from electron beam parameters which are less challenging and disruptive to measure in situ. The X-ray envelope can be assumed to be a close replica of the electron bunch, and

so the pulse duration for a given shot can then calculated from the ratio of two electron beam measurables: the peak current A_{max} and total charge Q_{Tot} of the electron bunch:

$$\tau = \frac{Q_{tot}}{A_{max}}. \tag{3.25}$$

This yields an upper limit on the pulse duration, though the quantitative studies of the pulse duration mentioned above indicate that the true durations may be up to a factor of 2 less than this upper limit [100, 101]. The FEL pulses also display an energy jitter due to effects stemming from both the accelerator, such as thermal fluctuations, and from the stochastic nature of the SASE process. A soft X-ray spectrometer exists in the Soft X-ray Materials Science (SXR) end-station, which can measure the time averaged spectrum, but for shot to shot information this information is again derived from the electron beam parameters. Using equation 3.18 and knowing that the $E_{photon} = hc/\lambda$ and the electron beam energy $E_e \approx \gamma mc^2$ in the limit of large γ, we can rearrange equation 3.18 to show that $E_{photon} \propto E_e^2$. For LCLS the central photon energy for a particular pulse is calculated using the equation:

$$E_{photon}[\text{eV}] = (E_e[MeV])^2 \times \frac{8330}{13720^2}. \tag{3.26}$$

Square brackets denote units used for each quantity. The constants in this equation are derived from both physical constants and the undulator parameters. At present shot to shot information about the exact form of the spectrum (such as bandwidth) is not available, though destructive measurements of the spectrum have yielded a pulse bandwidth of 0.5-1.0% of the photon energy.

Figure 3.13 show typical shot to shot statistics of the photon energy, pulse duration and pulse energy for a typical run in the low bunch charge mode. These were calculated and measured for a run performed in October of 2011, over 15000 consecutive laser shots.

3.4.3 Pump-probe experiments using X-rays

In addition to the FEL source, it is often desirable to include one or more additional optical lasers for use in a pump-probe setup. The main technical challenge associated with this kind of setup is achieving synchronisation between the FEL and the optical lasers. The electron energy jitter described previously will also be translated into a timing jitter relative to the RF field by the action of the bunch compressors [29] (since the path length is energy dependent), which means that the arrival times of X-ray pulses will also display a jitter. The arrival time can be measured relative to the RF reference using a phase cavity placed after the undulator and before the electron beam is dumped. By careful measurement of time zero, and by binning data accordingly by a combination of the phase cavity jitter and the delay stage positions in post-processing, we can successfully build up

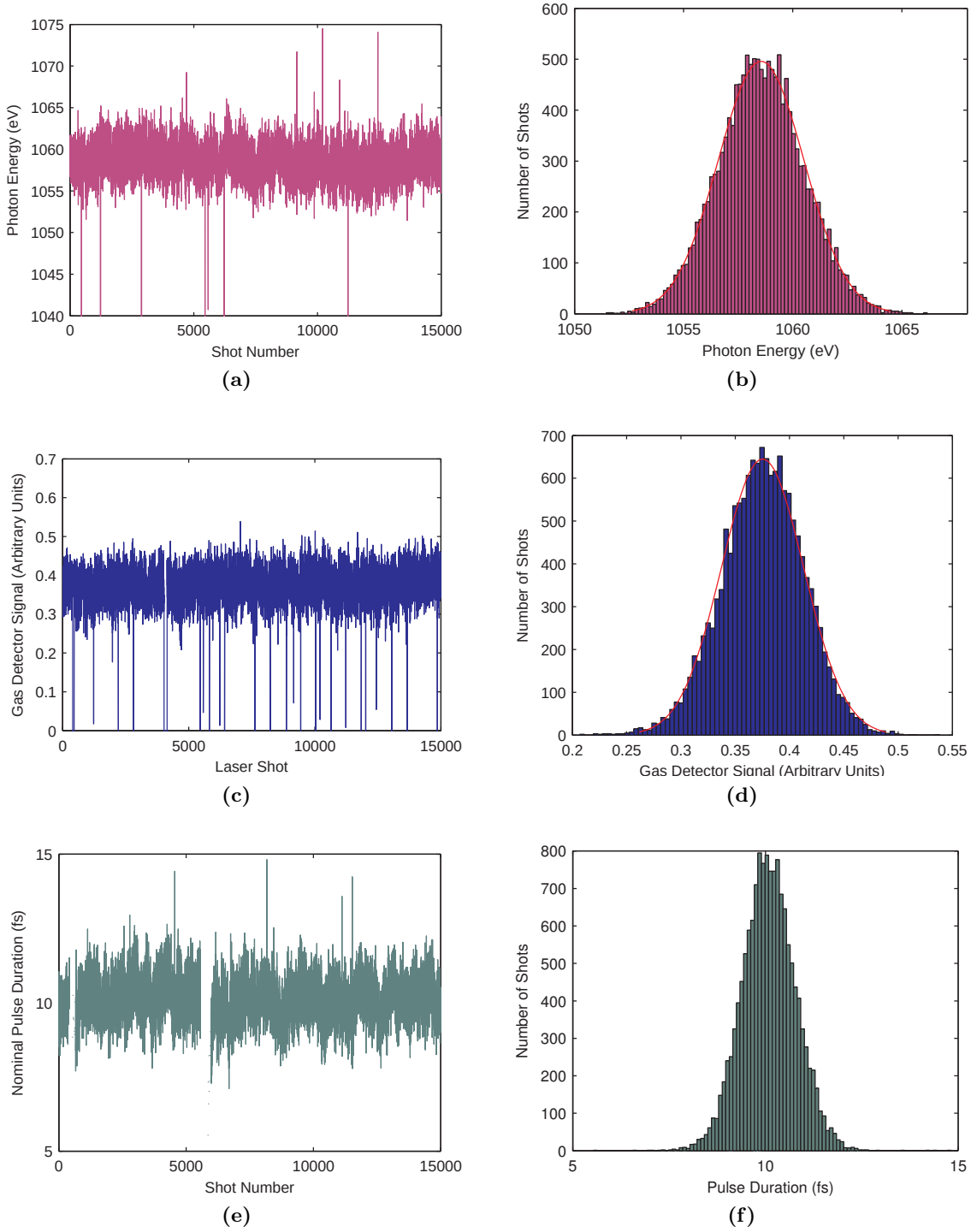


Figure 3.13: Shot to shot variability of LCLS electron beam and X-ray parameters for a low bunch charge mode run with a photon energy of 1060 eV for 15000 consecutive shots. **(a)** Photon Energy as a function of laser shot **(b)** Photon energy Histogram **(c)** Gas detector signal as a function of laser shot **(d)** Gas detector signal histogram. **(e)** Nominal pulse duration calculated using equation 3.25 as a function of laser shot **(f)** Pulse duration histogram. The gas detector values are proportional to the total photon flux. The histograms have had spurious low/high values omitted for better clarity of the overall distribution.

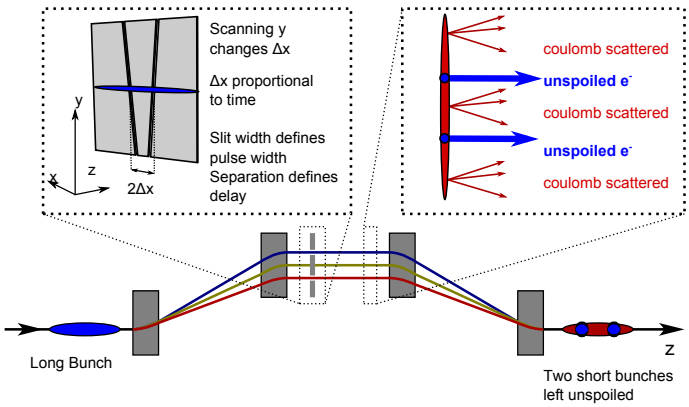


Figure 3.14: Principle of the emittance spoiler method for generation of time delayed X-ray pulses. A thin foil place in the beam between the second and third magnetics of a bunch compressor will spoil the electron beam through Coulomb scattering. By having two variable slits in the foil, two spatially separated parts of the beam will be left unspoiled which will be translated into two time delayed bunches after the bunch compressor.

a time resolved dataset. The phase cavity measurement technique is unfortunately only accurate to a few hundred femtoseconds, and so experiments using only this technique have been limited to processes that take place on picosecond rather than femtosecond timescales. Recently developed techniques such as the spectral time tool developed by Bionta et. al. [102] offer improved temporal resolution, on the scale of a few 10s of femtoseconds, and may usher in a new series of femtosecond scale studies in the near future.

It is also possible to perform X-ray Pump - X-ray probe experiments using a FEL, either by using a split mirror arrangement to create two pulse replicas similar to an optical setup, or through manipulation of the electron bunch itself. P. Emma et al. proposed a method in 2004 that would allow the creation of X-ray pulses as short as a few fs and potentially even sub-fs using relatively long electron bunches using a technique called emittance spoiling [103]. As described in section 3.3.3, at the centre of the bunch compressor, between the second and third bending magnets, an energy chirped electron beam has its initial longitudinal distribution or energy chirp mapped to a horizontal spatial distribution. A thin foil placed in the electron beam will cause Coulomb scattering, dramatically increasing the emittance of the particles and preventing them from contributing effectively to the lasing process. By placing a small vertical slit in the foil, only the small part of the electron beam that travels through the slit will be left unspoiled, and when the electron beam is re-compressed after the bunch compressor, lasing will only occur for this narrow unspoiled part. The final pulse duration is proportional to the width of the slit. This technique is advantageous as it can be implemented on any FEL with a bunch compressor, with a minimum of cost and additional equipment, and since the overall spatial distribution of the electron bunch remains unchanged there is minimal disruption to the workings of the accelerator, with the trade-off that since a large proportion of the initial electron bunch is spoiled, the pulse energies are typically much lower.

The same method also allows the creation of multiple, time-locked, X-ray pulses. If instead of using a single vertical slit, we use two slits in a V shape, two horizontally separated parts of the beam will be left unspoiled. After compression this will result in two unspoiled bunches separated in time. By moving the V-slit in the vertical direction relative to the beam we can continuously vary the slit separation distance and therefore the pulse separation with femtosecond precision. This technique is shown in figure 3.14. Since both pulses are produced by the same electron bunch the arrival time jitter does not affect the time delay of the two X-ray pulses, making it an attractive option for high precision femtosecond timescale measurements.

Chapter 4

Review of experimental techniques and technology

We have so far discussed both the methods by which short pulses of both optical and XUV - X-ray wavelengths can be generated, and the types of processes we would expect to occur when they interact with atoms and molecules. We can now describe the experimental methods by which these processes can be explored. This chapter reviews the principles behind experimental technology and methods common to the experiments described later in the thesis. A brief description of vacuum technology and design is presented. The requirements and properties of optics relevant for use with the XUV and X-ray wavelengths are discussed. The bulk of the chapter is dedicated to the discussion of photoion and photoelectron spectrometry using the TOF and VMI methods. Sample sources suitable for studying species in the gas phase are then discussed, before concluding with a description of the detectors used for measuring the products of ionisation.

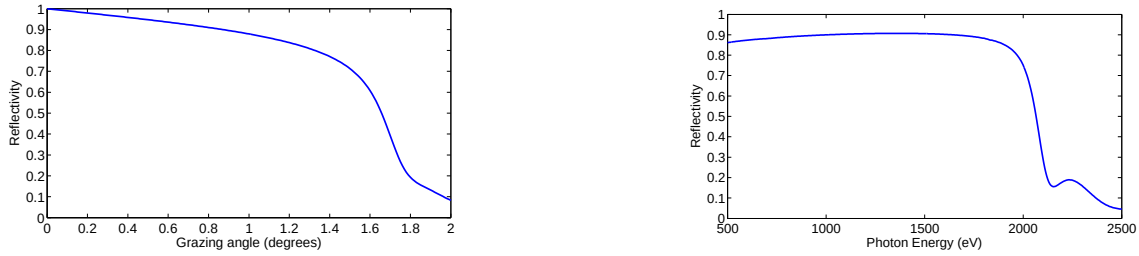
4.1 High vacuum technology

All of the experiments described in this thesis were performed under vacuum. There are several important reasons for this: (a) both XUV radiation from HHG and X-rays from a free electron laser will suffer heavy losses from absorption when propagated through atmosphere (b) many of the experimental techniques and detectors used for performing the measurements also require there to be little to no background gas in the region of the experiment (c) performing under vacuum is the simplest way of maintaining sample purity which is essential for high precision measurements. Vacuum when used in a scientific context can cover a wide range of pressures, and it is therefore useful to characterise different pressure ranges, as different ranges are needed for different types of experiment. Low vacuum can be classed as any pressure from atmospheric pressure ($\approx 10^3$ mbar) to 10^{-3} mbar and in general this is only utilised in the lab as a preliminary stage in achieving

lower vacuum. High vacuum (HV) is classed as the range from 10^{-4} to 10^{-8} mbar, which is suitable for gas phase experiments. Ultra-high vacuum (UHV) refers to any pressure lower than the high vacuum range, which is only absolutely required for condensed matter experiments, but advantageous in any experiment as contaminants will be less prevalent.

A complete vacuum chamber system is constructed of multiple components of varying material, size and purpose. Material possibly plays the most important part in chamber design, as any material in the vacuum will release trapped gases in various processes collectively called outgassing. Outgassing can be reduced by baking the chamber at elevated temperature. This will cause accelerated outgassing of the contaminants, and once the procedure has been completed we can typically gain an order of magnitude better vacuum, and is particularly useful in eliminating water contamination. The effect of the baking will depend on how long and at what temperature the system is baked at, with higher temperatures and longer baking times yielding better pressures. The other major limiting factor to the pressure is the connections between the different components of the vacuum system. The different components of a chamber using flanges of different standards. The three most commonly used standards used are Klein flange (KF), which use a rubber/Viton o-ring centred on a metal ring and a clamp to make the seal, ISO flanges which also use o-rings, but generally use bolts/clamps to connect the two flanges, and ConFlat (CF) connections, which use bolts to press a knife edge into a metal gasket to make the seal. CF connections are capable of reaching the highest vacuums (up to UHV) and are therefore used for construction of chambers where high vacuum is critical. ISO flanges are used for construction of chambers where UHV is not a necessity and for systems which need to be opened regularly. KF connections generally only perform up to mid-HV and are limited in size to approximately 50 mm diameter, and thus are generally used for constructing roughing lines or gas supply lines.

Vacuums are created and maintained within the chamber by using one or more suitable pumps to remove the background gases. As no single pump design is capable of bringing a chamber down from atmosphere to HV/UHV it is necessary to use two different types of pumps on each system: one to bring the chamber down to low (or 'rough') vacuum and then a second pump to bring it down from low to high vacuum ranges. Low vacuum is achieved with mechanical, positive displacement pumps. These operate by expanding the cavity so that gas from the chamber flows into the pump, and then sealing off the expanded section and exhausting it. These are capable of achieving pressures of approximately 10^{-3} and 10^{-2} mbar respectively. High vacuum pumps operate using either momentum transfer or entrapment. In the former type, the atoms/molecules in the chamber are physically knocked from the chamber. Entrapment on the other hand causes the gases to either condense on or react with a substrate. Entrapment pumps are capable of achieving better ultimate pressures than momentum transfer pumps, but are unable to cope with significant gas loads.



(a) (b)

Figure 4.1: Reflectivity of a 50 nm layer of C_4B on a SiO_2 substrate with surface roughness 1 nm σ. These specifications are taken from the LCLS AMO optics specifications, and values calculated using the CXRO database [104]. (a) Reflectivity as a function of grazing incidence angle in degrees, (b) Reflectivity as a function of photon energy for a fixed grazing angle of 0.87°.

4.2 X-ray/XUV optics and diagnostics

Both the X-ray and XUV region of the spectra have negligible reflectivity for any material at normal incidence for a single layer. Reasonably efficient normal incidence X-ray mirrors can be contructed from multiple layers of alternating high and low refractive index materials with reflectivities of 70%, with bandwidth ranging from a few to tens of eV [105, 106]. Reflectivity is dependent on the quality of the layer thickness, with imperfections leading to destructive interference and reduced reflectivity [107, pp. 99]. Since these layers are typically $1/\lambda$ in thickness, the lack of interface quality control at the Angstrom scale means such optics are not practical for the X-ray regime, or for light sources that cover a broad spectral region. Steering and focusing beams at X-ray wavelengths requires a different methodology compared used at grazing incidence, where the angle is small enough that the X-rays undergo total external reflection. The critical angle α_c for a given material is given by:

$$\alpha_c = \sqrt{\frac{n_a r_e \lambda^2 f_1^0}{\pi}} \tag{4.1}$$

where n_a is the atomic density, r_e is the classical electron radius and f_1^0 is the scattering factor, which to a first approximation is equal to the atomic number Z. Angles less than this critical angle will reflect efficiently. Figure 4.1 shows the reflectivity properties of an X-ray mirror as used by the soft X-ray sections of the LCLS beamline. Focusing can be achieved using one of two methods: a toroidal mirror, which takes the form of an elliptical paraboloid, or using Kirkpatrick-Baez optics (KBO) [108], which use two orthogonal planar optics that are dynamically bent to form a pair of parabolic optics with a common focus.

4.2.1 Flat-field spectrometry

X-ray/XUV photospectrometers provide both valuable diagnostics of the beam and in the case of HHG spectroscopy can reveal important information about the dynamics of the system. For XUV spectrometer (XUVS) and soft X-ray regions, spectrometers based around a concave grating [109] provide the best option as they combine good energy resolution and focusing properties into a single optic; with X-rays/XUV, the fewer optics the easier and more reliable the alignment. The different wavelength components λ in this case will be diffracted according to the following equation:

$$\frac{n\lambda}{x_0} = \sin\alpha + \sin\beta \tag{4.2}$$

where x_0 is the groove spacing, n is the diffraction order and α and β are the angles of incidence and diffraction respectively. The different wavelengths will be focused to plane defined by the Rowland Circle, whose radius is equal to half the radius of curvature of the grating. This presents a problem when we wish to look at multiple frequencies simultaneously, since typically our detector will be a flat plane and therefore by using a standard concave grating only a small portion of the spectrum will be in focus. Since this is not convenient, XUV spectrometers usually use a so-called flat-field grating [110], which instead of a periodic spacing uses a non periodic groove spacing which is a power series of the distance from the center of the grating, x':

$$x' = x_0 / \left(1 + \frac{2B_1}{R}x + \frac{2B_2}{R^2}x^2 + \frac{2B_3}{R^3}x^3 + \cdots\right) \tag{4.3}$$

where x_0 is in this case the average groove spacing, R is the radius of curvature. This spacing structure leads the spectrum to be focused approximately to a flat plane for a small enough detector.

4.3 Time-of-flight spectrometry

As discussed in section 2.2, photoion and photoelectron spectroscopy are powerful tools in probing dynamics and structure within atoms and molecules. The TOF technique is one of the oldest and most widespread techniques for ion/electron spectroscopy. The technique identifies charged particles of different species and energies by using the relationship between a particle's charge to mass ratio and/or kinetic energy, and the time it takes to travel/fly a known distance (its TOF, hence the name). Various implementations of the technique are capable of measuring a particle's charge, mass and kinetic energies at the point of its creation [111].

4.3.1 Basic operation - the ion mass spectrometer

The basic principle underlying a time-of-flight spectrometer (TOFS) was first proposed in 1946 by W. E. Stephens [112]. While TOFS now come in a huge range of configurations, all designs have four main components in common: a source of charged particles, a detector, and two regions in which the particles can propagate: one with an applied electric field used to accelerate the particles and another that is field free where the particles can propagate at constant velocity until they hit the detector after a certain well defined distance. This setup is shown schematically in figure 4.2a. Let us assume we create a collection of ions with initial kinetic energy $U_{k,0} = \frac{1}{2}mv_0^2$ where v_0 is the particle's initial velocity, charge q, mass m, all located at a distance s_a from the entrance to the drift tube. We will assume for the moment that the particle's velocity is constrained to the detector axis for the moment. The particles will be accelerated by the external field with strength E and they are then allowed to propagate in the field free drift tube with length D. The time taken to reach the detector T is therefore the summation of the time spent in the acceleration region, T_a and the time spent in the drift tube, T_D. Using the relations $v = D/T$ and $v_f = v_0 + at$ where a is the acceleration of the particle, these two times can be calculated to be:

$$T_a = \frac{v_f - v_0}{E}\left(\frac{q}{m}\right) \tag{4.4}$$

$$T_D = D\sqrt{\frac{m}{2U_k}}. \tag{4.5}$$

U_k in this case is the final kinetic energy $U_{k,0} + qEs_a$. From simple Newtonian mechanics it can be seen particles with an initial velocity away from the drift tube will be first decelerated to zero velocity, and then turned around by the electric field passing through the point of origin with velocity $v = -v_0$. As such, T_D is independent of the initial direction, and the effect of the initial direction is to add a so called 'turn-around' time $T_\pm$, which can be found by setting $v_f = -v_0$ in equation 4.4:

$$T_\pm = \frac{2|v_0|m}{qE} \tag{4.6}$$

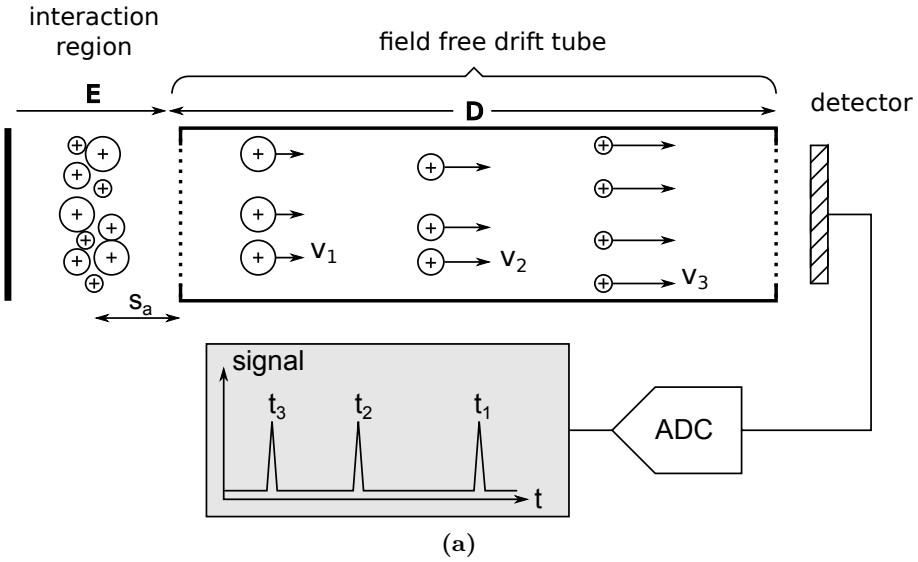
$$= \frac{2\sqrt{2mU_{k,0}}}{qE}. \tag{4.7}$$

The total TOF is then given by the equation:

$$T = \frac{\sqrt{2m}}{Eq}\left(\sqrt{U} \pm \sqrt{U_{k,0}}\right) + D\sqrt{\frac{m}{2U_k}}. \tag{4.8}$$

We can see from these equations that the drift time increases with increasing mass to charge ratio, and the initial kinetic energy causes a deviation from this peak in time which is linear with the particle's momentum. If we place a time-sensitive detector at the end

of the drift tube we will observe a series of peaks in the detected signal in time, each one corresponding to the different ion species. These can then be recorded using a oscilloscope or other analog-digital converter (ADC) recording system.



(a)

Figure 4.2: Principle of operation of a linear time-of-flight mass spectrometer. The spectrometer has a single acceleration stage with electric field E, and a field free drift tube of length D. The particles (ions) are created at a distance s_a from the entrance to the drift tube. As ions with different masses have different velocities, v, the different ion species reaching the detector will be separated in time t with the heavier (and therefore larger m/q) species being slower. By observing the electrical signal from a detector as a function of time, distinct peaks corresponding to the different species are observed.

This ideal case obviously does not hold for a real instrument, and there are two main factors that will lead to a broadening and smearing out of the distinct mass-charge peaks, namely that the ions will be created over a finite volume and over a finite time. The creation time problem is easily solved by our method of ionisation: a femtosecond laser source. Since ion/electron creation will be limited to the duration of the pulse, which for femtosecond systems is several orders of magnitude smaller than the flight times, the effect on the flight times is negligible. Similarly, the typically small focal diameter of the laser in comparison to the acceleration region makes the initial spatial spread negligible. For more general systems, the initial spatial distribution can also be corrected for through careful choice of the detector geometry. Since particles that are initially further from the drift tube will experience a larger acceleration than ones closer to the flight tube entrance, and therefore a higher final velocity, these particles will eventually catch up with the ones that are initially closer to the drift tube entrance. For a particle δs away from s_a the difference in energy from the mean, δU, is given by:

$$\delta U_k = (s_a \pm \delta s)Eq. \tag{4.9}$$

At a certain distance from the source, all the flight times for a given species will be the

same for all initial positions in the interaction region. This is known as the first order spatial focusing condition [113]. Placing your detector at this distance will maximise the mass-resolving power of the instrument. For a linear TOFS with a single accelerating region this distance is simply $2s_a$.

This simple setup may not always be sufficient to allow sufficient peak separation for sensible values of s_a, so in 1955, Wiley and McLaren demonstrated an improved TOF scheme which uses two acceleration regions to improve the resolution [114]. In the Wiley-Mclaren scheme, the acceleration region is split into two parts, the interaction region which has a small field E_s and a stronger accelerating region with field E_d, with. The primary advantage this scheme has is that the spatial focusing condition can be tuned for arbitrary values of D by changing the ratio between the two extraction fields. The spatial focusing condition can be found by choosing parameters that satisfy the following equation:

$$D = 2s_a\sqrt{k_0^3}\left(1 - \frac{d}{s_a(k_0 + \sqrt{k_0})}\right) \tag{4.10}$$

and k_0 is given by

$$k_0 = \frac{E_s s_a + E_d d}{E_s s_a} \tag{4.11}$$

where s is the distance of the source from the entrance to the second acceleration region and d is the length of the second region. Solving equation 4.10 for k_0 in this case allows you to calculate the ratio of the fields required for Wiley-McLaren operation for a given detector geometry.

While it is perfectly possible to use the above equations to convert a measured TOF spectra to a mass-charge spectra, the great difficulty lies in being able to define all the required parameters to sufficient accuracy, as the electric fields are rarely exactly to specification, due to external fields penetrating the system, and there is often a systematic delay between ion creation and acquisition due to delays inherent in the cabling and acquisition hardware. For practical purposes it is often much more convenient to reduce all the potential unknowns for a given term to a single calibration constant, which can then be found experimentally using a set of known peaks. For example, the reduced form of the ion TOF equation one stage spectrometer in spatial imaging mode is given by:

$$T = T_0 + A\sqrt{\frac{m}{q}} + B\frac{\sqrt{2mU_{k,0}}}{q}. \tag{4.12}$$

Here, A, B and T_0 are calibration constants can simply be found by solving the resultant simultaneous equations for two known mass/energy peaks, which are generally trivial to identify by comparison of background peaks and those which appear with an introduced sample species or known contaminant. T_0, which can be viewed as the flight time for infinitely fast particles, can also be estimated in X-ray experiments through observation

of a photon peak which comes from scattered X-rays, and provides a useful sanity check.

4.3.2 Electron time-of-flight - the energy spectrometer

The same technique used for ions can be also utilised for electrons. Since all electrons have identical mass, the TOF now becomes a powerful and simple method to measure the electrons kinetic energy at birth. Since in prototypical experiments the electrons will already have a reasonable kinetic energy at creation (tens or hundreds of eV), the electrodes at the interaction region are usually turned off and held at ground. In the case of very high energy electrons a retarding positive voltage can be applied such that the kinetic energy is reduced, increasing the resolution of the instrument at high electron energies at the expense of completely rejecting lower energy electrons. The experimental TOF in this case is then given by the equation:

$$T = t_0 + \frac{C}{\sqrt{U_{k,0} - E_R}} \tag{4.13}$$

where $U_{k,0}$ is the electron kinetic energy at creation, E_R is the retarding potential in volts, and C is the instrumental calibration constant, and T_0 is the zero flight time as before. The main limiting factor for electron TOF is signal strength and energy resolution which has led to the development of a multitude of more complex implementations of the technique using a combination of multiple refocusing electrodes and magnetic fields.

In order to rescale the TOF traces in either mass or energy scale, the yields must be scaled so that the total yield integral is conserved. This is achieved by applying the jacobian transformation:

$$Y' = Y \left| \frac{\partial T}{\partial X} \right| \tag{4.14}$$

where Y is the yield at time T and Y' is the yield rescaled in terms of the parameter $X = U_{k,0}, m$ and so forth. An equivalent numerical method is to rebin the data and integrate over a variable bin length.

4.3.3 Energy resolution and Collection Efficiency

Two key parameters of a TOFS are its energy resolution, i.e. the minimum detectable kinetic energy difference $\Delta E/E$, and the collection efficiency or acceptance which is typically measured in solid angle (steradians) where $S = 2\pi[1 - \cos(\theta)]$ where θ is the acceptance angle of the detector. Unfortunately, in a typical TOF setup, the two act against each other and so one must usually find a compromise between the two. The energy resolution

for a generic TOF is given by:

$$\frac{\Delta U}{U} = \sqrt{2\left(\frac{\Delta T}{T}\right)^2 + 2\left(\frac{\Delta l}{l}\right)^2}. \tag{4.15}$$

Here, T is the particle TOF and and l is the path length. Uncertainties in T come from uncertainties in the pulse duration, and timing electronics of the detector, whereas uncertainties in l stem from the difference in path lengths for different energies, which in turn depends on the acceptance angle of the detector (larger angles lead to a larger path uncertainty). By increasing the drift tube length we increase both the time resolution and decrease the acceptance angle, increasing the resolution, but the number of particles being detected will decrease as the solid angle of the detector decreases. The inverse situation is also true. Thus without significant modifications to the operation of the detector, we have to reach a compromise between energy resolution and collection efficiency.

4.3.4 Velocity map imaging

While time of flight gives us information about the kinetic energies and masses/charges of the particles, it is unable to provide much in the way of momentum information since we are limiting ourselves to observing only a small solid angle. Though angular information can be obtained by scanning a TOFS through multiple positions, this is both tedious and time consuming. The technique of VMI works by mapping particles with equal velocity to the same point on a 2D distribution [115]. Imagine we have an ensemble of particles with initial velocities of equal magnitude $|v_0|$, but with random directions. For simplicity we will initially assume that the velocities are constrained to the x-y plane so that $v_0 = \sqrt{v_x^2 + v_y^2}$, where z is the TOF propagation axis. We now accelerate these particles in an external field in the z direction, V_z, so that each particle gains additional kinetic energy equal to qV_z. The time of flight in this case can be approximated using equation 4.5. As the particle travels down the drift tube, the velocity sphere will expand as a function of flight time so that the radius of the sphere, R is given by:

$$R = D\sqrt{\frac{U_{k,0}}{qEs_a}} \tag{4.16}$$

Where $U_{k,0}$ is the initial kinetic energy of the particle. It can be seen from equation 4.16 that particles of equal initial kinetic energy will be mapped to the same radius on the detector, and the initial direction of the particle will define at what angle it will hit the detector. The particles emitted in the x-y plane (ie in the detector plane) will have the largest radius for a given energy and will therefore define the maximum energy we can collect.

Practically, a VMI spectrometer is constructed in a similar way to a Wiley-McClaren

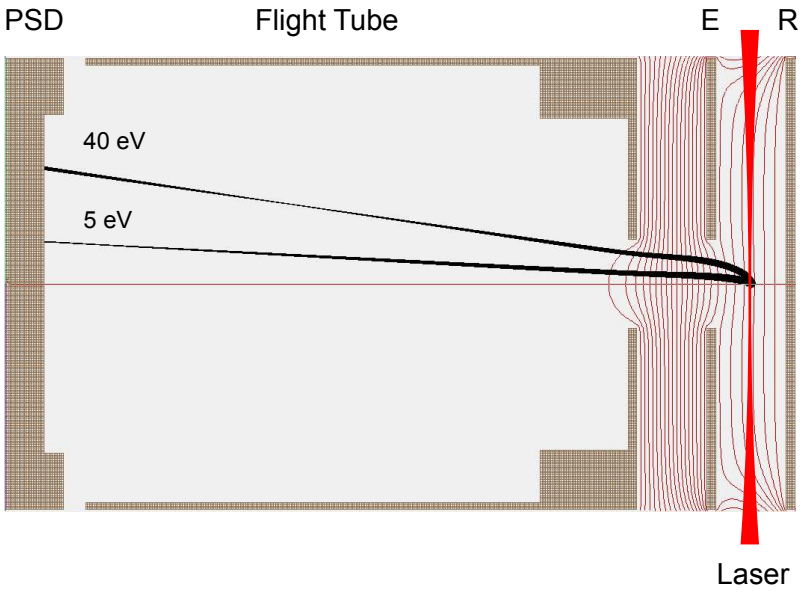


Figure 4.3: Electrode layout of a generic VMI spectrometer. An open electrode system with a solid repeller (R), an extractor (E) and a flight tube is used to image particles with equal initial velocity to the same point on a position sensitive detector. The black lines show particle trajectories for 5 eV and 40 eV, with initial velocities in the vertical direction, and initial positions spread over a 1mm radius sphere centred between the extractor and repeller. The repeller and extractor have voltages of $V_R = 3.0$ kV and $V_E = 2.2$ kV respectively. The field lines show increments of 125 V. Note that the 5 eV electrons are focused to a much sharper point at the MCP surface than the higher energy 40 eV electrons, but by changing the ratio of the extractor and repeller the resolution for high energy electrons could be optimised.

TOF except the grid electrodes are replaced with solid plates with circular apertures (so called 'open' electrodes) so that when a voltage is applied across the plates an electrostatic 'Einzel' lens is formed [116]. This is shown schematically in figure 4.3. The reason for using plates compared to grids is two-fold: it a) increases transmission to near 100%, and b) grids will tend to distort the electric fields to the detriment of the imaging process [117]. Typically 3 plates are used, a solid repeller, an extractor and a plate which forms the entrance to the drift tube which are held at voltages V_R, V_E and V_D respectively. V_R will define the degree of acceleration and thus the radius of the velocity sphere, with larger voltages allowing larger energies to be mapped to the detector. The ratio V_E/V_R will define the curvature of the lens and therefore how well the different velocities are focused. The ratio at which the focusing is maximised will be approximately constant for all values of V_R and will typically be around the 0.7 mark, although each individual instrument will have to be optimised experimentally. Like its TOF cousin, the VMI is capable of measuring both ion and electron distributions, and for ions, it is possible (and often preferable) to limit detection to a single fragment/species by gating the voltages applied to either the microchannel plate (MCP) plates or the phosphor screen so that the detector is sensitive for only a short range of TOFs that correspond to that particular charged species.

Compared to a TOF the VMI has the advantage that angular distributions can be mea-

sured directly in a single measurement, and the angular distributions can be interpreted qualitatively in real-time with relative ease. VMIs achieve near 4π collection for energies low enough so that the radius of the Newton sphere is smaller than the detector. This flexibility is at the expense of energy resolution since VMIs collects efficiently over a far larger range of initial positions, with even the best VMI typically limited to a few percent $\Delta E/E$, and this energy resolution is also energy dependent. A practical consideration for looking at high energy fragments is that any low energy fragments will tend to be heavily focused in the centre of the MCP, making it much harder to obtain high resolution measurements for both high energy fragments simultaneously, and the higher concentration of hits will deplete the MCP sensitivity in that region far faster than measurements where the signal is spread over the detector.

Measurement of the full 3D initial momentum distribution $I(x, y, z)$ would require a detector sensitive in both time and space, with x and y mapped to position on the detector and z can be retrieved from the time of flight. For a 2D, position sensitive detectors, what will instead be measured is a projection of the 3D distribution, akin to the Newton sphere being compressed into a flat disc, yielding a 2D distribution $P(x, y)$, which in general cannot be solved unambiguously. It is possible to retrieve the full 3D distribution however, using 2D data if the initial distribution has a spherical symmetry about an axis parallel to the detector plane (say x), which for many photoionisation processes involving a linear polarised laser is a valid assumption. In this case the projection P of $I(r, y)$ (now a function of radius $r^2 = x^2 + z^2$ and y in polar coordinates) is mathematically equivalent to an Abel transform [118, p. 70]

$$P(x, y) = 2 \int_x^\infty \frac{rI(r, y)}{\sqrt{r^2 - x^2}} \, \mathrm{d}r \tag{4.17}$$

The retrieval of the original 3D distribution I is then achieved though a mathematical process called an inverse Abel transform:

$$I(r, y) = -\frac{1}{\pi} \int_r^\infty \frac{\mathrm{d}P(x, y)}{\mathrm{d}x} \frac{1}{\sqrt{x^2 - r^2}} \, \mathrm{d}x \tag{4.18}$$

In practice however, using equation 4.18 to directly derive a distribution from the measured data is not practical, since the function contains a singularity at $r^2 = x^2$, experimental noise will be amplified by the derivative, and the fact that our measured projection is a digitised image. In practical terms, a large number of different numerical retrieval algorithms exist that are capable of retrieving the original 3D distribution, all with their own quirks and limitations/advantages*. Two commonly used algorithms are the PBASEX (Basis Set Expansion) algorithm [119], which models the 3D distribution using a large set of Legandre polynomials, and an iterative algorithm developed by Vrakking et. al. [120] which operate much like a FROG algorithm in that an initial 3D distribution is guessed,

*A good summary of a large number of methods including their relative accuracies can be found in the following reference [118, ch. 3].

projected onto the 2D plane and then the error between the reconstructed 2D distribution is used to improve the 3D distribution until the two 2D distributions converge.

4.4 Sample delivery systems

In order to study chemical samples using photoionisation processes, a suitable source of the sample is required. Key properties of any source are the sample density (the number of atoms/molecules in a given volume), the interaction volume (the effective size of the sources as seen by the laser focus) and the the temperature of the sample.

4.4.1 Gas samples

All experiments described in this thesis were performed in the gas phase. A tube target or gas cell is conceptually the simplest type of target and is constructed by simply taking a gas reservoir constructed from a piece of tube or other small volume and drilling two small holes to allow the photon source to propagate through the sample. The principle advantage of this type of source is that you can be sure that the sample is of reasonably constant pressure over the interaction region and in can also achieve higher sample densities of the source compared with other methods. This technique is completely unsuitable for studying charged particle fragments however since the high pressures and the geometry will make analysis using techniques such as TOF technically challenging, so these techniques are usually performed using a low density effusive or supersonic jet fired directly into the vacuum.

Effusive and supersonic sources aim to create a small beam of particles by expanding a high pressure though a small aperture into a lower pressure region. The velocity distribution of an ensemble of particles at thermal equilibrium is described by the well known Maxwell-Boltzmann distribution:

$$N_v = 4\pi N \left(\frac{m}{2\pi k_b T_0}\right)^{\frac{3}{2}} v^2 exp\left(\frac{-mv^2}{2k_b T_0}\right) \tag{4.19}$$

Where $_v$ is the number of molecules with velocity v, N is the total number of atoms/-molecules in the reservoir, k_b is the Boltzmann constant and m is the molecular mass and T_0 is the temperature. The mean free path λ_m (the average distance between collisions) of a molecule in such a system is given by:

$$\lambda_m = \frac{1}{\sqrt{2}\pi d^2 N_\rho} \tag{4.20}$$

Where d is the molecular diameter and N_ρ is the molecular number density. If we place a hole in the reservoir that allows the gas to flow into a region of lower pressure, there are

two possible regimes of behaviour depending on the diameter of the hole, d_n, compared to the mean free path [121]. In the case that $\lambda_m > d_n$, the molecules will not have time to collide much before they pass into the low pressure region. This behaviour is described as an effusive expansion [122] and in this case, the velocity distribution of the molecules remains largely unchanged as it passes through the hole, yielding a broad distribution in both velocity and in space.

The more interesting situation occurs when $\lambda_m < d_n$. In this case there will be many collisions in the vicinity of the hole. The collisions which are most effective at moving the molecules into the low pressure region will tend to have large velocity components that a perpendicular to the hole diameter. Assuming the source pressure is sufficiently high the expansion can be viewed as both isentropic and adiabatic. The effect of these collisions is to narrow the velocity distribution of the gas escaping into the low pressure region, and since the width of the velocity distribution defined the temperature, the sample can be cooled to the order of a few tens of Kelvin by the expansion. Since the velocity of the jet can exceed the local speed of sound, it is also referred to as a supersonic expansion. The cooling of the sample the supersonic expansion provides is advantageous when dealing with molecules as by you are limiting the number of vibrational states, making spectroscopic measurements more accurate. The beam may be further collimated and cooled by using one or more skimmers: a metal cone with a small aperture drilled in the top of the cone. By placing this in the jet it is possible to extract only the central, coolest part of the sample, while also significantly decreasing the overall interaction volume.

4.4.2 Solid and liquid sources

With gases maintaining a constant source pressure/sample density is reasonably trivial achieve using a good regulator for the gas bottles and through the use of feedback controls. Dealing with samples which are liquid at room temperature/pressure is significantly more troublesome. For measurement techniques that require the sample to be in gas phase, we are generally forced to work with whatever gas is produced via evaporation of the sample, though there are recent pushes to develop techniques that are capable of studying these materials in the condensed phase. The vapour pressure for some smaller molecules can be appreciable at room temperature (for example methanol (CH_3OH) has vapour pressure of 167 mbar at 25 °C), but for many samples of interest, particularly the larger biomolecules, the vapour pressure will be negligible [123]. Two ways around this are to simply heat the sample, as the vapour pressure increases with temperature, and for lower pressure samples, a suitable high pressure source can be prepared by flowing a higher pressure noble gas through the sample, which acts as a carrier for the sample of interest. Helium is often the gas of choice when working with high photon energies as its cross section is 2 orders of magnitude less than carbon, oxygen, etc. (see figure 2.2). With a liquid sample prepared in this fashion, the above techniques of effusive and supersonic sources

can be used with liquids, but the overall stability of properties like the sample density when compared to a pure gas source will depend on the speed and accuracy of feedback controls in maintaining the sample temperature.

Dealing with solids is no less challenging, and generating a suitable source is achieved using either evaporative or ablation methods. Evaporative, oven based sources achieve a gas source through heating of a powdered sample to very high temperatures in a crucible, which is allowed to flow through an aperture yielding an effusive jet [124, 125]. Ablation methods on the other hand use a pulsed laser source to ablate material off a bulk source [126, 127]. While this approach has a number of technical challenges to achieving a stable source, as the material in the focus must be constantly refreshed, they can provide higher sample densities than evaporative methods as you are not limited by the vapour pressure you can achieve, and also offers opportunities to study ionic species that are created in the resultant plasma.

4.5 Detectors

No matter what experimental method is chosen, a good detection system for the products is critical. Key requirements for a detector include a reasonable detection efficiency for a broad range of energies, good spatial/time resolution, and the ability to be operated for considerable times and across multiple experimental conditions without having to replenish or replace the detector. For most experiments, a microchannel plate (MCP) is the best choice of detector available at a reasonable price, and for detection of X-rays and XUV radiation, back illuminated CCD cameras offer an alternative worth considering.

4.5.1 Microchannel plates

A microchannel plate is an extension of the more general concept of a channel electron multiplier [128]. A glass capillary is coated in a substrate that will produce secondary emission of electrons if a particle or photon of sufficient energy collides with it. If we then apply an electric potential across the length of the channel, these secondary electrons will be accelerated down the channel and into the substrate again, each electron in turn creating more secondary electrons. The channel now acts as one continuous dynode, and a cascade amplification of the electron signal will occur. An MCP is constructed from a large number of theses channels mounted so that they lie at a small angle (8-12°) from the normal incidence of the plate so that particles normal to the plate are detected. Each channel is only a few to tens of microns in diameter and the plates themselves are ≈ 1 mm thick. Shape and size of the plate can vary depending on the application. A single plate is typically capable of an electron gain of 10^4, and by combing two plates in a chevron (V) configuration you can achieve a gain of 10^7. Because of the large potential differences

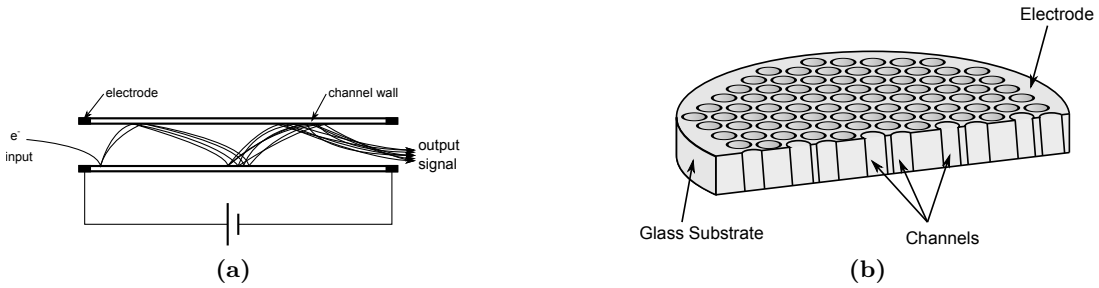


Figure 4.4: (a) A channel electron multiplier (b) structure of a single microchannel plate. A potential difference applied across the length of the channels will result in electron gain.

in the channel it is possible for spontaneous ionisation of any background gases in the channel to occur, which for sufficiently high pressures will cause a catastrophic avalanche of ionisation that can easily kill the detector. This means that MCPs can only be operated at a maximum pressure of about 10^{-5} mbar.

The resulting electron signal from MCP is then accelerated to an anode for detection. A simple metal anode will allow you to observe the integrated electrical signal as a function of time using an oscilloscope or a suitably fast ADC. Alternately one may obtain position sensitive data by using a phosphor screen anode, where the electrons are accelerated into a phosphorescent material that will convert the electron bunch into visible light, which is then observed using a CCD camera. There are a variety of different types of phosphor, with different persistence times and central wavelengths of the light they emit. For the experiments described in this thesis P47 ($Y_2SiO_5 : Ce$) was generally the phosphor of choice, as it has a short persistence time of 0.11 μs which makes it ideal for single shot measurements at a repetition rate of the order of a kilohertz. It is possible to get a time-dependent signal from a phosphor screen by adding a suitable decoupling circuit to the phosphor input, but the signal quality will be worse than from a metal anode, and there is no way of correlating the peak times to the position data in this case. Anodes that are capable of measuring both time and spatial information, such as delay line anodes, do exist but as they were not used in any experiments described in the thesis I will merely acknowledge their existence here.

Quantum detection efficiency (the probability of an ion/electron photon producing a measurable signal output) of an MCP depends strongly on the exact configuration of the device, but is typically 30-80% for particles, depending on the energy, and much lower for photons, typically maxing out at 15%. Typical rise/fall times for MCPs for a single electron hit are of the order of 1 ns. Dead times (the time taken for a channel to become active again after registering a hit) are of the order of a few 10s of microseconds. For integrating measurements the dead time is less important as the signal will be typically spread across the MCP and therefore the the count rate for a given channel is low compared to the overall count rate. For position sensitive measurements however it is quite possible for all of the interesting signal to be concentrated in a small part of the detector, so it is

important for the count rate to be sufficiently low as to not saturate the detector. The gain of the MCP and therefore the signal will increase exponentially with the voltage applied across the channels, but dark counts[†] will also increase, with detrimental effects on the signal to noise ratio. Thus operating voltages are chosen to be a compromise between signal quality and dark count rate, with higher vacuums yielding a lower dark count rate and thus allowing higher operating voltages and gains.

4.5.2 Cameras

Cameras have a wide variety of uses in the laboratory, and will vary in cost/operation according according to their application, with a sensor based on either CCD or complementary metal-oxide-semiconductor (CMOS) technology. For sensitive measurements generally a camera with a cooled CCD is used as they can provide reasonable frame rates and an excellent signal to noise ratio. Conversely, a cheap CMOS webcam generally sufficient for purposes such as checking beam alignment, qualitative observation of interaction regions, and even measurements of focal spots.

4.5.3 X-ray cameras

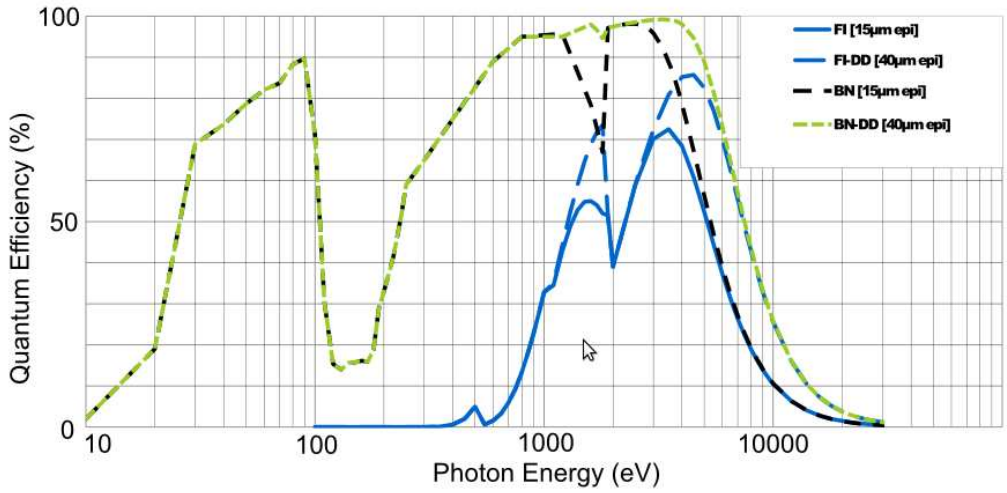


Figure 4.5: Quantum effeciency in the XUV/ Soft X-ray region of the spectrum for various types of CCD detector. FI = Front illuminated (normal CCD structure), BN = Back illuminated, DD = Deep depletion (extended depletion zone).

To achieve detection in the XUV/X-ray region requires a significant modification to the CCD structure. X-ray CCDs are achieved using a back-illuminated CCD. Here the typical CCD structure is reversed, and the silicone structure at the back of the CCD is chemically etched so that it is only a few 10s of microns thick. This allows transmission of

[†]Counts that come from spontaneous firing of a channel.

the XUV and X-ray regions. Compared to MCPs, an XUV camera has several advantages. The quantum efficiency for such cameras is 20-40% over the 10-100 eV range compared to typical detection efficiencies of 5% with an MCP. When cooled, they offer significantly better dark signal compared to MCPs.

The primary disadvantage of these cameras compared to MCPs is that the chip size will be limited in size, which in practical terms, you are limited to observing a much smaller part of the spectrum when using it as part of a flat-field spectrometer. The chips are also significantly more expensive than an MCP of equivalent area. As the CCD chip is uncovered they must be handled with extreme care, and are operated under vacuum to avoid contaminants condensing on the surface of the chip.

Chapter 5

Development towards XUV beamline components

This chapter describes work to test and commission elements of an XUV beamline. The apparatus was primarily constructed by Gavin Waters as part of his PhD at the University of Reading and the work shown here was completed under his supervision and direction. My contribution was in participating in the final commissioning of the system at Imperial College, and participated in the alignment of the system, testing of the Flat-field spectrometer and magnetic bottle apparatus. I also was also responsible for the development of Matlab based control software for the delay stage and Andor camera systems. At the end of the chapter I will briefly discuss future plans for the system for which significant parts of the beamline will be used for a new generation of measurements.

5.1 Scientific motivation

The application of HHG to studies of molecular systems falls broadly into two different areas: purely spectroscopic studies, where the properties of the molecular system are derived from the structure of the HHG spectra, and pump-probe measurements where an XUV pulse is used to either excite or ionise the molecule which is then studied using measurements such as absorption or photoion/electron studies. Since creating two XUV pulses that are both synchronised and of sufficient flux remains a technical challenge, a common technique is to use part of the laser used to drive the HHG process in an optical-XUV experiment [20, 129].

The equipment described in this chapter was designed such that it would form a flexible beamline that is capable of both types of measurement (but with a focus on IR-XUV pump-probe measurements), and one where the detector or experimental chamber could be easily modified or replaced. The original goals for this experiment were divided into

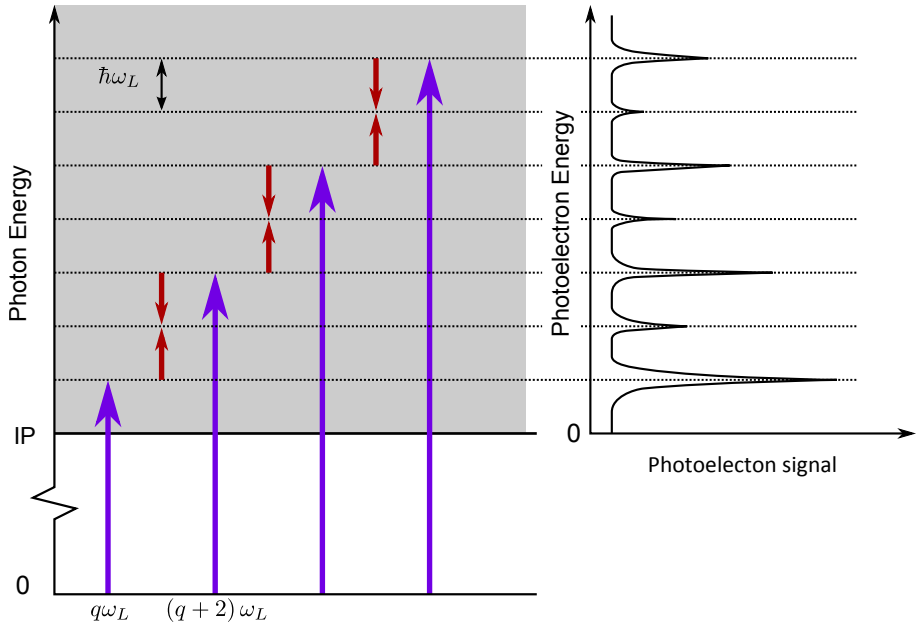


Figure 5.1: Principle of the RABITT technique. An IR field of frequency ω_0 and a comb of harmonics of frequency $q\omega L$ (q = 1,3,5$\cdots$) are focused into an ionising medium with ionisation potential IP. Two photon interference of the IR field and the high harmonics creates sidebands in the photoelectron energy spectra.

three distinct stages. Firstly we would need to demonstrate that all elements of the beamline were working correctly. This would involve testing and optimising the harmonic source, and testing that both initial experimental detectors, an electron TOF detector, and an XUV flat-field spectrometer (FFS) were capable of detecting the created harmonics.

The second step would be using both of those instruments in characterising the harmonics. As described in section 2.3.3, using multiple phase locked harmonics has the potential to yield a pulse of XUV radiation of sub-femtosecond duration. If we were to use such pulses in experiments, being able to characterise the pulses is crucial, and this requires being able to measure the spectral phase in addition to the spectral intensity of the harmonics. Since the typical methods of measuring ultra-short pulses (see section 3.2) can not easily be applied to the XUV region due to the lack of suitable optics, we require a method that works for this wavelength region. The reconstruction of attosecond beating by interference of two-photon transitions (RABITT) technique was the first technique to demonstrate this capability, and calculates the phases of individual harmonics through the interference of two-photon processes involving the harmonics and a weak IR field [60, 130].

Such measurements are performed using an electron TOF spectrometer. If the high harmonics are focused into a noble gas, the harmonics that have energy greater than the IP of the gas will directly ionise the gas, yielding a photoelectron spectrum with kinetic energy peaks equal to $U_k = E_{XUV} - U_{IP}$. If a small amount of the IR driving field is focused into the gas along with the XUV, two photon sum and difference processes yield

sidebands at kinetic energies equal to where the even harmonics would be. This is shown schematically in figure 5.1. A sideband of order $q+1$ (where q is the harmonic order) can come from two different quantum paths: through the absorption of harmonic q and the sequential absorption of an IR photon, or by absorption of harmonic $q+2$ and the emission of the IR photon. The total sideband signal will depend on the interference of these two paths, which in turn depends on the phases of both harmonics and the IR field. By varying the delay τ of the IR with respect to the XUV, the signal for sideband $q+1$ will be modulated according to the equation:

$$S_{q+1} = S_0 \cos((\omega_0 \tau + \phi_L) + \phi_q - \phi_{q+2} + \Delta\phi_{q+1}^{atomic}) \tag{5.1}$$

where ω_0 is the IR frequency, ϕ_L, ϕ_q and ϕ_{q+2} are the phases of the IR, harmonic q and harmonic $q+2$ respectively. $\Delta\phi_{q+1}^{atomic}$ is the atomic phase, a small correction that depends on the ionisation medium and the harmonic order. This can either be calculated theoretically, or to a first approximation neglected. When performing the experiment it is important the intensity is low enough so that two-photon processes are the dominant interactions [131], otherwise equation 5.1 will no longer be valid as contributions from other transitions will polute the sideband signal.

By taking a series of photoelectron energy traces as a function of delay, a 2D RABITT trace can be built up. The signal for each sideband as a function of laser delay can then be found by simply integrating over the total sideband signal. The relative phases of each harmonic can then be found by fitting a cosine function to the sideband signal and then solving equation 5.1. While this works well enough for sidebands with strong oscillations, for weaker sidebands it is preferable to perform the analysis in the Fourier domain. By performing a fast Fourier transform (FFT) on the sideband signal we will observe a strong peak around the fundamental oscillation frequency ($2\omega_0$) and the phase can be found by averaging the phase around the peak. By retrieving these phases and using them in conjunction with the measured spectra of the harmonics, through simple Fourier analysis we can then reconstruct the form of the XUV pulse in the temporal domain.

The final stage would be to apply the characterised attosecond pulses in a pump-probe experiment which uses both IR and XUV wavelengths. While there are many possibilities for this kind of experiment, the original experimental plan was to study molecular hydrogen in an XUV pump, IR experiment. XUV radiation filtered to the appropriate wavelengths is capable of elevating a hydrogen molecule into a so called super-excited state [132, 133]. These are highly excited states, 30-40 eV above the neutral H_2 ground state, and quickly decay via multiple possible channels, including auto-ionisation and fragmentation into two H^+ ions, and via neutral dissociation. By field ionising the excited molecule using a time delayed IR pulse, it is possible to track the evolution and decay of these short lived states, and their interaction with the IR field, through observation of the ion kinetic energies that result from dissociation of the molecular ion as a function of the pump-probe delay. This

technique could also be extended to other molecules, and indeed in the recent years since this experiment was originally planned, has been demonstrated as a technique capable of tracking the evolution of highly excited states in molecules [129].

During the course of my PhD studies, only the first goal was achieved, and these are the results that are presented in this chapter. Efforts towards achieving a RABITT measurement were undertaken but was ultimately unrealised due a combination of some untimely equipment failures, the change in focus of my studies towards the FEL based experiments and their analysis. However, a conceptually similar experiment on H_2 and D_2 was published by another group led by Sansone in 2010 [134]. In their experiment they used an isolated XUV attosecond pulse and a few cycle IR as the probe, and successfully demonstrated time dependent charge localisation on an attosecond timescale.

Despite the setbacks, important milestones were achieved in demonstrating that the system was capable of robust detection of harmonics using two different detection mechanisms. A new generation of students and researchers are currently adapting the equipment to be more suitable for the new focus of transient absorption measurements, and the work and technology described in this chapter will serve as groundwork for these studies.

5.2 Experimental apparatus

The experimental beam line consists of four separate chambers, two for generating and focusing the harmonics, and two experimental chambers for characterising the harmonics. The experimental line was designed to be modular so that different experimental chambers could easily be swapped in the line, or the pieces transported to other labs for use in other experiments.

5.2.1 Beamline

The incoming IR laser pulse can be sent through a beam splitter to create two individual lines. One line is sent directly to the chamber while the other is sent to a delay stage. The delay stage is in fact two different stages: a Physik Instrumente M-505.4DG that has a 100 mm travel range with minimum increments of 0.05 μm, and a piezo Physik Instrumente P-753.3CD with 38 μm travel range with minimum incremental 0.2 nm. The coarse stage can be used for correcting large beam path differences whereas the fine stage will be used for the performing pump-probe measurements. Both beams are then sent through separate $\lambda/2$ waveplates for rotating the polarization before being focused using two lenses of 670 mm focal length. The two beams then enter the vacuum system through two anti-reflective coated windows. At this point both the beams are parallel to each other.

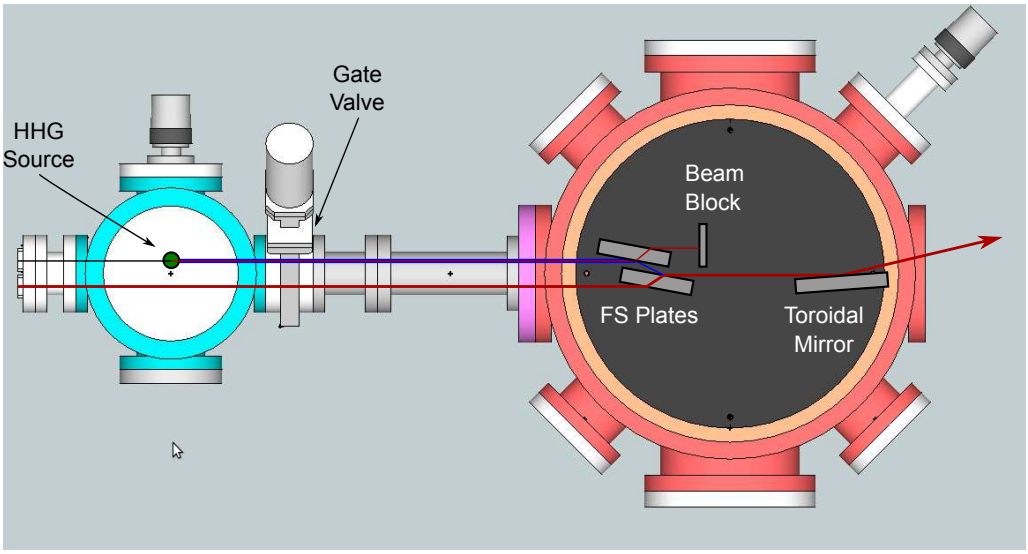


Figure 5.2: Schematic of the High Harmonic and recombination chambers.

A schematic of the vacuum line for the harmonic generation and recombination optics is presented in figure 5.2. The first chamber houses the HHG source: a differentially pumped tube target. A schematic of the tube target is shown in figure 5.3. The tube target is constructed from a 1 mm OD, 0.5 mm ID capillary which is encased in an outer sheath. 1 mm holes have been placed either side of the sheath to allow propagation of the laser through the target and that allows the target to be differentially pumped and reduce load on the rest of the chamber system. The outlet of the tube target was pumped by a separate SH-110 scroll pump. Gas flow into the system is controlled using a precision leak valve by Swagelok. The gas supply is held at a backing pressure larger than 1 bar so that any small residual leaks of the system (after leak testing for any detectable leaks) will not result in contamination of the gas system. Since we lacked an absolute measure of the pressure at the interaction region, the HHG chamber pressure was used as an indirect measurement since the pressure will be proportional to the flow rate. The target is mounted on an X-Y-Z manipulator for positioning with respect to the laser focus.

After the HHG chamber there is a gate valve and a short transfer section to the mirror chamber. The recombination chamber houses the recombination optics and a broadband, gold coated toroidal mirror to refocus both the IR and XUV collinearly in a 2f-2f focusing setup. The recombination optics are constructed from two fused silica plates (made by J.Fichou - Optique De Precision 03640306). The plates each have a thickness of 20 mm with a usable surface area of 90 mm $\times$ 15 mm and have anti-reflective coatings for both S and P polarized IR (one coating each side) and will transmit $\approx$50% of the XUV for energies 15-40 nm. For the correct polarisation the plates will remove $>$ 99.99 % of the IR of the generating beam. By rotating the polarisation using the $\lambda/2$ plates before the chamber it is also possible to allow approximately 25% of the IR to reflect off the plates to aid in initial alignment of the system and check the temporal overlap of the pulses. Spatial

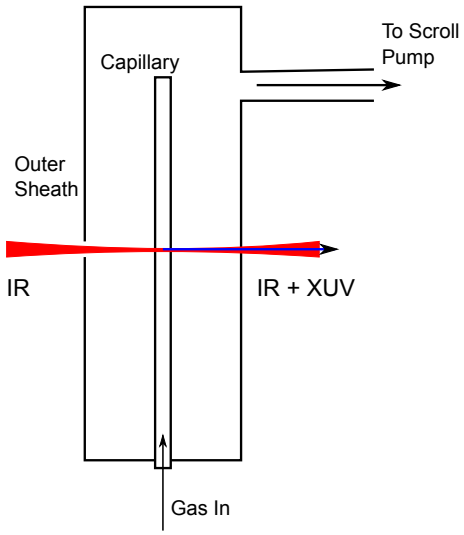


Figure 5.3: Schematic of the tube target used for generation of the harmonics. The differential pumping of the outer sheath allows reasonably high source pressures to be used without compromising the rest of the vacuum.

overlap of the two beam paths is achieved by allowing the IR beam to refract through the plate. From Snell's law the angle of incidence at both sides of the plates will be equal allowing two overlapped beams assuming the initial spatial separation of the beams is correct. For a grazing incidence of 10° the distance between the two beams is 11.4 mm.

5.2.2 XUV flat-field spectrometer

At the end of the beamline there is an XUV FFS designed and built by D. Neely. At the entrance to the chamber there is a motorised filter wheel that can contain up to 6 different filter/slit combinations. The grating is a Hitachi 001-0437 flat field grating with 1200 lines per mm nominal groove spacing, a radius of curvature = 5649 ± 20 mm, and gold coated. The grating is mounted on a simple kinetic mount, with a zero order beam block attached and is mounted on a linear translation stage, which can translate the grating in and out of the beam path in the vertical direction. If the grating is lowered, the beam will pass through the apparatus onto a prism fixed at 45° which directs a part of the beam through a focusing lens and through an exit window, allowing both imaging of the focus and temporal overlap and alignment of the beam without needing to break the vacuum of the system.

The detector is a Andor camera backlit CCD (DO420) with a spectral response as shown in figure 4.5. The CCD has a 256x1024 sensor, 26.6 mm x 6.7 mm, with a pixel size 26 μm^2 and an acquisition card which is capable of a maximum pixel digitisation rate of 1 MHz, yielding a maximum effective frame rate of ≈3.8 fps. The distance from the grating to the focal plane of the detector is 247 mm and the grazing angle used to image the harmonics was 4.5°. The calibration curve of the instrument is shown in figure 5.5. Since

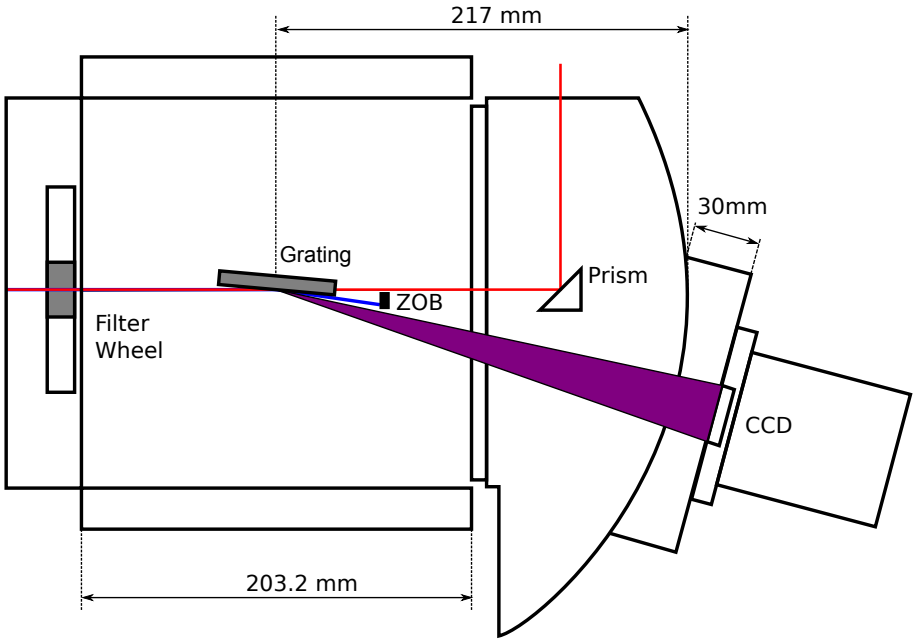


Figure 5.4: Schematic of the Flat-field spectrometer

the camera CCD chip is too small as to capture an entire spectra, the flange the camera is mounted on can be translated around the instrument to look at different spectral regions.

5.2.3 Magnetic bottle electron spectrometer

Located between the mirror chamber and the flat field spectrometer is the main experimental chamber, which for the commissioning experiments was a magnetic bottle electron spectrometer (MBES). As described is section 4.3.2, one of the major practical limitations of electron TOF spectrometry is achieving the requisite energy resolution and count rate. One way we could in principle increase the count rate of an electron spectrometer is to use a combination of electric and magnetic fields. Let us assume we apply a homogeneous magnetic field which is cylindrically symmetric in the z axis. In this case, the particle trajectories will be altered according to the Lorentz force. In the presence of a **B** field, any particle that has a velocity component perpendicular to the magnetic field will now be confined to a helical trajectory with radius given by the cyclotron radius r:

$$B\,|q|\,v_\perp = \frac{mv_\perp^2}{r} \tag{5.2}$$

$$\therefore r = \frac{mv_\perp}{B\,|q|}. \tag{5.3}$$

Thus for particles with low enough energy, the magnetic field will constrain the particles to radius smaller than the detector, increasing the collection efficiency, but with sacrificing

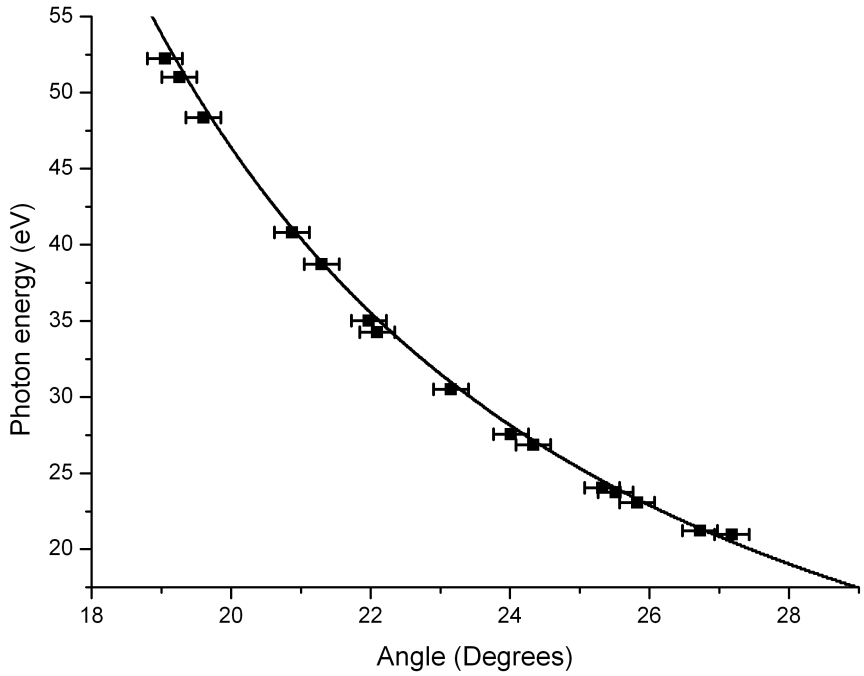


Figure 5.5: Calibration curve of the flat-field spectrometer

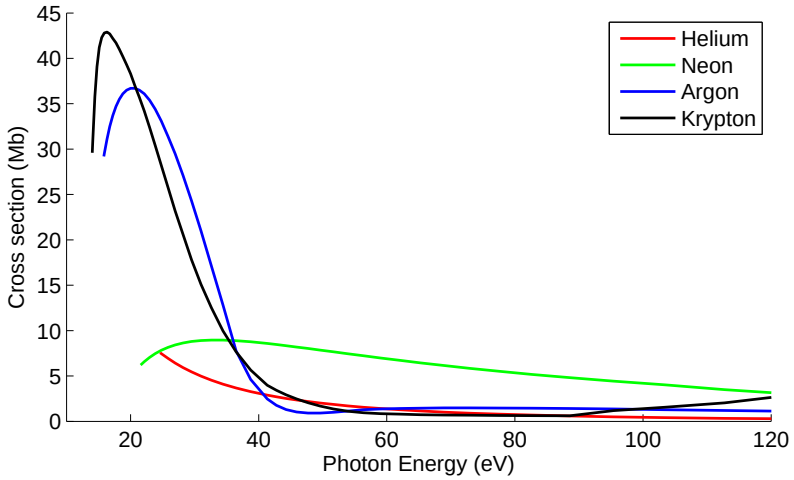


Figure 5.6: Single-photon ionisation cross-sections for the noble gases. Values taken from Proc. Royal Soc. 349 pp. 397 .

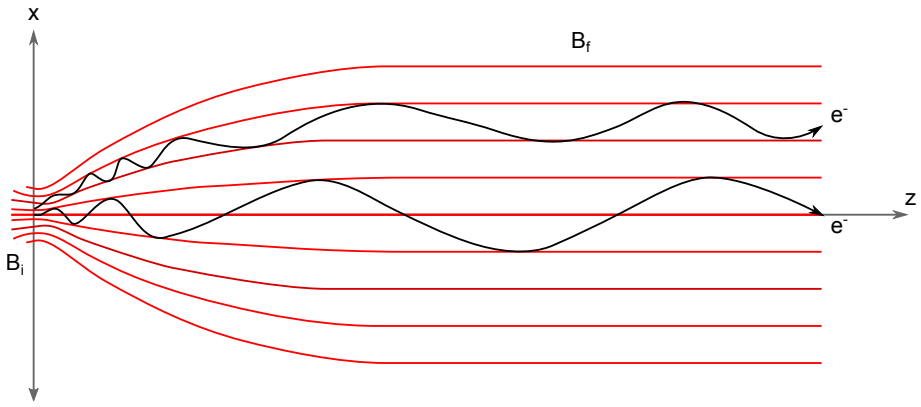


Figure 5.7: Principle of operation of the Magnetic Bottle electron spectrometer. The electrons' (black) trajectories are parallelised as they travel from the high magnetic field B_i to the low field B_f. The trajectories are constrained by the magnetic field lines (red).

energy resolution since for a given kinetic energy of the particle there will be a spread of velocities in the propagation axis of the detector.

It is, however, possible to get the best of both worlds by taking advantage of a non-homogeneous magnetic field, still cylindrically symmetric about z but now with a strength that changes as a function of z. Assuming the magnetic field changes slowly enough, the magnetic moment will be conserved [135, p. 592-596] and particles will be constrained by the field lines into a trajectory that results in a parallelisation of the electron trajectories. This is the underlying idea behind the operation of a MBES, which is shown schematically in figure 5.7. Its operation is described in depth by Kruit et al. [136] and can be summarised thus: a particle in a magnetic field has an angular frequency ω of:

$$\omega = \frac{eB}{m} \tag{5.4}$$

where e is the electron charge, B is the magnetic field and m_e is the electron mass. If we combine this expression with (5.2) we can obtain an expression for the radius of the electron's path, r as a function of its angular frequency:

$$r_i = \frac{v \sin\theta}{\omega} \tag{5.5}$$

where v is the velocity and θ is its angle relative to the flight tube axis so that $v_\perp = v \sin\theta$. Thus we can define its initial angular momentum, $L = mvr \sin\theta$, and substituting r for equation (5.5) yields:

$$L = \frac{m^2 v^2 \sin^2\theta}{eB}. \tag{5.6}$$

Assuming adiabatic invariance, the angular momentum of the electron should be conserved so that $L_i = L_f$, where the i and f subscripts denote the high and low magnetic fields

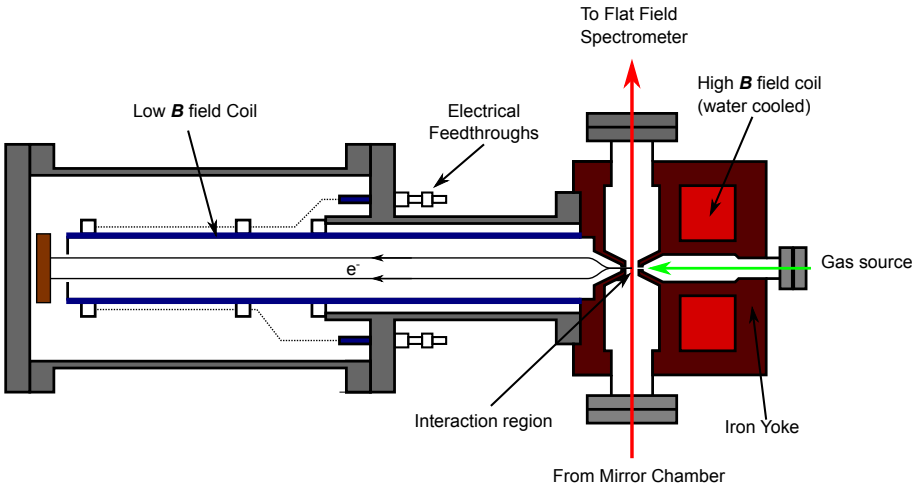


Figure 5.8: Schematic of the magnetic bottle electron spectrometer used in the experiment.

respectively. Cancelling common terms and rearranging, the relation between the magnetic field and particle velocity can be written as:

$$\frac{\sin\theta_f}{\sin\theta_i} = \left(\frac{B_f}{B_i}\right)^{\frac{1}{2}}. \tag{5.7}$$

It can be seen from equation (5.7) that if $B_f < B_i$ then then similarly $\sin(\theta_f) < \sin(\theta_i)$ and the electron motion will be parallelised. The degree of parallelisation can be found by solving equation (5.7) for the z velocity component v_z:

$$v_{zf} = v\left[1 - \frac{B_f}{B_i}\sin^2(\theta_i)\right]^{\frac{1}{2}}. \tag{5.8}$$

In the limit of $B_f << B_i$, $v_f \approx v$. Depending on the exact configuration this allows a 2π or even 4π collection solid angle. As in the case of standard time of flight, by keeping acceleration region small compared to the overall drift tube length the total time of flight can be approximated to T_D, and unlike a standard TOFS the collection efficiency is largely independent of the flight tube length, allowing both a high resolution and high collection efficiency in the same instrument, with the trade off of sacrificing any possibility of angular sensitivity.

The MBES used for these measurements uses a 50 cm drift tube. The strong magnetic field is generated by a coil with ≈1000 turns in a radius of 0.05 ±0.01 m coupled to an iron yoke. The weak field is generated by a coil with≈200 turns/m along the length of the drift tube. The electrons are then detected using a F4655-12FX-1CF203 two-stage (chevron) Hamamatsu integrating MCP assembly with an electrostatic grid 4 mm in front of the MCP.

Since the magnetic bottle relies on the magnetic field lines directing the electrons to

the detector, effective shielding of the drift tube from background magnetic sources such as turbo pumps was important to ensure a good signal of the MBES, and a Helmholtz coil pair was used to achieve this. A Helmholtz coil is constructing using two magnetic coils with identical current flow and size, resulting in a magnetic field within the coils that is approximately constant. The magnetic field for a single coil of n turns is given by:

$$B = \frac{\mu_0 n I R^2}{2(R^2 x^2)^{\frac{3}{2}}} \tag{5.9}$$

where I is the current, R is the radius of the roil, x is the position from the centre of the coil and μ_0 the vacuum permeability. By multiplying by two (as we have two coils) and setting $x = R/2$ and simplifying, we yield:

$$B \approx \left(\frac{4}{5}\right)^{\frac{3}{2}} \frac{\mu_0 n I}{R}. \tag{5.10}$$

By using two sets of coils in both the horizontal and vertical axes we can fully compensate for the background magnetic fields. Since the magnetic fields may vary depending on where or when the equipment is being used, the best operating conditions are usually found experimentally through iterating the coil currents for best signal quality and strength.

Acquisition was achieved using a Tektronix DPO 7250 digital phosphor oscilloscope, which was capable of a maximum time resolution of 250 ps with 200000 samples per trace. A simple effusive source was used, which propagated through a 1 mm aperture in one of the magnetic pole pieces into the interaction region via a precision needle valve which could accurately control the flow rate into the interaction region.

5.3 High harmonic optimisation

The harmonics were generated using the Coherent Legend. Given that the Legend typically operates stably at 1.9 mJ per pulse and at a 1 kHz repetition rate, and its beam diameter is $\approx$ 10 mm and given our chosen focusing conditions we would expect a diffraction limited focal spot of 34 μm diameter. Actual measurement of the focal spot size was achieved using a Wincam CCD beam profiler using a small part of the picked off beam. Using this method the actual beam diameter was measured to be 55$\pm$5 μm FWHM, which is approximately 1.6 times the diffraction limited size. The confocal parameter of the focus was measured to be 10$\pm$1 mm.

The pulse duration as measured by the spider was 50 fs FWHM. Using equation 3.4 the maximum achievable intensity using this set up under these parameters is calculated to be 2.2×10^{15} Wcm^{-2}: more than sufficient to generate harmonics.

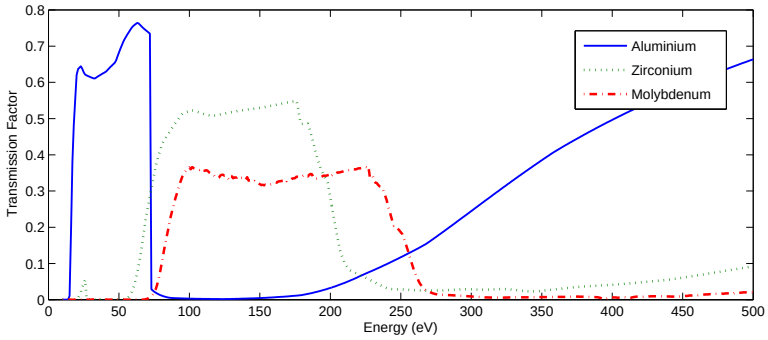
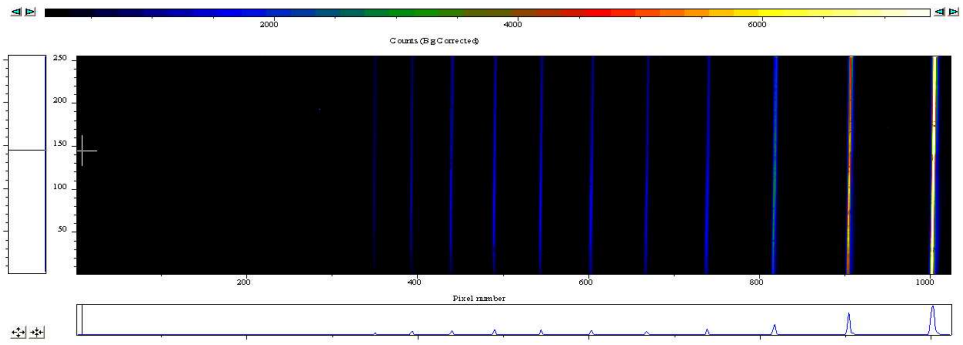


Figure 5.9: Transmission of 200 nm thick filters of aluminium, zirconium and molybdenum as a function of photon energy.

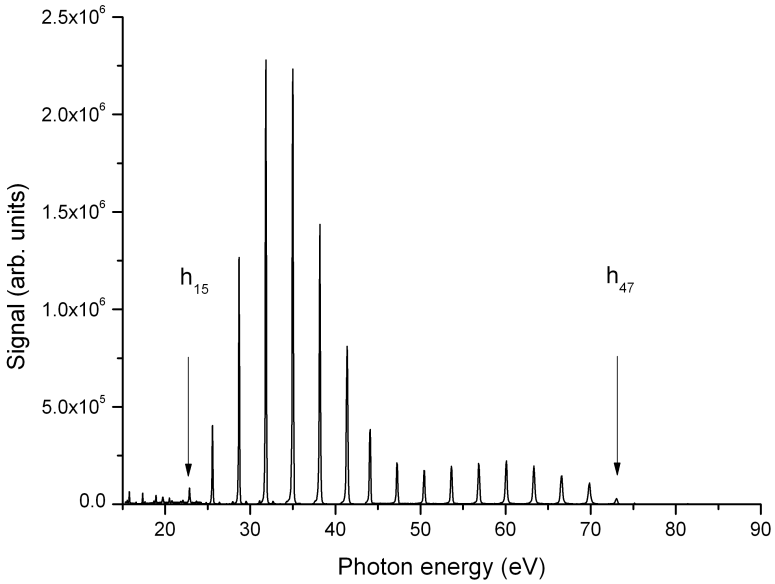
To filter out any residual IR from the harmonic beam, which for a CCD detector like the Andor would swamp the harmonic signal, a metal filter was placed in the filter wheel just before the grating. A thin (hundreds of nm) thick filter of metal can successfully eliminate almost all incident IR while still retaining a reasonable transmission of the XUV radiation (see figure 5.9). Aluminium was chosen for our purposes since its transmission window matches well with the expected transmission of the system. A thickness of 200 nm was chosen empirically by observing the best compromise in signal to noise. Any IR that still manages to get into the spectrometer via scattering can be successfully removed from the camera signal by taking a reference image for when the IR is propagating but the gas is off so that no harmonics are produced.

Figure 5.10 show the harmonics generated in argon. The pulse duration was measured to 55 fs, the pulse energy on target was 1.2 mJ with a HHG chamber pressure of 1.25×10^{-4} mbar. The images were taken by accumulating 10 pictures of 1s exposure time. Figure 5.10a shows a typical readout from the CCD. Clear features corresponding to the harmonic structure are observed. Since the CCD chip is not large enough to capture the full spectrum in one go, a full spectrum requires the chamber to be pumped up and the camera moved to a new central angle. Since CCD chips do not have as stringent operating pressures as an MCP, and the chamber is small relative to the pumps attached to it, the movement can be achieved with reasonable speed (of the order of 10-20 minutes). Figure 5.10b shows a complete spectrum, generated using 3 images taken at detector angles of 18, 23 and 27 degrees respectively. Harmonics up to the 47 th are observed and the spectrum follows the expected structure except for the weakly phased matched lower harmonics.

Optimisation of the phase matching conditions of the harmonics an be achieved by scanning the position of the tube target in the laser propagation direction and scanning the pressure of the HHG pressure (and therefore source pressure). These scans are shown in figure 5.11. They show that for on axis emission, i.e. short trajectory phase matching, the optimal position of the jet is when it is located 2 mm behind the focus. The pressure scan demonstrates that the total harmonic yield increases monotonically over the range

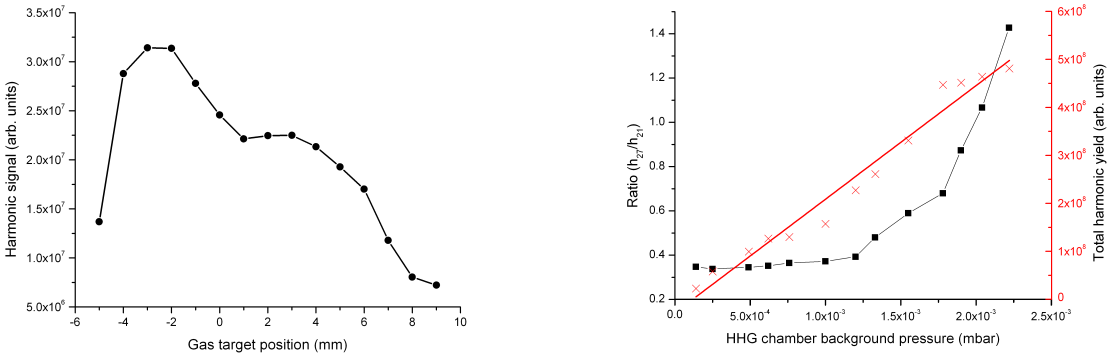


(a)



(b)

Figure 5.10: Harmonic signal as captured with the flat field spectrometer. (a) typical readout from the CCD camera. (b) Full calibrated spectrum constructed from 3 separate images taken at angles 18, 23 and 27°.



(a) **(b)**

Figure 5.11: Effect of the (a) position of the tube target with respect to the laser focus in the propagation axis, and (b) the pressure of the source gas on the harmonic signal.

of operating pressures, the relative yields of harmonics 21 and 27 starts to rapidly change beyond pressures of 1×10^{-3} mbar. As such this was chosen as the limit of our standard operating pressure for the next experiment using the electron detector.

5.4 Electron spectroscopy measurements

Now that we have successfully generated and detected harmonics using the flat field spectrometer we can now attempt to detect them using the magnetic bottle. For this experiment the harmonics were focused into the interaction region of the magnetic bottle so that we could observe the photoelectron spectra from ionisation. There are a large number of parameters to consider with the magnetic bottle and careful optimisation of each parameter is essential to obtain best signal.

Harmonics were generated in argon using the same set of conditions as described in previous sections. The detection of the harmonics will be performed by using the harmonics to directly ionise the valence electrons of a noble gas. The kinetic energy of the ejected electrons should then just be the difference in the ionisation potential and the harmonic photon energy. Neon was chosen as the gas since according to figure 5.6 it has a relatively flat absorption cross section over a large range of photon energies. Gas was flowed into the interaction region using a needle valve until the interaction region pressure approached 1×10^{-6} mbar, which was the maximum safe operating pressure for the MCP detector. Optimisation of the signal was achieved by slowly bringing the large and small B field coils up in current and then iterating between the two Helmholtz coils repeatedly until the best signal was achieved. The final operating voltages for the system are shown in table 5.1.

Component	Voltage (V)	Current (A)
MCP anode	2200	0
MCP back	1888	0
MCP front	391	0
MCP grid	0	0
Strong B-coil	67.5	5.0
Drift B-coil	2.6	5.1
Helmholtz V	11.7	4.7
Helmholtz H	13.5	4.5
Drift tube cage	0	0
Extractor	0	0

Table 5.1: Operating voltages and currents at optimal operating conditions for the magnetic bottle.

The time of flight trace will need to be converted to energy, and this is achieved numerically by rebinning the data for an energy vector with fixed bin size. The number of channels per bin will change depending on the energy bin due to the nonlinear relationship of energy to TOF, and the energy bin edges will almost certainly not line up exactly with a particular time channel. As such, the signal for times equal to the bin edges was calculated through a linear interpolation of the TOF signal, and the total signal for a given energy bin was calculated from trapezoidal integration of the signal using the two interpolated values and all time channels with TOFs that fell between the two bin edges. This method is shown schematically in figure 5.12. One potential problem is that a DC offset in the TOF traces will contribute to a larger proportion of the integral at lower energies leading to an artificially large signal, though this can be minimised or eradicated through correct selection of an offset voltage.

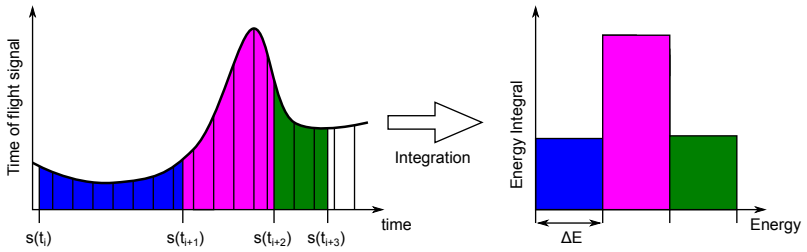


Figure 5.12: Principle of rebinning TOF traces into equal width energy bins. Linear interpolation is used to calculate the time of flight signal at times corresponding to the edges of equal width energy bins. The energy integral is calculated using a numerical integration of the time of flight using the two interpolated edges and the TOF channel signal enclosed in the two edges.

Figure 5.13 shows a harmonic signal as acquired using the magnetic bottle, averaged over 1600 laser shots (or 1.6 seconds of laser operation). Clear peaks corresponding to discrete harmonics of the source are observed. The harmonics of of a 800 nm laser are located at odd multiples of 1.55 eV. Given the ionisation potential of neon is 21.56 eV, we would expect that the lowest energy harmonic detected by the magnetic bottle would

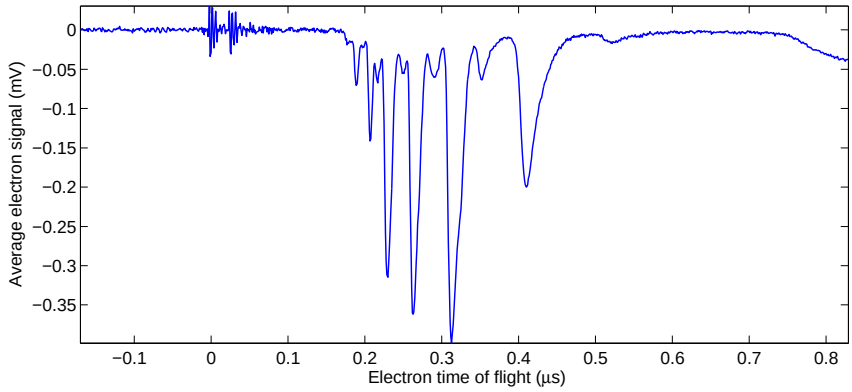


Figure 5.13: Electron time of flight signal acquired using magnetic bottle for neon ionised with high harmonics. Times are shown relative to a photodiode trigger.

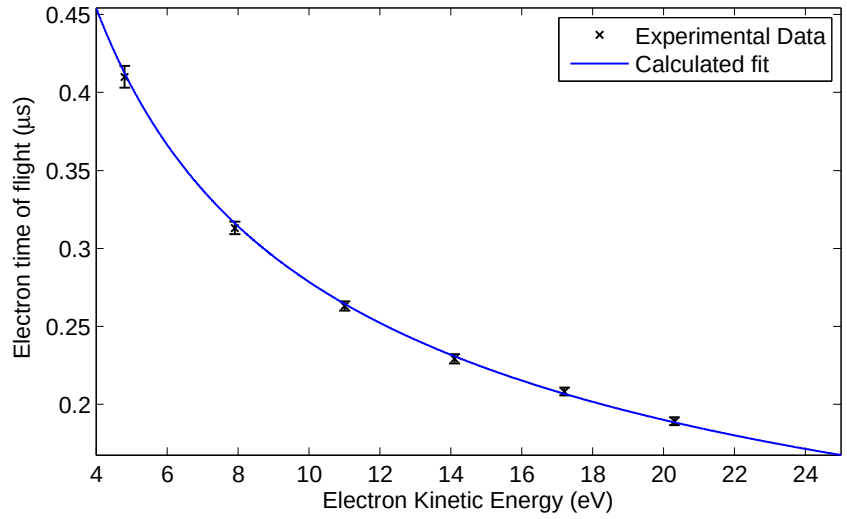


Figure 5.14: Calibration of the electron time of flight signal as produced by high harmonics. Experimental data circular points and line fitted to equation 4.13

be either the 15th harmonic at 23.25 eV or the 17th harmonic at 26.35 eV. The lowest energy peak will be the peak located at the longest TOF, which in this case is the peak located at 0.410 ± 0.007 μs. We can then use the flight times of the other peaks, and the knowledge that each one must be separated by 3.1 eV to infer the expected energy of each peak. Only one will produce a good fit however. Using Matlab's curve fitting tool, it was found that the first identifiable peak is the peak corresponding to the 17th harmonic. Using a least squares regression fitted to equation 4.13, the calibration coefficients were calculated to be C = 0.942 ± 0.019 μs eV$^{1/2}$ and T_0 = -0.0203 ± 0.0061 μs. Figure 5.14 shows the experimental data plotted against the calculated fit. Good agreement of the fit with the experimental data is observed.

By using the above calibration and applying it to the electron TOF signal we can show a fully converted energy spectrum. The energy spectrum shows that the instrument is

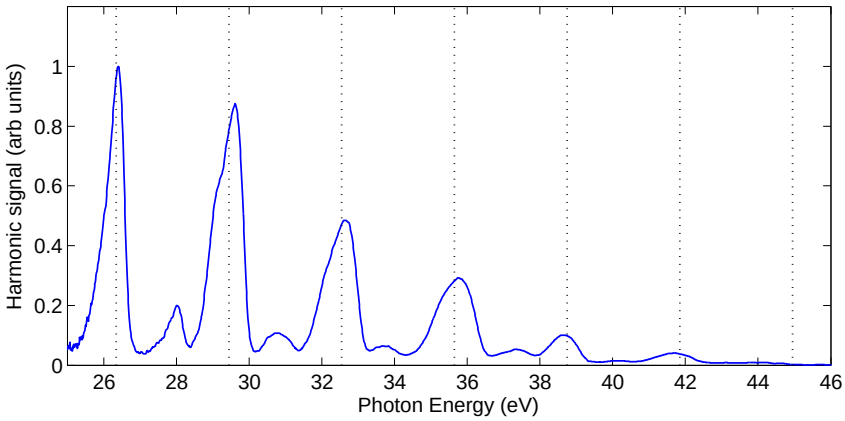


Figure 5.15: Normalised high harmonic signal recorded using the magnetic bottle. Yields have been calculated using interpolated rebinning, and normalised to the photoabsorption cross section of neon. Black dotted lines show theoretical locations of the harmonic peaks. A good match is observed.

capable of measuring the harmonic spectra, with a resolving power of 0.5 eV. There are also weak sidebands located at the energies equal to the even harmonics. These come from absorption of some residual IR which must have been present in the beam.

5.4.1 Future work

The commissioning experiments have demonstrated that the MBES has sufficient resolution to resolve both the harmonic structure and the sidebands from an 800 nm source. Future experiments in the group will be able to take advantage of the ability to characterise the XUV pulses, which will be a great advantage for any experiments for which the temporal structure of the harmonics is important. A recent focus of the Laser consortium is studying harmonics generated from plasma plumes [127]. The spectrometer provides the potential for experiments in studying the phase properties of the harmonics from these recently exploitable sources, which as of writing remains a largely untapped area of research.

5.5 Software development

Initially the control systems for the different parts of the experimental rig were operated using separate control software environment. While each of these programs had some degree of programmability, there is no easy way for the frameworks to communicate with each other. The new generation of experiments would require a far more robust acquisition framework since it is not practical to constantly switch between programs and change settings manually when operations like delay scans need to make multiple changes on the fly. The main two components of the existing rig that required new frameworks were the

piezo stage and the Andor camera, as they would form the foundation of any delay scan performed in the future.

A number of different options existed for building up the acquisition software, including Labview, Matlab or dedicated programs using compiled languages. It was decided that the new software would be written in Matlab for the following reasons (a) MATLAB was the language most prevalent in the group and the easiest to pick up for a non-programmer, allowing future user the best possible chance of modifying the program if required (b) The relative simplicity involved in adding functionality to the GUI and (c) easy integration with analysis software already existing within the group, and as any currently running Matlab session can access any functions of currently open figures or scripts currently on the path, it is a trivial matter for a master control script for a particular experiment to access and change settings on a currently open GUI.

Figure 5.16b shows a screen grab of the completed Andor acquisition software. The Andor acquisition program was coded by using an SDK supplied by Andor Technology. The SDK compiles individual C++ functions into individual MEX files which can be called. In order for these functions to be easily accessible to users, a fully functional GUI that emulates much of the functionality of the standard Andor software. The basic frame settings such as exposure time, and frame delay were automatically recalculated for the nearest acceptable value each time the user changed a setting. Three full acquisition modes were implemented, standard imaging mode, full vertical binning, where any vertical resolution is sacrificed and a simple integrated line out is read, and single track where only a single row of pixels is used.

CCD cameras are limited in frame rate by the speed of the ADC in the frame grabber. For the Andor PCI camera series with the CCI-010 frame-grabber, the maximum ADC rate is 1 MHz, which translates to frame-rates of 3.82 frames per second for a 1024×256 pixels. Binning the CCD in either the vertical or horizontal directions treats a group of pixels as a single 'super-pixel', allowing faster readout speeds and lower signal to noise at the expense of vertical or horizontal resolution. Additional sub-GUIs were coded that allowed user to change these settings, along with selecting additional features relevant to the acquisition mode. Implementing this feature would allow future users flexibility and choice in future experiments depending on whether speed or vertical/horizontal resolution is the primary requirement.

Cooling of the chip was successfully tested and implemented and the GUI feeds back the current temperature of the chip using a timer function that executes every second. All settings of the camera and properties such as the detector size, current temperature and so on are stored in a single application data structure which can be accessed easily by other scripts.

Figure 5.16a shows the GUI created for the Piezo stage. It uses a generic driver library (dll) that will work with most stages of a similar type, and the GUI has been designed

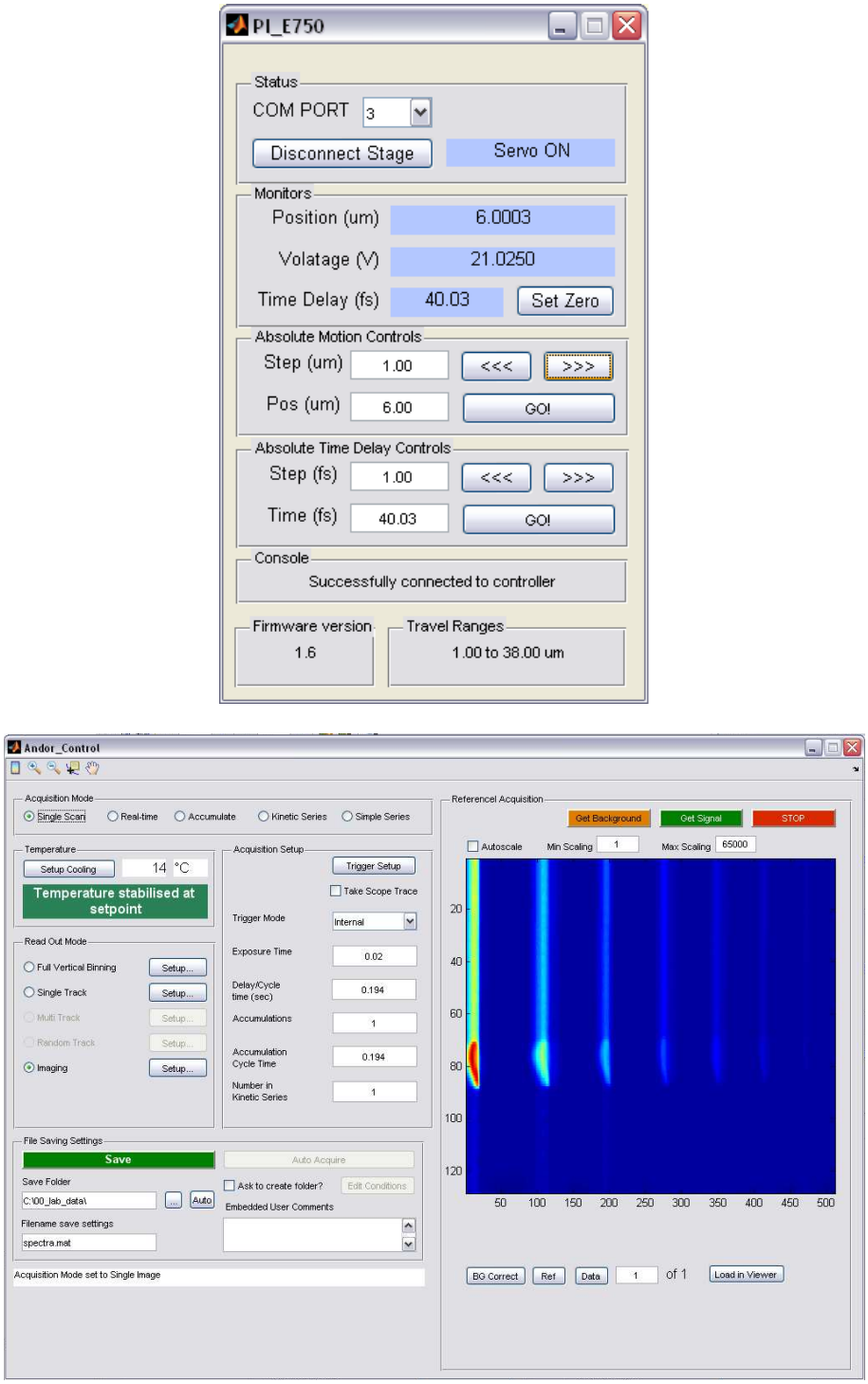


Figure 5.16: GUIs coded in Matlab for control of both the Piezo stage and the Andor camera.

so that it will automatically detect the model and firmware version and set the internal parameters of the GUI so that the user cannot select stage positions outside the range of the stage. A Matlab timer function is once again used to provide user feedback of properties such as the current position and applied voltage.

As well as position the user can also select a required time delay relative to an arbitrary zero which the user can set, or else it uses the minimum position of the the delay stage. The delay τ is simply calculated using $\tau = 2s/c$ where s is the position setting. Users can either choose an absolute position or time or increment in a chosen step size. These functions are then directly accessible using outside programs such that delay scans can be easily built up. For delays or positions outside the range of the stage an error is sent to a user console located at the bottom of the GUI and the position reverts to the last stored 'good value'.

5.6 Summary and Outlook

In this chapter we have demonstrated that all the elements of the described experimental beamline are capable of robust generation and detection of harmonics, and developed a series of software interfaces that will allow them to be used in future pump-probe experiments. Currently two new chambers are in the preliminary stages of design and construction, one to replace the harmonic chamber with a larger chamber capable of housing multiple HHG sources, and one to replace the magnetic bottle in the beamline with another gas source. This chamber will be used, among other experiments to generate harmonics using XUV excited molecules. The first source will be used to generate an XUV pulse, before using a relatively weak IR field to drive HHG in the excited molecule, with the aim to study the HHG spectrum of these excited molecules. Characterisation of these harmonics will remain an important part of the development of the new sources and of the eventual study of these molecules. As such, it is expected that both the magnetic bottle, the flat field spectrometer and the software developed for the line will see considerable use in future experimental runs performed by the newer members of the group.

Chapter 6

Molecular isomerization probed with soft X-rays

Because of the jitter inherent to SASE sources, such experiments remain technically challenging and require considerable post analysis work, but nonetheless are are an area of focus for LCLS experiments that study molecular and atomic systems. This chapter describes the AMO experimental station, including its detection systems and data acquisition methods, before describing an experiment performed in 2010 and analysed over the following months to use the LCLS source and a synchronised UV source to perform a UV pump, X-ray probe experiment to study the isomerisation of 1,3 cyclohexadiene.

6.1 The AMO experimental station

Although the LCLS facility has 6 different experimental end-stations, all of the experiments described in this thesis were performed using the AMO end station. The AMO station has been designed primarily for studying the interaction of X-rays with simple systems such as atoms, molecules and clusters. The station consists of 4 vacuum chamber systems: the single pulse shutter, used for experiments where using only a single X-ray pulse is desirable, the focusing optics, the high field physics end station and a diagnostics chamber, and described in depth by J. Bozek [137]. The shutter and diagnostic chambers were not used, and will not be described in depth, but allow the AMO chamber to operated in a single pulse mode and allow the absolute measurement of the FEL bandwidth and photon energy respectively. A total of five, 15 mrad (0.86°) grazing incidence optics steer the beam into the chamber. The optics are fused silica coated with 50 nm of B_4C, with calculated reflectivity $R \approx 0.9$-0.93 across the 500-2000 eV photon energy range. For five optics the total transmission would be expected to be $R^5 = 60$-70%. However experiments performed thus far using the chamber estimate transmissions in the range of 15-30% [28, 138]. Two of these optics, located in the focusing chamber, are Kirkpatrick-Baez type [108] mirrors

which are used to focus the x-rays down to a minimum of 1 μm^2 over a 480 - 2000 eV energy range. Larger foci can be achieved either through detuning the KBOs or by translating the high field physics chamber (HFPC) chamber in the FEL propagation axis. The HFPC is the main experimental chamber, which will now be described in more depth.

6.1.1 High field physics chamber

The HFPC has a focus on time of flight spectroscopy and has been designed to be highly modular in nature, allowing the use of a variety of detector/sample types. A schematic of the chamber in its standard configuration is shown in figure 6.1. The chamber fits a variety of sample delivery systems, including a single/double skimmed jet, a bubbler for liquid samples and stages for solid targets. For detection, the chamber has been designed to mount one of a selection of large TOF detectors, the standard options being a simple Wiley-Mclaren ion TOFS and electron/ion VMI.

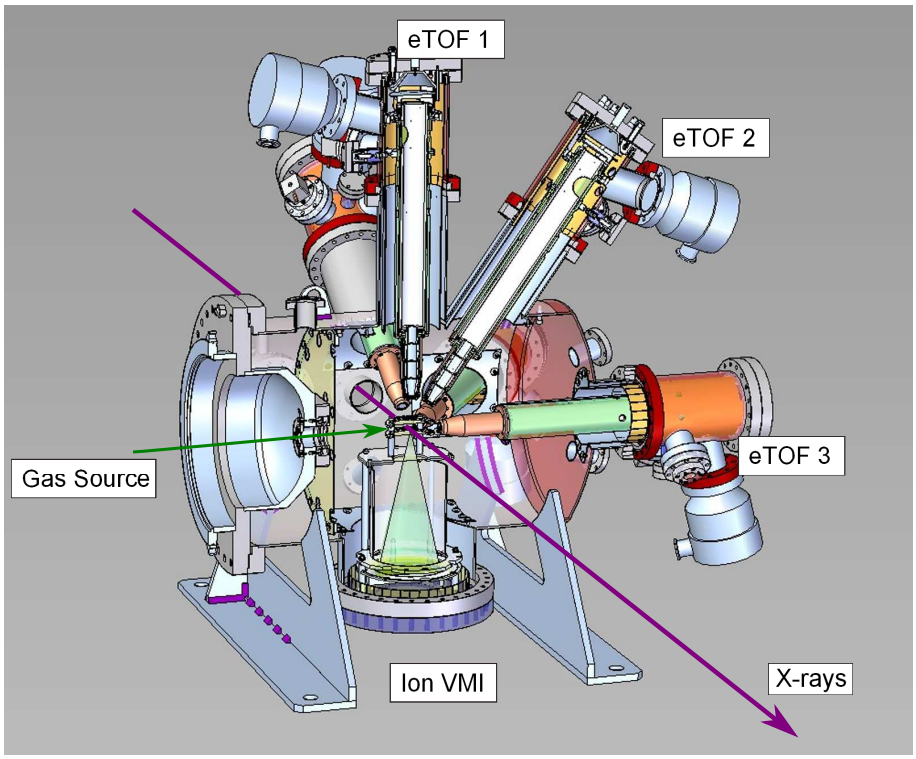


Figure 6.1: Schematic of the high field physics chamber in its standard configuration, including 5 high resolution Hemmers type electron TOFS, an ion VMI, and a skimmed gas jet. This figure was adapted from [139], with additional annotations.

In addition to the main detector, there are five high resolution electron TOF spectrometers. Photo-electron and Auger electron kinetic energies from X-ray ionisation can be many hundreds of electron volts. The TOF for such energies is extremely small, only hundreds of nanoseconds per m of drift tube, and it is therefore generally necessary to use

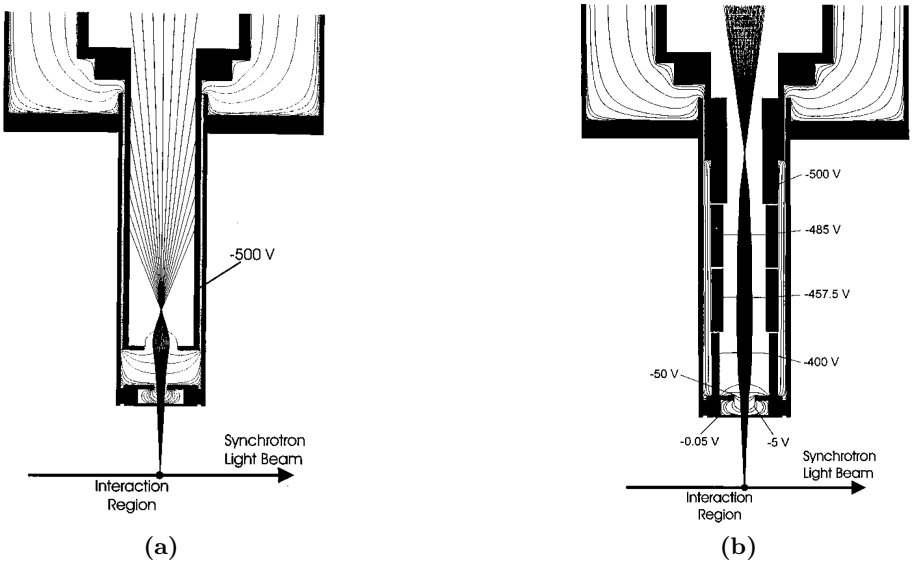


Figure 6.2: Schematic of the Hemmers electron TOF design for (a) a single retarding electrode and (b) multiple retarding electrodes and electron trajectories for an 505 eV kinetic energy. The single electrode design causes the electrons to defocus, reducing transmission, whereas the multi electrode design acts to refocus the beam, retaining peak transmission. Taken from Rev. Sci. Inst. 68 pp. 3809 [140].

a significant retarding voltage to slow down the electrons enough for good energy resolution. Since these retarding voltages are generally non-uniform, this has the adverse effect of defocusing the electron beam and thus decreasing an already small collection efficiency. In 1998 Hemmers et al. proposed a TOFS design that uses multiple electrodes to form an electrostatic lens. This lens refocuses the electron beam such that the transmission is retained even for very high retardations [140]. The electrode structure and electron trajectories for both a single and multiple electrodes case is shown in figure 6.2. The TOFS used on the HFPC are of a similar design, two mounted on the axes perpendicular to the X-ray beam and 3 more at certain 'magic angles' where the the signal intensity does not depend on the detection angle [28].

All instruments installed in the chamber have the option to be run concurrently, allowing in principle both electron and ion data to be acquired simultaneously in electron-ion coincidence measurements. As users are not allowed in the hutch when the X-rays are propagating since the beam can be a significant hazard, all systems, including voltage, camera and sample delivery settings are controlled remotely in the control room using LCLS's extensive data acquisition (DAQ) system.

6.1.2 Data acquisition and processing

The infrastructure of LCLS allows for a far more robust and complete data acquisition system than you would typically find in a university laboratory, and almost all possible

data is recorded to a hard disc cluster backed up to tape storage. The TOF traces, from all instruments are captured using a ADC system called Acqiris, which is capable of digitising signals with a maximum time resolution of 125 ps and 200,000 samples per trace for a total length 25 μs. Image data from both the VMIs and other diagnostics are captured using a number of CCD cameras. These, along with the FEL machine parameters such as electron beam energy, peak current and so forth are recorded on a shot by shot basis. There is also a system called Experimental Physics and Industrial Control System (EPICS) for 'slow' variables that aren't typically varied on a shot-to-shot basis, for example delay stage settings for the visible laser sources, chamber pressures, and any other user variables that may be relevant for the particular system.

In terms of 'online' analysis, the user has multiple tools at their disposal to provide a preliminary view of the data being acquired, whether images or TOF traces, including averaging, hit/edge detection. Given the limitations in computational resources compared to what is needed to fully process the data in real-time, the vast majority of analysis is done post-experiment. In principle, assuming that 80% of the available experimental time is utilised, data for approximately 2×10^7 shots can be acquired. The limited timeframe associated with an FEL beam time and the fact we are largely at the mercy of the accelerator scientists when it comes to the laser performance means that the team generally acquires data even if experimental conditions are less than ideal, as we need to make the most of whatever time is available. Downtimes of half a shift are unfortunately not as uncommon as would be liked. Thus a large part of the effort involved in these experiments, and indeed the work of this PhD has been in post analysis and sorting of the acquired data, as this can take many months or even years to complete. Data can quickly rack up and can easily top 1 GB of data being produced per minute when dealing with the possibility of both TOF and image data acquired at 120 Hz, and thus quickly writing to disk with as small a memory footprint as possible, rather than user friendliness of reading/processing the data, was the primary consideration when the DAQ was built up.

All data of a given run is initially written to disk in one or more binary data files in XTC format. Since these XTCs can be in excess of 100s of GB for a single run, efficiently parsing this data into a form that can be analysed is crucial. The XTC files can be read using a number of tools which sequentially parse the XTC files for relevant information on a shot by shot basis, which can then be analysed directly if you know the relevant languages or saved in a different, more friendly format for use in another language. LCLS provides two methods called myana and pyana which are written in the C++ and Python languages respectively.

In addition to the official LCLS tools there are some third party libraries developed by outside groups that use FELs. One I have experience in using is called CASS, which is set of tools by the CFEL group at the Max-Planck Society. Unlike the pyana and myana frameworks, the CASS system consists of a library of precompiled 'Postprocessors' written

in C++ which are designed to do a specific operation (such as grabbing a dataset, or multiplying two histograms). By combining multiple postprocessors together it is possible to create quite complex routines from simple building blocks. The postprocessors are called and configured using a simple .ini file which requires no programming knowledge. It can be compiled in both an online version which reads the data-stream directly, which can be used for preliminary online analysis, or an off-line version which processes a list of XTC files.

Given the relative complexity of obtaining the data, and the sheer volume of it produced, of of the primary challenges in analysis is developing a suitable working method by which large volumes of data can be analysed quickly and effectively, and even in this case it may be months or even years before conclusive results may be achieved. Even given the right framework, a significant section of the data may sit unanalysed as manpower is always limited. A significant amount of the effort expended in this PhD was in learning the relevant acquisition frameworks, and developing computing scripts in a variety of languages capable of analysing the output from the LCLS facility. Appendix A describes the LCLS data formats, server access, gives a brief overview on using the pyana analysis frameworks, representing the core of the knowledge gained in this area as part of my studies.

6.2 Time resolved studies of molecular isomerisation in 1,3-cyclohexadiene

An isomerization reaction is one in which the constituent atoms of a molecule remain the same, but there is a change in its molecular structure through bond breaking or twisting. The study of such reactions has been performed extensively in the last decade through the use of optical pump-probe experiments. While highly successful, the use of visible and IR wavelengths necessitates the use of high intensities in order to ionise the system being studied, which can potentially lead to distortion of the molecule during the measurement.

In August of 2010 I participated in an experiment headed by Vladimir Petrovic of the PULSE institute at SLAC to perform time resolved fragmentation imaging using a comparatively low intensity but short duration X-ray source. Using a timing scheme first demonstrated by Glownia et al. [29], we perform a UV pump, X-ray probe experiment on CHD (C_6H_8), a small ring molecule which is part of the cycloalkene group. The results were successfully published in Physical Review Letters in 2012 [30]. My contribution to the experiment was in analysing the time-of flight spectra and performing simulations in order to provide an energy calibration for the VMI spectrometer used for imaging the molecular fragments.

6.2.1 X-ray induced fragmentation as a probe for large molecules

Coulomb explosion imaging (CEI) is a technique that determines a molecule's structure through ionisation to a very high charge state, causing the molecule to break up into multiple measurable fragments [141]. The kinetic energy of a particular fragment will depend on the distance relative to the other positively charged fragments at the moment of ionisation, and thus the kinetic energy distribution of the ion fragments can reveal information about the structure of the molecule at the instance of ionisation. For Coulomb explosion imaging to be valid, the removal of the electrons from the molecule must be fast compared to the nuclear motion of the molecule, and the final charge state must be high enough that Coulomb repulsion of the fragments is the dominant contribution to the final kinetic energy of the fragments. Historically these experiments were performed by using either beam foil experiments [142], or though ion bombardment [143]. In the former scheme, an ion beam of the species to be studied is prepared and then accelerated to a few MeV in kinetic energy. By firing the ion through a thin foil, interactions of the valence electrons with the foil electrons leads to multiple electrons being stripped from the ion in less than a femtosecond. In the latter scheme, the collision of the molecule with a MeV kinetic energy ion leads to multiple ionisation. These experiments, while successful, had significant limitations in that they required a particle accelerator to be performed.

A significant advance in the technique accompanied the development of high intensity laser systems. Pioneering experiments performed by Frasinski et al. demonstrated the potential for using a high intensity laser source to drive dissociation in small molecules [144]. In their pioneering experiment using HI, they demonstrated that the ionisation under such conditions occurs sequentially, rather than directly, with the observed kinetic energy of 20 eV for the H^+ and I^{5+} fragments much lower than the expected 46 eV for Coulomb explosion of HI^{6+}, since the internuclear separation has already increased beyond equilibrium at each ionisation step. Further experiments performed by the Saclay group demonstrated the applicability of the laser driven CEI method to small molecules and hydrocarbons [145–147].

The great success of the laser driven CEI method is twofold, both making the technique more accessible to experimental groups, and the possibility of synchronising the ionisation source to other laser sources allowed the CEI technique to be employed in pump-probe experiments, which has allowed amongst other things the study of wavepacket evolution in excited systems [141, 148]. Although the ionisation occurs over many cycles of the pulse, by keeping the pulse short the time resolution can be kept equal to the pulse duration. The main disadvantage of this scheme is that since an visible/IR laser must ionise over many cycles, since there is no direct channel to the high charge states, and high intensities are required to ionise the system. This means that the laser contributes significantly to both the final energy of the fragments and can lead to the molecular structure being deformed. In an experiment performed on N_2, Baldit et al. demonstrated that the energy

release of the N_2^+-N_2^+ channel is dependent on both the pulse duration and intensity of the ionising pulse [149]. In their experiment, the energy difference between 10 fs pulses and 40 fs pulses was measured to be between 12-15 eV depending on the intensity, and both were lower than the Coulomb repulsion limit, though the 10 fs measurements were much closer. Additionally, experiments by Hishikawa et al. demonstrated that for the Coulomb explosion of $CO_2^{z+} \longrightarrow C^{p+} + O^{q+} + O^{r+}$ driven by a 1.1×10^{15} Wcm^{-2} laser, the O−C−O bond angle was observed with a mean amplitude of 40° compared to the field free amplitude of 12.5° [150].

Clearly using IR laser driven CEI has some limitations, which only becomes exacerbated when dealing with larger and more complicated systems. Using an X-ray source would be in principle be beneficial since the X-rays are capable of producing multiply charged ions through the comparatively simpler process of single photon absorption, which acts on unperturbed core electrons. Single photon absorption of an X-ray photon by the k-shell, as discussed in section 2.2.3, can lead to the ejection of multiple electrons in a cascade of Auger decay processes [151], and such schemes have been successfully used in the last decade to study nuclear motion in core-excited molecules [152–154]. However it has only been in the last few years that the requisite time resolution made available with SASE FELs has made pump-probe schemes technically feasible at the X-ray wavelengths. The aim of this experiment was to demonstrate that a similar scheme to IR driven CEI could be employed, but with the IR probe pulse replaced with a femtosecond X-ray pulse. The potential advantages of this scheme compared to the IR probe scheme are two-fold. The X-ray ponderomotive energy is negligible, of the order of 10s of meV compared to the several eV or more that IR sources generate, providing a comparatively 'field free' probe of the molecule. Secondly, the Auger process is both fast (occuring over 10s of femtoseconds) and capable of yielding high final charge states depending on the atomic number Z. For example, charge states of 6+ have been observed for single photon multiple ionisation in argon [155]. For lower Z atoms (neon and lower) the most probable final charge state after single photon absorption is 2+ [156], which while low is still sufficient to induce fragmentation in some molecules.

6.2.2 The ring opening of 1,3-Cyclohexadiene

A ring containing molecule can undergo a transformation through either a photoabsorption process or through heating of the molecule. The energy deposited into the molecule is quickly converted to vibrational energy, leading to the possibility of a σ bond being either formed (a ring-closing) or lost (a ring opening) at the expense of a π bond. This type of reaction is called an electrocyclic reaction and is a subgroup of a more general category of reactions called pericyclic reactions. An electrocyclic reaction is described as conrotatory if both termini (the two atoms involved in the bond breaking/forming) both rotate in the same direction or disrotatory in the opposite case, and which one the molecule undergoes

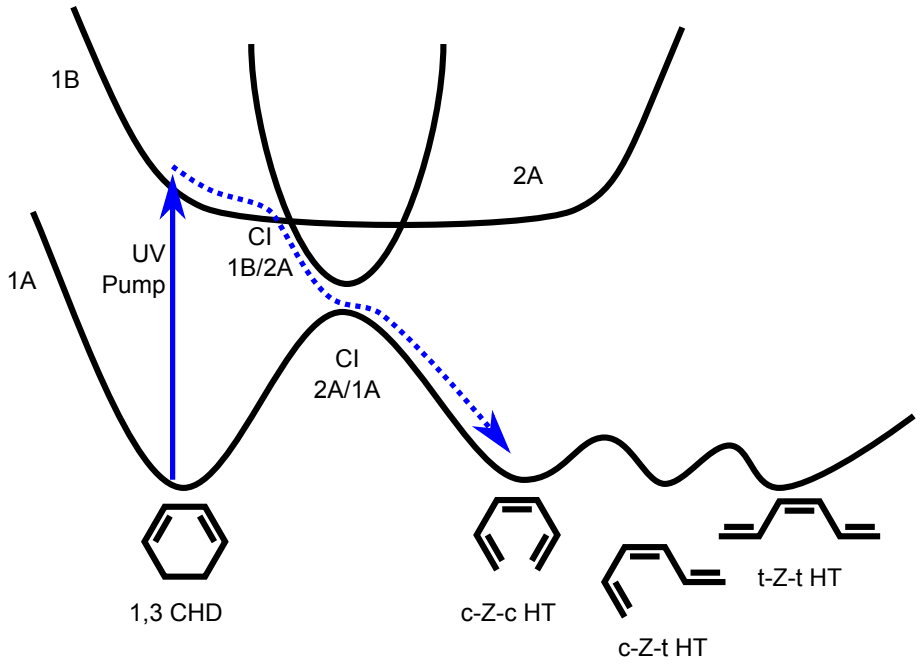


Figure 6.3: Energy level diagram and pump robe scheme for the CHD experiment. An inital UV pump promotes a wavepacket from the $1A_1$ state to the $1B_2$ state. This undergoes a non-radiative transition to the $2A_1$ state, and accelerates towards a conical intersection between the $1A_1$ and $2A_1$ states. The wavepacket then continues on to either the CHD or HT ground states. CIs denote conical intersections. In reality, the 2A/1A CI is a symmetry breaking intersection and actually lies out of the plane of the page in this diagram.

is dependent on both the electron configuration and the form of the initial excitation, and in general can be described using the Woodward-Hoffmann rules [157, p. 732]. For a photoabsorption induced isomerisation, the reaction is disrotatory if the number of electrons in the system is equal to 4n (where n = 1,2,. . .), and conrotatory for the number of electrons equal to 4n + 2, and the opposite is true for a thermal excitation.

CHD undergoes a conrotatory ring opening reaction on absorption of a UV photon, forming the linear molecule HT. The ring opening reaction of CHD to HT and its reverse reaction are of particular interest and have been extensively studied as they are one of the stages in the synthesis of vitamin D. In humans, naturally occurring 7-Dehydrocholesterol exposed to UV light from the sun undergoes isomerisation into previtamin D_3 which is then converted to vitamin D through thermal hydrogen migration. A similar reaction may also be utilised in industry by using Ergosterol, forming vitamin D_2 [157, p. 793].

A qualitative description of the energy level scheme and evolution of the system is shown in figure 6.3. In summary, CHD has a strong absorption centred at a wavelength of 250 nm and spanning the range 212 - 278 nm. This absorption results from the excitation from the $\pi\pi^*$ (1A) ground state to the 1B excited state, with the Frank-Condon vibrational modes dominated by pi double bond stretching and twisting. As the wavepacket accelerates, energy is deposited into the CH_2-CH_2 σ bond, and the molecule then undergoes

a non-radiative transition to the 2A state, circumventing the 1B/2A conical intersection. The wavepacket accelerates towards a pericyclic minimum, located at the halfway point between the CHD and HT ground states. There exists a symmetry breaking conical intersection between the 2A and 1A potential surfaces, and from there can either evolve into either back into ground state CHD or into the various HT isomers. The whole process from initial excitation to final product takes less than 200 fs to complete [158].

Numerous studies of the ring opening reaction have been done in optical pump-probe experiments, and have been summarised in a recent review article by Deb and Weber [159]. In 2000 Fuß et al. published a comprehensive study of the time evolution of the ring opening process using a strong IR field [158]. Using a UV pump and an 800 nm probe of around 100 fs duration, with a probe intensity of 2×10^{13} Wcm^{-2}, they studied the ion yields of different fragmentation species as a function of the pump-probe delay. Several key results were presented in this paper. Firstly, although the normalised ion yields of the parent species of both CHD and HT were near identical, the yields of the fragments differed significantly before and after fragmentation. In particular ions of mass number 51, 39, and 27 showed an order of magnitude increase, and the yields of the C^+ and H^+ fragments showed a 2 orders of magnitude increase, with the additional result that the kinetic energy of the H^+ fragments increased from 2.74 ± 0.15 to 4.82 ± 0.20 eV. Secondly, by observing the yield of transient ion species, they were able to measure the timescale of the evolution of the different states. If the molecule is ionised from the 1B state, a $C_6H_8{}^+$ ion in the ground is formed, whereas ionisation from the 2A state has approximately 2.5 eV of additional vibrational energy, which is sufficient to overcome the potential barrier for dissociation into H and $C_6H_7^+$. These ion peaks will only be present for delays shorter than the lifetime of the states, so by observing both the peak position and the decay time of the peaks, the time constants associated with those states can be calculated. Fuß calculated that the 1B and 2A states have time constants of 43 and 77 fs. These results were further supported by a study published one year later by Garavelli et al. [160], which showed both computational and experimental results in good agreement with the timescales presented by Fuß. A more recent study by Kosma et al. using a much shorter pulse duration (10 fs) yielded constants of 56 and 80 fs respectively [161].

6.2.3 Experimental setup

The experiment was performed using the HFPC under the standard configuration as shown in figure 6.1. During the course of the experiment we used an ion VMI spectrometer to image the ion fragments. The VMI had a total source to detector distance of 314 mm, and the fragments were imaged with an 80 mm MCP and a P46 phosphor anode. Images were acquired using an Adimec OPAL-1000 camera, a low noise CCD operated at 120 fps at a maximum resolution 1024 × 1024. Additionally for some runs we used the electron TOF opposite the VMI as an ion TOF (flight tube length 597 mm). The CHD gas source was

prepared by flowing 200 mbar of He through a room temperature sample of liquid CHD (vapour pressure $\approx$ 10 mbar at room temperature). This was passed through a pulsed gas jet and a single skimmer to form a molecular beam in the interaction region of the detector.

A pump pulse was prepared from the third harmonic of a 800 nm source from a Coherent Legend, generating a 50 fs, 50 μJ pulse centred at 266 nm ($\approx$ 4.6 eV), and was used to excite the CHD to the 1B state. After a variable delay the molecule was probed using a defocused X-ray pulse with energy greater than the core IP, causing core ionisation and Auger decay, eventually leading to fragmentation of the molecule. A large X-ray focal spot size (30×50 μm^2 compared to the minimum of 2 μm^2) was chosen to ensure an X-ray intensity where only single photon absorption processes are likely to occur. The LCLS was operated in the 40 pC mode, with a nominal pulse duration of 70 fs, and a pulse energy of the order of 1 mJ. Assuming 20 % transmission, this yields an approximate intensity of 1.4×10^{14} Wcm^{-2} and a ponderomotive energy of 0.0267 meV. The photon energy was 850 eV; though ideally we would have liked to operate much closer to the carbon K-edge, at the time of the experiment this photon energy was lowest energy at which stable operating conditions of the LCLS could be achieved.

Overlap between the optical and X-ray sources was achieved in three stages. Initially the signals from photodiodes were observed on an oscilloscope and altered so that they overlapped, getting the pulses overlapped to within a few nanoseconds. Overlap of the UV and the IR source laser was achieved by looking at the yield of the H^+ yield as a function of the pump-probe delay, which as mentioned in section 6.2.2 is larger for HT. Figure 6.4 shows UV-IR ion TOF traces, and subfigures 6.4b and 6.4c show delay scans for the H^+ and $C_6H_n^+$ species. The two species display the same behaviour as described in section 6.2.2, with the H^+ peaking before plateauing off at long delays, and the $C_6H_7^+$ peak displays a transient peak around time zero, confirming temporal overlap of the IR and UV beams.

Finally, overlap of the 800 nm IR source and the X-rays was achieved by performing a cross correlation of the two sources using N_2. Core ionisation of N_2 yields a doubly charged ion after Auger decay. If a variable delay IR pulse is introduced, delays for which the IR comes after the X-rays results in dissociation of the $N_2{}^{2+}$ ion. If we observe the VMI signal gated on the N_2^{2+}/N^+ fragments, for delays for which the IR is late, we would expect to see fragments imaged at higher kinetic energies since the N^+ fragments will gain additional kinetic energy from the dissociation. This behaviour is observed in figure 6.5, which shows two VMI images using the above configuration for a delay for which the IR comes early, and another for which the IR comes late. For the late delay a clear shift in signal to higher kinetic energies is observed.

By combining all three techniques, the X-ray-UV temporal overlap can be calculated. Slow drifts of the timing of the X-rays relative to the RF frequency were observed over the

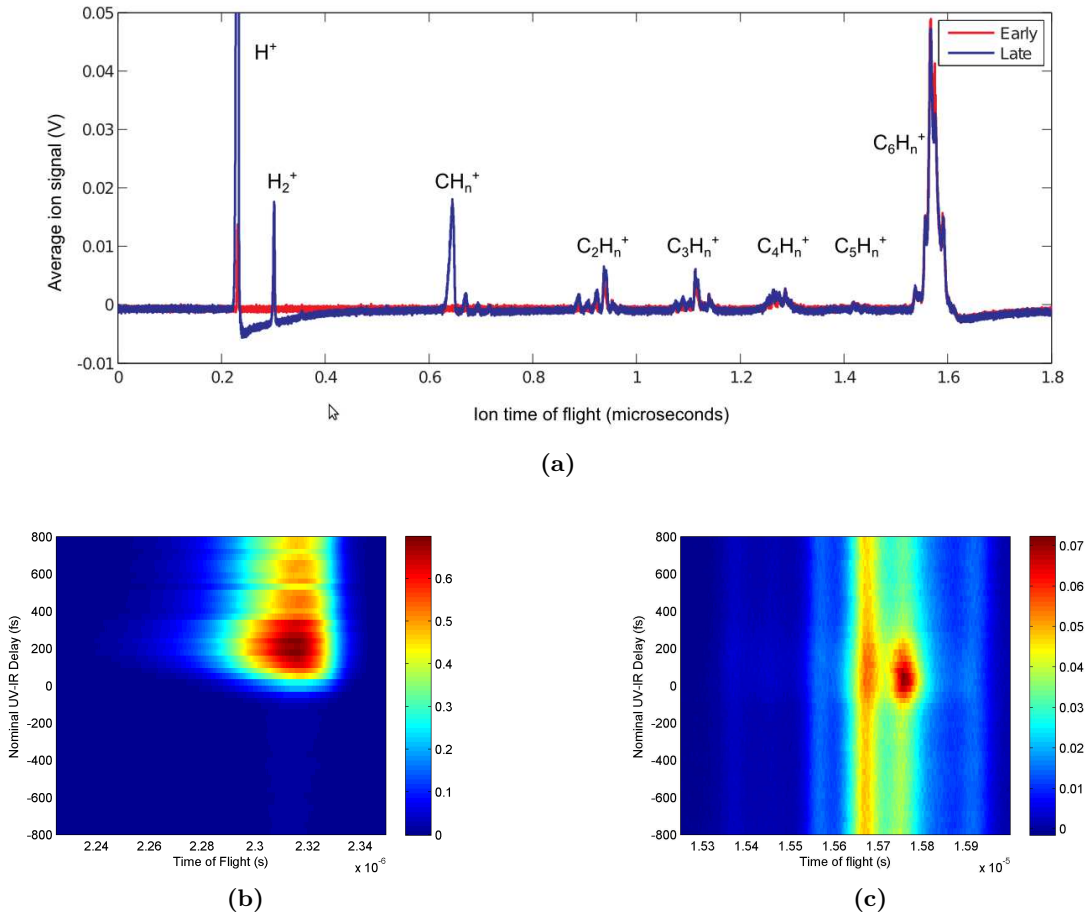


Figure 6.4: (a) Two ion TOF traces for IR early(red) and late (blue). The actual MCP voltage was negative, we have taken the negative of the signal so that ion signals are positive. Below: UV-IR delay scans for the 1,3 cyclohexadiene ion TOF spectra for the (b) H^+ and (c) C_6H_n ion species. The H^+ peak shows a peak near τ_0 and then plateaus and the $C_6H_7^+$ species displays a transient peak, which is the expected behaviour.

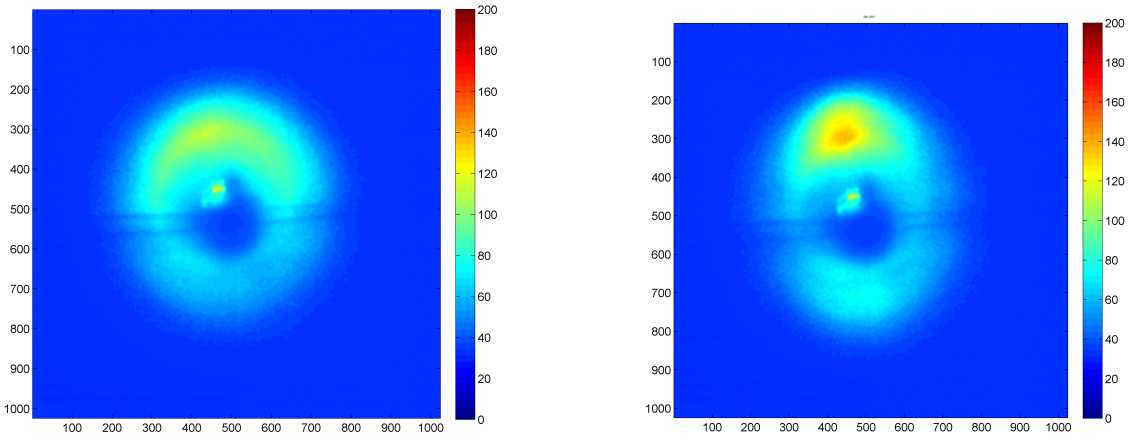


Figure 6.5: Dependence of the X-ray - IR delay on the kinetic energy distribution of the N^+/N_2^{2+} fragments. The two images show raw VMI data for (a) IR early delays and (b) IR late delays. Though the MCP damage obscures the distribution, a clear shift to higher kinetic energies associated with the dissociation of the N_2^{2+} ion is observed.

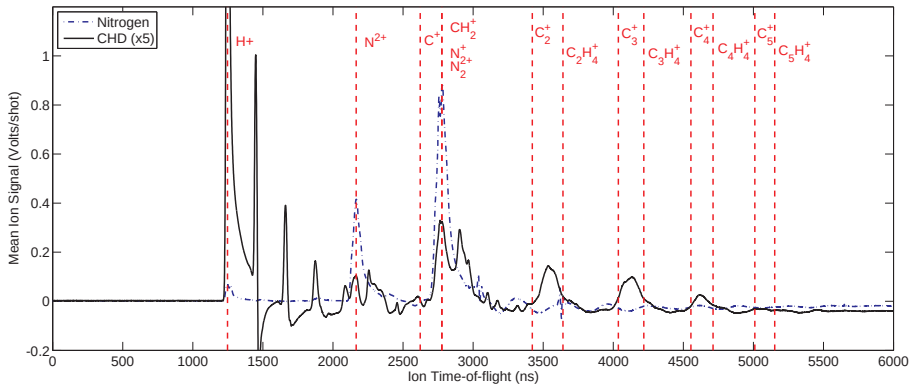


Figure 6.6: Ion time-of-flight spectrum of X-ray fragmentation of CHD (black solid) and Nitrogen (blue dashed). The CHD spectrum has been multiplied by 5 to improve clarity of the peaks compared to the Nitrogen peaks. Red dashed vertical lines show the TOFs for both N and CHD fragment species. A poor decoupling from the MCP caused ringing/echo artefacts, most noticeable after the H^+ peak.

course of a day, and so final analysis and determination of the temporal overlap position was performed in post analysis. The overall timing jitter between the X-ray and optical sources, after correction using the phase cavity jitter timings from the machine parameters, was calculated to be ± 300 fs. The optical beams were propagated co-linearly with the X-rays (through the use of a 'holey' mirror) into the interaction region, intersecting the molecular beam at 90°.

Figure 6.6 shows the ion TOF signal decoupled from the VMI for two runs, one with CHD and one with N_2. The spectra was calibrated using equation 4.12 and the known H^+ and N^{2+} peaks at T = 1.248e-6 and T = 2.166e-6 s respectively, yielding calibration

constants of T_0 = 6.9020e-07 s and A = 5.5780e-07. The decoupling of the signal from the MCP was not impedance matched, causing ringing/echo artefacts in the form of false peaks in the TOF signal.

6.2.4 Data analysis methods

Since at the time of the experiment I was still a relative novice to the LCLS analysis frameworks, the analysis was performed using the comparatively simpler method of using HDF5 files with Matlab. HDF5 is a hierarchical data format with a data structure similar to a computer's file system, with data stored in structures called groups and datasets*. Ideally we would prefer to use Matlab's powerful vectorised calculations abilities to simply take each relevant dataset and bin/average the data accordingly, however there are two technical problems with this approach. Firstly, an individual dataset may be several gigabytes large, and limits of RAM on a standard computer system prevent the analysis of the entire dataset in one go. Secondly, the DAQ occasionally fails to write some part of the data for a given shot, and in the HDF5 file this is not recorded in any way: the data is simply missing. Hence we cannot use the size of the datasets or their indices as an absolute reference of the shot number. Instead, the different shots were correlated by comparing the time stamps of each row of the different data sets. For a given time of flight trace, the time stamp associated with that trace was recorded and a search performed on the other needed datasets for a matching time-stamp value. If any of the other datasets were missing this timestamp, the shot was rejected, otherwise the calculations proceeded. Binned or averaged data was then built up by iterating through all TOF traces.

As described in section 3.4.3, the arrival time of the X-rays relative to the RF frequency of the accelerator (the signal to which the optical laser are locked to) displayes a jitter of a few hundred femtoseconds, but this can be corrected for by using the measured phase cavity times of the beamline data. The delay for each shot was calculated by using the fit time of the FEL phase cavity data, t_{pc}, and the EPICS delay stage read-back position s, using the equation:

$$\tau[\text{ps}] = \left(t_{pc}[\text{ps}] - \frac{2 \times (s[\text{mm}] - s_0[\text{mm}])}{c[\text{mm/ps}]} \right) \tag{6.1}$$

where s_0 is the stage position for τ_0. Square brackets indicate units used for the calculations. There were two delay stages which controlled the UV and the IR beam delays.

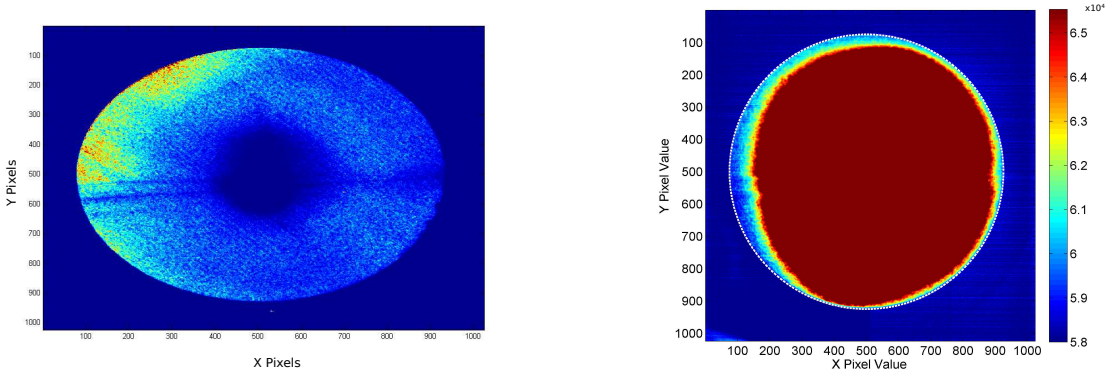
Analysis on the VMI images was performed by my colleague Marco Siano in collaboration with members of PULSE. One major problem which was uncovered only in the couple of days leading up to the experiment was the discovery of a large area of reduced sensitivity on the MCP. This damage is shown in figure 6.7a and significantly limited the

*These are roughly analogous to folders and tables respectively.

usable region of the detector. Attempts in using ion picking methods were unsuccessful in correcting for the non-uniform gain. Since the fragmentation pattern was not expected to display any angular dependence, and the fact the MCP damage limited our ability to perform such analysis anyway, the angular distribution of the fragments was neglected.

The inversion was performed on 512x512 (2x2 pixel binned) images using a PBASEX algorithm. The algorithm used 256 radial basis functions and Legandre polynomials of order 2. The kinetic energy release spectrum in this case is calculated from the radial distribution. However in order to convert between radius in pixels to energy, we required a calibration curve to map position to energy. Since we lacked an unambiguous independent energy calibration measurement for this particular experiment (which is usually achieved experimentally), I was tasked with performing simulations of the VMI at different operating conditions in order to calculate a theoretical energy to radius relationship.

6.2.5 Simion simulations and VMI calibration



(a) **(b)**

Figure 6.7: MCP dark counts for the detector used in the experiment (a) Summation of 2600 images. The area of reduced sensitivity is clearly visible. (b) The same run, but with the counts allowed to numerically saturate in order to see the MCP-phosphor edge for use in the energy to pixel value calibration. The white circle shows the numerically fitted circle, with center at 500,500 and a radius of 425 pixels.

Often the best method of getting a feel for how a particular TOF/ion optic system will operate is to computationally model the system and calculate the trajectories for particles of different energies and charges. Doing so will allow an estimate of the energy calibration of the system if for whatever reason an experimental calibration is unavailable. Simion is one of the most commonly used software suites for this purpose, and provides the user with the ability to construct an ion/electron optics system by defining a number of electrodes in a 3D grid system, and solving the Laplace equations for the system. By applying voltages to the electrodes both the electric field lines and a particles trajectory through them can be modelled with reasonable accuracy assuming you work within the limits of the program

(for example space charge effects are not accounted for). The calculated values must however be taken with a grain of salt, since the simulations cannot account for unknowns such as penetration of stray fields from background sources, and must ideally be tested against an experimental measurement of the properties of the detector.

The main properties of the VMI that must be evaluated are the conversion factor from energy to radius R on the detector, the energy resolution and the dependence of the source position to the observed radius. In a more general experiment we would also wish to consider the angular resolution of the detector, but since the damage to the MCP rendered such analysis impossible, it was neglected in my analysis and we consider purely radial distributions and dependences.

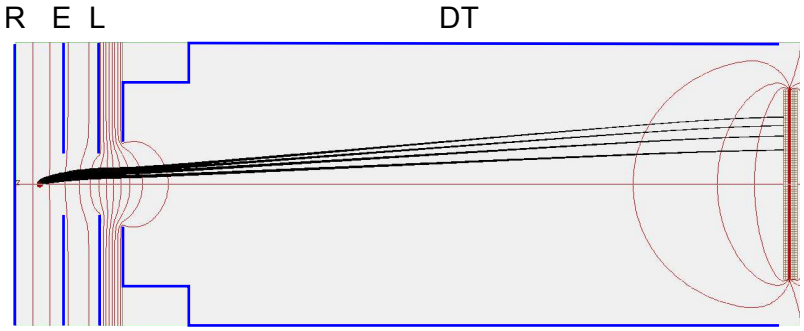


Figure 6.8: Potential array used for the Simion calculations for the VMI calibration. Blue overlays are the electrodes. Voltages used were R = 3000 V, E = 2130, L = 1600, DT = -960, MCP = -2000. Red lines are equal potential lines of 312.5 volt increments. Black lines are electron trajectories of energy = 5, 10, 15, 20 eV, ejected perpendicular to the propagation axis.

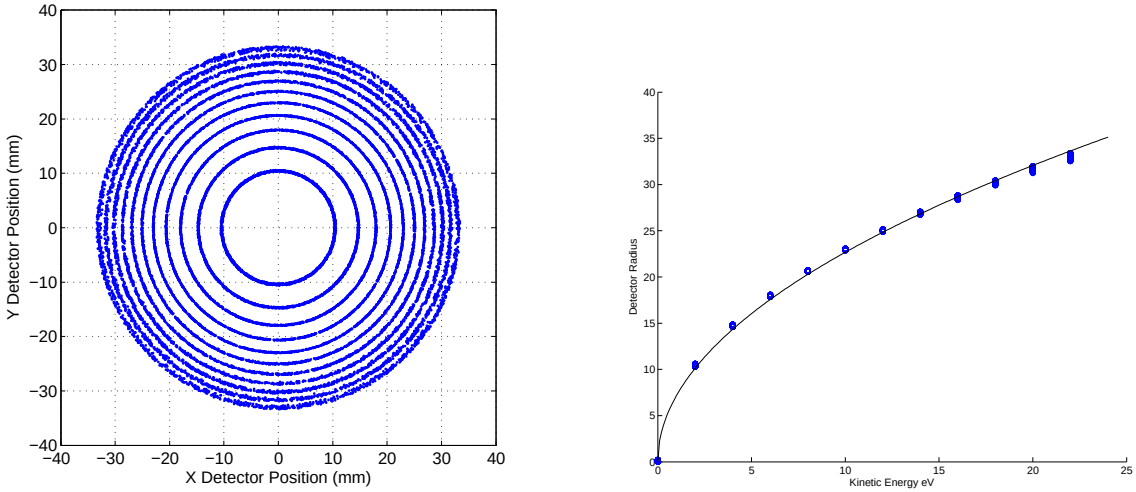
Figure 6.8 shows the potential array geometry used for the simulations, and the general configuration of the detector. The VMI had a total of 4 electrodes, including a standard repeller and extractor plate (labelled R and E respectively), an additional lens (labelled L) and a drift tube (D). The dimensions of the electrodes were as follows: the R-E distance was 20 mm, the E-L distance was 15 mm, the L-D distance was 10 mm, and the aperture diameters of the E, L and D electrodes were 26, 26 and 36 mm respectively. The voltage settings matched those used in the experiments, with R, E and L set to 2000, 1350, 1000 volts respectively. The drift tube was held at -960 V. This was a practical choice since we lacked suitable power supplies that could supply a sufficiently high voltage that could yield the necessary voltage ratios using only positive voltages.

Since the radius of the Newton sphere is defined by the particles that fly perpendicular to the flight tube axis, we limited the initial electron velocity distribution to the X-Y plane, and varied the initial kinetic energy in a linear series of 1 eV spacing, and charge equal to 1. Under these conditions we would expect to see a series of sharp rings on the detector, and the radial position of these rings yields the radius of the velocity sphere for the experimental ion distribution. Using equation 4.16 and condensing the experimental and physical constants to a single experimental calibration constant, and assuming a charge

of 1+, we can see that in the ideal case the radius R as a function of electron kinetic energy at birth $U_{k,0}$ can be described by the equation:

$$R = C\sqrt{U_{k,0}}. \tag{6.2}$$

The origin position of each particle is of course not directly centred at the optimum point of the interaction region, but is instead defined by the overlap of the X-ray source with the molecular beam. The electron origin points were randomised as to produce a spherical distribution centred at the interaction region and 1 mm in radius. Given our focus was an order of magnitude smaller than this, this value is used as a worse case scenario. The conditions for a 'hit' were either the electron hitting the electrode structure, or having a position in z equal to the distance to the detector plane (325 mm relative to the optimal source position). The ions positions in space, and kinetic energies at destruction were then recorded to either a text file or excel worksheet, achieved using a LUA† script.



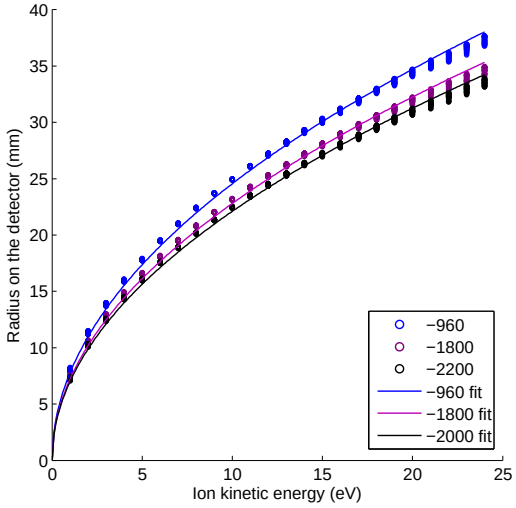
(a) **(b)**

Figure 6.9: Simulated projected velocity spheres for ion kinetic energies 0 24 eV. Voltage settings are 2000, 1350 and 1000 volts for R, E and L respectively. (a) The hit positions on the MCP detector. (b) The position to energy mapping. We can see that under the experimental conditions we used optimal focusing occurs for ions of approximately 10 eV. Black solid line is a fit for the equation.

Figure 6.9a shows the projected velocity sphere for ions with energy of 2 eV increments as would be measured by the MCP. The ring structure is well reproduced confirming that the VMI was operating as expected using this voltage configuration. Figure 6.9b shows the same data but with the radius plotted as a function of initial kinetic energy. It can be seen that for these voltages, ions of energy approximately equal to 10 eV were optimally focused. The solid line is a least squares fit to equation 6.2.

It was discovered in the course of the simulations that the fact that the MCP potential

†LUA is general purpose scripting language which Simion uses as a batch scripting language as of version 8.



(a)

Voltage (V)	C	C_1	C_2
-960	7.764	8.320	0.4743
-1800	7.211	7.744	0.4735
-1900	7.155	7.675	0.4739
-2000	7.094	7.631	0.4729
-2200	6.989	7.501	0.4737

(b)

Figure 6.10: Dependence of the MCP voltage on the simulated velocity spheres. (a) The hit positions on the MCP detector for 3 MCP voltages, -960 (same as the drift tube), -1800 and -2200 volts, which represent the extremes under normal operation. Higher voltages map the ions to smaller radii due to an electrostatic lens formation. (b) Fit parameters for different voltage settings.

had a significant effect on the final radial distribution. Since the flight tube was held at a negative voltage, and the front of the MCP plates were also held at a negative potential, the resultant field lines produced a lensing effect, and mapped ions to a smaller radial position than they would be detected in the field free case. Figure 6.10 shows the energy to position mapping for 3 different MCP potentials ranging from -960 V (the same as the flight tube potential) and -2200 (the maximum potential that can be applied to a dual layer MCP). Table 6.10b show the coefficients fitted using a least squares methods, for both equation 6.2 and a modified form with a variable exponent, $R = C_1 U_{k,0}^{C_2}$.

The raw data of course is of course not binned in position but instead in camera pixels, so we require another conversion between position on the detector and the pixel number of the detector. A run was performed looking at the dark counts from the MCP, from which the edge of the MCP phosphor is visible. Fitting the phosphor edge to the circle equation $R^2 = (x-a)^2 + (y-b)^2$, the MCP size was calculated to be centred at (500,500) pixels, and with a radius of 425 pixels. Figure 6.7b shows the images used to calculate the edge, with the fitted edge superimposed in white. Using these calculated values, and knowing the phosphor screen has a diameter of 76 mm, this yields a conversion factor of 11.18 pixels/mm.

The simulations so far have assumed that our ion source is well centred in the VMI interaction region. Practically this can sometimes be difficult to achieve. As a sanity check, investigations into the dependence of the detection position as a function of the source position were performed to see what effect the variance from the ideal source position had on the projected ions. Figure 6.11 shows the dependence of the projected velocity

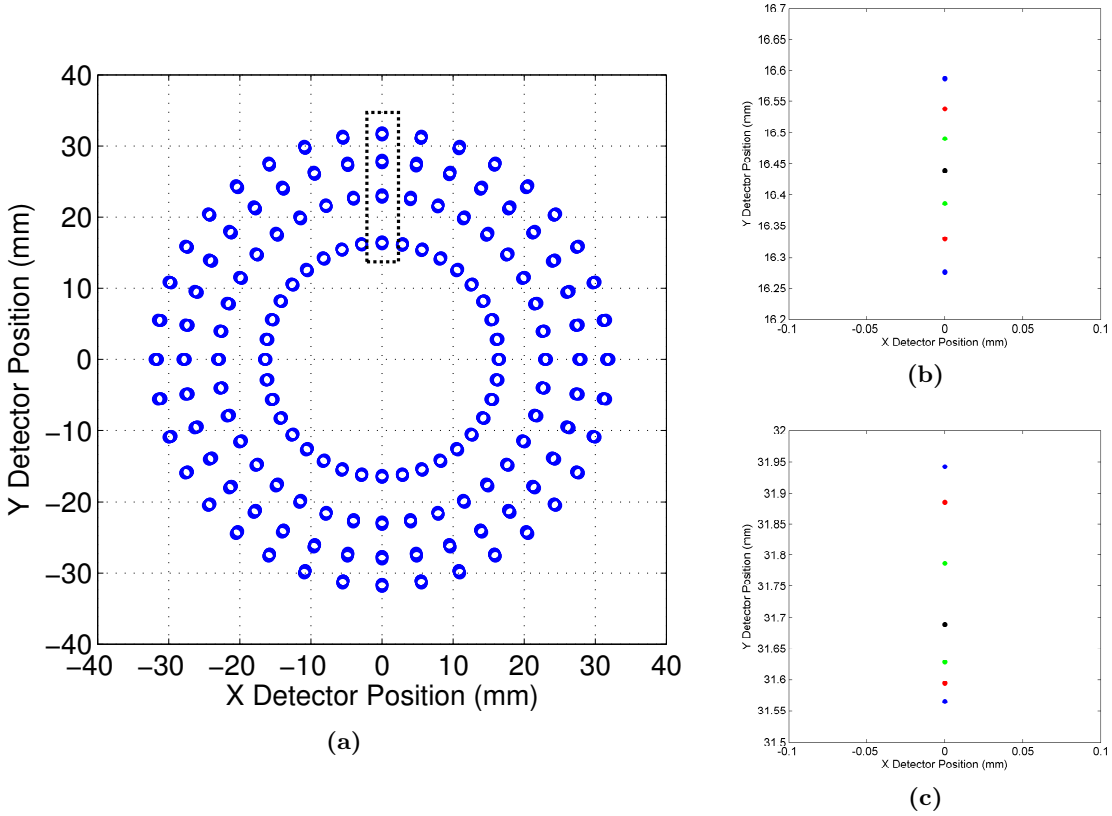


Figure 6.11: VMI detection radius as a function of the Z position of the source. (a) Scatter plot of detection position for ion kinetic energies of 5-20 eV in 5 eV increments, increments of 10° of ejection angle in the X-Y (detector) plane, and Z position relative to the centre of the VMI source region of ± 3 mm. (b) and (c) show enlarged plots of the region highlighted in (a), and correspond to ion kinetic energies of (b) 5 eV and (c) 20 eV. Black, Green, Red and Blue points denote source positions relative to the center of ± 0, 1, 2 and 3 mm respectively. This translates to a radial deviation of ± 0.2 mm.

sphere on the position relative to the optimum source position in the z direction (i.e. in the propagation axis plane). For these simulations, four ion energies ranging from 5 - 20 eV were used, and the source position was varied from the optimum source position by ± 3 mm, in 1 mm increments. The sub-plots of the figure show zoomed in regions of the particles emitted in the Y axis direction. As expected there are slight variations in the final radius of the projected velocity sphere since the particles will experience more or less acceleration in the z direction. However the observed shift is less than ± 0.5 mm for the energies simulated, which will not lead to a significant deviation in observed kinetic energy.

Figure 6.12 shows the dependence of the projected velocity sphere on the position relative to the optimum source position in the Y direction). This would correspond to a displacement in either the FEL propagation axis, or in the molecular beam axis. Since the VMI is cylindrically symmetric the same behaviour will be observed if the displacement is in an arbitrary direction confined to the X-Y plane. The displacement of the source in

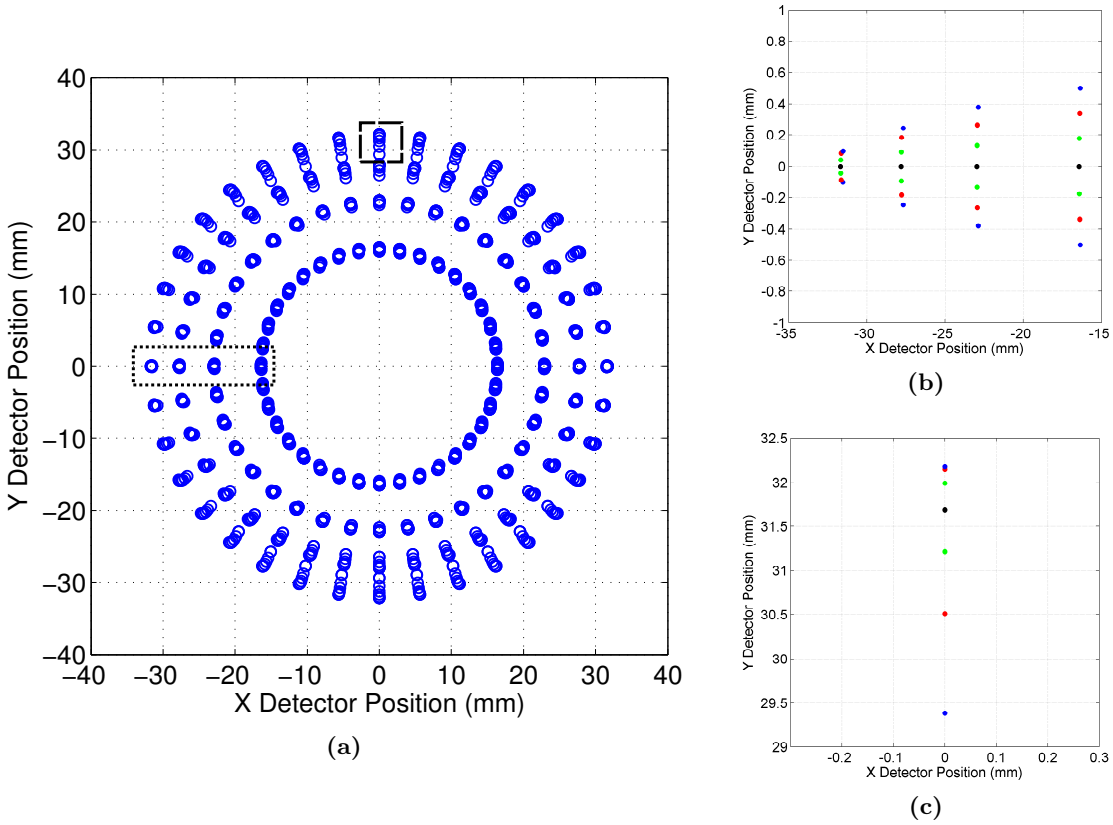


Figure 6.12: VMI detection radius as a function of the Y (X-ray propagation axis) position of the source. (a) Scatter plot of detection position for ion kinetic energies of 5-20 eV in 5 eV increments, increments of 10° of ejection angle in the X-Y (detector) plane, and Y position relative to the centre of the VMI source region of ± 3 mm. (b) and (c) show enlarged plots of the regions highlighted in (a) with dotted and dashed lines respectively. Black, Green, Red and Blue points denote source positions relative to the centre of ± 0, 1, 2 and 3 mm respectively. It can be seen that the source position introduces an ellipticity to the imaged fragments.

this case leads to an induced ellipticity of the projected velocity sphere, and a displacement of the velocity sphere from the exact centre of the detector. Since this is nearly always impossible to completely eradicate, the centre of the image is found experimentally. Ellipticity, which may also be introduced by a tilt in the camera observation angle can be corrected for in post-analysis of the images through rebinning to correct for the experimentally observed eccentricity of what should be circular/spherical features.

Centring of the image in the ideal case can be achieved by centroiding of the image (assuming a symmetric distribution). Once again however the damage to the detector causes a problem. Since the damage is non-uniform across the detector and not centred exactly where our distribution may be on a given experimental run, a simple analysis by using a centre of gravity calculation is not possible. The method used to experimentally centre the data was to calculate for each initial guess of the centre coordinates, (x,y), the quantity T was calculated for the region of the image of radius between 275 and 325 pixels,

with T given by:

$$T(x,y) = (Q_1 - Q_2)^2 + (Q_3 - Q_4)^2 + (Q_1 - Q_3)^2 + (Q_2 - Q_4)^2 \tag{6.3}$$

Where Q_n is the total signal for each of the 4 quadrants of the image. By calculating T over all reasonable guesses of the centre (x,y), the centre may be found at the location where T reaches a minimum.

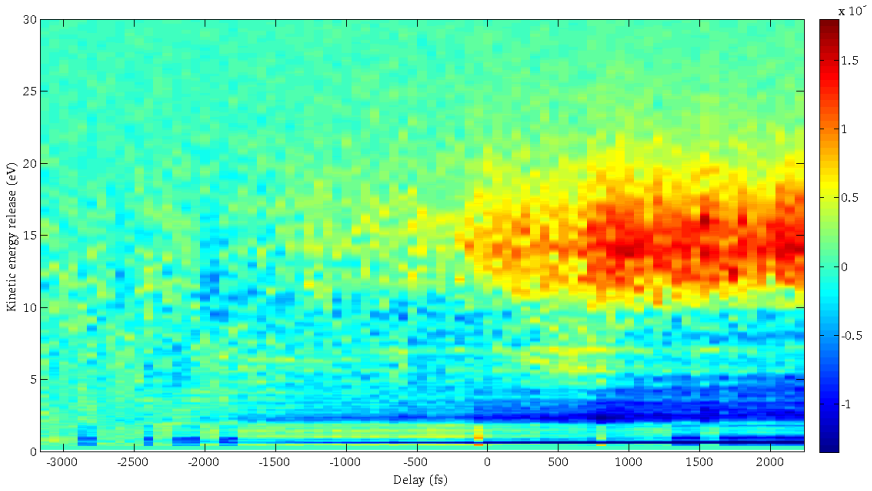
6.2.6 Results

The following section presents results from both the VMI and ion TOF detectors for UV pump, X-ray probe runs where the temporal and spatial overlap of both the UV and X-ray beams could be verified. As described in section 6.2.2, the complete wavepacket evolution from CHD to HT is expected to occur on a timescale of the order of 200 fs. Given our timing resolution was approximately 300 fs under the experimental conditions available to us, we would not expect it to be possible to fully track the wavepacket evolution between the two species as is possible for the IR based experiments, and as such a complete comparison of the results using the two techniques was not possible.

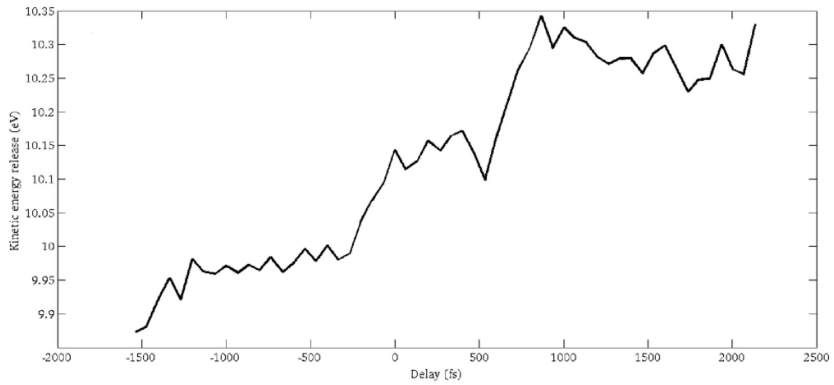
However, the timing resolution is more than sufficient to demonstrate that the UV pump, X-ray probe experiments are sensitive to changes in the molecular geometry, and this experiment can be used to evaluate the technique's potential as a general tool for tracking the structural or electronic changes in molecules. The results from both the VMI and ion TOF measurements support the conclusion that it can indeed be used, with both the kinetic energy and total number of ions increasing for time delays where the X-rays come after UV excitation, corresponding to a change from the CHD to HT geometry.

Figure 6.13a shows the kinetic energy release as calculated from the ion VMI images, for delays between -3000 to +3000 fs from the measured τ_0. The columns represent a single time-binned kinetic energy spectra, minus the average spectra from very early delays (-3000 to -2000 fs) to show the difference in the kinetic energy distribution as a function of the pump-probe delay. While the difference is broadly flat for delays where τ is less than τ_0, for delays where τ is greater than τ_0 there is a clear shift towards higher kinetic energies centred at 14 eV and a depletion in signal for energies lower than 5 eV. This is behaviour is reinforced in figure 6.13b, which shows the average kinetic energy of the ion fragments, calculated by integrating the VMI signal over over the 2 - 30 eV energy range, as a function of delay. The average kinetic energy is observed to increase after delays = τ_0 before reaching a plateau at longer delays.

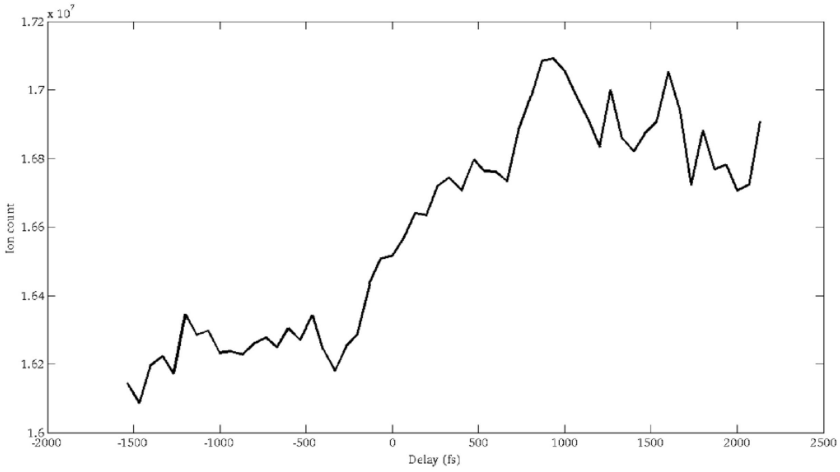
As well as the kinetic energy, an increase was also observed in the total ion counts, calculated using centroiding of the VMI images. Figure 6.13c shows that for delays where $\tau > \tau_0$, an increase in the total ion counts increased by 5%. Similar behaviour was also



(a)

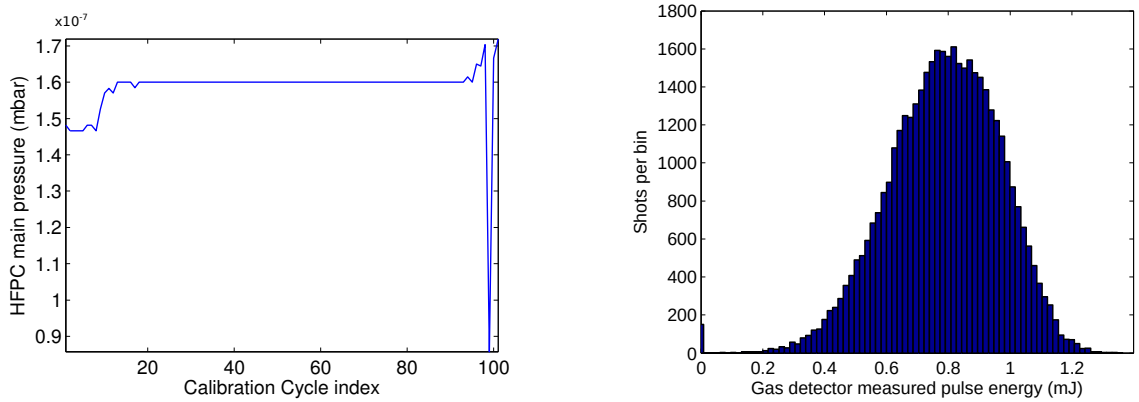


(b)



(c)

Figure 6.13: (a) Kinetic energy release spectrum as a function of UV - X-ray delay in femtoseconds. The Z values show the difference between the corresponding KER spectrum and a reference KE spectrum obtained as an average for early delays in the (-3000,-2000) fs range. (b) Average kinetic energy and (c) ion counts as a function of the UV - X-ray delay over the same range of delays.



(a) **(b)**

Figure 6.14: (a) Average HFPC main chamber pressure as a function of delay cycle. Only cycles 11-95 were used for the ion signal analysis as to eliminate errors due to a fluctuating sample density. (b) Pulse energy histogram for the delay scan as measured by the first pair of gas detectors.

observed in a separate run using the ion TOFS. While the resolution of our ion TOFS was unfortunately insufficient as to yield any kinetic energy information of the ion fragments, the total ion yield for several species were observed to increase for longer pump-probe delays. Figure 6.14 shows the HFPC main chamber pressure as a function of the calibration cycle (delay position) and the pulse energy histogram for a UV - X-ray ion TOF delay scan for delay times equal to $\pm$ 3500 fs around τ_0. To eliminate fluctuating sample density as a possible source of change in the ion yield, we selected only calibration cycles for which the main chamber pressure was equal to 1.7$\pm$0.2 $\times 10^{-7}$ mbar, corresponding to nominal UV - X-ray delays of $\pm$ 2644 fs. Additionally, the single shot TOF spectra were normalised to the pulse energy to remove the effect of a fluctuating pulse energy. Since we are operating in the linear regime, the total ion signal should be proportional to pulse energy. The individual traces were therefore normalised to the total pulse energy as measured by the mean of the first pair of gas detectors. The data was finally binned according to equation 6.1, with approximately 500 traces per bin, and each bin was then averaged to yield a final delay scan.

Applying these constraints to the TOF data yields the delay scan as shown in figure 6.15a. This shows the average normalised ion signal for the full TOF trace as detected by the ion TOF detector as a function of the UV-X-ray delay. Increases in the ion yields for several species were observed, with the most dramatic changes in the H^+ and C^+ species. These increases are more visible in subfigures 6.15b and 6.15c, which show the numerically integrated signal as a function of the delay corresponding to the peaks associated with the H^+ and C^+ species, integrated over time windows of 2.300-2.340 μs and 6.425-6.525 μs respectively, and show that increases in ion signal of approximately 10% occur in both species. These increases are qualitatively comparable with X-ray fragmentation ion yields measured by the PULSE institute using the ALS synchrotron, where they measured

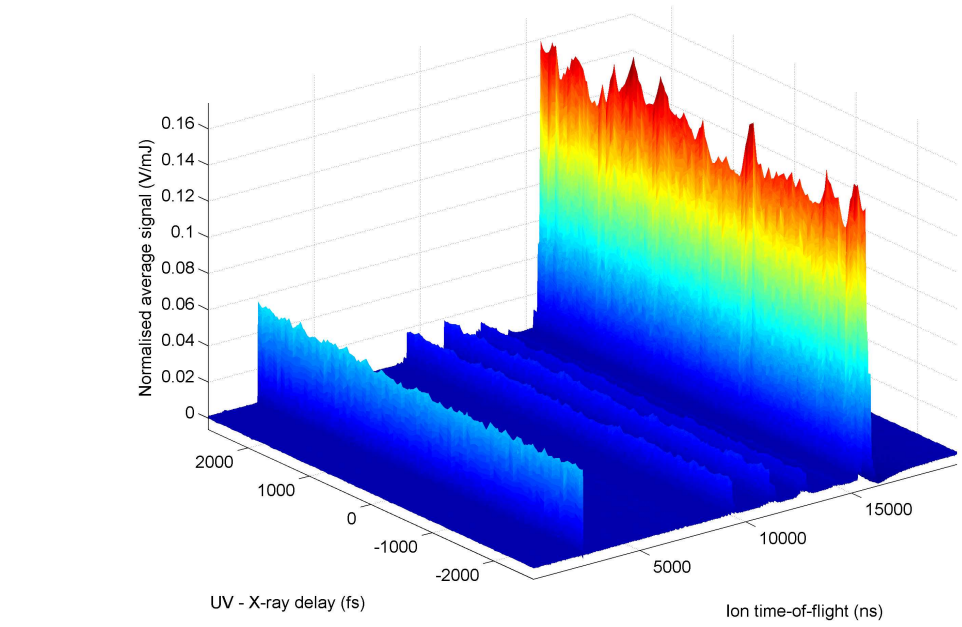
relative changes in the H^+ and C^+ ion yields of 15% from ground state CHD and HT [30, supp. mat.].

6.2.7 Discussion

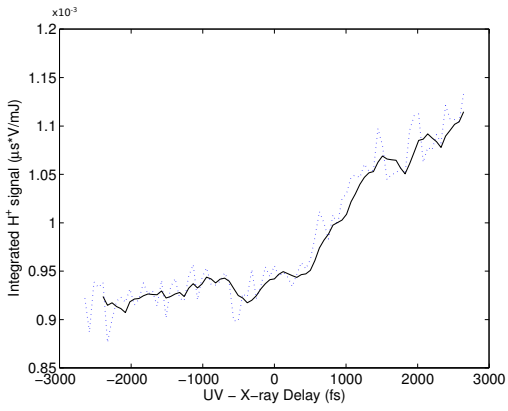
The observed increases in ion counts and kinetic energy described previously are likely to be underestimates, since there will be large background of ions produced from non-UV excited molecules. Despite this background however, both the ion counts and the kinetic energy of the fragments are observed to increase by over 5% for delay times in which the X-rays arrive after UV, so we can say with certainty that the fragmentation pattern is dependent on the pump-probe delay. However the observed changes occur on a timescale much longer than would be expected if the difference was due purely to the electronic excitation of CHD. The observed increases take place over a time period in excess of 1 ps before reaching a plateau at longer delays, which is much longer than the 200 fs duration of the CHD-HT transformation, even taking our time resolution into account. The observed timescales are however consistent with the evolution of the HT into its various rotational isomers reported by Anderson and Lochbrunner [162, 163].

In order to understand the increase in the kinetic energy release of the fragments, two theoretical studies were performed to investigate two possible explanations: the geometry dependence and the dynamics of the Auger decay of the different molecules. Calculations, which are described in more detail in the supplementary material of [30], were performed by the PULSE institute to determine the branching ratios of the Auger transitions of the core excited molecule to the final doubly charged ion. The results showed that X-ray ionization and consequent Auger decay leave the dications of both species in an electronically excited state. This excess internal energy is then converted to the kinetic energy of the fragments when the molecule breaks up. Fragmentation is the only energetically allowed relaxation route since the calculated energies (of the order of 5-10 eV) are insufficient to create a triply charged ion, and a radiative decay will occur on a much longer timescale (see section 2.2.3. Figure 6.16 shows the branching ratios for CHD in the ground and 1B excited state, and ground state HT. While these calculations reproduce ratios more accurately than energies, the results clearly show a geometry dependence in the kinetic energy release, with shift to higher energies for the HT geometry compared to both ground state and electronically excited CHD. These theoretical results are therefore consistent with the conclusion that the additional kinetic energy release observed for long delays is is a result of presence of HT.

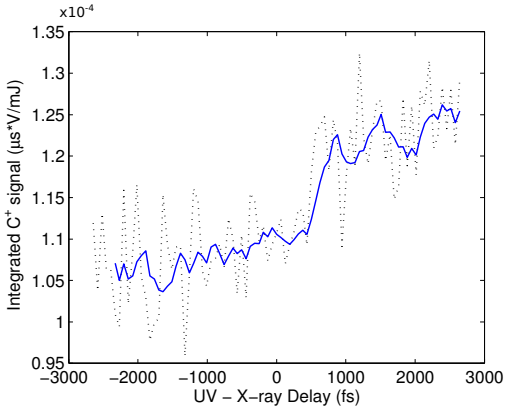
The other possibility is that during isomerisation, the bond lengths of the C-H bonds within the molecule changed sufficiently as to explain the observed difference, since the Coulomb explosion kinetic energy as described previously depends on the initial distance of the two atoms. Calculations performed by the PULSE group confirmed a decrease



(a)



(b)



(c)

Figure 6.15: (a) The average normalised ion TOF signal as a function of the UV - X-ray delay. The lower plots show the total integrated ion signal as a function of UV - X-ray delay for the (b) H^+ and (c) C^+ ion species. Traces were normalised to pulse energy. Dashed line is the data binned according to the norminal delay positions. Solid line is a moving average with a 315 fs window.

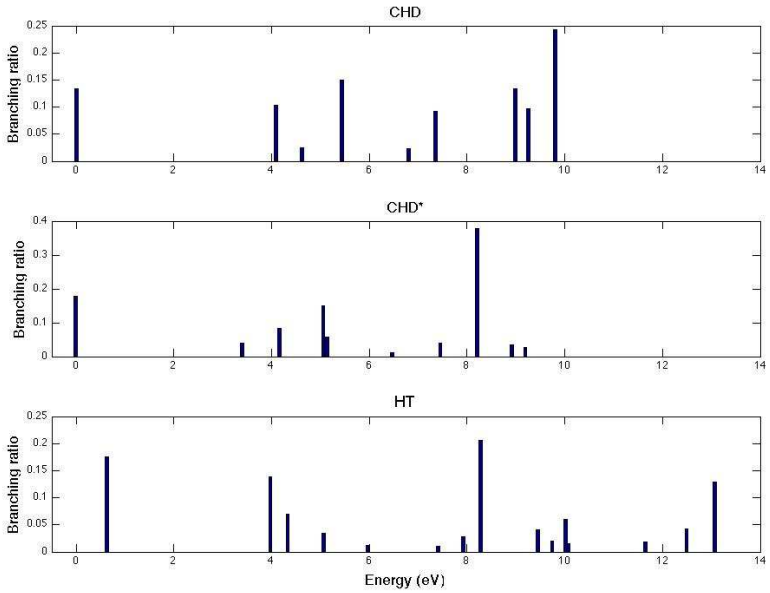


Figure 6.16: Branching ratio for purely-electronic component of Auger transitions into various doubly charged ions of CHD, 1B2 excited CHD*, and HT in the ground state CHD and HT geometries, in single-orbital approximation. The excess energy is in each case referenced to the ground state of CHD^{2+}. This is 0.63 eV lower than the ground state of HT^{2+}. This calculation predicts the rates more accurately than the energies. A shift to larger energies is observed for the HT geometry.

in the average C-H bond length during the first 300 fs of the reaction. This however contributed to only a 1% change in the kinetic energy. Given the observed changes, we can conclude that the change in the Auger decay channels of the two species is the most likely explanation of the kinetic energy difference.

In summary, all evidence gathered supports the case that the observed changes in both the ion TOF and VMI are consistent with the evolution of CHD into the various isomers of HT. Given this interpretation it can be said with confidence that the scheme proposed successfully tracks the structural changes of CHD following UV excitation that were accessible given the timing resolution available to us at the time of the experiment was performed. As such this experiment serves as a good proof of principle for the technique of using X-ray fragmentation as a probe of time resolved changes in molecular systems. We anticipate that the method can be extended successfully to more general experiments in tracking structural and electronic changes in molecules.

6.3 Conclusions

There were several limitations of this experiment, stemming from both the MCP damage and the limits of the FEL timing synchronisation at the time of the experiment. Nonetheless, we were able to demonstrate that X-ray induced fragmentation can be successfully

used as a probe of the molecular dynamics, with both the ion count and the average kinetic energy release displaying sensitivity to the evolution of the system, albeit with only picosecond resolution in this experiment. In general we anticipate that that the experimental scheme may be applied to a large variety of systems, especially for molecules with lower atomic numbers where Auger decay is the dominant decay route. This covers a significant number of biologically relevant and interesting molecular systems. Interpretation of such studies will depend on improved understanding of the Auger decay channels of these core-excited molecules, and this experiment highlights the need for additional theoretical studies into the fragmentation dynamics of molecules of this type. However, the comparatively simple theoretical studies described earlier have still provided some information about the dynamics.

There are several ways in which the scheme described in this thesis may be improved. The major limitation of this experiment was the 300 fs timing jitter between the pump and probe pulses. Future experiments which could utilise the scheme at LCLS using the current capabilities of the facility will benefit greatly from both the shorter (< 10 fs using the 20 pC bunch) pulse durations that are now available to users, improvements to available X-ray timing diagnostics located at the AMO end chamber (described at the end of section 3.4.3), with timing jitters closer to tens rather than hundreds of femtoseconds, and the possibility of operating at photon energies closer to the carbon K-edge (current lower limit on photon energy is now 290 eV). In principle such schemes should eventually be able to be performed with femtosecond timing resolution as timing synchronisation between the pump and probe pulses improves and the pulse durations provided by seeded FEL sources approach the 1 fs limit and will hopefully even approach attosecond resolution in the long term. With these improvements, tracking the wavepacket evolution along the excited state potential surfaces should be realised, and through comparison with the IR data a true measure of the effect the IR pulse has on the dynamics of the fragmentation should be achieved.

Chapter 7

Multi-particle X-ray processes explored using partial covariance mapping

The unprecedented intensities that a SASE FEL is capable of reaching allow for X-ray ionsation of a system through previously inaccessible channels. The preference of X-rays to ionise atoms from the core combined with the high intensity can yield multi-photon processes including but not limited to multiple core hole creation [138]. The study of these processes is important, as not only do they yield important information about the electronic structure of the sample with resolution that single photon processes cannot access [26], but the processes are also relevant when applied to other methods that utilise intense X-ray pulses, such as coherent diffraction imaging [164]. Ionisation damage of the sample places an inherent limit on the time in which useful data can be gathered [25].

This chapter presents results from an LCLS experiment that took place in August of 2011, and headed by Raimund Feifel of Uppsala University, to study correlated photoionisation events in atoms and molecules. In these experiments we aim to demonstrate that an enhanced version of the covariance mapping technique pioneered by Frasinski et al. can successfully be used to identify and unravel multiple ionisation pathways, and yield information of the branching ratios of such processes. This technique, which we call partial covariance mapping, was first used in an experiment performed with the objective to perform two-photon electron spectroscopy in order to probe the chemical environment of small hydrocarbons and organic molecules. We use neon as a test case to evaluate the capabilities of the method before presenting results on the hydrocarbons acetylene (C_2H_2) and ethane (C_2H_6).

7.1 Software development for data conversion

For the experimental runs described in this chapter, a large proportion of the experimental team would be committed to preliminary analysis of the data acquired during the day's

runs. Although full analysis may not be completed for several months or even years after the last day of beam time, the preliminary findings help shape the schedule of the runs, and inform the science team of the most promising operating conditions as to make the best use of the limited run time. The collaborative nature of the LCLS projects and the fact these sources have only been open to user groups for 2-3 years means that within any experimental team there will likely be those with minimal experience in the LCLS systems, and among the group there will also be significant variation in programming ability and knowledge. Given the relative difficulty in extracting particular elements of data from the XTC files using the LCLS systems, ensuring that the analyis group had access to easily accessible and interpreted datasets was of paramount importance, which necessitated an easy method of converting the data.

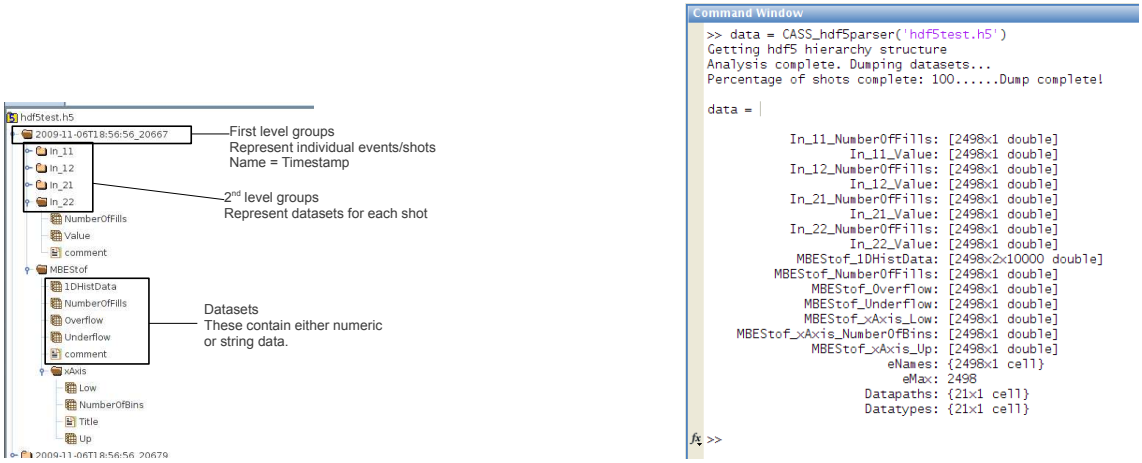
In the weeks/months leading up to the experimental runs, a significant investment of time was spent in learning the CASS and Pyana analysis frameworks and developing a set of scripts that a user unskilled in either language could utilise to extract information with a minimum of effort. Since Matlab is both a widely utilised and comparatively simple language, and also has open source equivalents (such as Octave and SciLab) that can freely read the Matlab data format, I wrote two different conversion routines to convert the relevant XTC data to a number of 'bitesize' .mat files that would be a) flexible enough to be used on a variety of different experimental setups, b) easy to use for anyone with minimal computational knowledge of the languages they were written in.

This section overviews the methodology and optimisation of the code. The source codes and instructions on how you might use the codes in a practical setting are described in far greater detail in the appendices A.4 and 7.1.2.

7.1.1 CASS based converter

The first conversion routine was a two step process which first used CASS to generate an HDF5 file which contains all the relevant data, and then uses a Matlab script to extract the data from the HDF5 file. The reasoning behind this approach was since CASS requires only a small .ini file to be configured, the HDF5 file can be generated with minimal effort assuming that a working copy of CASS already exists on the LCLS systems.

The conversion process to extract the data to Matlab was achieved using a number of custom Matlab scripts. Matlab has had native HDF5 support since version 2007a, however usage of the library requires a reasonable knowledge of the file structure and, for good performance, knowledge of low level operations. However since the CASS HDF5 postprocessor dumps the data in a specific format, which is that each shot has its own top level folder/group, and the group format within each shot is identical. An example of an HDF5 file folder structure as produced by CASS is shown in figure 7.1b. As such, I would be able to create a generic function that would be able to dump all data contained within



(a) **(b)**

Figure 7.1: (a) Outputs for the CASS HDF5 postprocessor with data from 4 beamline variables (the gas detectors) and Magnetic Bottle TOF data. (b) Output of the conversion function in 'dumb' mode. This was performed on a test XTC which contains 2498 shots.

the HDF5 file which would work independent of the exact form of the data dumped using the CASS postprocessor, while still flexible enough for users to customise the output for the more experienced user. The source code and instructions on the use of the function are explained in depth in appendix A.4. In summary, the function uses two main methods: in the 'dumb' mode, it first gets the common names of all relevant datasets by looking at the first group. Knowing that each 1st level group will be identical, it then iterates over all 1st level groups in the HDF5 file to get the shot names, and then iterates through all groups in the HDF file and dumps each dataset in each folder to the same field in a Matlab data structure, which are automatically generated from the paths. In the 'smart' mode, it operates much the same way, except it uses a user defined configuration file which can customise the format of the output structure by, for example, grouping several variables into the same array, splitting 2D arrays into multiple variables, and reducing redundant data by only extracting certain variables once (such as the TOF configuration parameters).

7.1.1.1 Performance Optimisation

The HDF5 is a self describing data format, in the sense that each group and dataset is named and described in metadata, rather than say a binary dataset in which the format of the data is described once in a header and the data for a given byte is then inferred from this structure. This has the advantage of making the file easy for a human to interpret, but at the expense of file size since there is a huge amount of redundant 'metadata'. While this was not a significant issue when performed on the LCLS systems, each 1 hour run was producing an HDF5 file of 80 GB for a single run compared to an 35 GB xtc size, and as

such the conversion process was not efficient in disk usage. During the experiment each run was limited to 1 hr duration before restarting the acquisition so that the HDF5 files could be kept to a manageable size.

The large file size also caused problems. One significant drawback of this type of data format is that each time the program tries to access a particular dataset it must search from the beginning of the file as the exact location of the dataset cannot be inferred in the same way a binary set can be. Initial implementations of converter used high level functions in Matlab to retrieve the datasets sequentially. Initial testing using a small HDF5 provided by LCLS of approximately 3000 shots worked well, however when testing was done on more realistic datasets of several hundred thousand shots the read time was found to be unacceptably increasing with the shot number. Whereas the first 5000 shots took approximately 100 seconds to be written, for a 5000 shot block starting at the 200,000th shot the read time was over an order of magnitude larger, and conversion of an entire dataset would have taken of the order of days rather than hours. This behaviour can be explained by the fact that the Matlab high level read function does not 'remember' its position in the file each time the function is called, and needed to search through the entire file for each shot. Breakdown of the execution time using Matlab's diagnostic tool set revealed that the execution time of the read function increased linearly with shot number, confirming this hypothesis.

The function was completely rewritten to use low level Matlab HDF5 functions. Using these functions, the file could be kept open for the duration of the read process. For this function the read time was consistently 100-200 seconds per 5000 shots, independent of the initial shot number. With this performance the conversion was fast enough at that some data could be made available to the users within 2 hours of the run completing, but for some runs it took several days to complete the conversion, with effective conversion rates of 5-20 Hz.

7.1.2 Pyana based converter

There are several significant limitations of the above system. The requirement that the data be converted to HDF5 format each time and the inefficient way CASS writes the file placed a severe bottleneck on the effective transfer rates. To perform the conversion at LCLS also required the use of one of their few Matlab licences, so the conversion was dependent on proprietary software. Additionally, CASS is no longer officially supported by LCLS beyond 2011, so now the converter relies also on software for which support depends on outside assistance. It was decided that a new system would be required for future experiments. In the last couple of years or so, the LCLS computing department has developed a Python based analysis framework called pyana. The Python language is a comparatively simple language that has access to some rather extensive libraries, including

the NUMPY and SciPy libraries. These emulate much of Matlab's functionality including linear algebra, image processing, graphing and most importantly, saving and loading to native Matlab formats. Given the problems and limitations that were encountered with the previous scheme, it was decided to code a similar set of functions that would instead run using the pyana framework. The advantage of using this scheme would be twofold: 1), the conversion step to HDF5 could be bypassed completely since pyana can both read direct from the XTC files and then write directly to Matlab format, and 2) would be future proof since it would depend only on the pyana system which is constantly updated by LCLS, and if for some reason a read function was changed it would be well documented so future users would be able to adapt the code easily without needing input from myself.

The operation and source code of the converter is described in depth in appendix A.5. The converter is coded as a module which can easily be integrated into an existing user installation/release of pyana, and a shell script was written which simplifies the process of installation to a single command. The module has been coded to use several different sub-converters which each address a specific data type, such as the TOF data, the electron beam data, etc. The module is configured using a text configuration file, in which the user both selects which converters to use and specifies advanced options such as the names of EPICS variables and the output names of the Acqiris traces, and also the properties of the output files. Once run the program will automatically parse the relevant data and automatically write it to the scratch directory of the experiment.

7.1.2.1 Performance

There were several advantages of this system that made it superior to the CASS based converter. By eliminating a conversion step we can now start converting immediately to .mat format after the run has been completed and successfully written to HDF5, reducing the delay between a run finishing and making data accessible to users. Secondly, the pyana data reading procedure is truly sequential so the conversion time is consistently linear with the number of shots. The main bottleneck in this case was simply reading and writing the files from/to disk. Performance of the read process was upwards of 100 Hz so runs could be converted on similar timescales to the acquisition. Pyana in the future is also slated to be modified to allow conversion of an unfinished XTC, which in principle should allow for conversion almost in real-time.

7.1.2.2 Summary

Two conversion schemes for inexperienced LCLS users to convert the data into a format that could be read by Matlab and open source equivalents have been presented. It is expected that the pyana based converter in particular will be of great asset to both the

laser consortium and future collaborators of LCLS experiments, and will enable users of all programming ability to quickly and effectively contribute to the analysis of such experiments.

7.2 Chemical shifts in molecules probed using double-core-hole photo-electron spectroscopy

For an atom bound within a molecule, the exact binding energy for the electrons of a given atomic species will depend on the chemical environment (i.e. what else it is bound to), differing by as much as 10 eV for the core electrons. An excellent example of this effect is the molecule ethyl trifluoroacetate ($CF_3COOC_2H_5$) for which the difference in core binding energies for the carbon atoms in the methyl and tri-fluro groups is larger than 8 eV [5] (See figure 7.2). The study of these effects, collectively referred to as chemical shifts, was pioneered by Siegbahn et al. back in the 1960s [4], and proved to be very successful in measuring relative binding energies of core electrons in both bulk solids and free molecules. This method fails however when it comes to molecules that have atoms in very similar chemical environments, such as carbon, nitrogen and oxygen molecules in hydrocarbons and aromatic molecules, since the energy level differences are so small as to be non-measurable by traditional methods. For example, the difference in energy of the core electrons in the C_2H_2 and C_2H_6 molecules differs by less than 1 eV [26]. However in recent years interest has been revived in this area, with a focus on so called double core hole (DCH) states, where two electrons are removed from the K-shell, for which the binding energies display a much higher sensitivity than the single core hole (SCH) states.

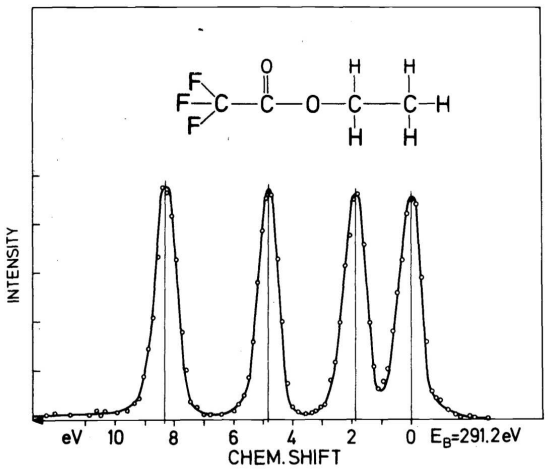


Figure 7.2: Carbon 1s binding energies for the ethyl trifluoroacetate ($CF_3COOC_2H_5$) molecule. The four different peaks correspond to the different functional groups of the molecule shown above the plot. The more electronegative groups display an increased binding energy relative to the methyl group. Figure taken from Pure Appl. Chem. **48**, 1, pp. 77-97 [5].

7.2.1 Double-core-hole spectroscopy for chemical analysis

As described in section 2.2.3, the absorption of an X-ray photon by an atom/molecule of sufficient energy leads to the creation of a core-hole state, which leads to the production of a photoelectron with kinetic energy that is the difference of the photon energy and binding energy, before then decaying via Auger electron emission in the case of small Z atoms. If the atom/molecule absorbs another X-ray photon before the core hole is filled, we can create an atom or molecule with a completely hollow K-shell, a so called DCH state. In this case the binding energy of the core electrons will also depend on the repulsion between the two core holes. For molecules, there is the possibility for the creation of both single-site DCHs (ssDCHs), where both holes are located within a single atom of the molecule, and two-site DCHs (tsDCHs), where the holes are located on different atoms, with the latter predicted to exhibit a much larger chemical shift, since the magnitude of the repulsion between the two holes will depend on their location and the geometry of the molecule since the Coulomb repulsion increases inversely with the bond distance. As such there is a great deal of interest in experimentally creating and measuring the products of the creation of these states.

While theoretical treatments of DCH states have been available for over two decades, with the inital theoretical treatments performed by Cederbaum et al. in the mid 1980s [26, 165], the opportunity for studying them experimentally has only been made available in the last few years. DCH states can be created using synchrotron radiation via single-photon double ionisation, but the relative probability of creating these states compared to the SCH state is equal or less than 10^{-4}, making them extremely difficult to detect. Nevertheless in 2010 J. H. D. Eland et al. demonstrated it was possible to resolve ssDCH states in NH_3 and CH_4 via this channel by utilising an efficient multi-coincidence technique [166] (see below). Other groups have also demonstrated similar results [167].

The high intensities provided by FELs on the other hand allow the creation of DCH states with much higher probability via two-photon absorption processes, which are accessible with the short pulses and tight focusing conditions available at the LCLS light source. In this X-ray two-photon electron spectroscopy (XTPPS) scheme, the second photoelectron will have kinetic energy equal to the photon energy plus the single ionisation potential, minus the double ionisation potential (DIP). Experimental studies on DCH states have already been performed, yielding experimental evidence of ssDCHs in atoms [138], and in small molecules [28, 168]. Very recently published results by Salen et al. have also demonstrated that the tsDCH states in small molecules can be resolved using XPS using the AMO chamber at LCLS [169]. The Salen method resolves the states by looking at the differences in electron yield in both the tight focusing condition, where DCH states should be relatively abundant and a loose focusing, low intensity condition where the single core hole states should dominate. By subtracting the yields of the two regimes, the products of the nonlinear processes can be extracted out of the background of linear processes.

The aim of the collaboration was to be able to resolve and untangle the DCHs for a variety of larger molecules, including the smaller hydrocarbons, such as acetylene (C_2H_2) and ethane (C_2H_6) and of smaller organic molecules such as pyrimidine($C_4H_4N_2$) and formamide (CH_3NO). Theoretical studies by Tashiro et al. [170] and Takahasi et al. [27] have evaluated the DIPs in small molecules and nucleobases respectively, and cover the molecules we investigated in the experiment.

7.2.2 Two-dimensional spectroscopy

A general problem of one dimensional spectral analysis (such as the Salen method described above) is that it is generally not possible to resolve the different contributions of a single peak. As an example, let us consider a simple case of the fragmentation of a molecule such as CO, as observed using an ion TOF system. In the average spectrum we would expect to see a C^+ peak, but since that peak could come from multiple possible decay routes (e.g. $CO^{2+} \longrightarrow C^+ + O^+$ and $CO^{3+} \longrightarrow C^+ + O^{2+}$, etc.), the average spectrum would not yield any information about the branching ratios of the channels or whether they are present for a given set of experimental parameters. The case is similar for electron TOF studies (as in our case), since any processes which yield the same (or similar) final kinetic energies of the ejected electrons will be indistinguishable in the 1D spectra.

To remove this ambiguity, it is beneficial to move to a two-dimensional analysis, where instead of looking just at average spectra/number of hits, we instead look at which pairs of particles are detected in correlation or coincidence with each other (i.e. detected on the same shot) [172]. Using such schemes, a two-dimensional map is constructed, in which

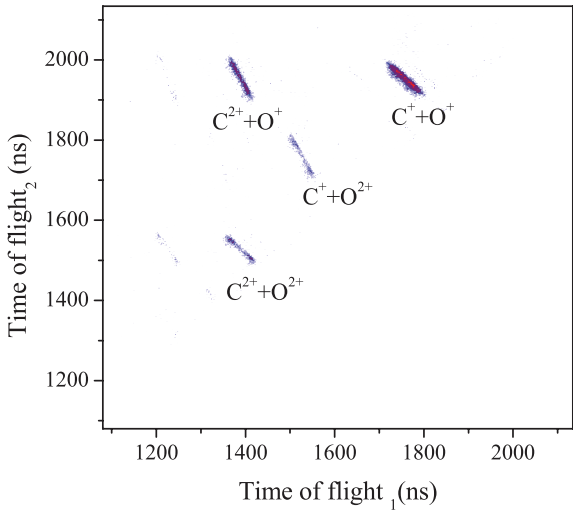


Figure 7.3: Coincidence map of the fragmentation of CO after heavy ion bombardment. The islands reveal that the C^+ species, which would would manifest as a single peak in the average one-dimensional spectrum, has contributions from both the $CO^{2+} \longrightarrow C^+ + O^+$ and $CO^{3+} \longrightarrow C^+ + O^{2+}$ decay routes. Figure taken from Phys. Rev. A **81** 012704. [171]

pairs of correlated particles show up as islands or peaks on the map. An example of such a 'coincidence map', taken from a 2010 study by Mizuno et al. which studied the fragmentation of CO under heavy ion bombardment [171], is shown in figure 7.3. Four islands are visible, which each correspond to a pair of particles formed from four different decay channels, which would have been impossible to resolve by simply looking at the average spectra of hits.

Such multi-particle TOF techniques have been used extensively in synchrotron studies to study processes such as molecular fragmentation and dissociation [173, 174]. Similar techniques have been used to study electrons in single photon double ionisation processes [175], including the DCH studies described previously [166, 167], and Auger decay processes [176]. Such techniques are by no means limited to TOF based techniques however, and conceptually similar two dimensional correlation spectroscopic techniques have been widely used in a large variety of disciplines related to optical and vibrational spectroscopy. For a comprehensive overview of such techniques, see Noda et al. [172].

For our experiment, the aim was to detect coincident pairs of electrons that result from either the creation or the Auger decay of a DCH state for a given laser shot. For prototypical coincidence measurements, such as the electron studies performed using synchrotron radiation described in the previous paragraphs, the ionisation rate must be kept far lower than the pulse repetition rate in order to limit the number of false coincidences (i.e. electrons from different ionisation events arriving at the detector for a given shot). This method works well for high repetition sources such as a synchrotron, though even in this case a trace may take many tens of hours to be acquired. For a lower repetition rate source like LCLS, which is at best limited to a 120 Hz repetition rate, the timescales involved in order to acquire a trace using this method becomes prohibitively long: we would likely need an entire shift to gain sufficient statistics on a single measurement. We therefore require a different method to resolve these correlations, one which can be performed on the timescale of hours as opposed to days.

7.2.3 Covariance mapping

In 1989 Frasinski et al. proposed and successfully demonstrated a statistical technique called covariance mapping that can obtain the degree of correlation between two particle fragments of a given set of TOFs or energies, even for experimental data where multiple hits are detected each shot [177, 178]. This technique can resolve correlations between particles using low repetition rate sources (the original demonstration used a 10 Hz laser source) and ionisation rates comparable to the laser repetition rate, making it ideal for use under the conditions the LCLS can provide. Statistically, the covariance, $\mathrm{Cov}(x, y)$ describes the degree of similarity between two sets of random variables with finite variance [179, p. 406] (i.e. how much they change with each other). If we take two random variables,

x and y the covariance is mathematically defined as:

$$\mathrm{Cov}(x, y) = E\left[(x - E[x])(y - E[y])\right] \tag{7.1}$$

where $E[x]$ and $E[y]$ are the expected values of x and y respectively. For unweighted variables, 7.1 can be expressed in terms of the arithmetic means of the variables and their products:

$$\mathrm{Cov}(x, y) = \overbrace{\langle xy \rangle}^{\text{Correlated product}} - \overbrace{\langle x \rangle \langle y \rangle}^{\text{Uncorrelated product}} . \tag{7.2}$$

In our case we wish to see how much the yield for a particular ion/electron at a given energy/TOF changes with respect to all the other fragments. Since our time of flight trace will consist of at least several thousand discrete channels/samples per trace, a simple way to achieve this is to simply calculate the covariance for every pair of channels. For channels that correspond to the flight times of two correlated particles we would expect a strong covariance. For such purposes equation 7.1 can be rewritten in terms of two time of flight traces X and Y:

$$\mathrm{Cov}(X(t_1), Y(t_2)) = \frac{1}{N}\sum_{i=1}^{N}\left[X_i(t_1)Y_i(t_2)\right] - \left[\frac{1}{N}\sum_{i=1}^{N}X_i(t_1)\right]\left[\frac{1}{N}\sum_{i=1}^{N}Y_i(t_2)\right] \tag{7.3}$$

where $X(t)$ and $Y(t)$ is the signal for the time of flight channels at time t, i is an index denoting a particular laser shot and N is the total number of laser shots. In this general example X and Y are treated as separate traces, but there is no reason they cannot be part or all of the same trace if one wishes to compare correlated ions or electron pairs. For electron spectra the same principle applies except X and Y are instead the TOF traces binned according to energy given by equation 4.13.

When calculated for all combinations of channels, a 2D map of the form shown in figure 7.4 is generated. This figure, taken from [177], shows a covariance map generated from ion TOF spectra for multi-photon ionisation and fragmentation of the CO molecule using a 10 Hz sub-picosecond duration IR laser. This paper proved the power of the technique, demonstrating for the first time the multiple channels involved in the dissociation of the multi-photon ionised CO molecule. For example, the covariance map clearly shows the single O^+ peak correlates with both the C^+ and C^{2+} species, revealing that the single peak has contributions from both the $CO^{2+} \longrightarrow C^+ + O^+$ and $CO^{3+} \longrightarrow C^{2+} + O^+$ channels respectively. Furthermore, from the height of the islands and their shape it is possible to determine both yields/branching ratios and the momentum information of the channels respectively. The angle of the feature relative to the autocorrelation line yields the charge ratio of the fragments in the case of ions. In the same paper they show covariance maps for the triatomic molecules N_2O (a linear molecule) and SO_2 (bent), and demonstrate that the shape of the covariance features reflects the difference in momentum distribution

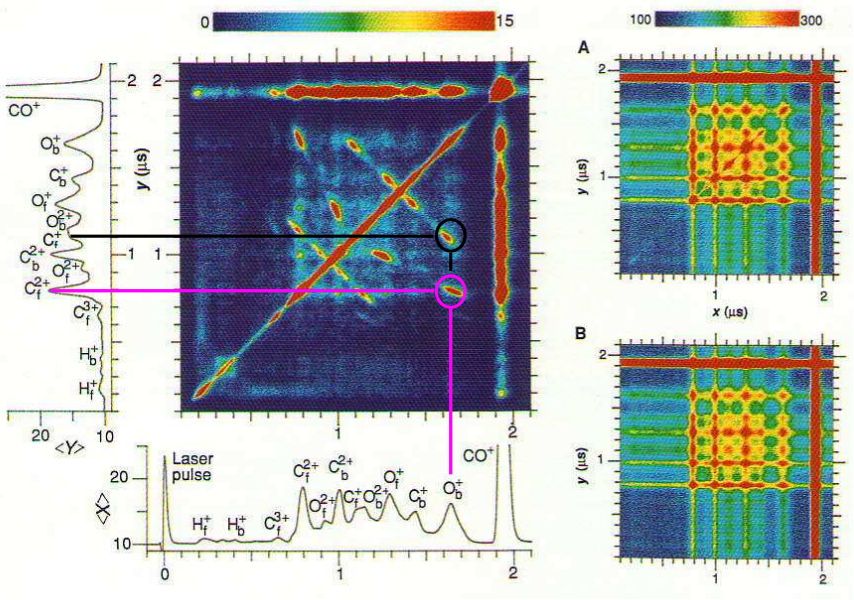


Figure 7.4: Covariance map generated from TOF spectra from the multi-photon ionisation and fragmentation of CO. The covariance map reveals that the single O^+ peak corresponds with both the C^+ (black label) and C^{2+} (magenta), corresponding to the $CO^{2+} \longrightarrow C^+ + O^+$ and $CO^{3+} \longrightarrow C^{2+} + O^+$ channels respectively. Graphs A and B show the correlated and uncorrelated product respectively. Figure adapted from Science **246**, p.1029-31 [177].

between the three fragments for the two different geometries.

The great strength of covariance mapping (and where most work has been done to date) has been in its application to ion TOF studies using intense lasers. These are sources for which a low ionisation rate is a highly impractical experimental constraint, due simply to the intensities required for multi-photon and tunnel ionisation. After their initial demonstration using CO, Frasinski and others of the Reading University group performed additional studies using picosecond and femtosecond sources on the fragmentation of small diatomics, such as N_2 [180] and I_2 [181], determining that charge symmetric channels were the predominant fragmentation channels [182]. Similar studies were performed on triatomics such as CO_2 [183], with similar conclusions. Furthermore, in 1991 Frasinski et al. demonstrated that the covariance mapping technique could be extended to the general multidimensional case, successfully implementing a three-fold covariance technique to study the fragmentation of N_2O [178]. This paper also demonstrated the requirement to move to higher order covariance in order to unambiguously resolve three particle processes. They also successfully demonstrated that the technique could be equally applied to electron-ion correlations in an experiment performed on H_2, in this case resolving the spread of kinetic energies of the electrons associated with the creation of the H_2^+ and H_2^{2+} ions [183].

Further work utilising the technique has been performed by various groups, and the technique continues to be used to the present day using femtosecond laser sources to

study the fragmentation channels and kinetic energy releases in both molecules [184–186] and clusters[187]. Wang et al. have also utilised the technique extensively, again looking into properties of fragmentation, although they used electron beam bombardment as the ionisation source [188–190]. Using this technique they were successfully able to measure both the cross sections and determine the major fragmentation pathways of molecules such as carbonyl sulphide. A comprehensive statistical treatment of the technique as applied to both of these methods was published in 2012 by Cornaggia [191]. In a very recent paper by Hansen et al., they modify the covariance formula to instead look at *angular* correlations using a VMI spectrometer, with which they studies molecular torsion in axially chiral molecules [187].

The technique is, however, not limited to the field of TOF spectrometry, and is a general technique that can be applied to range of signals that have significant correlations in a highly fluctuating signal. For example, an analogous technique was developed in parallel by Noda et al. for the applications of IR and Raman spectroscopies [192]. Covariance mapping has also been suggested as a robust diagnostic for both gas chromatography [193] and for analysing the products of fission reactions [194].

To utilise this technique for the purposes of TOF spectroscopy, some experimental requirements must be fulfilled. Firstly, we must be able to acquire TOF data on a single shot basis, by either acquiring and storing each individual trace in full, or by using a time-to-digital converter (TDC) card or another type of electronic discriminator which is capable of calculating and recording the times of individual particle hits, though in this case we lose any height information. Secondly, as with any coincidence measurement, we must be working with a TOF system where the collection efficiency of the instrument is high, as for a typical TOF system where the angle of collection is only a few degrees, we will not collect all fragments from a single event for most shots. Using extremely high retardations as is the case with high resolution spectrometers such as the Hemmer's TOF in general can not be used as it has a good energy resolution over only a small range and far more importantly an unacceptably low collection efficiency. From a statistics point of view, the single shot spectra must also exhibit a statistical shot-to-shot variation, which holds true for particles generated in a dilute gas phase.

7.2.3.1 Partial Covariance Mapping

While the covariance mapping technique is a very powerful and well developed tool in detangling correlated processes in photoionisation events, it does have some limitations when applied to real ionisation sources. For the calculated covariance to be meaningful, we rely on the assumption that any correlations in the TOF traces are either entirely or at least predominantly due to internal processes in the system being studied. This is, in general, not the case as experimental conditions can also effect the shot by shot yield of a

given species. Let us consider the single photon ionisation case, where the cross section is simply proportional to the intensity. Therefore it is also proportional to the pulse energy, to first approximation. Pulses with more energy (and therefore more photons) will, on average, produce more electrons in every channel than pulses with less photons, which manifests as a number of false correlations in the covariance map, as every peak will now display a degree of correlation with every other peak due to a fluctuation in the overall ionisation rate.

Since we were using an FEL source where the pulse energy can vary by as much as 100% of the peak values (see figures 3.13c and 3.13d), this fluctuation becomes a considerable hurdle in applying covariance mapping to FEL sources. We could potentially resolve this by binning our data with pulse energy, but this would require an experiment to be run for far longer in order to get reasonable statistics for each bin. Instead, our group demonstrated another, statistical solution to the problem, which is to instead calculate the *partial* covariance $\mathrm{pCov}(x, y : z)$. The partial covariance calculates the covariance of variables x and y as it would be if the third variable z was held at a constant value. In general the partial covariance is mathematically defined as:

$$\mathrm{pCov}(x, y : z) = \mathrm{Cov}(x, y) - \frac{\mathrm{Cov}(x, z)\mathrm{Cov}(y, z)}{\mathrm{Cov}(z, z)} \tag{7.4}$$

where $\mathrm{Cov}(x, y)$ is as defined in equation 7.2. Since we wish to remove the effect of the varying pulse energy E of the X-ray pulses from the TOF covariance map (using our TOF channels X and Y as before), and given that $\mathrm{Cov}(z, z)$ is simply the variance of z, $\mathrm{var}(z)$ our equation in terms of these measurements is therefore given by:

$$\mathrm{pCov}(X, Y : E) = \mathrm{Cov}(X, Y) - \frac{\mathrm{Cov}(X, E)\mathrm{Cov}(Y, E)}{\mathrm{var}(E)} \tag{7.5}$$

where the covariance of each element is calculated using equation 7.3 [195].

7.2.4 Experimental setup

The aim of the experiment was to apply the covariance mapping technique to electron TOF data in order to see correlated electrons from the creation and decay of a DCH state. The kinetic energies of both the photoelectrons and Auger electrons are of the order of several hundred electron volts without retardation. The requirements for both a high energy resolution and high collection efficiency in order to detect correlated particles necessitated the use of a MBES. A specially constructed MBES, designed and tested by the R. Feifel group in Uppsala, Sweden was installed in the HFPC. The MBES, based on a design pioneered by the J.H.D. Eland group [175], has a 2.0 m long drift tube and a total source detector distance of 2.115 m. A solenoid with a turn density of 488 turns/m is used to generate a drift region magnetic field of between 1.0-7.0 $\times 10^{-3}$ T. The high field

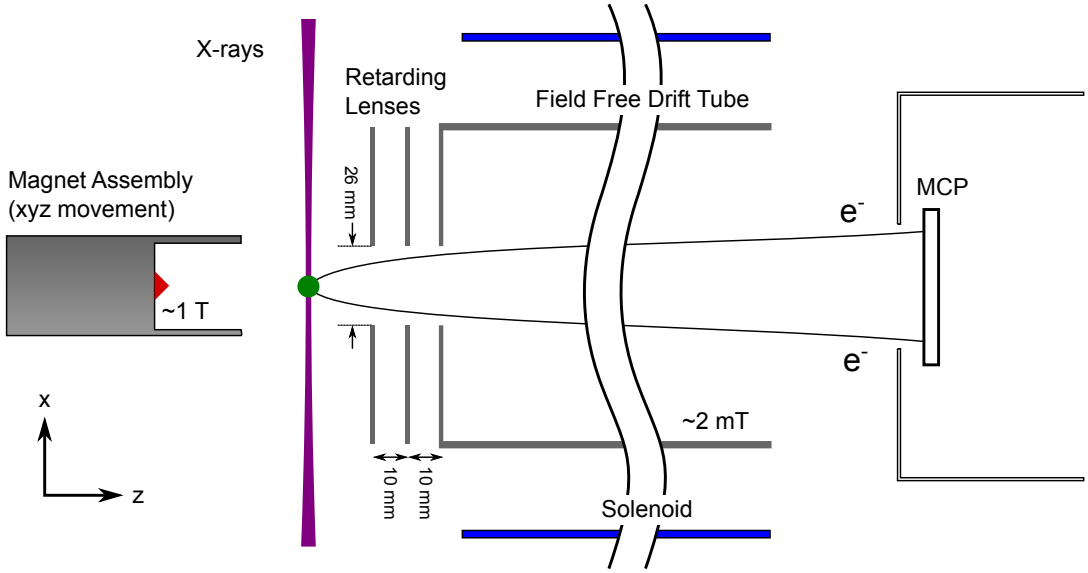


Figure 7.5: MBES used for the correlation experiment. The flight tube length has been truncated to better show all the elements of the spectrometer. The total source detector distance is 2.115 metres. The molecular beam source propagates in the axis coming out of the page (y axis).

region is produced by soft iron core shaped into a cone with an aperture of 90°, attached to a cylindrical rare earth permanent magnet, capable of generating a 1 T magnetic field at the cone tip. In addition to the magnetic fields, a series of repeller plates were installed just before the flight tube that allowed retardation of the electron kinetic energies. The detector configuration and the geometry of experimental apparatus is shown in figure 7.5.

For the all experimental runs described in this chapter, the FEL was run at 120 Hz using both the 20 and 40 pC bunch charge modes, corresponding to nominal pulse durations of between 12 and 6 fs respectively, depending on the run. The photon energies were tuned to be just above the ionisation potentials of the core electrons (or the minimum LCLS photon energy) for the sample of interest. The gas was inserted into the interaction region using a heated Even-Lavie valve and a 200 μm skimmer, with backing pressures in the 2-4 bar range. A summary of the experimental parameters of the different runs is presented in table 7.1. The optimal conditions for the focusing optics were found by observing the ion TOF spectrum in neon. Figure 7.6 shows an ion-picked TOF spectrum at optimal focus using 12 fs pulses at a photon energy of 1400 eV and a pulse energy of 0.8 mJ. Using equation 4.12, assuming zero kinetic energy (KE), and knowing that the peaks at 3.927×10^{-6} s and 1.200×10^{-5} s correspond to the photon peak (t_0) and the Ne_2^+ species respectively allows a mass calibration with a constant of $A = 2.5529 \times 10^{-6}$. Lines corresponding to the odd charge states of neon and some background ions are shown. The clear series of neon peaks all the way to the Ne^{9+} charge state is a clear indication we were in the optimal focusing conditions. The other experimental parameters such as the gas jet timings were scanned to maximise the integrated signal of the Ne^{9+} peak.

Property	Value	Unit
Drift Tube Length	2.0	m
Permanent Magnet Field	1	T
Solenoid Current	1.5-5.0	A
Solenoid Field	2.0-6.7	mT
Retardation Voltages	0-150	V
MCP Front	200	V
MCP Back	2400	V
MCP Anode	2600	V
HPC Pressure	1-6.0	10^{-9} Torr

Table 7.1: Experimental settings for the magnetic bottle and detectors for the double core hole experiments.

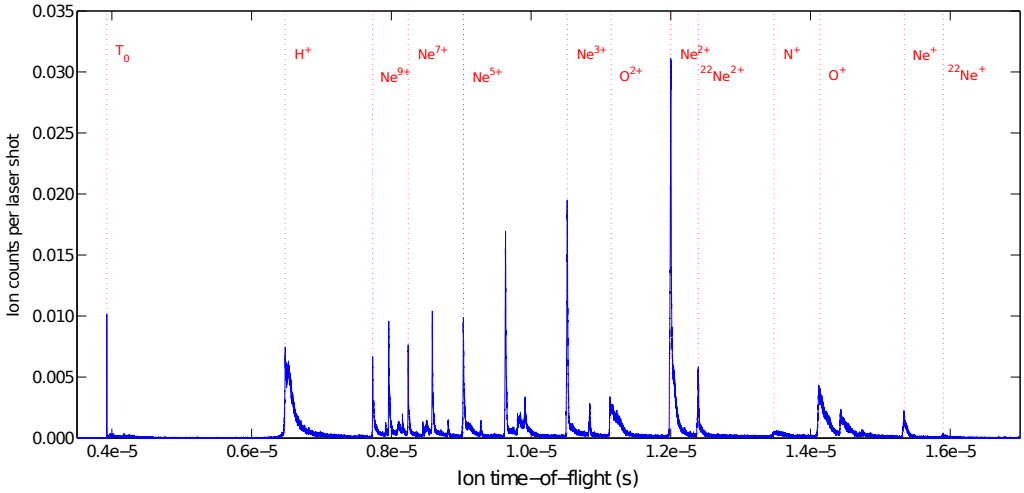


Figure 7.6: Neon ion TOF spectrum at optimal focusing of the X-ray Beam for a photon energy of 1400 eV. The spectrum (solid blue line) was generated using an ion picking routine to count the total number of events per channel, and divided by the total number of laser shots to get the count rate. The TOFs corresponding to both neon and some residual background species have been marked with red dotted lines. Charge states up to Ne^{9+} are clearly visible.

7.2.4.1 Investigations into the gas detector and electron beam values

The intensity correction required for implementing the partial covariance mapping technique requires that we have an accurate measure of the pulse energy on a shot by shot basis, and so I performed some studies into the different machine parameters for different runs to evaluate their reliability and whether they are sufficiently accurate for the partial covariance measurements to be meaningful. Ideally we would prefer to measure the energy as close to the interaction region as possible, but given the relation $\mathrm{Cov}(aX, bY) = ab\mathrm{Cov}(X, Y)$, where a and b are constants, and if we assume that that attenuation/transmission factor from the FEE to the focal region, k_{tran}, is non-random

Run	Energy (eV)	Charge (pC)	ρ_{12}	ρ_{13}	ρ_{34}
64	490	20	0.995	0.912	0.875
89	490	20	0.996	0.926	0.894
98	490	20	0.999	0.836	0.791
102	490	40	1.000	0.994	0.996
138	590	20	0.995	0.912	0.872
164	1060	40	0.911	0.447	0.280

Table 7.2: Pearson correlation coefficients for the different pairs of gas detector measurements for a selection of different experimental runs.

on a shot by shot basis, then equation 7.5 becomes:

$$\mathrm{pCov}(X, Y : k_{tran}E) = \mathrm{Cov}(X, Y) - \frac{k_{tran}\mathrm{Cov}(X, E)k_{tran}\mathrm{Cov}(Y, E)}{k_{tran}^2\mathrm{var}(E)}. \tag{7.6}$$

The k_{tran} factors in the correction term cancel in this case, yielding exactly the same result as 7.5. Therefore using the values from either pair of gas detectors will be valid assuming the case that the relative shot to shot pulse energy is accurately represented.

The most important test was to ensure that the gas detectors were accurately representing the total energy of the pulse during the course of the experiments. Since all 4 detectors are based on the same technology and each pair of detectors views the same part of the beam, we would expect the measured value of each gas detector to be proportional to each of the others if functioning correctly. A simple graphical approach to this problem was to create a density scatter plot of correlated gas detector measurements on a 2D map. In this view, 2 detectors that measure exactly the same energy (or a proportional value) each shot would produce a map with straight line, whereas 2 detectors which have no degree of correlation with each other would produce a circular distribution on the map. To quantify the degree of correlation between two variables x and y with a linear relationship with each other, we can use the Pearson correlation coefficient (PCC), ρ, which is mathematically defined as:

$$\rho_{(x,y)} = \frac{\mathrm{Cov}(x, y)}{\sqrt{\mathrm{var}(x)\mathrm{var}(y)}} = \frac{\langle xy\rangle - \langle x\rangle\langle y\rangle}{\sqrt{\mathrm{var}(x)\mathrm{var}(y)}}. \tag{7.7}$$

This coefficient is essentially the normalised covariance and is a dimensionless coefficient that varies in magnitude from 1 (perfectly correlated) to 0 (no correlation), and when squared, also yields a measure of how much the variation in one set of variables can be explained by the variation in the other set.

Figures 7.7a to 7.7d show correlation plots for different pairs of gas detectors for a single run, using approximately 400,000 shots, and table 7.2 shows the PCC for three pairs of gas detectors (both before attenuation, both after attenuation, and 1 before and 1 after) for a selection of runs spread over a number of days and different operating conditions. Though the absolute values vary, the gas detectors show a consistent trend in their degree

of correlation. The first two gas detectors exhibit almost perfect correlation, with $\rho_{12} \approx 1$ in all runs analysed. Conversely, the degree of correlation between the gas detectors after attenuation varies significantly depending on the run, and is consistently lower.

The second test required was to ensure that the relationship between the electron counts per shot, N_e and the measured pulse energies were sensible. The total electron counts for a given shot were calculated through a simple numerical integration of the TOF signal over the region of interest divided by the mean integral of a single electron count (since the MCP yields a distribution of different pulse heights and thus integrals). Figures 7.8a to 7.8c show the mean electron counts as a function of pulse energy as measured by the two pairs of gas detectors. Both pairs exhibit a linear trend, which is to be expected since we are dominated by 1-photon processes. The generally low number of counts unfortunately limits the statistics in the N_e error, however over all runs studied the standard deviation of the electron counts followed $\sigma \approx 1.4\sqrt{N_e}$, which is larger than the theoretical limit of $\sqrt{N_e}$ but still reasonable. The intercept of the linear trends also show clearly for which runs the calibration of the gas detectors is inaccurate. Run 98 is the clearest

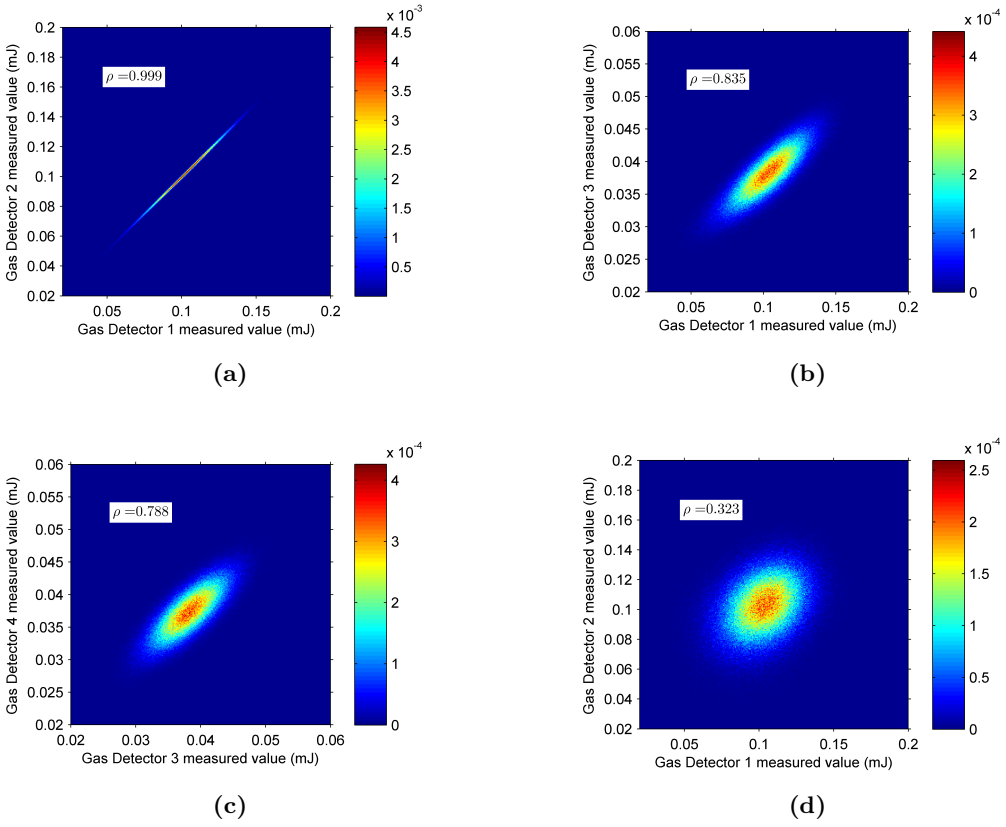
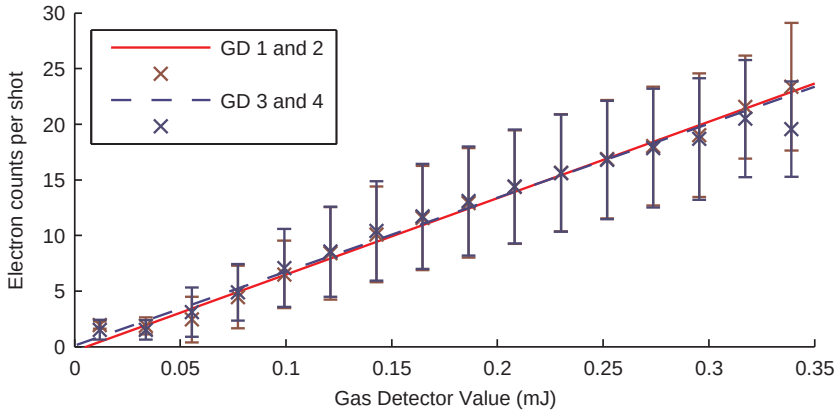
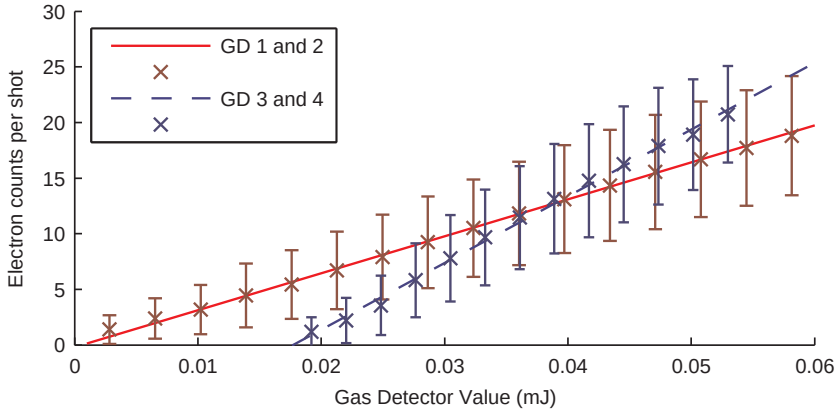


Figure 7.7: Correlation plots for the measured photon energy for the four different gas detectors for a run operated at 20 pC at a photon energy of 490 eV. (a) 1 and 2 (both before attenuation), (b) 1 and 3 (before and after), (c) 3 and 4 (both after), (d) 1 and 2 which have been shifted by 1 shot with respect to each other to decorrelate the two sets. The Pearson correlation coefficients are shown on the insets.

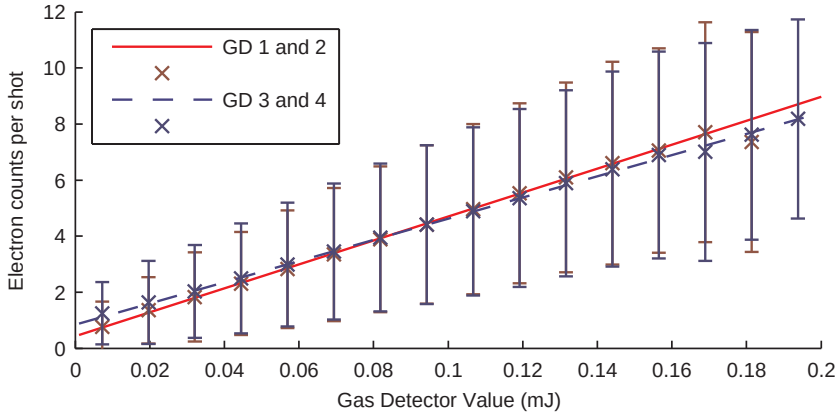
example of this: whereas the first pair show the expected intercept, the intercept of the second pair is shifted by a significant amount.



(a)



(b)



(c)

Figure 7.8: Electron counts as a function of pulse energy as measured by the pairs of gas detectors before and after attenuation for runs (a) 63, (b) 98 and (c) 138. The first pair has been multipled by the attenuation coefficient (calculated from the mean values of each pair of detectors) so that the scales are comparable.

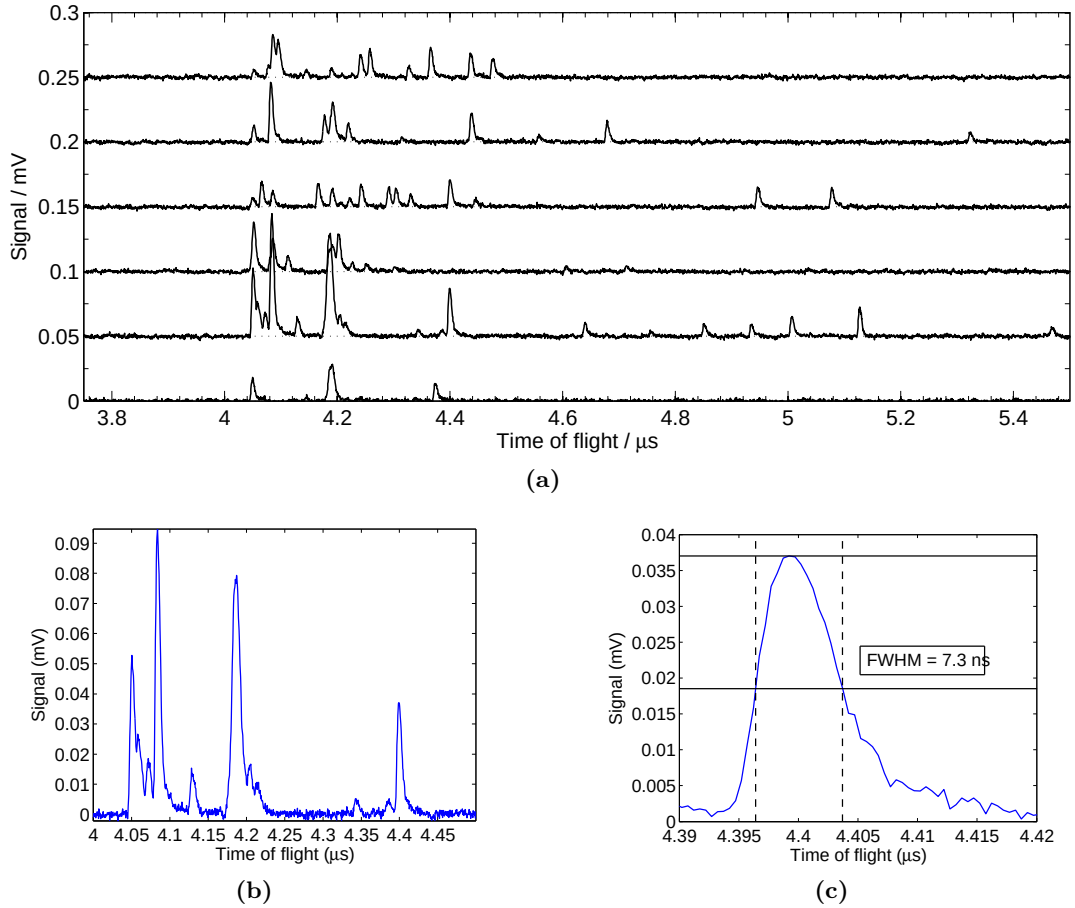


Figure 7.9: Single shot TOF data for neon irradiated with 1065 eV. (a) Six different single shot traces as acquired by the Acqiris digitiser. (b) A zoomed in view of one of the traces, showing that under our experimental conditions the count rate was sufficiently high as to produce pile ups of multiple overlapping peaks. (c) A single electron hit. FWHM pulse duration was calculated as 7.3 ns for this hit. 7 - 8 ns FWHM for a single hit was typical under our experimental conditions.

From these studies it is reasonable to conclude that the first pair of gas detectors were over the course of the experiment sufficiently accurate to be used for the partial covariance correction, and for the calculations shown below, and average of the first pair of detectors was used as the measure of the relative pulse energy.

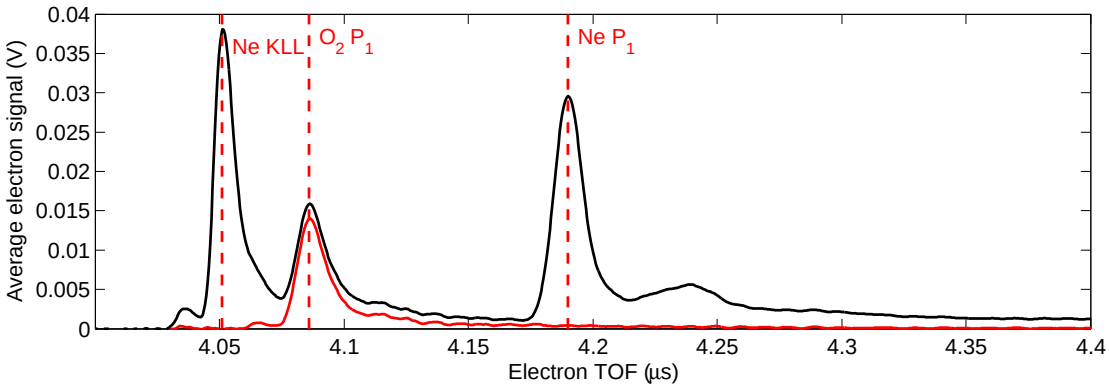
7.2.5 Neon

Before studying the larger molecules, a number of runs were performed on neon. Neon is an atom that has been well studied in both synchrotron studies and prior LCLS experiments, including experimental confirmation of DCH energies observed using standard electron TOF techniques [28]. As such, it provides an excellent benchmark by which the partial covariance mapping technique can be evaluated for accuracy. Theoretical and experimental values for both the IP and DIP of neon are in close agreement with each other, yielding

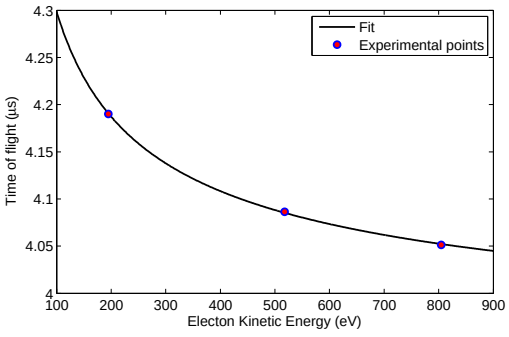
values of 870.21 and 1863 eV respectively [196].

The magnetic bottle was operated with a solenoid current of 1.5 A and 2 bar of neon backing pressure. The LCLS was operated using a nominal photon energy of 1050 eV for the neon runs, and analysis of the electron beam data yielded a measured photon energy of 1065 eV. Using this photon energy value and the above ionisation potentials, the main photoelectron energy P_{main} = 194.79 eV. Figures 7.9a and 7.9b shows single shot TOF data, demonstrating both the variability in the overall counting rate, and the fact we are operating in a count rate regime where pile-ups are occurring: a perfect test of the covariance technique. Figure 7.9c, shows a pulse as produced by a single electron hit, with a FWHM duration of 7.3 ns. This pulse duration was similar for other analysed shots, with typical single hit pulse widths in the range of 7-8 ns. This is much longer than we might expect for a typical MCP signal, and has negative implications for our energy resolution as discussed below.

The covariance maps were generated using scripts written in both Matlab and using the LCLS pyana frame works. For each run, the time of flight traces were converted to



(a)



(b)

Method	E_R	T_0	C
Simion	0.03	3.926	3.628
Expt	0.03	3.918	3.805

(c)

Figure 7.10: (a) Electron TOF spectra for runs 105 (neon) and background. (b) Electron energy versus time of flight for the 3 peaks identified in (a) with a least squares best fit applied to the data. R^2 = 0.9998. (c) Simion and experimentally determined conversion coefficients as defined in 4.13. T_0 is in μs and C is in units of μs eV$^{\frac{1}{2}}$

electron kinetic energy was using equation 4.13, yielding a trace binned into equal width energy windows using the same method as described in section 5.4.

An initial estimate of the TOF coefficients were calculated using Simion for multiple repeller plate voltages and optimised magnet positions, and are shown in table 7.10c. However since the experimental calibration will likely be different, the final calibration was achieved using the experimental TOF traces, using the peak locations of the photoelectron and Auger peaks. Figure 7.10a and 7.10b show the identified unambiguous TOF peaks and the calculated fit respectively. The derived calibration, yielding constants of $T_0 = 3.18$ and $C = 3.79$ assuming the time is given in microseconds and the electron energy is in eV. The values are summarised in table 7.10c.

Figure 7.11 shows a logarithmic plot of the electron kinetic energy spectrum for neon rebinned into 1 eV wide bins, over the 0-1200 eV range. Features corresponding to Auger and valence ionisation in neon are observed. The valence feature is centred at 1040 eV which given the energy resolution is consistent with a neon valence ionisation potential of 21.6 and 48.5 eV. Additionally, lines corresponding to core ionisation of the neutral, 2+ ground state ion, 3+ ground state ion and 4+ ground state ion. The peak widths however are significantly wider than we would hope for, with each peak in excess of several eV FWHM and the auger/valence features are several tens of eV broad. Two possible explanations are an insufficient time resolution stemming from a wide MCP pulse width. Assuming a 7 ns pulse width for a single electron hit (FWHM), in the kinetic energy domain this corresponds to a 10.7 eV spread of energies at 200 eV, and 120 eV at 1000 eV. The other possible explanation is the finite FEL pulse bandwidth, which at 0.5-1.0% of the central wavelength corresponds to a FWHM bandwidth of 5-10 eV at our photon

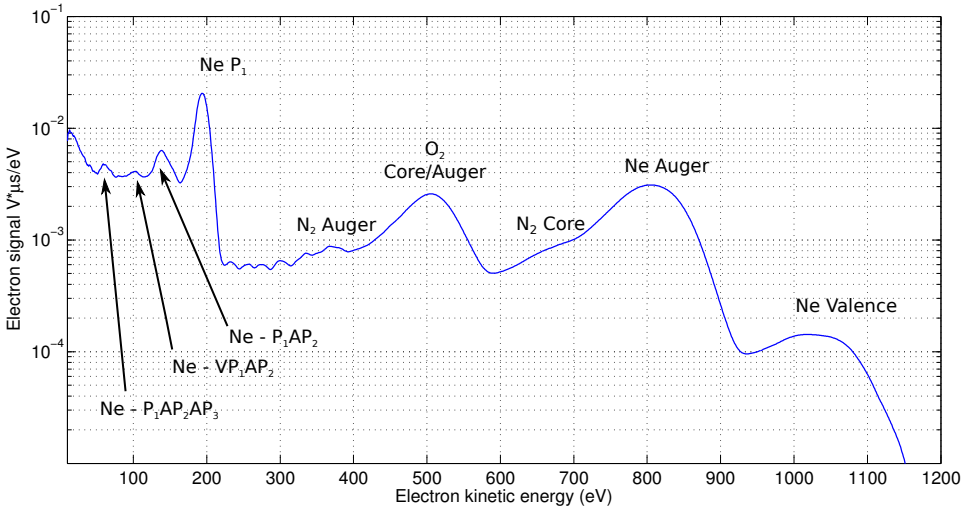


Figure 7.11: Neon electron energy spectra for kinetic energies 0-1200 eV irradiated with a 1065 eV FEL pulse, plotted on a logarithmic scale to enhance the low lying peaks. Contributions from both Neon core, valence and Auger electrons, as well as core/Auger features of the background oxygen and nitrogen species are present.

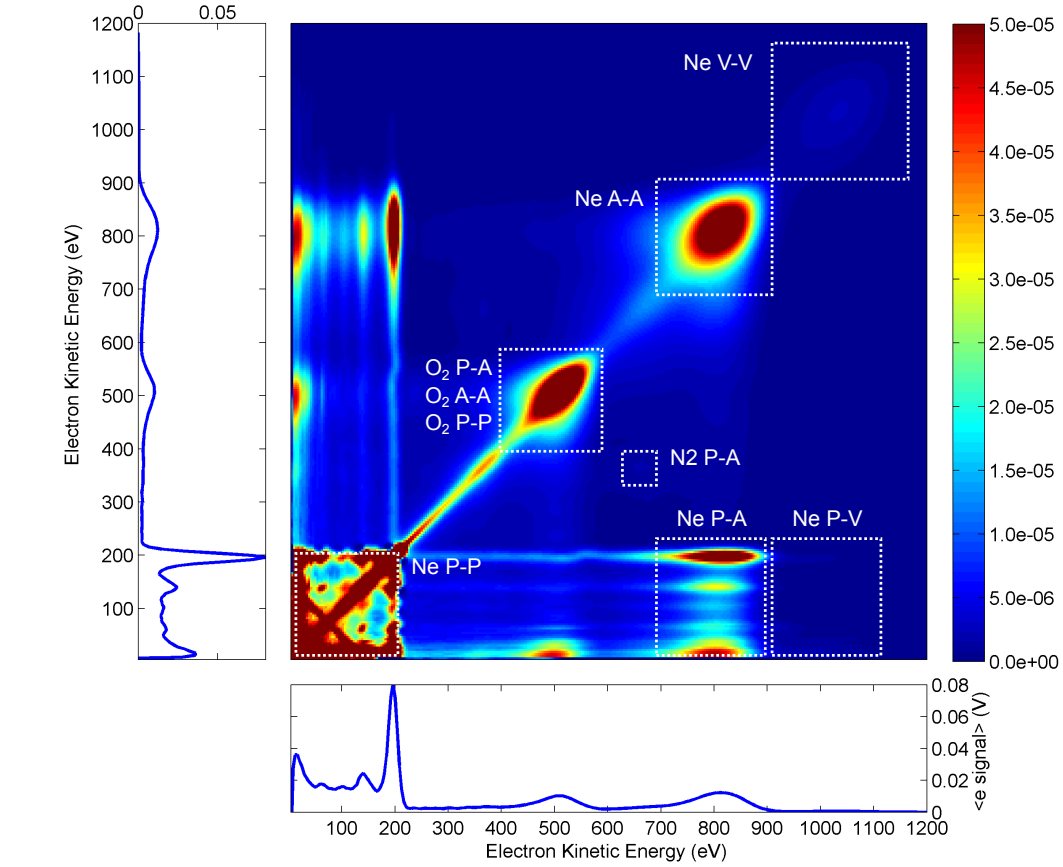
energy.

Figure 7.12 shows a covariance map generated over the same range with a 4 eV bin size. Already a great number of correlation features are visible in this map. The smaller subplots show the standard covariance and intensity correction respectively, and we can see the partial covariance formula successfully eliminates contributions that stem only from pulse energy fluctuations. While a single process may involve multiple electrons, each island or feature in the map will, assuming the islands are well separated, be the manifestation of the correlation between only two electrons. For example while a simple PA process (core ionisation plus auger decay) will produce only one island, whereas a PAP process will show up in three features corresponding to the three possible pairs. To simplify the labelling of these features, a bold type will be used to signify which two electrons of a given process correspond to the feature being described. So for example the label $\mathbf{P_1}\mathrm{A}\mathbf{P_2}$ denotes a feature corresponding to a correlation of the first and second photoelectrons of a PAP process.

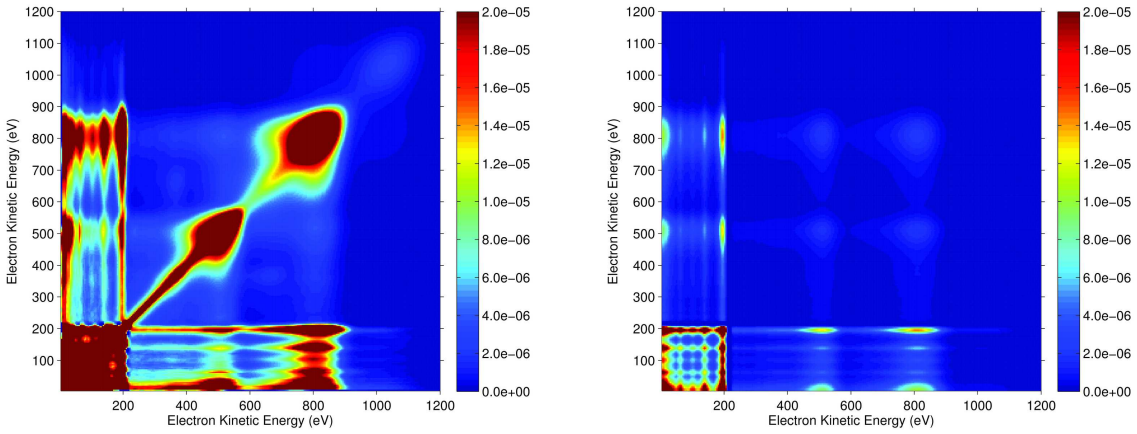
It is important to understand where every feature comes from, since not all of them will be the result of the processes we are interested in, and instead can be the results of artefacts from either digitization, ringing or another experimental effect such as background gases. A covariance map generated from the same spectra on both axis such as figure 7.12 will display two features which maps generated from distinct traces will not replicate. Firstly, the map will be mirrored in the axis X = Y, and the largest and most obvious feature of the map will be the prominent line in the X = Y axis. This is the autocorrelation line, and will be present simply because every channel will be correlated with itself.

Near the autocorrelation line are features that can be explained by neon valence-valence (VV), Auger-Auger (AA) and core-core processes (PP). Core-valence (PV) and core-Auger (PA) correlations are observed in the lower sections of the map. The Neon PP features at low energy and the Ne core-valence and core-Auger features will be discussed in further detail. The neon VV feature is centred at 1025 eV. We also see correlations that correspond to background species, specifically oxygen and nitrogen molecules, with K-edges at 544.5 [197] and 409.5 eV [198] respectively, corresponding to electron energies of 520.5 and 655.5 eV for our photon energy. The Auger energies for the decay of the single core hole of these species are expected to have electron energies in the range 508-512 eV and 355-370 eV [199]. Since the oxygen photoelectron and Auger energies are at similar energies and all contribute to the broad feature centred at 504-512 eV and our energy resolution unfortunately forbids resolving much structure. Conversely, we also see a clear photoelectron-Auger correlation corresponding to the nitrogen $\mathbf{P_1A}$ thanks to their energy separation of ≈300 eV.

Figure 7.13 shows a 0.5 eV resolution covariance map of the core photoelectron - photoelectron region between X = Y = 10 - 220 eV. As described in section 3.3.2, the photon energy of the FEL can vary significantly on a shot by shot basis, which presents a



(a)



(b) **(c)**

Figure 7.12: (a) Covariance map of neon electrons of energy 4-1200 eV. The TOF traces were binned in energy with bin width = 4 eV. The white annotations denote areas of the map corresoponding to both neon and background species nitrogen and oxygen. The 1D plots show the mean electron signal. (b) The covariance. (c) The correction.

problem when measuring photoelectron spectra since the electron energy will jitter with the pulse energy. This will lead to further broadening the TOF peaks, or in the case of the covariance maps, turns a single peak into a line structure. For photoelectron-photoelectron features, this line will be in the X = Y direction since the kinetic energies of both particles will increase and decrease together. Additionally, the jitter can introduce 'depletion' correlation artefacts of negative covariance near the photoelectron peaks (these can be seen on figure 7.13a near the K-line features. Pure Auger electron features on the other hand will be unaffected by the jitter since they are independent of photon energy. While this effect distorts our features, it can be beneficial since the shape of the distortion yields information on the type of correlation.

A correction can be applied to sharpen the photoelectron features by using equation 3.26 to calculate the shot to shot photon energy. In this case we can user a modified version of equation 4.13, which now becomes:

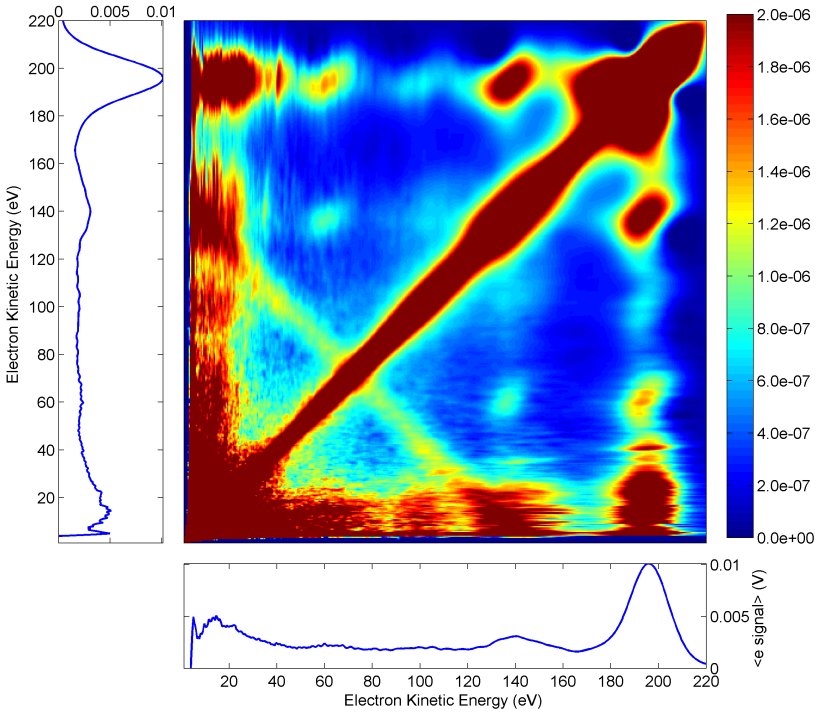
$$T = t_0 + \frac{C}{\sqrt{U_{k,0} - E_R - (\Delta E_{photon})}} \tag{7.8}$$

Where ΔE_{photon} is the photon energy for a given shot minus the mean energy of the run. This should sharpen up the photoelectron features, although this will be at the further expense of the Auger features' resolution. The effect of this correction can be seen by comparing figures 7.13a and 7.13b which show the uncorrected and jitter corrected plots respectively. The jitter correction yields rounder features and the artefacts adjacent to feature 1 are also eliminated, although the overall width of the feature remains the same in this case since we are limited in resolution by other factors.

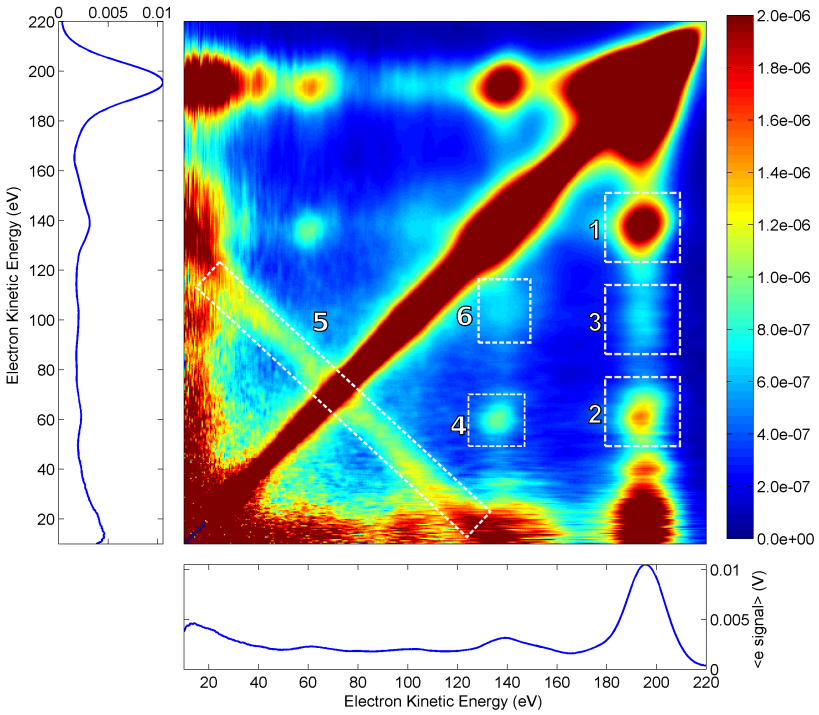
We see in these figures at least 6 distinct features. Features 1 to 3 are located on the main $1s^{-1*}$ ionisation photo-line, with energy equal to 194±5 eV. Islands 1 and 3 are energetically equivalent to sequential PA processes, corresponding in energy to the $\mathbf{P_1}A\mathbf{P_2}$ and $\mathbf{P_1}AP_2A\mathbf{P_3}$ ionisation routes respectively, with measured kinetic energies of $\mathbf{P_2}$ = 139±5 eV and $\mathbf{P_3}$ = 60±5 matching well with the expected values of 136.6 eV and 59.5 eV respectively [200]. Feature 4 would then make sense given this interpretation, corresponding to the $P_1A\mathbf{P_2}A\mathbf{P_3}$ correlation.

Feature 2 could in principle come from 3 different processes in which a valence ionisation occurs before a second core hole is formed: $\mathbf{P_1}VA\mathbf{P_2}$, $\mathbf{P_1}AV\mathbf{P_2}$ and $V\mathbf{P_1}A\mathbf{P_2}$. All of these processes have identical final states, and identical P_2 energies equal to 100.4 eV, matching well to our observed energy of 101±5 eV. Since it is correlated with P_1 of the main $1s^{-1}$ line, and given if we were core ionising the singly charged ion we would also expect a correlation with kinetic energy 168.1 eV, we can eliminate the last process as a candidate since we observe no such correlation feature. The other two processes could be distinguished in the

*The negative superscripts denote the vacancy of each shell, a convenient notation for describing hollow atoms.



(a)



(b)

Figure 7.13: (a) Covariance map of neon electrons of energy 10-220 eV. The TOF traces were binned in energy with bin width = 0.5 eV. (b) The same region, but with the energy shifted to compensate for the photon energy jitter. Note that the features associated with Ne 1s photoionisation become more spherical.

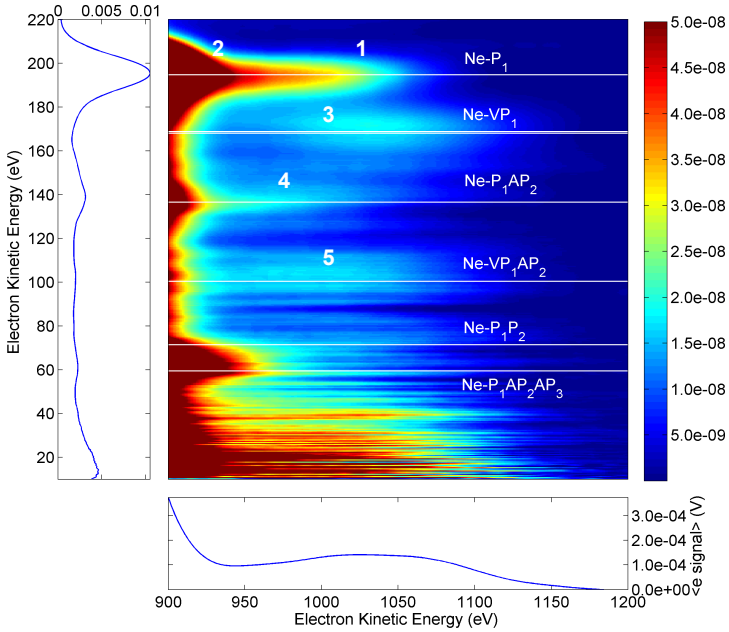
core-valance correlations, since we would expect electron kinetic energies of 1017.8 and 998.5 eV respectively in this case, though given our energy resolution we may not be able to resolve this unambiguously for our experimental conditions. Since however the P_1VAP_2 process requires a valence absorption before the core hole has undergone Auger decay, we may expect this process to be far less probable than the P_1AVP_2 process given neon's short Auger lifetime of 2.7 fs, making the latter the most likely candidate.

Feature 5 is perhaps the most striking feature visible in the low energy region, and is a clear signature of single photon core-valence (**VP**) ionisation of the form $Ne \rightarrow Ne1s^{-1}2p^{-1}$ or $Ne \rightarrow Ne1s^{-1}2s^{-1}$. These one-photon, two particle process requires conservation of kinetic energy between the two particles, which leads to the observed line normal to the autocorrelation axis. Such correlations have been previously observed in synchrotron studies of neon by Hikosaka et al. [201], and the observed sum of the energies of 144±4 eV agrees with measured values of the 2p-np shake up series reported by Martensson et al. [202] at energies of 51.2 and 46.9 eV with respect to the main P_1 line respectively, which correspond to observed total kinetic energies of 143.7 eV and 148.0 eV respectively for our 1065 eV photon energy. Their experiment successfully resolved two lines and our inability to resolve both lines is yet another good indication our energy resolution is sub-optimal for this particular experiment.

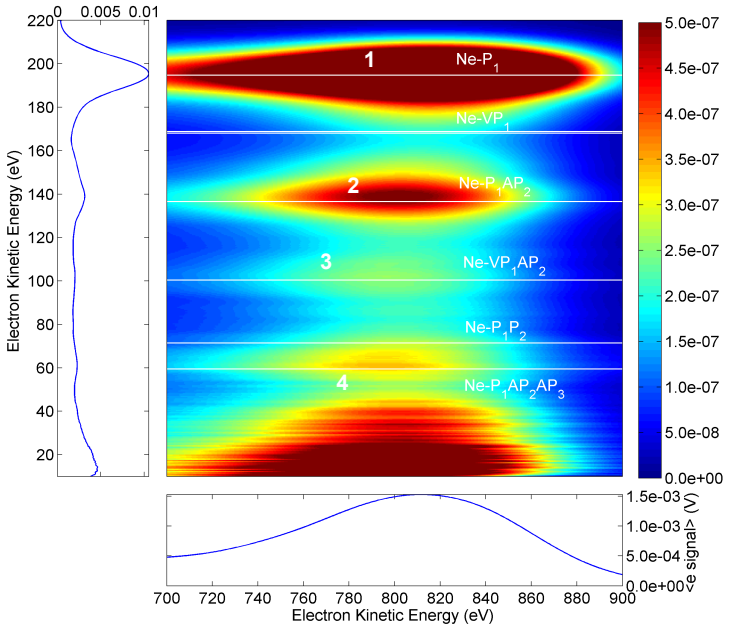
Feature 6 as of writing remains an enigma. Centred at (138,105)±5 eV, it is energetically compatible with either the P_1AP_2 and P_1AVP_2 process in one axis. However a correlation with both processes is clearly nonsensical and the combination of the two energies does not seem to match any known processes that we have so far identified. Further work into identifying this peak is required.

There is a large amount of signal and structure in the lower end correlations (sub 30 eV) however it is believed this is noise produced by electrons that are emitted from the magnet interacting with the focused beam. As such any real signal that may exist in the very low end region is obscured by noise.

Electrons resulting from ionisation of neutral neon from the 2s and 2p shells are expected to have kinetic energies of 1065-21.6 = 1043.4 eV and 1050-48.5 = 1016.5 eV respectively. Figure 7.14a shows an expanded view of the core-valence correlation region, and again we can identify a number of clear features corresponding to different photoionisation routes. For clarity, horizontal lines corresponding to the photoelectron energies for a given process have been added. The last P electron listed in the label is the electron we would expect a correlation for a given feature that lies on the line. Feature 3 corresponds to two-photon core-valence ionisation, the $\mathbf{VP_1}$ process. The centre of the peak is located at 1030±5 eV which is the average of the two kinetic energies we would expect for 2s and 2p ionisation, which makes sense considering the cross sections of the two states should be similar at this photon energy so we would expect equal contributions from both energies. Features 1 and 2 both correlate with the main $1s^{-1}$ line and may have contributions



(a)



(b)

Figure 7.14: (a) Covariance map of neon electrons of energy X = 900 - 1200 eV and Y = 10 - 250 eV (the core-valence correlationn region). (b) Covariance map of neon electrons of energy X = 700 - 900 eV and Y = 10 - 250 eV. Both the TOF traces were binned in energy with bin width = 0.5 eV and were energy shifted to compensate for the photon energy jitter.

from any route for which core ionisation is the first step. The valence electron energies for the P_1AVP_2 and P_1VAP_2 processes are approximately 67 - 92 and 47 - 76 eV respectively[†], corresponding to kinetic energies of 973-998 and 989-1018 eV. We can also identify a feature corresponding to the $P_1A\mathbf{VP_2}$ correlation (feature 5). Feature 4 is energetically compatible with energies corresponding to either $P_1A\mathbf{P_2}V$ or the $P_1AP_2\mathbf{A}V$ processes.

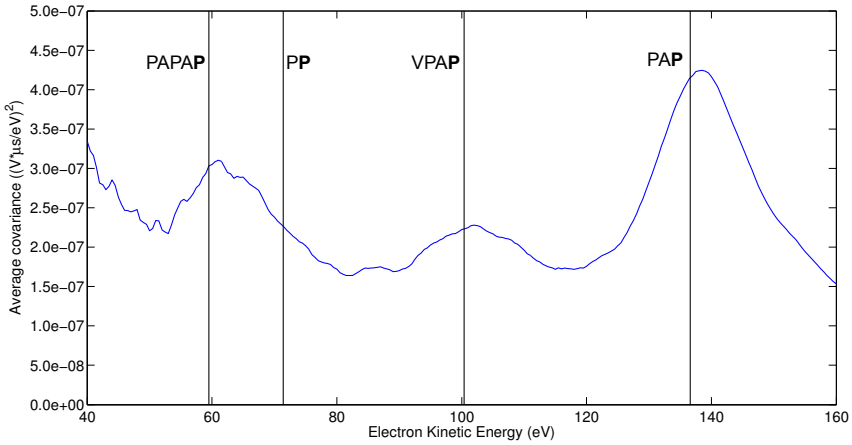
Figure 7.14b shows an expanded view of the neon core-Auger correlation region. Again, horizontal lines corresponding to the photoelectron energies have been added. We can see that the Auger peak in the photoelectron spectrum has contributions from four different Auger decay routes. The broad Auger peaks are generated from a number of different decay channels, and our energy resolution reduces these peaks to a single continuous feature. Nonetheless, four correlations with the photoelectron energies are observed. Feature 1 has contributions from both the main Auger decay of the SCH $\mathbf{P_1A}$ and the decay of the 3+ SCH $\mathbf{P_1}AP_2\mathbf{A}$. Feature 2 correlates with the same Auger electrons, only this time with the second SCH photoelectron: the $P_1\mathbf{AP_2}$ and $P_1A\mathbf{P_2A}$ correlation features. Feature 4 again correlates with the same Auger features, but for the $P_1\mathbf{A}P_2A\mathbf{P_2}$ and $P_1\mathbf{A}P_2\mathbf{AP_2}$ correlations. Feature 3 is the $P_1\mathbf{A}V\mathbf{P_2}$ correlation.

7.2.5.1 Double core hole signatures?

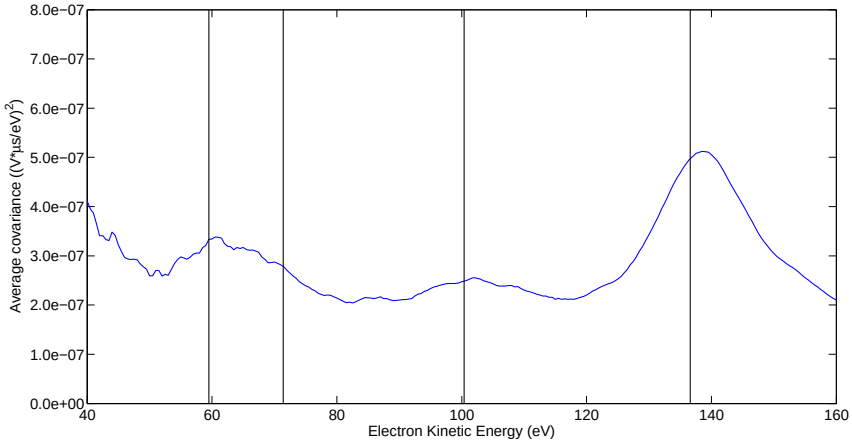
There is no clear feature corresponding to $\mathbf{P_1P_2}$ DCH creation in the photoelectron region of the covariance map, nor is there a peak in the Auger feature correlations corresponding to $\mathbf{P_1}P_2\mathbf{A}$. This is not unexpected considering our energy resolution at these energies. In some of the first experiments performed at LCLS by Young et al. [138] performed at the same nominal photon energy observed a clear signature of double core hole creation in the Auger electron spectra. As such it is initially surprising that we do not observe a similar signature. for their measurements they were using a 80 fs nominal (20-40 fs actual) pulse duration compared to our sub 10 fs duration. Additionally their observed signature was in the Auger electron energies which they were able to observe with far higher energy resolution with their use of the hemmers type TOF system. The wings of feature 3 in figure 7.12a and feature 4 of figure 7.14b overlap with the energy we would expect the double core hole, however no distinct peak can be resolved. The most likely scenario is that due to our poor energy resolving power both the peaks are smeared into each other, causing what should be two distinct peaks to appear as one.

Another possible explanation for our lack of signal is our choice of pulse durations. Our choice of using the low bunch charge mode to yield short pulses was originally chosen so that we would yield the most intense possible pulses on the assumption that short pulses will yield a higher peak intensity. However as mentioned in section 3.3.2 the intensity

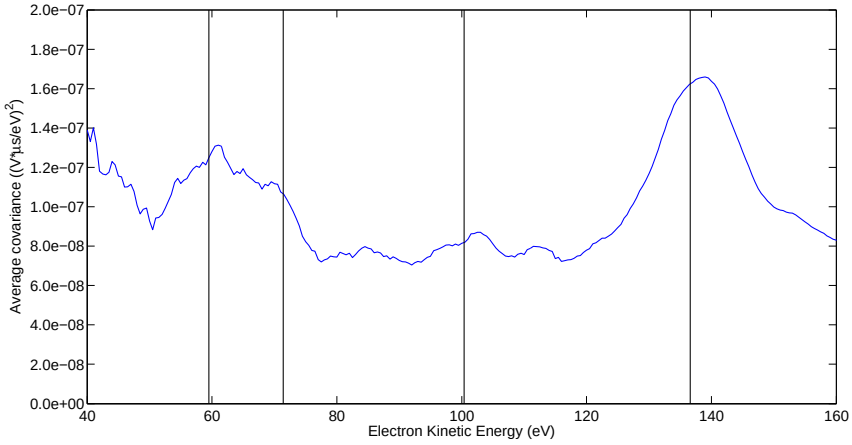
[†]Calculated using LANL Atomic Physics Codes located here: http://aphysics2.lanl.gov/cgi-bin/ION/runlanl08d.pl



(a)



(b)



(c)

Figure 7.15: Average line outs of the core-Auger region of the covariance map for a 10 eV width centred at (a) 767 eV (b) 805 eV and (c) 874 eV, which approximately correspond to the expected Auger energies for Ne^{3+} SCH,, Ne^{+} SCH and Ne^{2+} DCH. A possible shoulder corresponding to the energy of the P**P** process is visible for the higher energy Auger electrons.

profile of an FEL pulse is heavily dependent on the initial conditions of the electron bunch and as such may only be described by statistics. Our overall temporal profile is formed from a number of random phase modes. The number of spikes/modes within the pulse scales with the pulse duration, and for longer pulses we may expect that there will statistically be a greater number of higher intensity spikes which are capable of driving the DCH process than for our conditions were the number of modes was much smaller. We unfortunately have no data for longer pulse durations with which to test this hypothesis. These results do highlight the need for further investigations in to the pulse duration dependence of nonlinear processes for these sources.

It may be argued that the peak we have attributed to the $\mathbf{P_1}AP_2A\mathbf{P_3}$ process (feature 3) is in fact the DCH peak, and that the observed shift in the peak is simply due to an inaccurate energy calibration. However if this were the case then given the height of the core-core feature we would also expect a reasonably strong $P_1\mathbf{P_2A}$ correlation on the covariance map. The Auger energy of the decay of the DCH state is expected to be we would expect an Auger decay with higher kinetic energy, 868-74 eV [203], and there is no strong feature associated with this region. A correlation in this region may become more visible if we restrict ourselves to looking at only higher energy Auger correlations. The $P_1P_2A\mathbf{A}$ and $P_1AP_2\mathbf{A}$ processes are energetically equivalent, whereas for the $P_1P_2\mathbf{A}$ process the Auger energy is not energetically accessible by the other decay routes. Figure 7.15 show line outs of figure 7.14b. The line outs were formed by integrating the covariance over channels corresponding in energy to a 10 eV window, centred at (a) 767 eV (b) 804.5 eV and (c) 874 eV which approximately correspond to the expected Auger energies for Ne^{3+} SCH,, Ne^{+} SCH and Ne^{2+} DCH. A shoulder on the $P_1AP_2A\mathbf{P_3}$ peak which corresponds to the energy of the $P_1\mathbf{P_2}$ photo-line starts to appear. Although this evidence is inconclusive it does suggest that with a better energy resolution we would be able to successfully resolve the double-core hole features unambiguously.

7.2.6 Discussion

The main limitations on the interpretation of this analysis can be traced to the the sub-par performance of the detector. Especially towards the high energies the energy resolution of the instrument was insufficient to resolve the individual peaks of the Auger and valence features. Despite these issues however, the experiment has nonetheless demonstrated the ability of partial covariance mapping to resolve multiple overlapped processes using raw TOF spectra, and on timescales much shorter than coincidence methods applied to a synchrotron source. Reasonable statistics were achieved over the course of a 1 hour experimental run. If the detector energy resolution can be improved we would expect greatly enhanced structure to the maps and in principle even more detailed correlations between different processes may be resolved.

7.2.7 Hydrocarbons

Having demonstrated that the partial covariance mapping technique can successfully used with a relatively unstable source, we can now attempt to apply the same methods to other molecules in the hopes of resolving the DCH states. The remainder of this analysis will be focused on the molecules of C_2H_2 and C_2H_6. These two molecules are similar enough in structure that the main features of the maps should be broadly similar. The primary difference that should be observed is the location of the peaks corresponding to the tsDCH energies. The theoretical study of the ionisation potentials of C_2H_2 and C_2H_6 by Tashiro et al. [170] list the experimentally measured single ionisation potentials as 291.1 and 290.8 eV, the theoretical ssDCH potentials at 650.2-651.265[‡] and 648.8-649.7 eV and the tsDCH energies at 594.6-598.3 and 589.0-591.4 eV for C_2H_2 and C_2H_6 respectively.

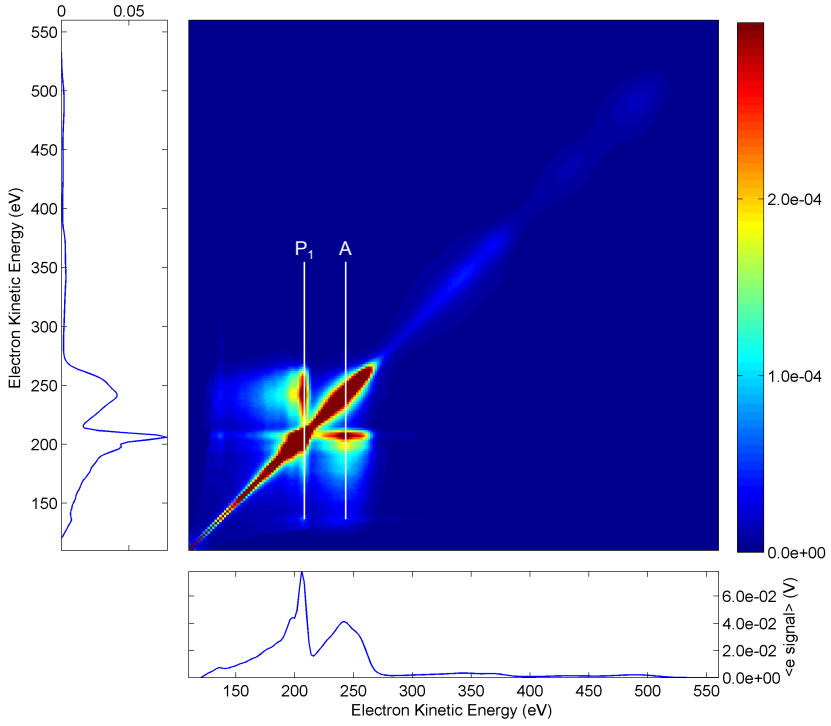
For the experiments performed on the hydrocarbons, the LCLS was operated again in the 20 pC bunch charge mode, yielding pulses less than 10 fs in duration, with a photon energy as close to the carbon K-edge as possible, which at the time was a nominal photon energy of 490 eV, which was the minimum photon energy available at the time. The photon energy as calculated using the electron beam parameters was measured to be 498 eV. Under these conditions we would expect the main P1 line to be at an energy of 206.8 and 207.9 eV, the ssDCH photoelectrons to be at 137.5-138.6 and 139.1-140.0 eV, and the tsDCH photoelectrons at 190.5-194.2 and 199.8-197.4 eV for the C_2H_2 and C_2H_6 molecules respectively. Since we would not expect interesting features below an energy of 100 eV, the MBES was operated using a retardation voltage of 100-150 V depending on the run, so as to maximise the energy resolution for the lower energy electrons. Calibration constants used for conversion are listed in table 7.3. Both the samples were mixed with 50% helium to reduce the sample density while maintaining overall source pressure.

Figure 7.16 and 7.17 show covariance maps generated for the full expected range of electron kinetic energies for C_2H_2 and C_2H_6 respectively, and are shown for two different vertical scales so that the lower features are enhanced. The strongest off diagonal features are, as expected the main P_1 line and the corresponding Auger decay. The highest energy on-diagonal features once again corresponds to valence ionisation of the hydrocarbon and background species. An additional island corresponding to ionisation of the helium

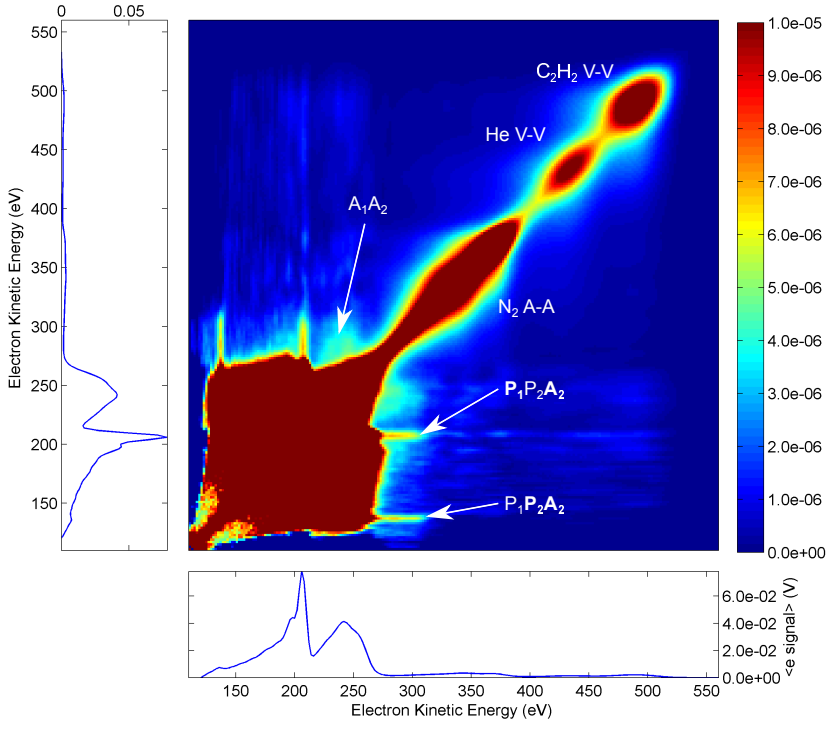
[‡]The range covers the values produced by the two different computational methods used in the paper, ΔSCF and CASSCF.

Nominal Voltage	E_R	T_0	C
100 eV	100.07	3.931	3.517
150 eV	151.02	3.934	3.459

Table 7.3: Electron TOF calibration coefficients used for the hydrocarbon runs for retardation voltages of 100 V and 150 V. T_0 is in μs and C is in units of μs $eV^{1/2}$

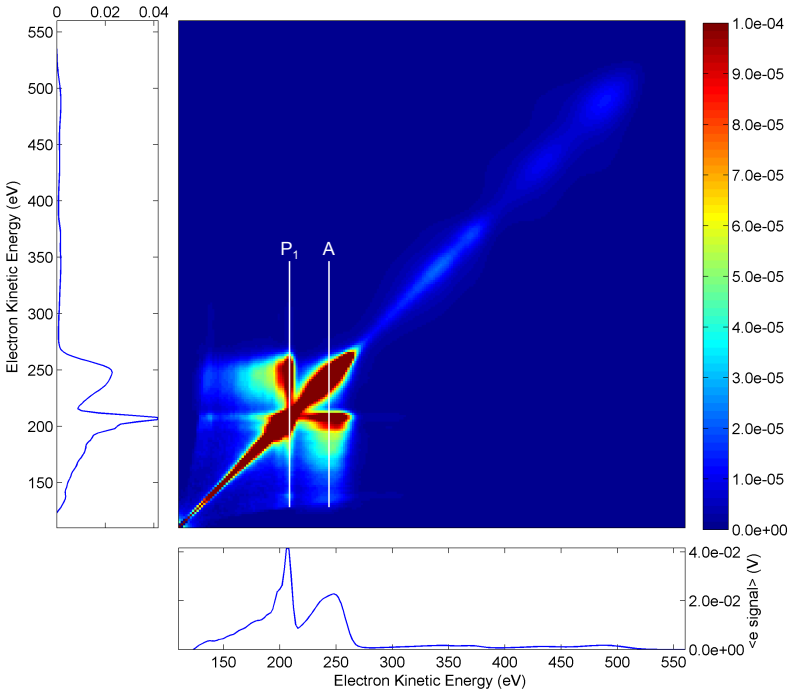


(a)

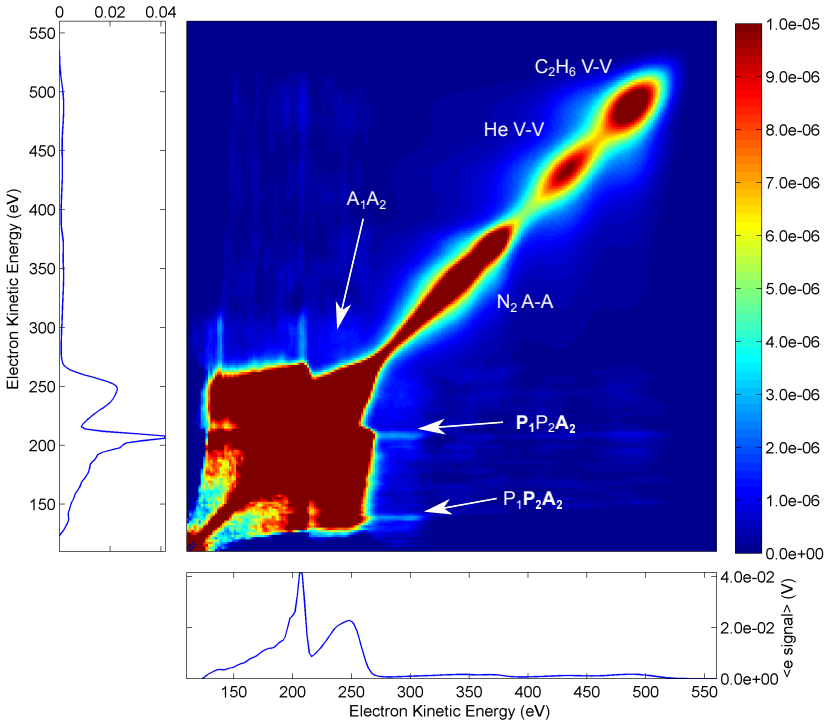


(b)

Figure 7.16: Covariance maps for electron energies of 110 - 560 eV for C_2H_2. Areas of interest are labelled for each sample.



(a)



(b)

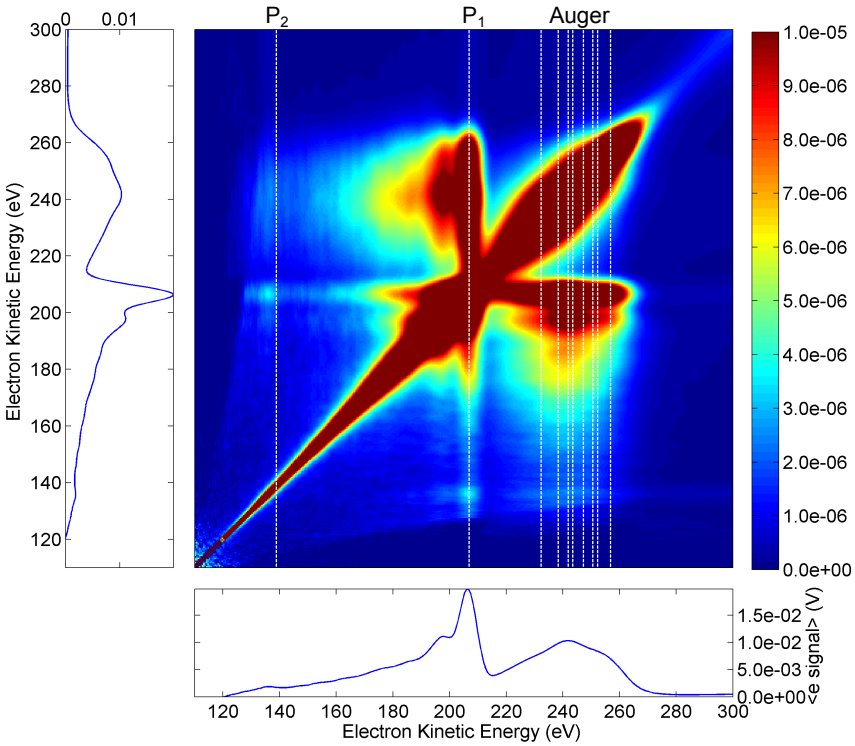
Figure 7.17: Covariance maps for electron energies of 110 - 560 eV for C_2H_6. Areas of interest are labelled for each sample.

carrier gas is present at energies centred at ≈440 eV is consistent with electrons energies corresponding to the second ionisation potential of helium, 54.4 eV. The feature centred at ≈350 eV is once again background Auger processes from N_2. The strongest off-diagonal feature is the carbon $\mathbf{P_1A}$ correlation.

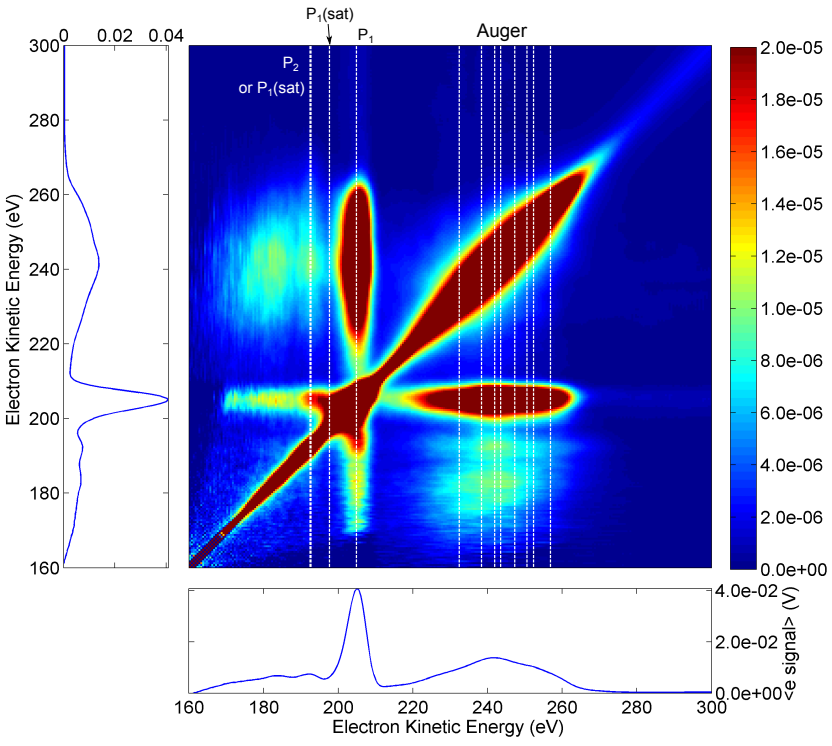
Compared to to the neon data, both C_2H_2 and C_2H_6 show extremely clear signatures of ssDCH creation. For a double core hole process, we would expect a total of 6 unique islands, and indeed all 6 islands corresponding to the ssDCH are observed in both species. The clearest evidence is the feature corresponding to $\mathbf{P_1P_2}$ correlation. For C_2H_2 this peak is located at (207,136)±3 eV and for C_2H_6 it is located at (207,137.5)±3 eV which are both energetically compatible with the theoretical values states above. We also see clear features corresponding to correlations with both the P_1 and P_2 electrons with the A_2 On the lower scale map we also observe peaks corresponding to the $P_1\mathbf{P_2A_1}$, $\mathbf{P_1}P_2\mathbf{A_1}$ and $P_1P_2\mathbf{A_1A_2}$ correlations.

For all six of these islands we would expect that the intensities of the peaks should be broadly similar, assuming that there are no other contributions to the peak. For example we would expect the P_1A to be significantly more intense since it will have contributions from both the SCH and DCH processes. However for islands that are energetically possible from only the ssDCH, we would expect similar intensities since the probability of detecting two particles from any part of the process should be similar. However the covariance maps do not show this, as the islands corresponding to the $P_1\mathbf{P_2}A_1\mathbf{A_2}$ and $P_1\mathbf{P_2A_1}A_2$ show an order of magnitude difference in integrated signal. A possible explanation is an energy dependent detection efficiency: the detection efficiency of a magnetic bottle is expected to drop off for higher energy electrons. However, if this was the case we would not expect such a difference between energetically close contributions. The average covariance signal for X = (133-139) eV (the energy range corresponding to the ssDCH for C_2H_2) drops by a factor of 5 from X = 245 eV to 285 eV. Conversely if we compare the integrated signal of the $P_1AP_2\mathbf{AP_3}$ and $\mathbf{P_1}AP_2A\mathbf{P_3}$ islands of the neon data (two islands for which there should be no overlap in contributions), we find that the integrated signal changes by less than a factor of 2, despite a much larger energy difference. As such it is not believed that the energy dependent detection efficiency can alone account for the differences in the observed signal. Currently this remains an open question and further investigations into the detection efficiency of the detector are needed before this discrepancy can be resolved.

The driving force behind this experiment was to attempt to observe the tsDCH since these should have the clearest signature of chemical sensitivity. Given that the cross-sections of both the ssDCH and the tsDCH should be similar, the fact we clearly observe the ssDCH in both species should mean that we will observe signatures of the tsDCH. However, the problem here is that for both C_2H_2 and C_2H_6 the photoelectron energies corresponding to the creation of the tsDCH lie reasonably close to the main 1s line of both species, which given our earlier issues with energy resolution may make them difficult to



(a)



(b)

Figure 7.18: Covariance maps for C_2H_2 for electron energies of 160 - 500 eV for (a) 100 V and (b) 150 V retardations.

resolve experimentally. Figures 7.18a and 7.18b show an expanded view of the C_2H_2 data for electron retardation energies of 100 and 150 V respectively. The lines show expected kinetic energies of the Auger, main 1s line, the DCH states and the 2 strongest satellites of the main, line which are located at kinetic energies of -7.2 and -12.4 eV relative to the main line [204].

The improved resolution of the 150 V retardation map allows the separation of the core-Auger correlation features into 3 main observable features, corresponding to correlations with the main P_1. The 12.4 eV satellite overlaps in energy with tsDCH, as such it will not be possible to resolve the tsDCH through observation of the P_2A correlations, although a clear island that is energetically compatible with both processes is present. The low energy end of the Auger feature can be attributed to the $P_1\mathbf{AP_2}$ correlation. The P_2 photoelectron is expected to have an energy of 498-316 = 182 eV. Although the photoelectron satellites energetically overlap with the tsDCH, in principle the photoelectron and its satellite should not be correlated since only one or the other process can occur for a given ionisation event of the neutral, so unless some false correlations are being introduced, we would expect

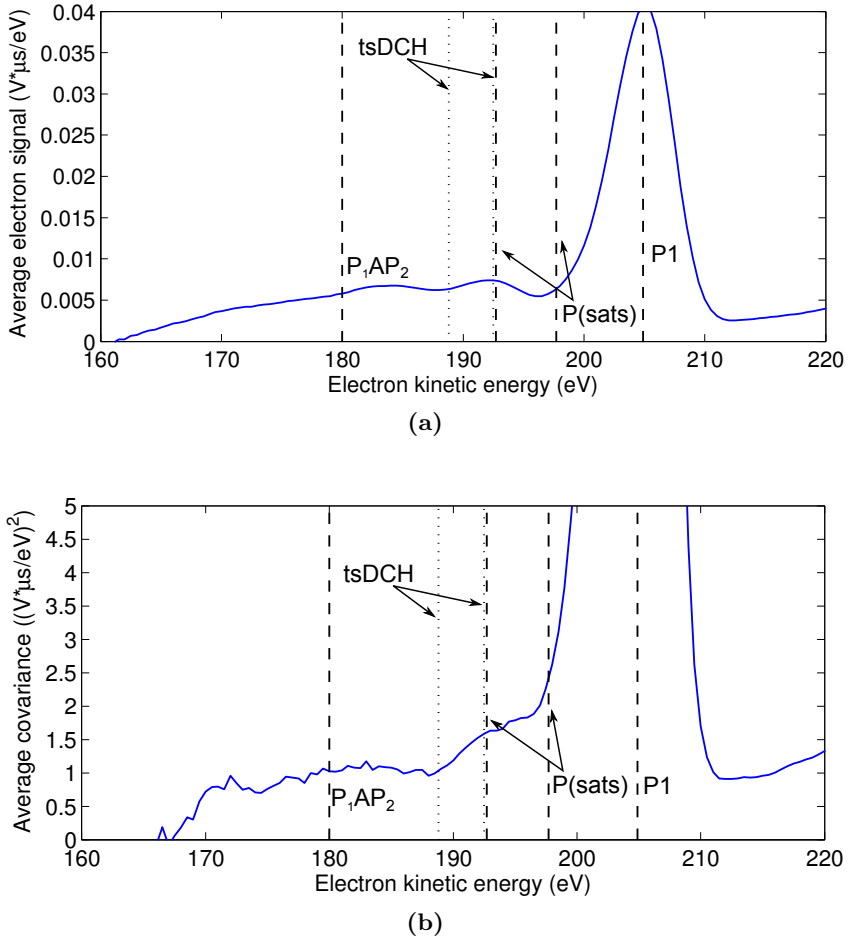
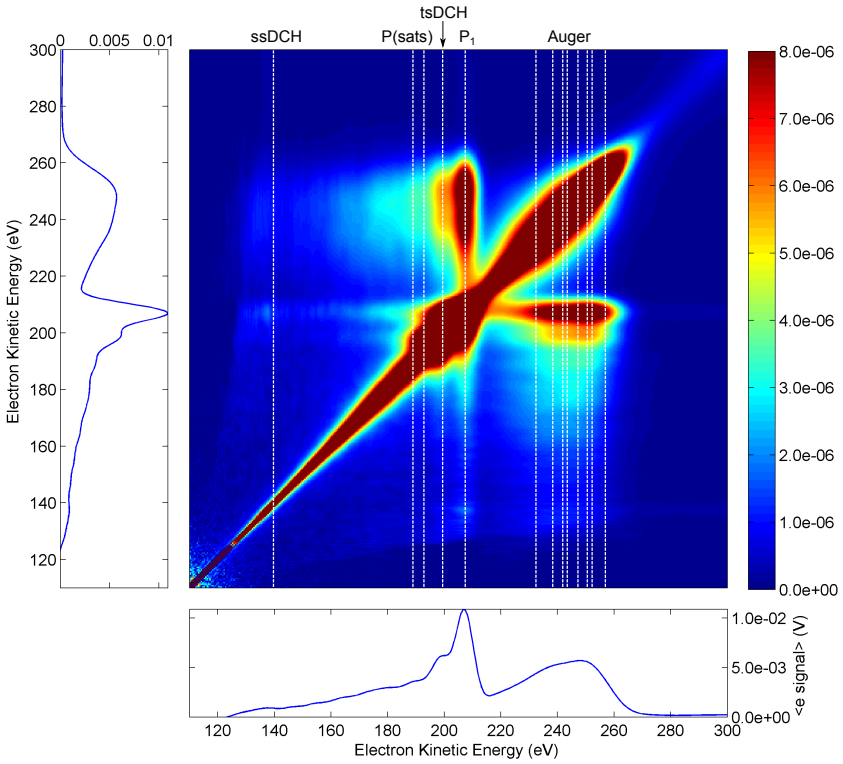
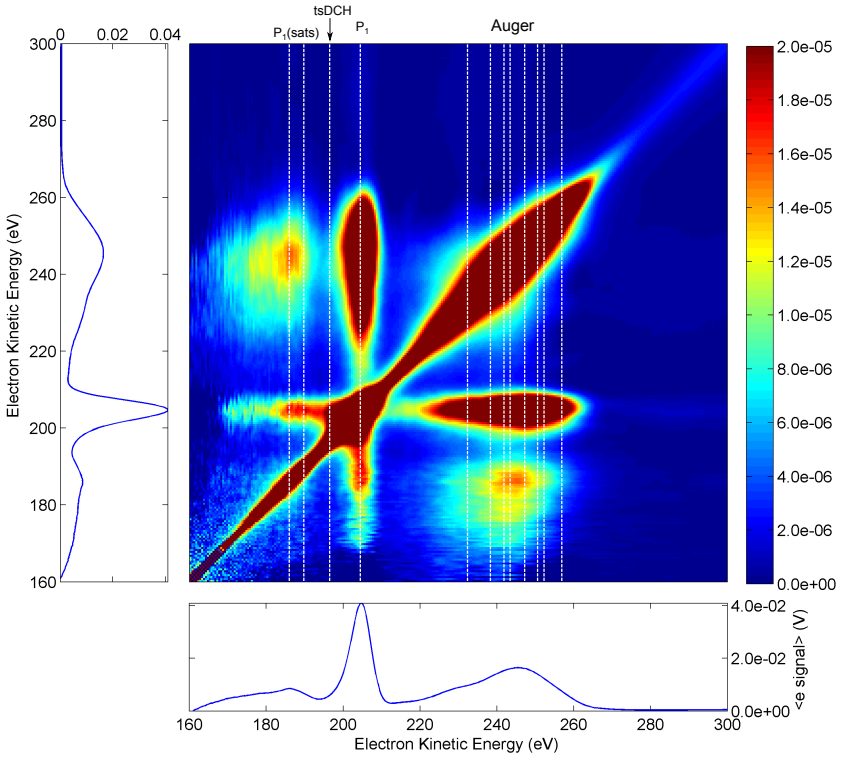


Figure 7.19: Comparison of the average kinetic energy spectrum (a) with the integrated covariance of the P_1 correlations (b) for C_2H_2.



(a)

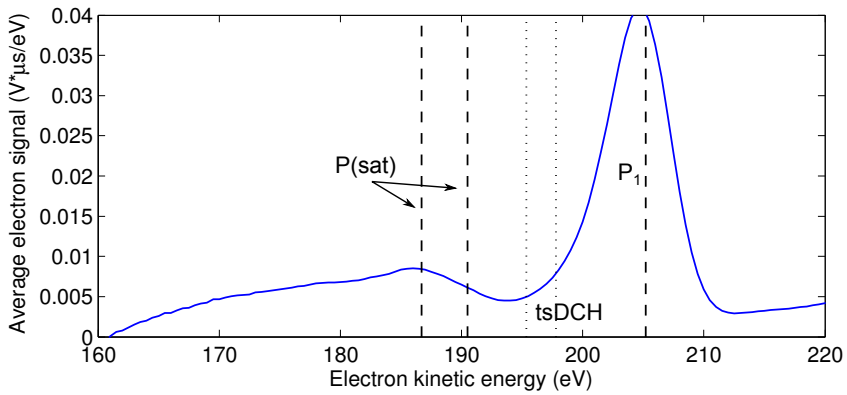


(b)

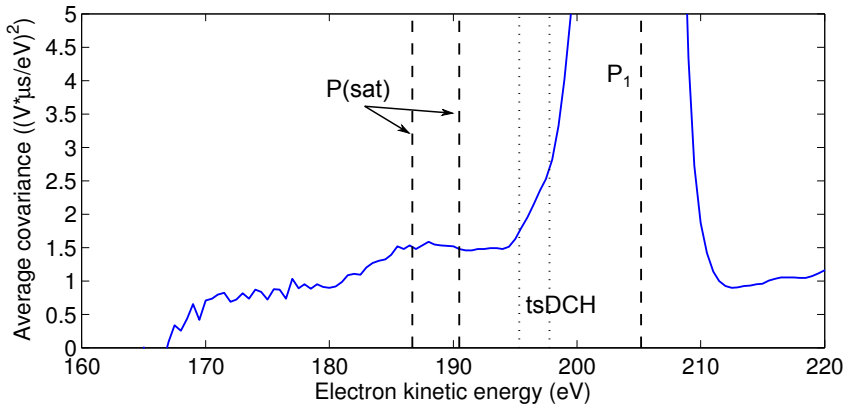
Figure 7.20: Covariance maps for C_2H_6 for electron energies of 160 - 500 eV for (a) 100 V and (b) 150 V retardations

that a peak or shoulder in the covariance map along the P_1 line to be from correlated processes such as P_1P_2. Figure 7.19b shows the average covariance for X = 203-207 eV. A clear shoulder is observed at the energies we would expect the tsDCH photoelectron to be.

With C_2H_6 the situation is potentially better as the tsDCH photoelectron energies lie further away from the photoelectron line and the satellites of the main line do not overlap with the tsDCH photoelectron energy. The two largest satellites are expected to be observed at energies relative to the main line of -14.7 and -18.5 eV [205], which are located at least more than 5 eV away from the expected energy of the tsDCH. If we again compare the average kinetic energy spectra (figure 7.21a) with a line out of the average covariance corresponding to P_1 correlations (figure 7.21b), again a shoulder is observed at the expected energy of the tsDCH correlation. This peak however cannot be unambiguously attributed to a true correlation with the tsDCH. The autocorrelation line is observed to a have a finite width since the MCP pulses also a have a finite width, a group of channels associated with a hit at a particular time will always be correlated. Since



(a)



(b)

Figure 7.21: Comparison of the average kinetic energy spectrum (a) with the integrated covariance of the P_1 correlations (b) for C_2H_6

this autocorrelation feature will most probably overlap with our expected 'true' $\mathbf{P_1P_2}$ correlations.

7.3 Conclusions

The major result of this work has been the demonstration of the applicability of the covariance mapping technique to unstable sources, and demonstrating successfully that the machine parameters of the LCLS data system can be successfully used to correct for both photon energy jitter and pulse energy fluctuation. The has been successfully demonstrated in neon, and from the maps we were able to detangle multiple ionisation channels from the simple TOF. The most striking feature which was successfully extracted was the observation of single photon double ionisation, and the clear correlation line corresponding to two particles with equal sum of kinetic energies is excellent evidence that the technique is functioning correctly. The evidence for DCH creation in neon was unfortunately not as definitive, however a shoulder corresponding to the $\mathbf{P_2A_1}$ correlation was was observed which suggests that with a superior energy resolution we would have been able to successfully resolve the DCH states.

Conversely, the observation of ssDCH features in hydrocarbons is both striking and unambiguous, with all six islands corresponding to the four particle correlations having been observed. Observation of the tsDCH states on the other hand is less robust, unfortunately limited by the energy resolution of our experiment and the broadness of the features meant that we were unable to unambiguously resolve peaks corresponding to the tsDCH. However there are still good indications that this technique at least has the potential to be a powerful tool in the field of DCH spectroscopy.

In order to fully evaluate the technique, further work needs to be completed on the existing data to see if further information can be extracted, and additional focus needs to be placed on the biomolecule data which as of writing has yet to be explored in great detail. A full deconvolution of the peak structure using nonlinear peak fitting for each trace may prove successful in extracting the weaker features which may be obscured by the broad stronger features, however as this must be performed on a trace by trace basis this will prove to be computationally daunting, and requires an expert knowledge of the response function of the detector to accurately fit the peaks to individual hits. For future experiments, further work should be performed in ensuring that we are not limited by the detector response function. However, given the promise these results contain, there are further plans for experiments that utilise the technique (see section 8.1).

While the experiments of this thesis have focused on the applications of covariance mapping to electron and ion spectroscopy as performed using FELs, it needs to be stressed that the technique may be applied to any experiment in which correlated measurables may

be observed with a fluctuating source. As such, it is expected that this technique may find uses in broader areas of research.

There are also numerous possibilities for extending the covariance mapping techniques to the more general case where were look at the degree of correlation between multiple sets of fragments. For a DCH state, a total of 4 correlated electrons are produced so in principle to fully characterise DCH states using this technique we would need to extend the calculation to at least 4 dimensions, which although conceptually and computationally daunting will be the focus of future efforts in the field. Frasinski et. al. demonstrated that covariance mapping can be successfully extended to the triple coincidence case [178], proving that the covariance technique can be generalised to the multi-dimensional case.

In the long term it is also expected that the improved spectral stability of future generations of seeded FEL sources in the coming years will also further improve the technique's potential through the elimination of pulse energy jitter and a narrow line width eliminating broadening of the features.

In summary, the a proof of concept of the technique of partial covariance mapping has been applied to the study of the creation of multiple core holes in both atoms and molecular systems, and it is expected that with additional development it will become a powerful tool in study of multi-particle X-ray processes.

Chapter 8

Conclusions

The central theme of this thesis has been in describing how coherent, femtosecond duration pulses of wavelengths spanning the XUV to soft X-ray wavelengths can be generated and how they can be used to study both the structure and the evolution of the dynamics of a molecular system.

In chapter 2 we discussed the ways in which light spanning from the optical to Hard X-ray wavelengths may interact with both bulk and gas phase materials. A selective description of ultrashort pulses and their propagation through bulk materials is presented. The principle behind photoexcitation and photoionisation is presented spanning from direct ionisation by X-rays, and how the highly excited core-hole states left through K-shell ionisation can decay, before considering multi-photon and field induced ionisation processes. The chapter concludes with a description of the strong field regime and how high intensity lasers may be used to generate coherent XUV radiation using the process of HHG.

Chapter 3 described the technology requirements and characteristics of light sources suitable for the experiments described in the thesis. In doing so we compare femtosecond optical laser systems and commercially available systems with the large scale national facilities that form a FEL source. The techology behind such sources was described and methods by which the key properties of the sources may be characterised.

Chapter 4 describes experimental techniques and technology common to the experiments of the thesis and the study of charged products of photoionisation in general. The chapter describes the technique of TOF spectrometry, and how the technique may be used to study both the mass, charge and energy of the fragments of photoionisation processes. A selective review of vacuum technology is presented. The necessity of high reflectivity grazing incidence optics for the focusing of X-rays is discussed, and the requirements of vacuum technology to study species in the gas phase. Finally the properties and merits of various detectors are discussed, with a focus on X-ray cameras and MCP detectors.

Chapter 5 presents work completed in testing various beam-line components constructed for use in an XUV beam line. High harmonic measurements using both a flat field spectrometer and a magnetic bottle electron spectrometer are presented. We then discuss work completed towards building up a robust acquisition framework for the flat field spectrometer and the delay stages. We then discuss how these elements will be used in future experiments performed at the laser consortium to study molecules using both HHG spectroscopy and absorption measurements.

Chapter 6 first describes the experimental capabilities of the AMO end station of the LCLS facility, including a description of the TOF systems available to the user as part of the main experimental HFPC. A historical view of CEI is presented, with a focus on discussing both the successes and limitations of systems studied using IR driven CEI, and how using X-ray induced fragmentation as an alternative probe method may provide a comparatively field free probe of the molecule. An experiment to study the molecular isomerisation of CHD is then presented: by using a UV pump to initiate the ring opening reaction of CHD and by then using a short duration X-ray pulse to induce fragmentation we observed that for UV - X-ray delays where the X-rays come after UV excitation, the ion yields of the H^+ and C^+ species increase by $\approx 10\%$ using a TOF detector over a 1-2 ps timescale, and similar increases for the total ion yield were observed using a VMI spectrometer. Over the same timescale the average kinetic energy of the fragments was observed to increase. These changes can be explained by the evolution of CHD into HT, demonstrating that X-RAY fragmentation can be used as a probe of the molecular geometry.

Chapter 7 describes an experiment to demonstrate that a modified form of the covariance mapping technique proposed by Frasinski et al. can be successfully applied to the study of TOF spectrometry even when using an unstable source such as an FEL. Using the technique in combination with a high collection efficiency MBES, we successfully resolve multiple ionisation and decay pathways in neon using short intense X-ray pulse. The covariance mapping technique successfully detangles the multiple contributions to single peaks in the average kinetic energy spectrum, revealing the contributions from multiple processes. We then successfully apply the same method to the application of DCH spectroscopy: the 6 islands corresponding to ssDCH in both C_2H_2 and C_2H_6 were observed, and the measured double ionisation potentials of the species were found to be energetically compatible with theoretical studies published by Tashiro et al. [170]. While the evidence for tsDCH creation was less unambiguous, correlations features that were energetically compatible with the expected energies of the core electrons were observed in both species.

8.1 Future directions

The equipment and software development described in chapter 5 will see extensive use as part of the new projects undertaken by the group to study molecular systems using both HHG spectroscopy of XUV excited systems, and absorption measurements that study the transmission of the XUV as a function of property of the system. These studies will supplement the studies undertaken by other sections of the laser consortium and will form a fundamental part of the Laser Consortium's drive to applying the these techniques to the study of systems in the condensed phase.

The CHD experiment has successfully demonstrated that X-ray fragmentation has the potential to be an attractive alternative to the multi-photon driven CEI. Our results were limited by the available timing resolution of the facility at the time of the experiment. Since then, the available timing resolution and since the experiment was performed the accuracy of the available diagnostics has improved by an order of magnitude. Further studies in more general systems, backed by theoretical studies into the auger decay and deformation of these molecules will eventually be able to fully evaluate the extent to which the X-ray induced fragmentation technique provides a field free probe of the molecular systems.

With the potential of the partial covariance mapping technique successfully demonstrated it will form a valuable tool in the longer term strategies of applying nonlinear DCH spectroscopy to molecular systems. The long term aim of such studies will to be to successfully apply the techniques developed to ever more complex systems, with the eventual aim to study molecules in the condensed phase. Additionally, since it is a general technique that may be applied to any signal which is periodic in both time and space, we anticipate that it will be useful in other fields. The software developed as part of the analysis of this experiment will continue to be used as part of future experiments. The software will provide future collaborators easy and effective methods to quickly analyse the data acquired during these runs, enabling both better use of the beamtime and more comprehensive results, and has already been used successfully in two further beamtimes.

In October of 2012, just before submission of this thesis, an additional beamtime, again head by the Feifel group, was undertaken at the LCLS to further our studies of DCH states in molecules. In particular this beamtime studied the nitric oxide (NO) molecule, and the aminophenol (C_6H_7NO) molecule, composed of a benzene ring with both an alcohol and amine group. The differences in the DIPs in the case of a structural isomer are expected to be more subtle than than those with different functional groups [206]. This experiment took advantage of the recently lowered minimum photon energy of LCLS, and performed several runs near to the carbon k-edge, allowing us to avoid a large amount of signal from contaminants such as water. The data obtained from this experiment is at time of writing still almost entirely unanalysed, however preliminary results from initial analysis performed during the run were promising and a difference in

the covariance maps of 2-aminophenol and 4-aminophenol were observed, although further work is needed before this can be attributed to chemical shifts of the core states with a reasonable degree of certainty. Assuming further analysis is successful, it is anticipated that the results from these experiments will be presented at conference within the next few months, and submitted for publication in the next 6-8 months.

Additionally, in the immediate term, our collaborators have in the planning and proposal submission stages at least two new experiments in the near future using both the LCLS and FLASH sources, focused on both DCH spectroscopy in further molecules, and nonlinear X-ray processes such as two-photon absorption in a number of systems. In the longer term, with the range of photon energies available at LCLS now extending from the carbon K-edge to the multi keV regime, SACLA now open for user experiments, the new XFEL project due to come online within the next few years, and LCLS II beginning construction in 2014, both the accessibility and range of science that can be achieved with these sources will continue to improve exponentially. The future has never been brighter for X-ray science.

Appendix A

LCLS Data Handling

The appendix details how to access and use the LCLS computing resources and also includes the instructions and source code for the conversion scripts I have written to assist data conversion and analysis. This appendix assumes a working knowledge of rudimentary UNIX bash/shell commands.

A.1 Server information

Pool name	Purpose
psexport	External SSH access and downloading/transferring data. Running analysis scripts makes the computing department angry.
pslogin	Login Server. SSH allows access to the analysis pool servers.
psananeh	Near experimental hall analysis server
psanafeh	Far experimental hall analysis server
psana0x0y	Alernate analysis servers. x = 1:2, y = 1:6

Table A.1: Names of the different LCLS server pools and their purposes.

Access to the LCLS computing resources and the stored data from each experiment requires you are registered with a SLAC user account. Access to the servers is achieved using SSH using either a UNIX terminal or an equivilent windows terminal application such as Putty of Cwgwin. Once access to any of the computer systems is achieved, the entire file system is accessible using the same paths across all servers. All of the files relevant to a given experiment are located in the folder **/reg/d/psdm/[INST]/[INST]xxxxx/**, where xxxxx is the 5 digit experiment number and [INST] is the 3 character code of the endstation you are using (AMO,SXR etc.). This folder contains 3 folders: hdf5, scratch and xtc. **/hdf5/** is where autogenerated HDF5 files are stored, **/scratch/** is a large scratch folder is where large files produced via analysis codes can be saved to, and **/xtc/**

is where the raw data for each run, stored as XTC files, is located. Your home folder is found at the location **/reg/neh/home/**[**username**].

A.2 Data storage format

LCLS stores all the data for a given experiment in massive binary files called XTC files. These are monolithic files, upwards of several 10s of gigabytes large for a given run. These are found in the experiment XTC folder described in the previous section. The file names use the syntax **eXXX-rYYYY-sZZ-cNN.xtc**, where XXX is a 1-3 digit number which is unique for each experiment. YYYY is a 4 digit number which corresponds to the run number used in the electronic logbook. ZZ and NN are the stream and chunk numbers. These relate to how the DAQ splits the data up between several files, generally to keep the bandwidth and file size to manageable levels. For example for an experiment using multiple cameras (high bandwidth data sources) a single stream is required per camera. For the purposes of analysis, in general there is no reason not to analyse all files of a given run.

The format has been designed primarily for speed of writing rather than pure accessibility so directly reading these files is problematic at best. Fortunately there are a number of frameworks that exist that simplify reading this data. The frameworks have a number of functions that can access different types of data, which in summary are:

Ebeam data: All data relevant to the Free electron laser itself, including shot by shot information on the electron beam energy, size, and such like.
FEE (Front End Enclosure) data: Convoluted name, but in reality is just the Gas Detector data. These measure the pulse energy of the FEL before and after attenuation. There are 4 values in total, 2 before, 2 after attenuation.
Acqiris data: This is any 1D time resolved data converted to a digital waveform using the Acqiris analogue to digital converters. This will most often be the time-of-flight data from the detectors, but may also include things like photo-diode data which have been placed in these channels. Each device has an address, eg. AmoETof-0 and each device may contain several channels (for example the AMO e-TOF device is in fact 5 different individual detectors, all with a unique channel).
EPICS data: These are so called slow variables which include all data that is not measured on a shot by shot basis. These will include things like chamber pressures, voltages and such like. Each of them is assigned a unique name. A complete list of variables can be found in the logbook entry for a given run, and the Logbook keeper for an experiment should keep track of what name relates to which experimental parameter.
Camera data : Image data from both fast and slow cameras. Each camera will have a unique address associated with it.

There are two currently supported analysis frameworks provided by LCLS, myana, a C++ based framework, and pyana, a python based framework. Since they are both based on the same C source code, much of the functionality is the same. A complete description of the analysis frameworks, including in depth user examples and function libraries can be found on the SLAC wiki, called confluence, found at:

`https://confluence.slac.stanford.edu/display/PCDS/Users`.

A.3 An overview of the Pyana analysis framework

The three analysis frameworks use the same structure and workflow for analysing the data. Since the amount of data for a given run is so large, data is processed sequentially on a shot by shot basis (or event, as it is called in the XTC), and accessing data across shots is only achievable if explicitly stored within the analysis script. A complete analysis script requires breaking down what data is needed and how often it needs to be called or analysed. In general, configuration data of the devices is called once per job (a job being an entire analysis batch, comprising one or several individual experimental runs). When performing scans, the XTC records data as part of a structure called a a calibration cycle. For variables which only change once for every step, like a delay position, these variables can be retrieved only once every cycle. Data like the actual TOF traces, machine data or detector images need to be done for every shot, and will be processed on an event by event basis. Then at the end of the run/job clean up saving the data is performed. For example, using a pyana module, we can see that a number of functions have already been built, and each of these functions is called at a different time in the analysis process. Table A.2 describes when each function is called and for what kind of task it should be used.

Function name	Purpose/Position in flow
__init__(self)	Initial configuration
beginjob(self, evt, env)	Called once at the beginning of the job
beginrun(self, evt, env)	Called at the beginning of every experimental run
begincalibcycle(self, evt, env)	Called at the beginning of every scan position
event(self, evt, env)	Called on every event (ie, every laser shot)
endcalibcycle(self, env)	Called after at the end of a scan position
endrun(self, env)	Called at the end of every run
endjob(self, env)	Called at the end of every job

Table A.2: Pyana module functions and workflow.

A.3.1 An example pyana module

Below is an example source code for a pyana module I have created which averages the analog waveforms for shots that satisfy certain photon energy and pulse energy conditions,

and saves the result to a matlab file.

```
#--------------------------------------------------------------------------
# File and Version Information:
#  $Id: template!pyana-module!py 2987 2012-02-25 03:28:58Z salnikov@SLAC.STANFORD.EDU $
#
# Description:
#  Pyana user analysis module WaveformEnergyBin...
#
#------------------------------------------------------------------------

"""User analysis module for pyana framework.

This software was developed for the LCLS project.  If you use all or
part of it, please give an appropriate acknowledgment.

@version $Id: template!pyana-module!py 2987 2012-02-25 03:28:58Z ...
     salnikov@SLAC.STANFORD.EDU $

@author Richard J. Squibb
"""

#----------------------------------
#  Module's version from SVN --
#----------------------------------
__version__ = "$Revision: 2987 $"
# $Source$

#--------------------------------
#  Imports of standard modules --
#--------------------------------
"""Modules are imported using the syntax:

import modname ------> imports all library functions of module with name "modname"
import modname.sub ----> imports just the sublibrary of "modname" with name "sub"
import modname as myname ----> like import modname, but renames the module within the ...
     code to myname. Useful for shortening convoluted library names
"""

import sys                      # Standard system functions
import logging                  # System Logging
import os                       # OS specific functions (folder manipulation etc)
import numpy                    # Numpy libary for array manipulation
import scipy                    # Matlab like functionality
import scipy.io as sio          # Matlab i/o
import matplotlib.pyplot as plt # Matlab plotting functions


#----------------------------
# Imports for other modules --
#----------------------------

#---------------------------------
# Local non-exported definitions --
#---------------------------------

# local definitions usually start with _

#------------------
# User Functions --
#------------------

# Saves a .mat file of the currently stored variables

#---------------------
#  Class definition --
#---------------------
class WaveformEnergyBin (object) :
    """Class whose instance will be used as a user analysis module. """

    #--------------------
    #  Class variables --
    #--------------------

    # usual convention is to prefix static variables with s_
    s_staticVariable = 0
```

```
73
74      #----------------
75      #  Constructor --
76      #----------------
77      def __init__ ( self, elow=0.0, ehigh=5.0, tofaddress="AmoETof-0", channel=0, ...
            plow=450.0, phigh=2000.0) :
78          """Class constructor. The parameters to the constructor are passed
79          from pyana configuration file. If parameters do not have default
80          values  here then the must be defined in a .cfg file which is specified. All ...
                parameters
81          are passed as strings, convert to correct type before use using int(), float() ...
                and such like.
82
83          elow = Lower limit for the pulse energy in mJ : default 0 mJ
84          ehigh = upper limit for the pulse energy in mJ : default 5 mJ
85          tofaddress = Address for the time of Flight Detector : default is the AMO eTofs
86          channel = acqiris channel : default is the first channel
87          plow = lower limit for the photon energy in eV: default is lower limit for AMO ...
                station 450 eV
88          phigh = higher limit for the photon energy in eV : default is lower limit for ...
                AMO station 2000 eV
89
90          """
91
92          # Acquiris modules
93          self.TOFaddress = str(tofaddress)
94          # Energy binning limits, coinvert to floats and then save to the self.struct.
95          self.elow = float(elow)
96          self.ehigh = float(ehigh)
97          # The channel which contains the data
98          self.datachannel = float(channel)
99
100         self.plow = float(plow)
101         self.phigh = float(phigh)
102         # Display these values to the user on the command prompt
103         """%d and %s display decimals and strings respectively. These are defined in
104         the brackets after the string you want to display"""
105
106         print( 'Passed values for elow = %d and Ehigh = %d' %(self.elow, self.ehigh) )
107
108     #--------------------
109     #  Public methods --
110     #--------------------
111
112     def beginjob( self, evt, env ) :
113         """This method is called once at the beginning of the job. It should
114         do a one-time initialization possible extracting values from event
115         data (which is a Configure object) or environment.
116
117         @param evt    event data object
118         @param env    environment object
119         """
120
121         # Preferred way to log information is via logging package
122         logging.info( "WaveformEnergyBin.beginjob() called" )
123
124
125     def beginrun( self, evt, env ) :
126         """This optional method is called if present at the beginning
127         of the new run.
128
129         @param evt    event data object
130         @param env    environment object
131         """
132
133         # Setup counters
134         self.counter = 0
135         self.procEvt = 0
136
137         ###################################
138         # --- User defined parameters ---
139         ###################################
140
141         self.ScratchLocation = '/reg/neh/home/rjsquibb/'      # The location to save the ...
                mat files (home folder)
142
143
144         ###########################################################
```

```
145         # --- Data extraction which only needs to be done once
146         # (eg, acquiris time info, sample interval etc.) ---
147         ############################################################
148
149         # Get run number
150         self.runNo = evt.run()
151         # Get experiment number
152         self.expNo = evt.expNum()
153         # Print info
154         print('Processing data for experiment %d, run %d' %( self.expNo, self.runNo ))
155
156         # Grab the acquiris configuration data
157         acqConfig = env.getAcqConfig(self.TOFaddress)
158
159         #Acqiris timestamp data
160
161         """try and except are structures that allow for error handling, it attempts to ...
                perform the functions
162         in the try section, if it comes across an error, then the expect functions are ...
                done instead. In this case if
163         for some reason the acquiris object cant be read, it informs the user"""
164         try :
165
166             """Different parts of the object are accessed like a struct is in matlab eg, ...
                    struct.field1"""
167             self.sampInterv = acqConfig.horiz().sampInterval()                  # Sample ...
                    interval of the trace
168             self.iMax = acqConfig.horiz().nbrSamples()                          # Number ...
                    of samples in trace
169             self.fullScale = acqConfig.vert(self.datachannel).fullScale()       # Full ...
                    vertical scale in Volts
170             self.offset = acqConfig.vert(self.datachannel).offset()             # ...
                    Vertical offset in Volts
171             self.gain = acqConfig.vert(self.datachannel).slope()                # ...
                    Vertical gain in Volts/bit
172
173             """Linspace, part of the scipy library, operate much the same as its matlab ...
                    equivilent
174             We can construct a time vector for the TOF trace using the variables ...
                    obtained above. """
175             self.T = scipy.linspace(0,self.sampInterv*(self.iMax),self.iMax)    # Time Vector
176
177         except :
178             print('Acqiris data damaged for event %d' %( self.counter ))
179
180         # Prepare the data container for the averaged waveform.
181         self.W = numpy.zeros(self.iMax,dtype=numpy.int64)
182
183         logging.info( "WaveformEnergyBin.beginrun() called" )
184
185     def begincalibcycle( self, evt, env ) :
186         """This optional method is called if present at the beginning
187         of the new calibration cycle.
188
189         @param evt    event data object
190         @param env    environment object
191         """
192
193         logging.info( "WaveformEnergyBin.begincalibcycle() called" )
194
195     def event( self, evt, env ) :
196         """This method is called for every L1Accept transition.
197
198         @param evt    event data object
199         @param env    environment object
200         """
201         # Increment event counter
202         self.counter += 1
203
204         # Reset Event damage flag to false
205         self.damageflag = False
206
207         ##############################
208         # ---Get Acquiris TOF Data---
209         ##############################
210
211         # Grab the acquiris data for channel 0
212         acqData = evt.getAcqValue(self.TOFaddress, 0, env)
```

```
213
214             try :
215                 """Since the waveform can be represented by the raw integer data, we convert ...
                        from volts back to integers to save space
216                 You can access type conversion in the numpy library eg, numpy.int16(), ...
                        numpy.double() etc."""
217                 wf = numpy.int16((acqData.waveform()+self.offset)/self.gain)   # returns a ...
                        waveform array of numpy.ndarray type.
218
219             except :
220                 print("Waveform data damaged for event %d" %( self.counter ))
221                 self.damageflag = True
222
223             ##############################
224             # ---Get Electon Beam Data---
225             ##############################
226
227             # Grab electron beam structure using evt data methods
228             ebeam = evt.getEBeam()
229
230             # Tries to read the structure and put shot variables into individual variables
231             try :
232                 EBeamCharge = ebeam.fEbeamCharge         # The electon beam total charge (nC)
233                 EBeamEnergy = ebeam.fEbeamL3Energy       # Electron beam energy           (MeV)
234                 PhotonEnergy = (EBeamEnergy**2.0)*(numpy.divide(8330.0,(13720.0**2.0)))
235
236             # If the data can't be found, print error, flag event as damaged
237             except :
238                 print "EBeam data damaged"
239                 self.damageflag = True
240
241             ##############################
242             # ---Get Gas Detector Data---
243             ##############################
244             feeGasDets = evt.getFeeGasDet()
245
246             """Numpy.shape gets the size of the array."""
247             if numpy.shape(feeGasDets) != (4,) :
248
249                 print "Gas Detector data damaged"
250                 self.damageflag = True
251
252             else :
253                 GasDetectors = feeGasDets                # The 4 gas detector values
254
255             ########################################################################
256             #  --- Add waveform to the summation if it satisfies conditions ---
257             ########################################################################
258
259             """ if structures follow much the same rules as any other language. 0 and 1 can ...
                    represent False and True as well"""
260
261             # Only if all data is undamaged
262             if self.damageflag == False:
263
264                 # Average the gas detector values
265                 """These parts access different parts of an array. Note that to get the ...
                        first two elements you need 1:3, not
266                 1:2 as in the case of matlab!!"""
267                 GasDet1 = numpy.mean(GasDetectors[1:3])
268                 GasDet2 = numpy.mean(GasDetectors[3:5])
269
270                 # Only if the pulse energy satisfies user constraints
271                 if GasDet2 ≥ self.elow and GasDet2 ≤ self.ehigh and PhotonEnergy ≥ self.plow ...
                        and PhotonEnergy ≤ self.phigh:
272
273                     # Add waveform to summation
274                     """W += wf is analogous to W = W + wf"""
275                     self.W += wf
276
277                     # Increase counter of processed events by one
278                     self.procEvt += 1
279
280             """Logical comparison functions are similar to matlab. x % y calculates ...
                    remainder of x/y, so in this
281             case we are checking to see if the processed events is an integer multiple of 100"""
282
283             if self.procEvt % 100 == 0 and self.procEvt != 0 :
```

```
284
285             print('Processed %07d events' % (self.procEvt))
286
287
288     def endcalibcycle( self, evt, env ) :
289         """This optional method is called if present at the end of the
290         calibration cycle.
291
292         @param evt    event data object
293         @param env    environment object
294         """
295
296         logging.info( "WaveformEnergyBin.endcalibcycle() called" )
297
298     def endrun( self, evt, env ) :
299         """This optional method is called if present at the end of the run.
300
301         @param evt    event data object
302         @param env    environment object
303         """
304
305         logging.info( "WaveformEnergyBin.endrun() called" )
306
307     def endjob( self, evt, env ) :
308         """This method is called at the end of the job. It should do
309         final cleanup, e.g. close all open files.
310
311         @param evt    event data object
312         @param env    environment object
313         """
314
315         """ You can also construct strings from multiple string objects just adding them ...
                 together like arrays.
316         To convert numbers to strings you use the str() function"""
317
318         print('Finished, analysis used ' + str(self.procEvt) + ' out of ' + ...
                 str(self.counter) + ' shots')
319
320         self.W = (self.W/self.procEvt)*self.gain - self.offset
321
322         """A very simple example of the plotting functions for a 2D plot."""
323
324         plt.plot(self.T,self.W)
325         plt.show()
326
327         """ The program will pause until the plot is closed, then execute the next commands.
328         To save data as a .mat file, we construct a dictionary object. A dictionary is ...
                 defined with the syntax:
329
330             dict = {key1: variable1, key2: variable2, ... , keyN: variableN }
331
332         A key is a unique name you give to the variable, and the variable is the actual ...
                 data."""
333
334         savedata = {'TimeVector': self.T, 'Waveform': self.W}
335
336         # Asks user for a save name
337         """input(message) asks for user keyboard input after displaying "message"
338         The full filename is constructed using the earlier defined scratch location and ...
                 the user input """
339         self.savename = self.ScratchLocation + str(input('Please choose a save filename'))
340         print 'Saving' + self.savename
341
342         """We can now save the dictionary using the scilab io sublibrary."""
343
344         sio.savemat(self.savename,savedata)
345
346         """ The script is now complete! """
347
348         logging.info( "WaveformEnergyBin.endjob() called" )
```

A.3.2 Creating a pyana user release

Most of the code and methods required to extract data from the XTCs using pyana already exist as part of an official release. Rather than code absolutely everything from scratch, the LCLS ICT guys have set up the software to allow the automatic creation of a basic skeleton of the code required, which you can then populate with your own analysis code. This process is referred to as creating a User Release or alternatively a test release. Creating a test release is achieved using the following bash command:

```
1 newrel ana-current myrelease
```

Where 'myrelease' is whatever name you wish to give the release. Just make sure its relatively unique. On running the newrel command it creates a folder with the name 'myrelease' which contains only a single file called SConstruct. This file should not be edited, as it is used by the compiler. We now need to create a package. A package is a series of Python modules grouped for a specific task, and these can contain as many or as few scripts as needed. To create a package perform the following commands:

```
1 cd ./myrelease
2 sit_setup
3 newpkg mypackage
```

'sit_setup' is a command that needs to be run from the release folder every time you want to do work with a particular release. Running the 'newpkg' command now creates a new folder at the location ./myrelease/mypackage and creates three new files. We now bneed to create a directory for all the source codes and scripts:

```
1 mkdir ./mypackage/src
```

A sample source module can be generated using the command:

```
1 codegen -l Pyana-module mypackage mymodule
```

Where mymodule is the name of the module you wish to create. Otherwise you can import existing modules/Scripts by dragging them into the /src directory. Once all scripts are written, they are compiled using the command:

```
1 scons
```

A.4 CASS HDF to Matlab converter

This section describes the CASS and matlab based conversion script I have written to convert data from the LCLS xtc files to .mat files. It describes how to use cass to generate an HDF5 file using the CASS framework, and then how to extract data from the HDF5 file using the CASS_hdf5parser matlab function I have written. The end of the section lists the source code for the matlab script.

A.4.1 Generating an HDF5 file using CASS

Parameter	Function
-q	Will quit CASS after it has completed processing all files. For the purposes of dumping data to hdf5, you should generally specify this parameter
-r	CASS will usually indicate the rate at which the data is processed. This option will turn off this option.
-f inifile	This specifies the path to the .ini file that configures how the data is processed and eventually written to the hdf5 file.
-o outputfile	This specifies the path and file name to the output hdf5 file which you wish to write the data to. This can be user specified.
-i txtfile	This specifies a path and file name of a text file containing the full paths to all the XTC files you wish to process.

Table A.3: Optional arguments used for running CASS

CASS is written and mainatined by the CFEL group, and as of writing the source code of the latest version may be found at:

http://www.mpi-hd.mpg.de/personalhomes/gitasg/Downloads/cass.latest.tar.gz.

Assuming a correctly compiled CASS binary, the executable is run from the command line using the command:

```
1 cass_offline
```

The optional parameters of the system are shown in table A.3. How CASS processes and writes the data is specified using a .ini configuration file. This is a simple text file that can be tailored to your particular needs. The basic flow of a CASS execution can be described as:

1. It grabs an event and all its associated data from an XTC file
2. It uses a converter to find the particular dataset we are interested in.

Converter	Function
pp100	Gets raw images from a CCD camera
pp110	Gets an Acqiris dataset for the specified detector
pp120	Gets a specified beam line variable
pp130	Gets a specified EPICs variable
pp1001	Dumps postprocessors to an HDF5 file.

Table A.4: List of CASS Postproccessors relevant to HDF5 file creation.

3. It processes that data in some way for the user using one or more Postprocessors.

The purpose of the ini file is to define using a set of rules which converters and processors we wish to use and on what data they should be used on. These are the modules that interpret data from the XTC file and find the data that we are interested in. There are 5 converters in total:

Machine - Epics and beam line data
Acqiris - Acqiris digitiser data. This will often be where Time of flight data comes in.
Acqiris - Acqiris data captured by a Time to Digital converter
CCD - camera image data
pnCCD - pnCCD image data

A Postprocessor is an individual module that performs an individual function. Postprocessors can be combined with each other to perform more complex tasks. Each postprocessor has a unique numerical ID which is used to identify it when coding the ini file, and will also have optional arguments and parameters that allow you to tailor it's behaviour to your needs. The number of Postprocessors is too large to describe in detail in this guide, however table A.4 lists important ones for HDF5 data generation.

A.4.2 Example ini file for configuring CASS

```
;Call converters for acqiris and beamline/epics data
[Converter]
Used = Acqiris, Machine

;Intensity Data
[PostProcessor]
In_11/ID=120
In_11/ConditionName=DefaultTrueHist
In_11/VariableName=f_11_ENRC
[PostProcessor]
In_12/ID=120
In_12/ConditionName=DefaultTrueHist
In_12/VariableName=f_12_ENRC
```

```
[PostProcessor]
In_21/ID=120
In_21/ConditionName=DefaultTrueHist
In_21/VariableName=f_21_ENRC
[PostProcessor]
In_22/ID=120
In_22/ConditionName=DefaultTrueHist
In_22/VariableName=f_22_ENRC

;Magnetic Bottle TOF
[PostProcessor]
MBEStof/ID=110
MBEStof/ConditionName=DefaultTrueHist
MBEStof/InstrumentId=5

; Dump HDF5s
[PostProcessor]
HDF5Dump/ID = 1001
HDF5Dump/ConditionName=DefaultTrueHist
```

In this case, CASS reads 5 different XTC datasets (4 beamline variables, the Gas Detector values, and 1 Acqiris instrument, in this case a magnetic bottle trace) using the pp120 and pp110 Postprocessors and then we use pp1001 (the hdf5 dump postprocessor) to write them to an HDF5 file.

A.4.3 CASS_hdf5parser conversion script

Parameter	Function
{DataPath}	Path to the hdf5 dataset excluding the shot folder.
{ReadColumns}	Columns within that dataset you wish to extract. This is the same syntax as Matlab, so for example, 1 will get the first column, 1:2 will get the first two columns or : will get all columns.
{OuputName}	The name you want the variable to be called in the Matlab structure. This is arbitrary.
{OutputColumns}	The columns of the variable {OutputName} you want the data written to. These can be whatever you like but they must be the same size as {ReadColumns}
{ShotRule}	Either 'single' for writing only for a single shot or 'all' if you want to write for all shots.

Table A.5: List of parameters for the CASS_hdf5parser matlab function

CASS_hdf5parser is a matlab function I have designed to dump all the datasets written to an hdf5 file using CASS's HDF5 postprocessor (pp1001) to a matlab structure. This function was designed as an extremely simple method to get all the data within an HDF5 file produced by CASS, and in its simplest use requires absolutely no knowledge by the user of its exact data structure, only that it was produced using CASS.

The syntax used to call the script is **CASSdata = CASS_hdf5parser(hdf5file,*shots*,*userpars*)**. Italics denote optional arguments. This will dump all datasets to variables specified in the file 'userpars' for the shot numbers specified by the variable 'shots' found in the HDF5 file 'hdf5file' into the structure 'CASSdata'. The parameter file is a text file which follows the following syntax:

These parameters are specified in a column format within the text file:

{DataPath1} {ReadColumns1} {OutputName1} {OutputColumns1} {Shotrule1}
{DataPath2} {ReadColumns2} {OutputName2} {OutputColumns2} {Shotrule2}
...
{DataPathN} {ReadColumnsN} {OutputNameN} {OutputColumnsN} {ShotruleN}

Where the parameters are specified as described in table A.5

A.4.4 Source Code

```
function CASSdata  = CASS_hdf5parser(hdf5file,varargin)

%CASS_HDF5PARSER Parses an HDF5 file produced by CASS and sums the
%datasets
%   This function takes an HDF5 file produced using the CASS hdf5dump
%   postprocessor and produces a structure that contains all the
%   datasets found within the HDF5 file.
%
%   CASSdata = CASS_hdf5parser(hdf5file) will dump all detected datasets
%   from all shots in the HDF5 file 'hdf5file' into the structure
%   'CASSdata'.
%
%   CASSdata = CASS_hdf5parser(hdf5file,'all') will will dump all detected
%   datasets from all shots in the HDF5 file 'hdf5file' into the structure
%   'CASSdata'.
%
%   CASSdata = CASS_hdf5parser(hdf5file, shots) will dump all detected
%   datasets in the HDF5 file 'hdf5file' from the shots specifed in the
%   vector 'shots' to the structure 'CASSdata'. This can be used for large
%   datasets or for users with memory limitations, as one can limit the
%   size of the output structure this way.
%
%   CASSdata = CASS_hdf5parser(hdf5file,'ask') will ask the user via a
%   dialog to specify which shots should be dumped. This is useful if the
%   user is unsure of the number of shots in the hdf5 file.
%
%   CASSdata = CASS_hdf5parser(hdf5file,shots,userpars) will dump all
%   datasets to variables specified in the file 'userpars' for the shot
%   numbers specified by the variable 'shots' found in the HDF5 file
%   'hdf5file' into the structure 'CASSdata'.
%
%   Copyright Richard Squibb 2011
%   Version b.1.2 - 04 August 2011
%   ------------------------------------------------------------------------

%   Gets the full hdf5 file structure. From this we can parse the rest of
%   the hdf5 file

hdf5fid = H5F.open(hdf5file);
ticID = tic;
disp('Getting hdf5 hierarchy structure');

switch nargin

  % In the case the HDF5 structure is not specified
  case {1,2}
    % Evaluates the HDF5 structure
    hdf5_structure = CASS_hdf5struct(hdf5file);

  otherwise

    % Checks to see if character is a string
    if (ischar(varargin{2}) == 1)

      % If it is, checks the argument is valid
      if (strcmp('eval',varargin{2}) == 1)
```

```
57
58          % Evaluates the HDF5 structure anyway
59          hdf5_structure = CASS_hdf5struct(hdf5file);
60
61        else
62          %Throws an Error
63          error('Not a valid HDF5 structure argument.');
64
65        end
66
67        % If it is not a string, it sets the structure using varargin
68      else
69
70        hdf5_structure = varargin{2};
71
72      end
73  end
74
75  %   Gets the number of shots from the size of the group (num folders - 1)
76  eMax = hdf5_structure.eMax;
77
78  %   Shot number definition and processing
79  %   ====================================
80
81  %   Gets the shots to be analysed based on user input and the
82  %   variable 'nargin'
83  switch nargin
84
85    % The default case, all shots are used
86    case 1
87      usedshots = 1:eMax;
88      [~, eUsed] = size(usedshots);
89
90      % The case used if the shot numbers are user specified
91    case {2,3,4}
92      %   If the input is a character, it checks to ensure the input is
93      %   a character type, and assigns the variables accordingly.
94      if ischar(varargin{1}) == 1
95
96        switch varargin{1}
97
98          %   Creates a dialog that will ask the user to specify the
99          %   shots to be used.
100
101         case 'ask'
102
103           usedshots = inputdlg(['Please choose which shots to dump. '...
104             ,'Number of shots is ',num2str(eMax),': ']);
105
106           eval(['usedshots =',usedshots{1}]);
107
108           if isnumeric(usedshots) == 0
109
110             error('Not a valid input. Shots should be numeric');
111
112           end
113
114           [dummy, eUsed] = size(usedshots)
115
116          %   Uses all shots. Same behavior as case 1, but for cases
117          %   where the varrules are specified.
118
119         case 'all'
120
121           usedshots = 1:eMax;
122           [dummy, eUsed] = size(usedshots);
123
124         otherwise
125
126           error('Unexpected value for input "shots"');
127
128       end
129
130     end
131
132     %   If the input is numeric, it simply uses the number specified.
133     if isnumeric(varargin{1}) == 1
134
```

```
135         usedshots = varargin{1};
136         [dummy, eUsed] = size(usedshots);
137
138       end
139
140       %   Checks to see if the shot numbers are within range.
141       if max(usedshots) > eMax || min(usedshots) < 1
142
143         % Else it will throw an error informing the user it is out of
144         % range of the valid shot numbers.
145         error('One or more shots are out of range!');
146
147       end
148
149     otherwise
150       % In the case there are more inputs than expected, an error will be
151       % thrown informing the user.
152       error('Unexpected number of inputs!');
153
154   end
155
156   % Sorts the shot numbers
157   usedshots = sort(usedshots);
158
159
160   %   Variable/dataset Processing
161   %   ===========================
162
163
164   %  This section gets the dataset paths to be processed, and the variables
165   %  they will be written to based on the path names.
166   %  In the case of no rules specified, the parser will find the dataset
167   %  paths and generate automatic variable names for matlab
168
169   % Gets the shotnames for this particular run
170
171   ITinput.eUsed = eUsed;
172   ITinput.start = usedshots(1);
173   ITinput.shot = ITinput.start;
174   ITinput.index = 1;
175
176   % Open the group.
177   gid = H5G.open(hdf5fid,'/');
178   % Iterate over all members of the group.
179   [status, idx_out, ITоutput] = ...
          H5L.iterate(gid,'H5_INDEX_NAME','H5_ITER_INC',ITinput.start,@H5Literator_func,ITinput);
180
181   %   Close the group
182   H5G.close(gid);
183
184   %   Gets the shotnames
185   shotnames = ITоutput.shotnames;
186   %   Gets the datatypes
187   LCLSdatatypes = hdf5_structure.LCLSdatatypes;
188   %   Gets the datapaths
189   LCLSdatapaths = hdf5_structure.LCLSdatapaths;
190
191   %   Gets the number of 1st level variables the hdf5 folder has
192   [n_variables, ~] = size(LCLSdatapaths);
193
194   %   Creates formatted names for structure names
195   LCLSvarnames = strrep(LCLSdatapaths,'/','_');
196
197
198   %   Gets number of paths from the size of the array
199   [n_paths,~] = size(LCLSdatapaths);
200
201   %   This part of the function loads any user defined rules for input/output
202   %   processing if they are specified
203   switch nargin
204
205     %   In the case of the userpars being undefined, the function does not
206     %   use the variables and therefore does not load them
207     case {1,2,3}
208
209       %%%%  Dummy case: Does nothing
210
211     %   In the case the varrules being defined, the function simply loads
```

```
212     %   from the text file the relevant parameters
213     case 4
214
215       %   Open the user parameter file, get the variables and then close
216       %   the file.
217       userpars = varargin{3};
218       fid = fopen(userpars);
219       datapathcell = textscan(fid,'%s %s %s %s %s %s');
220       fclose(fid);
221
222       %   Put the parameters into individual variables.
223       userpars_paths = datapathcell{1,1};
224       userpars_incol = datapathcell{1,2};
225       userpars_vars = datapathcell{1,3};
226       userpars_outcol = datapathcell{1,4};
227       userpars_outtype = datapathcell{1,5};
228       userpars_datatype = datapathcell{1,6};
229
230       %   Gets the number of defined variables from the size of the
231       %   userpars variable
232       [n_userpaths, ¬] = size(userpars_paths);
233
234
235       %   Finds the indices of the variables that match the user
236       %   specified dataset outputs.
237       for i = 1:n_userpaths
238
239         k = strfind(LCLSdatapaths,userpars_paths{i,1});
240         emptyk = cellfun(@isempty,k);
241         k(emptyk) = {0};
242         userpars_indices(i) = find(cell2mat(k)==1);
243       end
244
245     otherwise
246
247       error('Unexpected number of input variables!')
248
249   end
250
251   %   This part of the function is reponsible for writing the datasets in the
252   %   HDF5 file to matlab variables. This is all datasets in the case of
253   %   userpars being undefined, or the user specified variables in the case
254   %   of them being defined
255   %   ================================================================
256   %   ================================================================
257
258   %   Sets a counter that is used to execute some commands at the start and
259   %   end of the shot loop
260   counter = 1;
261
262   %   Displays message at the start of the dumping process
263   disp('Analysis complete. Dumping datasets...');
264   fprintf(1,'Percentage of shots complete:     ');
265   switch nargin
266
267     %   In the case the datasets and their output are not user specified,
268     %   the function will output all datasets to variables that are
269     %   automatically named by the programming.
270
271     case {1,2,3}
272
273       %   This for loop iterates over all shots specified by the user or all
274       %   shots in the hdf5 file
275       for i = 1:eUsed
276
277         %    This for loop iterates over all variables found in the hdf5 file
278         for j = 1:n_paths
279
280           %   Gets the path to the variable
281           temppath = [shotnames{i},'/',LCLSdatapaths{j}];
282
283           switch LCLSdatatypes{j}
284
285             case 'H5T_STRING'
286
287               % Does nothing, may be implemented if I can figure out how
288               % to read strings from H5 files. At the moment this is here
289               % to stop the program breaking.
```

```
290
291             otherwise
292
293               %   Gets datatype
294               tempdata = hdf5read(hdf5file,temppath);
295               structname = LCLSvarnames{j};
296
297               % Prepares full data container if it is the first shot
298               if counter == 1
299
300                 %   Gets the size of the dataset
301                 [datasize_1, datasize_2] = size(tempdata);
302                 data_assigned = zeros(eUsed,datasize_1,datasize_2);
303                 eval(['data.',structname,' = data_assigned;']);
304
305               end
306
307               %   Assigns the data to the relevant structure
308
309               eval(['data.',structname,'(',num2str(i),',:,:) = tempdata;']);
310
311               %   If it is the last shot, it compresses the data down
312               if counter == eUsed
313
314                 eval(['data.',structname,' = squeeze(data.',structname,');']);
315
316               end
317
318           end
319
320         end
321
322         %   Raises the counter by one
323         counter = counter + 1;
324
325         %   Displays completion percentage
326         percentage = ceil((i/eUsed)*100);
327         fprintf(1,'\b\b\b%03d',percentage);
328
329       end
330
331     % In the case of the user parameters being specified, it does a more
332     % complex assignment/writing routine
333     case 4
334
335       %   This for loop iterates over all shots specified by the user or all
336       %   shots in the hdf5 file
337       for i = 1:eUsed
338
339         %    This for loop iterates over all variables found in the hdf5 file
340         for j = 1:n_userpaths
341
342           m = userpars_indices(j);
343
344           %   Gets the path to the variable
345           temppath = [shotnames{i},'/',LCLSdatapaths{m}];
346
347           switch LCLSdatatypes{m}
348
349             case 'H5T_STRING'
350
351               % Does nothing, may be implemented if I can figure out how
352               % to read strings from H5 files. At the moment this is here
353               % to stop the program breaking.
354
355             otherwise
356
357               %   Gets data
358               dataID = H5D.open(hdf5fid,temppath);
359               tempdata = H5D.read(dataID);
360               H5D.close(dataID);
361               eval(['datatowrite = ',userpars_datatype{j,1},...
362                   '(tempdata(',userpars_incol{j,1},',:));']);
363               structname = userpars_vars{j,1};
364
365               %   Gets the size of the dataset
366               [datasize_1, datasize_2] = size(datatowrite);
367
```

```
368             %   Checks whether it is to write the data for a
369             %   single shot or all shots
370             outtype = userpars_outtype{j};
371
372             if (strcmp('all',outtype) == 1)
373
374               eSize = eUsed;
375
376             elseif (strcmp('single',outtype) == 1)
377
378               eSize = 1;
379
380             end
381
382
383             %   If it is the first shot, does certain
384             %   operations to prepare the data containers
385             if counter == 1
386
387               outcol{j,1} = userpars_outcol{j};
388
389               %   If it is a single column of data it assigns
390               %   the relevant output column zeros
391
392               if datasize_1 == 1
393
394                 eval(['data.',structname,'(1:eSize,',outcol{j,1},',1:datasize_2) = ...
                        ',userpars_datatype{j,1},'(0);']);
395
396                 %   If the output is an array it prealocates
397                 %   the relevant space.
398               else
399
400                 switch outcol{j,1}
401
402                   case ':'
403
404                     eval(['data.',structname,'(1:eSize,1:datasize_1,',...
405                       '1:datasize_2) = ',userpars_datatype{j,1},'(0);']);
406
407                   otherwise
408
409                     eval(['data.',structname,'(1:eSize,',outcol{j,1},...
410                          ',1:datasize_2) = ',userpars_datatype{j,1},'(0);']);
411                 end
412               end
413
414             end
415
416             %   Writes the data on shot 1 always, else it will
417             %   only write if the user has specified  'all'.
418             if (counter == 1) || (strcmp('all',outtype) == 1)
419
420               %   Assigns the data to the relevant structure
421               if datasize_1 == 1
422
423                 eval(['data.',structname,'(',num2str(i),',',outcol{j,1},...
424                      ',:) = datatowrite;']);
425
426               else
427
428                 eval(['data.',structname,'(',num2str(i),...
429                      ',:,:) = datatowrite;']);
430
431               end
432
433             end
434
435             %   If it is the last shot, it compresses the data down
436             if counter == eUsed
437
438               eval(['data.',structname,' = squeeze(data.',structname,');']);
439
440             end
441
442             %   Clears used variables in case of assignment
443             %   errors on the next loop.
444             clear tempdata datatowrite data_assigned
```

```
445
446           end
447
448         end
449
450         %   Raises the counter by one
451         counter = counter + 1;
452
453         %   Displays completion percentage
454         percentage = ceil((i/eUsed)*100);
455         fprintf(1,'\b\b\b%03d',percentage);
456
457       end
458
459     otherwise
460
461   end
462
463   %   Data cleanup
464   data.eNames = shotnames';
465   data.eMax = eUsed;
466   data.Datapaths = LCLSdatapaths;
467   data.Datatypes = LCLSdatatypes';
468
469   %   Outputs the data structure
470   CASSdata = data;
471
472   % Close HDF files
473   H5F.close(hdf5fid);
474
475   %   Displays done message
476   disp('......Dump complete!');
477   toc(ticID);
478
479   end
480
481   % This is the iterative function for the shot names
482   function [status data]= H5Literator_func(~,name,data)
483
484   data.shotnames{data.index} = name;
485
486   if data.shot ≥ (data.start + data.eUsed - 1)
487     status = 1;
488   else
489     status = 0;
490   end
491
492   data.index = data.index + 1;
493   data.shot = data.shot +1;
494   end
```

—

A.5 Pyana converter

This section describes how to set up and run MatConverter.py, the pyana based converter script I have written.

A.5.1 MatConverter.py

The MatConverter.py module has been designed for ease of use and should dump most data of interest relevant to AMO experiments to .mat files that can be easily read by Matlab or the Open source versions like Octave or SciLab. The MatConverter.py script needs to be placed in the /src directory of a pyana release. Assuming pyana is compiled, the script is run using the command:

```
1 pyana –c MatConverter.cfg /path/to/xtc/
```

Where MatConverter.cfg is a configuration file as described below, and /path/to/xtc/ is the full folder path to the xtc file to be converted. The pyana module has several different extractors which each extract a different part of the XTC file.

Parameter	Type	Function and syntax
use_ebeamdata	Bool	Electron beam data such as electron energy, bunch charge, current, etc. Default is False. Turn it off for runs where the FEL is off!
use_phasecavity	Bool	Phase cavity jitter timings and measured charges. Default is False. Turn it off for runs where the FEL is off. (eg, IR only runs)
use_epics	Bool	Convert specified EPICS variables. Default is False.
use_gasdetectors	Bool	Gas Detector (x-ray intensity) data. Default is False. Turn it off for runs where the FEL is off! (eg, IR only runs)
use_etof	Bool	Any/all electron TOF acqiris waveforms. Additional configuration required. Default is False.
use_itof	Bool	Any/all electron TOF acqiris waveforms. Additional configuration required. Default is False.
use_cameras	Bool	Any cameras that image on a shot by shot basis. Additional configuration required. Default is False.
shotsperfile	Int	The number of shots to dump per mat file.
savelocation	str	The base folder to which the data will be saved. Default is the user home directory.
epicsnames	struct	List of EPICS variable names and the names they will be given in the mat files. synatx is {'MatVarName1': 'EpicVarName1','MatVarName2': 'EpicVarName2',...,'MatVarNameN': 'EpicVarNameN'}
etof_channels	int	Channels of the etof device to use. Can either be a single value or a list in square brackets []
itof_channels	int	Channels of the itof device to use. Can either be a single value or a list in square brackets []
camsources	struct	List of camera addresses to use. Synatx is {'MatVarName1': 'Address1','MatVarName2': 'Address2',...,'MatVarNameN': 'AddressN'}

Table A.6: List of configuration parameters for the MatConverter.py pyana module

A.5.2 Example .ini configuration file

```
# Change the name of the pkg (currently mat_conv_pkg) to your package name
# if you made a custom package instead of the default installation

[pyana]
# ----------------------
# DONT EDIT THESE ONES!
# ----------------------
modules = mat_conv_pkg.MatConverter
num-cpu = 1
skip-events = 0
#----------------------

[my_ana_pkg.MatConverter]

# Decide which extractors to use (True or False)

use_ebeamdata = True
use_phasecavity = True
use_epics = True
use_gasdetectors = True
use_cameras = True
use_etof = True
use_itof = False

# User configuration options
shotsperfile = 1000
savelocation = /reg/d/psdm/amo/amo43912/scratch/testdata/

# EPICS variable configuration. Keep this definition on a single line.
epicnames = {'hfpPressure': 'AMO:HFP:GCC:03:PMON'}

# What TOF channels to use on each instrument. Single channel can be a single number,
#list should be enclosed by square brackets, separated by commas. Count from zero.

#etof_channels = 0
#itof_channels = 0

# Addresses of the TOF detectors
etof_address = AmoETof-0
itof_address = AmoITof-0

# Camera variable configuration. Keep this definition on a single line.
camsources = {'VMI': 'AmoVmi-0|Opal1000-0'}
```

A.5.3 Source Code

```
#--------------------------------------------------------------------------
# File and Version Information:
#  $Id: template!pyana-module!py 2987 2012-02-25 03:28:58Z salnikov@SLAC.STANFORD.EDU $
#
# Description:
#  Pyana user analysis module MatConverter...
#
#------------------------------------------------------------------------

"""User analysis module for pyana framework.

This software was developed for the LCLS project.  If you use all or
part of it, please give an appropriate acknowledgment.

@version $Id: template!pyana-module!py 2987 2012-02-25 03:28:58Z ...
     salnikov@SLAC.STANFORD.EDU $

@author Richard J. Squibb
"""

#---------------------------------
#  Module's version from SVN --
#---------------------------------
__version__ = "$Revision: 2987 $"
# $Source$

#--------------------------------
#  Imports of standard modules --
#--------------------------------
import sys
import logging


#-----------------------------
# Imports for other modules --
#-----------------------------

import pyana             # Pyana return codes
import os                # OS specific functions (folder manipulation etc)
import numpy             # Numpy libary for array manipulation
import scipy             # Matlab like functionality
import scipy.io as sio   # Matlab input/output functions


#----------------------------------
# Local non-exported definitions --
#----------------------------------

# local definitions usually start with _

#--------------------
# User Functions --
#--------------------

# Saves a .mat file of the currently stored variables
def savematfile ( self ) :

    # Prepare data dictionary (equivilent to matlab structure)
    print 'Preparing data dictionary'

    # Find number of shots in the file
    self.eMax = self.procEvtThisFile

    # Populates dictionary structure to be saved to the file
    self.data['eMax'] = numpy.int16(self.eMax)

    # Electron beam data
    if self.use_ebeamdata :

        # Save data to dictionary
        self.data['EBeamCharge'] = self.EBeamCharge
        self.data['EBeamEnergy'] = self.EBeamEnergy
        self.data['EBeamPosX'] = self.EBeamPosX
        self.data['EBeamPosY'] = self.EBeamPosY
        self.data['EBeamAngX'] = self.EBeamAngX
        self.data['EBeamAngY'] = self.EBeamAngY
        self.data['EBeamCurrent'] = self.EBeamCurrent

```

```
78          # Cleanup
79          del self.EBeamCharge
80          del self.EBeamEnergy
81          del self.EBeamPosX
82          del self.EBeamPosY
83          del self.EBeamAngX
84          del self.EBeamAngY
85          del self.EBeamCurrent
86
87      # Phase Cavity Data
88      if self.use_phasecavity :
89
90          # Save data to dictionary
91          self.data['PCTime1'] = self.PCTime1
92          self.data['PCTime2'] = self.PCTime2
93          self.data['PCCharge1'] = self.PCCharge1
94          self.data['PCCharge2'] = self.PCCharge2
95
96          # Cleanup
97          del self.PCTime1
98          del self.PCTime2
99          del self.PCCharge1
100         del self.PCCharge2
101
102     # eTOF Waveform Data
103     if self.use_eTOF :
104
105         for ch in self.eTOF_channels :
106             exec 'self.eTOF' + str(ch) +'[\'W\'] = self.eW' + str(ch)
107             exec 'self.eTOF' + str(ch) +'[\'horpos\'] = self.ehorpos' + str(ch)
108             exec 'self.data[\'eTOF' + str(ch) + '\'] = self.eTOF' + str(ch)
109             exec 'del self.eW' + str(ch)
110
111     # iTOF Waveform Data
112     if self.use_iTOF :
113
114         for ch in self.iTOF_channels :
115             exec 'self.iTOF' + str(ch) +'[\'W\'] = self.iW' + str(ch)
116             exec 'self.iTOF' + str(ch) +'[\'horpos\'] = self.ihorpos' + str(ch)
117             exec 'self.data[\'iTOF' + str(ch) + '\'] = self.iTOF' + str(ch)
118             exec 'del self.iW' + str(ch)
119
120     if self.use_cameras :
121
122         for cam in range(self.ncameras) :
123             exec 'self.' + self.camKeys[cam] + '[\'frames\'] = self.' + ...
                      self.camKeys[cam] + 'frames'
124             exec 'self.data[\'' + self.camKeys[cam] + '\'] = self.' + self.camKeys[cam]
125             exec 'del self.' + self.camKeys[cam] + 'frames'
126
127     # Gas detector data
128     if self.use_gasdetectors :
129
130         # Save Gas Detector data to struct
131         self.data['GasDetector'] = self.GasDetectors
132         # Cleanup
133         del self.GasDetectors
134
135     # All Epics variables
136     if self.use_EPICS :
137
138         for variable in range(len(self.epicsKeys)) :
139
140             # Puts EPICS variable into data array.
141             exec 'self.data[\'' + self.epicsKeys[variable] + '\'] = self.' + ...
                      self.epicsKeys[variable]
142
143             # Cleanup
144             exec 'del self.' + self.epicsKeys[variable]
145
146     # Formats counters into leading zero decimals.
147     expStr = '%01d' %(self.expNo)
148     runStr = '%04d' %(self.runNo)
149     matStr = '%03d' %(self.nMats)
150
151     # Constructs foler for the run using the scratch folder and the run number
152     folderStr = self.ScratchLocation + 'e' + expStr + '-r' + runStr + '/'
153
```

```
154       # Creates folder for the run if it does not exit
155       if not os.path.exists(folderStr):
156           os.makedirs(folderStr)
157
158       # Constructs a name for the mat file to be saved under.
159       self.savename = folderStr + 'e' + expStr + '-r' + runStr + '-' + matStr + '.mat'
160       print 'Saving' + self.savename
161
162       # Saves .mat file using scipy matlab interface. The mats are not compressed as this
163       # increases the save time by a factor of 10. Can be activated if required though.
164       sio.savemat(self.savename,self.data)
165
166       # Delete data structure
167       del self.data
168
169
170
171   # Creates empty data fields that can be populated using .append method
172   def cleardatafields ( self ) :
173
174       # Create empty data structure
175       self.data = {}
176
177       # -------------------------
178       # -- Create empty lists --
179       # -------------------------
180
181       # EBeam Data
182       if self.use_ebeamdata :
183
184           self.EBeamCharge = []
185           self.EBeamEnergy = []
186           self.EBeamPosX = []
187           self.EBeamPosY = []
188           self.EBeamAngX = []
189           self.EBeamAngY = []
190           self.EBeamCurrent = []
191
192       # Phase Cavity data
193       if self.use_phasecavity :
194
195           self.PCTime1 = []
196           self.PCTime2 = []
197           self.PCCharge1 = []
198           self.PCCharge2 = []
199
200       # eTOF Waveforms
201       if self.use_eTOF :
202           for channel in self.eTOF_channels :
203               exec 'self.eW' + str(channel) + ' = []'
204               exec 'self.ehorpos' + str(channel) + ' = []'
205
206       # iTOF Waveforms
207       if self.use_iTOF :
208           for channel in self.iTOF_channels :
209               exec 'self.iW' + str(channel) + ' = []'
210               exec 'self.ihorpos' + str(channel) + ' = []'
211
212       # Cameras
213       if self.use_cameras :
214           for camera in range(self.ncameras) :
215               exec 'self.' + self.camKeys[camera] + 'frames = []'
216
217       # Gas Detectors
218       if self.use_gasdetectors :
219
220           self.GasDetectors = []
221
222       # Epics autogenerator
223       if self.use_EPICS :
224
225           for variable in range(len(self.epicsKeys)) :
226
227               codetoexec = 'self.' + self.epicsKeys[variable] + ' = []'
228               exec codetoexec
229
230   #--------------------
231   #  Class definition --
```

```
232 #--------------------
233 class MatConverter (object) :
234     """Class whose instance will be used as a user analysis module. """
235
236     #--------------------
237     #  Class variables --
238     #--------------------
239
240     # usual convention is to prefix static variables with s_
241     s_staticVariable = 0
242
243     #----------------
244     #  Constructor --
245     #----------------
246     def __init__ ( self,
247                    savelocation = '~/',
248                    use_ebeamdata = 'False',
249                    use_phasecavity = 'False',
250                    use_epics = 'False',
251                    use_gasdetectors = 'False',
252                    use_cameras = 'False',
253                    use_etof = 'False',
254                    etof_channels = '[]',
255                    etof_address = 'AmoETof-0',
256                    use_itof = 'False',
257                    itof_channels = '[]',
258                    itof_address = 'AmoITof-0',
259                    shotsperfile = 1000,
260                    epicnames = {},
261                    camsources = {} ) :
262         """Class constructor. The parameters to the constructor are passed
263         from pyana configuration file. If parameters do not have default
264         values  here then the must be defined in pyana.cfg. All parameters
265         are passed as strings, convert to correct type before use.
266         """
267
268         # User configuration options
269         self.filesize = int(shotsperfile)               # The number of shots per mat ...
              file. Reduce or increase depending on waveform size
270         self.ScratchLocation = savelocation             # Folder to save the files as ...
              specified
271
272         # Inform user of the settings so far
273         print '\nSaving %d shots per .mat file in folder %s\n' %(self.filesize, ...
              self.ScratchLocation)
274
275         # ------------------------------------------------
276         # -- Decide what data to dump based on config file --
277         # ------------------------------------------------
278
279         if use_ebeamdata == 'True' :
280             self.use_ebeamdata = True
281             print 'EBeamData will be dumped.'
282         else :
283             self.use_ebeamdata = False
284             print 'EBeamData will NOT be dumped.'
285
286         # Phase Cavity Data
287         if use_phasecavity == 'True' :
288             self.use_phasecavity = True
289             print 'Phase Cavity Data will be dumped.'
290         else :
291             self.use_phasecavity = False
292             print 'Phase Cavity Data will NOT be dumped.'
293
294         # Gas Detector Data
295         if use_gasdetectors == 'True' :
296             self.use_gasdetectors = True
297             print 'Gas Detector Data will be dumped.'
298         else :
299             self.use_gasdetectors = False
300             print 'Gas Detector Data will NOT be dumped.'
301
302         # ETOF acqiris data
303         if use_etof == 'True' :
304             self.use_eTOF = True
305             print 'eTOF acqiris Data will be dumped'
306             exec 'self.eTOF_channels = ' + etof_channels
```

```
307             else :
308                 self.use_eTOF = False
309                 print 'eTOF acqiris Data will NOT be dumped'
310 
311             # ITOF acqiris data
312             if use_itof == 'True' :
313                 self.use_iTOF = True
314                 print 'iTOF acqiris Data will be dumped'
315                 exec 'self.iTOF_channels = ' + itof_channels
316             else :
317                 self.use_iTOF = False
318                 print 'iTOF acqiris Data will NOT be dumped'
319 
320             # Configure EPICS names and variable IDs if neccessary
321             if use_epics == 'True' :
322                 self.use_EPICS = True
323             else :
324                 self.use_EPICS = False
325 
326             # Checks to see if any epics variables have been defined
327             if not epicnames :
328 
329                 self.use_EPICS = False
330 
331             # If so, it sorts the keys into a list and displays the
332             # variables to be dumped to the user
333             if self.use_EPICS :
334 
335                 exec 'self.epicsinfo = ' + epicnames
336 
337                 # Print the names of the epics variables
338                 self.epicsKeys = self.epicsinfo.keys()
339 
340                 for a in range(len(self.epicsKeys)) :
341 
342                     print 'Recording EPICS variable ' + self.epicsinfo[self.epicsKeys[a]] + ...
                            ' as variable ' + self.epicsKeys[a]
343 
344             else :
345 
346                 print 'No EPICS variables defined in the Config file.'
347 
348             # Sort camera sources
349             if use_cameras == 'True' :
350                 self.use_cameras = True
351             else :
352                 self.use_cameras = False
353 
354             # Checks to see if any camera addresses have been defined
355             if not camsources :
356 
357                 self.use_cameras = False
358 
359             # If so, it sorts the keys into a list and displays the
360             # variables to be dumped to the user
361             if self.use_cameras :
362 
363                 exec 'self.caminfo = ' + camsources
364 
365                 # Print the names of the epics variables
366                 self.camKeys = self.caminfo.keys()
367                 self.ncameras = len(self.camKeys)
368 
369                 # Show user configuration of EPICS variables
370                 for a in range(self.ncameras) :
371 
372                     print('Recording Camera with address ' + self.caminfo[self.camKeys[a]] + ...
                            ' as variable ' + self.camKeys[a])
373 
374             else :
375 
376                 print 'No Camera addresses defined in the Config file.'
377 
378 
379 
380             # Acquiris modules
381             self.eTOFaddress = etof_address
382             print( "eTOF address is %s" % ( self.eTOFaddress ) )
```

```
383             self.iTOFaddress = itof_address
384             print( "iTOF address is %s" % ( self.iTOFaddress ) )
385 
386         #--------------------
387         #  Public methods --
388         #--------------------
389 
390         def beginjob( self, evt, env ) :
391             """This method is called once at the beginning of the job. It should
392             do a one-time initialization possible extracting values from event
393             data (which is a Configure object) or environment.
394 
395             @param evt    event data object
396             @param env    environment object
397             """
398 
399             # Preferred way to log information is via logging package
400             logging.info( "MatConverter.beginjob() called" )
401 
402 
403         def beginrun( self, evt, env ) :
404             """This optional method is called if present at the beginning
405             of the new run.
406 
407             @param evt    event data object
408             @param env    environment object
409             """
410 
411             # Setup counters
412             self.counter = 0            # Event counter
413             self.procEvt = 0            # Number of useful events
414             self.procEvtThisFile = 0    # Number of useful events for the given file
415             self.nMats = 0              # Number of .mat files saved
416             self.forcequit = False      # Fatal error flag
417 
418             ###################################
419             # --- User defined parameters ---
420             ###################################
421 
422             self.datachannel = 0        # Acqiris channel of interest
423 
424             ######################################################################
425             # --- Data extraction which only needs to be done
426             # --- once (eg, acquiris time info, sample interval etc.)
427             ######################################################################
428 
429             # Get run number
430             self.runNo = evt.run()
431             # Get experiment number
432             self.expNo = evt.expNum()
433             # Print info
434             print '\nProcessing data for experiment %d, run %d' %( self.expNo, self.runNo )
435 
436             # ----------------------------------------
437             # -- Grab the acquiris configuration data --
438             # ----------------------------------------
439 
440             # eTOF configurations
441             if self.use_eTOF :
442 
443                 # Get configuration object
444                 eTOFConfig = env.getAcqConfig(self.eTOFaddress)
445 
446                 try :
447 
448                     sampInterv = eTOFConfig.horiz().sampInterval()*1e9                  ...
                            # Sample interval of the trace in nanoseconds
449                     iMax = eTOFConfig.horiz().nbrSamples()                              ...
                            # Number of samples in the trace
450                     nbrChannels = eTOFConfig.nbrChannels()                              ...
                            # Number of channels in the device
451                     T = scipy.linspace(0,sampInterv*(iMax),iMax)                        ...
                            # Time Vector
452 
453                     # If the channels have not been defined (empty array) then autogenerate
454                     # based on the number of channels in the device
455                     if not self.eTOF_channels :
456 
```

```
457                     self.eTOF_channels = range(nbrChannels)
458
459                 # Record config for all defined channels
460                 for channel in self.eTOF_channels :
461
462                     fullScale = eTOFConfig.vert(channel).fullScale()                    ...
                            # Full vertical scale in Volts
463                     offset = eTOFConfig.vert(channel).offset()                          ...
                            # Vertical offset in Volts
464                     gain = eTOFConfig.vert(channel).slope()                             ...
                            # Vertical gain in Volts/bit
465
466                     # Create a structure for the given TOF detector
467                     exec 'self.eTOF' + str(channel) + ' = {}'
468                     # Write configuation settings to appropriate dictionary
469                     exec 'self.eTOF' + str(channel) + '[\'sampInterv\'] = sampInterv'
470                     exec 'self.eTOF' + str(channel) + '[\'iMax\'] = iMax'
471                     exec 'self.eTOF' + str(channel) + '[\'T\'] = T'
472                     exec 'self.eTOF' + str(channel) + '[\'gain\'] = gain'
473                     exec 'self.eTOF' + str(channel) + '[\'offset\'] = offset'
474                     exec 'self.eTOF' + str(channel) + '[\'fullScale\'] = fullScale'
475
476             except :
477                 print 'Fatal error: Acqiris config data for eTOFs is damaged or ...
                        instrument does not exist. Quitting....'
478                 logging.info( "Force quit: Acqiris configuration improperly defined" )
479                 self.forcequit = True
480
481         # iTOF configurations
482         if self.use_iTOF :
483
484             # Get configuration object
485             iTOFConfig = env.getAcqConfig(self.iTOFaddress)
486
487             try :
488
489                 sampInterv = iTOFConfig.horiz().sampInterval()*1e9                      ...
                        # Sample interval of the trace in nanoseconds
490                 iMax = iTOFConfig.horiz().nbrSamples()                                  ...
                        # Number of samples in trace
491                 nbrChannels = iTOFConfig.nbrChannels()                                  ...
                        # Number of channels in the device
492                 T = scipy.linspace(0,sampInterv*(iMax),iMax)                            ...
                        # Time Vector
493
494                 # If channels have not been defined (empty array) then autogenerate
495                 # a channel list based on number of channels in the device
496                 if not self.iTOF_channels :
497
498                     self.iTOF_channels = range(nbrChannels)
499
500                 # Record config for all defined channels
501                 for channel in self.eTOF_channels :
502
503                     fullScale = iTOFConfig.vert(channel).fullScale()                    ...
                            # Full vertical scale in Volts
504                     offset = iTOFConfig.vert(channel).offset()                          ...
                            # Vertical offset in Volts
505                     gain = iTOFConfig.vert(channel).slope()                             ...
                            # Vertical gain in Volts/bit
506
507                     exec 'self.iTOF' + str(channel) + ' = {}'
508                     # Write configuation settings to appropriate dictionary
509                     exec 'self.iTOF' + str(channel) + '[\'sampInterv\'] = sampInterv'
510                     exec 'self.iTOF' + str(channel) + '[\'iMax\'] = iMax'
511                     exec 'self.iTOF' + str(channel) + '[\'T\'] = T'
512                     exec 'self.iTOF' + str(channel) + '[\'gain\'] = gain'
513                     exec 'self.iTOF' + str(channel) + '[\'offset\'] = offset'
514                     exec 'self.iTOF' + str(channel) + '[\'fullScale\'] = fullScale'
515
516             except :
517                 print( 'Fatal error: Acqiris config data for iTOFs is damaged or ...
                        instrument does not exist. Quitting....' )
518                 logging.info( "Force quit: Acqiris configuration improperly defined" )
519                 self.forcequit = True
520
521
522         # Prepare data structures for storage
```

```
523             cleardatafields( self )
524
525             logging.info( "MatConverter.beginrun() called" )
526
527         def begincalibcycle( self, evt, env ) :
528             """This optional method is called if present at the beginning
529             of the new calibration cycle.
530
531             @param evt    event data object
532             @param env    environment object
533             """
534
535             # No need for any recording in this section, we are getting epics variables on ...
                    every shot
536
537             logging.info( "MatConverter.begincalibcycle() called" )
538
539         def event( self, evt, env ) :
540             """This method is called for every L1Accept transition.
541
542             @param evt    event data object
543             @param env    environment object
544             """
545             # Force quits if there was a problem in the configuration
546             if self.forcequit :
547                 return pyana.Terminate
548
549             # Increment event counter by one
550             self.counter += 1
551
552             # Reset Event damage flag to false
553             self.damageflag = False
554
555             # ------------------------------
556             # -- Camera configuration info --
557             # ------------------------------
558
559             if self.procEvt == 0 :
560
561                 if self.use_cameras :
562
563                     # Iterate over all cameras
564                     for camera in range(self.ncameras) :
565
566                         print( self.caminfo[self.camKeys[camera]] )
567                         firstframe = evt.getFrameValue( self.caminfo[self.camKeys[camera]] )
568
569                         try :
570
571                             # Grab frame configuration data
572                             bitdepth = firstframe.depth()
573                             width = firstframe.width()
574                             height = firstframe.height()
575                             datasize = firstframe.data_size()
576
577                             # Write the information to the camera dictionary structure
578                             exec 'self.' + self.camKeys[camera] + ' = {}'
579                             exec 'self.' + self.camKeys[camera] + '[\'bitdepth\'] = bitdepth'
580                             exec 'self.' + self.camKeys[camera] + '[\'width\'] = width'
581                             exec 'self.' + self.camKeys[camera] + '[\'height\'] = height'
582                             exec 'self.' + self.camKeys[camera] + '[\'datasize\'] = datasize'
583                             print self.camKeys[camera]
584
585                             # Print info
586                             printstring = "Camera with address %s has width %d, height %d, ...
                                    bitdepth %d and datasize %d"
587                             print(printstring % ( self.camKeys[camera], width, height, ...
                                    bitdepth, datasize ) )
588
589                         except :
590                             print( "Camera data for address %s damaged, terminating ...
                                    program..." % ( self.camKeys[camera] ) )
591                             return pyana.Terminate
592
593             ##########################
594             # ---Get Acquiris Data---
595             ##########################
596
```

```
597             # Grab the acquiris data for each eTOF channel
598             if self.use_eTOF :
599
600                 for channel in self.eTOF_channels :
601
602                     acqData = evt.getAcqValue(self.eTOFaddress, channel, env)
603
604                     # Try to grab the acqiris waveform for the shot
605                     try :
606                         # Waveform in int16 form (raw digitizer data)
607                         exec 'offset = self.eTOF' + str(channel) + '[\'offset\']'
608                         exec 'gain = self.eTOF' + str(channel) + '[\'gain\']'
609                         exec 'ewf' + str(channel) + ' = ...
                                numpy.int16((acqData.waveform()+offset)/gain)'
610                         exec 'ehorpos' + str(channel) + '=acqData.timestamp(0).pos()'
611
612                     # If the data can't be grabbed, flag data as damaged, inform user
613                     except :
614                         print( "eTOF Waveform data in channel %d damaged for event %d" % ( ...
                                channel, self.counter ) )
615                         self.damageflag = True
616
617             if self.use_iTOF :
618
619                 for channel in self.iTOF_channels :
620
621                     acqData = evt.getAcqValue(self.iTOFaddress, channel, env)
622
623                     # Try to grab the acqiris waveform for the shot
624                     try :
625                         # Waveform in int16 form (raw digitizer data)
626                         exec 'offset = self.iTOF' + str(channel) + '[\'offset\']'
627                         exec 'gain = self.iTOF' + str(channel) + '[\'gain\']'
628                         exec 'iwf' + str(channel) + ' = ...
                                numpy.int16((acqData.waveform()+offset)/gain)'
629                         exec 'ihorpos' + str(channel) + '=acqData.timestamp(0).pos()'
630
631                     # If the data can't be grabbed, flag data as damaged
632                     except :
633                         print( "iTOF Waveform data in channel %d damaged for event %d" % ( ...
                                channel, self.counter ) )
634                         self.damageflag = True
635
636             ##########################
637             # --- EPICS Variables ---
638             ##########################
639
640             """These variables do not vary on a shot by shot basis but are saved every shot ...
                    for completeness sake,
641             and ease of synching up values to particular shots, and they don't increase the ...
                    file size by very much.
642             The variables of interest will vary but the method for calling them is the same ...
                    no matter what,
643             using env.epicsStore().value(INSERT VAR NAME HERE).
644             """
645
646             # This loop iterates over all epics variables specified in the config file if ...
                    EPICS variables are used
647
648             if self.use_EPICS :
649
650                 for variable in range(len(self.epicsKeys)) :
651
652                     tempdata = env.epicsStore().value(self.epicsinfo[self.epicsKeys[variable]])
653
654                     try :
655
656                         # Write epics value
657                         exec self.epicsKeys[variable] + ' = tempdata.values'
658
659                     except :
660
661                         # Write failure value to the variable
662                         print( 'Epics variable %s is damaged for event %d' % ...
                                (self.epicsinfo[self.epicsKeys[variable]], self.counter) )
663                         codetoexec = self.epicsKeys[variable] + ' = 0'
664                         exec codetoexec
665
```

```
666         ##############################
667         # ---Get Fast Camera Data---
668         ##############################
669
670         if self.use_cameras :
671
672             for camera in range(self.ncameras) :
673
674                 # Grab frame data
675                 frame = evt.getFrameValue( self.caminfo[self.camKeys[camera]] )
676
677                 try :
678                     # Save frame and convert to 16 bit int
679                     exec self.camKeys[camera] + 'fr = numpy.int16(frame.data())'
680
681                 except :
682                     # If frame is damaged, flag event as damaged and inform user
683                     print( "Frame data for camera %s is damaged for shot %d" % ( ...
                             self.camKeys[camera], self.counter ) )
684                     self.damageflag = True
685
686         ##############################
687         # ---Get Electon Beam Data---
688         ##############################
689         if self.use_ebeamdata :
690
691             ebeam = evt.getEBeam()
692
693             try :
694                 EBeamCharge = ebeam.fEbeamCharge          # The electon beam total charge (nC)
695                 EBeamEnergy = ebeam.fEbeamL3Energy        # Electron beam energy          (MeV)
696                 EBeamPosX = ebeam.fEbeamLTUPosX           # ELectron beam X position      (mm)
697                 EBeamPosY = ebeam.fEbeamLTUPosY           # Electron beam Y position      (mm)
698                 EBeamAngX = ebeam.fEbeamLTUAngX           # ELectron beam angular X       ...
                        (mrad)
699                 EBeamAngY = ebeam.fEbeamLTUAngY           # Electron beam angular Y       ...
                        (mrad)
700                 EBeamCurrent = ebeam.fEbeamPkCurrBC2      # ELecton beam peak current     (A)
701
702             # If the data can't be found, print error, flag event as damaged
703             except :
704                 print( "EBeam data damaged for event %d" %(self.counter) )
705                 self.damageflag = True
706
707         ##############################
708         # ---Get Gas Detector Data---
709         ##############################
710
711         if self.use_gasdetectors :
712
713             GasDetValues = evt.getFeeGasDet()
714
715             if numpy.shape(GasDetValues) != (4,) :
716
717                 print( "Gas Detector data damagedfor event %d" % (self.counter) )
718                 self.damageflag = True
719
720             try :
721                 GasDetectors = GasDetValues         # The 4 gas detector values
722
723             # If the data can't be found, print error, flag event as damaged
724             except :
725                 print( "Gas Detector data damaged for event" % (self.counter) )
726                 self.damageflag = True
727
728         ##############################
729         # ---Get Phase Cavity Data---
730         ##############################
731
732         if self.use_phasecavity :
733
734             PhaseCav = evt.getPhaseCavity()
735
736             try :
737
738                 PCTime1 = PhaseCav.fFitTime1          # The fit time from the first cavity
739                 PCTime2 = PhaseCav.fFitTime2          # The fit time from the second cavity
740                 PCCharge1 = PhaseCav.fCharge1         # The charge measured at the first cavity
```

```
741                 PCCharge2 = PhaseCav.fCharge2       # The charge measured at the second ...
                        cavity
742
743             except :
744
745                 print ( "Phase Cavity data damaged for event %d" %( self.counter ) )
746                 self.damageflag = True
747
748         ############################################################
749         #  --- Add data to lists only if all data is undamaged ---
750         ############################################################
751
752         if self.damageflag == False:
753
754             # Adds EBeam Data of shot to the lists
755             if self.use_ebeamdata :
756
757                 self.EBeamCharge.append(EBeamCharge)
758                 self.EBeamEnergy.append(EBeamEnergy)
759                 self.EBeamPosX.append(EBeamPosX)
760                 self.EBeamPosY.append(EBeamPosY)
761                 self.EBeamAngX.append(EBeamAngX)
762                 self.EBeamAngY.append(EBeamAngY)
763                 self.EBeamCurrent.append(EBeamCurrent)
764
765             # Adds Phase Cavity Data
766             if self.use_phasecavity :
767
768                 self.PCTime1.append(PCTime1)
769                 self.PCTime2.append(PCTime2)
770                 self.PCCharge1.append(PCCharge1)
771                 self.PCCharge2.append(PCCharge2)
772
773             # Adds the Acqiris Waveforms to the list
774
775             # eTOF waveforms
776             if self.use_eTOF :
777
778                 for ch in self.eTOF_channels :
779
780                     exec 'self.eW' + str(ch) + '.append(ewf' + str(ch) + ')'
781                     exec 'self.ehorpos' + str(ch) + '.append(ehorpos' + str(ch) + ')'
782
783             # iTOF waveforms
784             if self.use_iTOF :
785
786                 for ch in self.iTOF_channels :
787
788                     exec 'self.iW' + str(ch) + '.append(iwf' + str(ch) + ')'
789                     exec 'self.ihorpos' + str(ch) + '.append(ihorpos' + str(ch) + ')'
790
791             # Adds the Gas Detector Data to the list
792             if self.use_gasdetectors :
793
794                 self.GasDetectors.append(GasDetectors)
795
796             if self.use_EPICS :
797
798                 # Adds EPICS variables to the list
799                 for variable in range(len(self.epicsKeys)) :
800
801                     codetoexec = 'self.' + self.epicsKeys[variable] + '.append(' + ...
                            self.epicsKeys[variable] + ')'
802                     exec codetoexec
803
804             if self.use_cameras :
805
806                 for camera in range(self.ncameras) :
807
808                     exec 'self.' + self.camKeys[camera] + 'frames.append(' + ...
                            self.camKeys[camera] + 'fr)'
809
810             # Increase counter of processed events by one
811             self.procEvt += 1
812             self.procEvtThisFile += 1
813
814
```

```
815         #Informs the user every hundred shots to give a feel for how fast the thing is ...
                performing
816         if self.procEvt % 100 == 0 and self.procEvt != 0 :
817
818             print( 'Processed %07d events' % (self.procEvt) )
819
820         # Saves .mat file if the number of proccessed shots is an integer multiple of ...
                the file size, and is not empty
821         if self.procEvtThisFile == self.filesize and self.procEvt != 0 :
822
823             # Add one to the .mat file counter
824             self.nMats += 1
825             # Save mat file
826             savematfile(self)
827             # Clear Data Fields
828             cleardatafields(self)
829             # Reset file event counter
830             self.procEvtThisFile = 0
831
832     def endcalibcycle( self, evt, env ) :
833         """This optional method is called if present at the end of the
834         calibration cycle.
835
836         @param evt    event data object
837         @param env    environment object
838         """
839
840         logging.info( "MatConverter.endcalibcycle() called" )
841
842     def endrun( self, evt, env ) :
843         """This optional method is called if present at the end of the run.
844
845         @param evt    event data object
846         @param env    environment object
847         """
848         if self.procEvtThisFile != 0:
849             self.nMats += 1
850             savematfile(self)
851
852         logging.info( "MatConverter.endrun() called" )
853
854     def endjob( self, evt, env ) :
855         """This method is called at the end of the job. It should do
856         final cleanup, e.g. close all open files.
857
858         @param evt    event data object
859         @param env    environment object
860         """
861
862         # Saves last mat file with whatever data remains unsaved
863
864
865         # Prints finishing message
866         print('All shots saved!')
867
868         logging.info( "MatConverter.endjob() called" )
```

Bibliography

[1] L. R. Khundkar and A. H. Zewail. 'Ultrafast molecular reaction dynamics in real-time: Progress over a decade.' *Annual Review of Physical Chemistry*, **41**, 15–60 (1990). doi:10.1146/annurev.pc.41.100190.000311.

[2] A. H. Zewail. 'Femtochemistry: Atomic-scale dynamics of the chemical bond†.' *J. Phys. Chem. A*, **104**, 5660–5694 (2000). doi:10.1021/jp001460h.

[3] W. Rontgen. 'On a new kind of rays.' *Nature*, **53**, 274–276 (1896). doi:10.1038/053274b0.

[4] K. Siegbahn, C. Nordling and G. Johansson. *ESCA applied to free molecules*. North-Holland, Amsterdam; London (1969).

[5] K. Siegbahn. 'Electron spectroscopy and molecular structure.' *Pure and Applied Chemistry*, **48**, 77–97 (1976). doi:10.1351/pac197648010077.

[6] T. A. Ezquerra, M. C. Garcia-Gutierrez, A. Nogales and M. Gomez. *Applications of Synchrotron Light to Scattering and Diffraction in Materials and Life Sciences*. Springer (2009).

[7] D. H. Bilderback, P. Elleaume and E. Weckert. 'Review of third and next generation synchrotron light sources.' *Journal of Physics B: Atomic, Molecular and Optical Physics*, **38**, S773–S797 (2005). doi:10.1088/0953-4075/38/9/022.

[8] J. R. Schneider. 'Photon science at accelerator-based light sources.' *Reviews of Accelerator Science and Technology*, **03**, 13 (2010). doi:10.1142/S1793626810000348.

[9] P. B. Corkum. 'Plasma perspective on strong field multiphoton ionization.' *Physical Review Letters*, **71**, 1994–1997 (1993). doi:10.1103/PhysRevLett.71.1994.

[10] M. Lewenstein, P. Balcou, M. Y. Ivanov, A. L'Huillier and P. B. Corkum. 'Theory of high-harmonic generation by low-frequency laser fields.' *Physical Review A*, **49**, 2117–2132 (1994). doi:10.1103/PhysRevA.49.2117.

[11] M.-C. Chen, P. Arpin, T. Popmintchev, M. Gerrity, B. Zhang *et al.* 'Bright, coherent, ultrafast soft x-ray harmonics spanning the water window from a tabletop light source.' *Physical Review Letters*, **105**, 173901 (2010). doi:10.1103/PhysRevLett.105.173901.

[12] T. Popmintchev, M.-C. Chen, D. Popmintchev, P. Arpin, S. Brown *et al.* 'Bright coherent ultrahigh harmonics in the keV x-ray regime from mid-infrared femtosecond lasers.' *Science*, **336**, 1287–1291 (2012). doi:10.1126/science.1218497.

[13] W. Boutu, S. Haessler, H. Merdji, P. Breger, G. Waters *et al.* 'Coherent control of attosecond emission from aligned molecules.' *Nature Physics*, **4**, 545–549 (2008). doi:10.1038/nphys964.

[14] R. Torres, T. Siegel, L. Brugnera, I. Procino, J. G. Underwood *et al.* 'Extension of high harmonic spectroscopy in molecules by a 1300 nm laser field.' *Optics Express*, **18**, 3174–3180 (2010). doi: 10.1364/OE.18.003174.

[15] M. C. H. Wong, J.-P. Brichta, M. Spanner, S. Patchkovskii and V. R. Bhardwaj. 'High-harmonic spectroscopy of molecular isomers.' *Physical Review A*, **84**, 051403 (2011). doi:10.1103/PhysRevA.84.051403.

[16] C. Vozzi, R. Torres, M. Negro, L. Brugnera, T. Siegel *et al.* 'High harmonic generation spectroscopy of hydrocarbons.' *Applied Physics Letters*, **97**, 241103–241103–3 (2010). doi:doi:10.1063/1.3526752.

[17] P. Agostini and L. F. DiMauro. 'The physics of attosecond light pulses.' *Reports on Progress in Physics*, **67**, 813–855 (2004). doi:10.1088/0034-4885/67/6/R01.

[18] M. Hentschel, R. Kienberger, C. Spielmann, G. A. Reider, N. Milosevic *et al.* 'Attosecond metrology.' *Nature*, **414**, 509–513 (2001). doi:10.1038/35107000.

[19] A. L. Cavalieri, N. Muller, T. Uphues, V. S. Yakovlev, A. Baltuska *et al.* 'Attosecond spectroscopy in condensed matter.' *Nature*, **449**, 1029–1032 (2007). doi:10.1038/nature06229.

[20] F. Krausz and M. Ivanov. 'Attosecond physics.' *Reviews of Modern Physics*, **81**, 163–234 (2009). doi:10.1103/RevModPhys.81.163.

[21] J. Marangos. 'Introduction to the new science with x-ray free electron lasers.' *Contemporary Physics*, **52**, 551–569 (2011). doi:10.1080/00107514.2011.607290.

[22] H. N. Chapman, S. Bajt, A. Barty, W. H. Benner, M. J. Bogan *et al.* 'Coherent imaging at FLASH.' *Journal of Physics: Conference Series*, **186**, 012051 (2009). doi:10.1088/1742-6596/186/1/012051.

[23] M. M. Seibert, T. Ekeberg, F. R. N. C. Maia, M. Svenda, J. Andreasson *et al.* 'Single mimivirus particles intercepted and imaged with an x-ray laser.' *Nature*, **470**, 78–81 (2011). doi:10.1038/nature09748.

[24] A. Barty, C. Caleman, A. Aquila, N. Timneanu, L. Lomb *et al.* 'Self-terminating diffraction gates femtosecond x-ray nanocrystallography measurements.' *Nat Photon*, **6**, 35–40 (2012). doi:10.1038/nphoton.2011.297.

[25] J. Spence. 'X-ray imaging: Ultrafast diffract-and-destroy movies.' *Nat Photon*, **2**, 390–391 (2008). doi:10.1038/nphoton.2008.115.

[26] L. S. Cederbaum, F. Tarantelli, A. Sgamellotti and J. Schirmer. 'On double vacancies in the core.' *The Journal of Chemical Physics*, **85**, 6513 (1986). doi:10.1063/1.451432.

[27] O. Takahashi, M. Tashiro, M. Ehara, K. Yamasaki and K. Ueda. 'Theoretical molecular double-core-hole spectroscopy of nucleobases.' *The Journal of Physical Chemistry A*, **115**, 12070–12082 (2011). doi:10.1021/jp205923m.

[28] N. Berrah, L. Fang, B. Murphy, T. Osipov, K. Ueda *et al.* 'Double-core-hole spectroscopy for chemical analysis with an intense x-ray femtosecond laser.' *Proceedings of the National Academy of Sciences*, **108**, 16912 –16915 (2011). doi:10.1073/pnas.1111380108.

[29] J. M. Glownia, J. Cryan, J. Andreasson, A. Belkacem, N. Berrah *et al.* 'Time-resolved pump-probe experiments at the LCLS.' *Optics Express*, **18**, 17620–17630 (2010). doi:10.1364/OE.18.017620.

[30] V. S. Petrović, M. Siano, J. L. White, N. Berrah, C. Bostedt *et al.* 'Transient x-ray fragmentation: Probing a prototypical photoinduced ring opening.' *Physical Review Letters*, **108**, 253006 (2012). doi:10.1103/PhysRevLett.108.253006.

[31] G. New. *Introduction to nonlinear optics*. Cambridge Univ. Press, Cambridge (2011).

[32] P. A. Franken, A. E. Hill, C. W. Peters and G. Weinreich. 'Generation of optical harmonics.' *Physical Review Letters*, **7**, 118–119 (1961). doi:10.1103/PhysRevLett.7.118.

[33] G. H. C. New and J. F. Ward. 'Optical third-harmonic generation in gases.' *Physical Review Letters*, **19**, 556–559 (1967). doi:10.1103/PhysRevLett.19.556.

[34] P. W. Atkins and R. Friedman. *Molecular quantum mechanics*. Oxford University Press, Oxford; New York (2011).

[35] J. E. Lennard-Jones. 'The electronic structure of some diatomic molecules.' *Trans. Faraday Soc.*, **25**, 668–686 (1929). doi:10.1039/TF9292500668.

[36] A. Einstein. 'Über einen die erzeugung und verwandlung des lichtes betreffenden heuristischen gesichtspunkt.' *Annalen der Physik*, **322**, 132–148 (1905). doi:10.1002/andp.19053220607.

[37] 'NIST x-ray form factor, attenuation and scattering tables.' http://physics.nist.gov/PhysRefData/FFast/html/form.html. URL `http://physics.nist.gov/PhysRefData/FFast/html/form.html`.

[38] J. M. Hollander and W. L. Jolly. 'X-ray photoelectron spectroscopy.' *Acc. Chem. Res.*, **3**, 193–200 (1970). doi:10.1021/ar50030a003.

[39] H. A. Bethe and E. E. Salpeter. *Quantum mechanics of one- and two-electron atoms*. Springer (1957).

[40] P. Auger. 'Sur les rayons β secondaires produits dans un gaz par des rayons x.' *Compt. Rend.*, **180**, 65–68 (1925).

[41] R. Santra. 'Concepts in x-ray physics.' *Journal of Physics B: Atomic, Molecular and Optical Physics*, **42**, 023001 (2009). doi:10.1088/0953-4075/42/2/023001.

[42] E. J. McGuire. 'K-shell auger transition rates and fluorescence yields for elements be-ar.' *Physical Review*, **185**, 1–6 (1969). doi:10.1103/PhysRev.185.1.

[43] P. Weightman. 'X-ray-excited auger and photoelectron spectroscopy.' *Reports on Progress in Physics*, **45**, 753–814 (1982). doi:10.1088/0034-4885/45/7/002.

[44] J. Martin and L. Mandel. 'Electron energy spectrum in laser-induced multiphoton ionization of atoms.' *Applied Optics*, **15**, 2378–2380 (1976). doi:10.1364/AO.15.002378.

[45] Z. Deng and J. H. Eberly. 'Multiphoton absorption above ionization threshold by atoms in strong laser fields.' *Journal of the Optical Society of America B*, **2**, 486–493 (1985). doi:10.1364/JOSAB.2.000486.

[46] S. Augst, D. Strickland, D. D. Meyerhofer, S. L. Chin and J. H. Eberly. 'Tunneling ionization of noble gases in a high-intensity laser field.' *Physical Review Letters*, **63**, 2212–2215 (1989). doi:10.1103/PhysRevLett.63.2212.

[47] {Luke Chipperfield}. 'High harmonic generation with few-cycle pulses.' Ph.D. thesis, Imperial College London (2007).

[48] {David Hoffman}. 'High harmonic generation using multicolour fields.' Ph.D. thesis, Imperial College London (2011).

[49] M. Lein, N. Hay, R. Velotta, J. P. Marangos and P. L. Knight. 'Role of the intramolecular phase in high-harmonic generation.' *Physical Review Letters*, **88**, 183903 (2002). doi:10.1103/PhysRevLett.88.183903.

[50] S. Baker, J. S. Robinson, M. Lein, C. C. Chirilă, R. Torres *et al.* 'Dynamic two-center interference in high-order harmonic generation from molecules with attosecond nuclear motion.' *Physical Review Letters*, **101**, 053901 (2008). doi:10.1103/PhysRevLett.101.053901.

[51] S. Baker, J. S. Robinson, C. A. Haworth, H. Teng, R. A. Smith *et al.* 'Probing proton dynamics in molecules on an attosecond time scale.' *Science*, **312**, 424–427 (2006). doi:10.1126/science.1123904.

[52] J. Grant-Jacob, B. Mills, T. J. Butcher, R. T. Chapman, W. S. Brocklesby *et al.* 'Gas jet structure influence on high harmonic generation.' *Optics Express*, **19**, 9801–9806 (2011). doi:10.1364/OE.19.009801.

[53] M. B. Gaarde, J. L. Tate and K. J. Schafer. 'Macroscopic aspects of attosecond pulse generation.' *Journal of Physics B: Atomic, Molecular and Optical Physics*, **41**, 132001 (2008). doi:10.1088/0953-4075/41/13/132001.

[54] P. Balcou, P. Sali'eres, A. L'Huillier and M. Lewenstein. 'Generalized phase-matching conditions for high harmonics: The role of field-gradient forces.' *Physical Review A*, **55**, 3204–3210 (1997). doi:10.1103/PhysRevA.55.3204.

[55] P. Salières, A. L'Huillier and M. Lewenstein. 'Coherence control of high-order harmonics.' *Physical Review Letters*, **74**, 3776–3779 (1995). doi:10.1103/PhysRevLett.74.3776.

[56] A. Zaïr, M. Holler, A. Guandalini, F. Schapper, J. Biegert *et al.* 'Quantum path interferences in high-order harmonic generation.' *Physical Review Letters*, **100**, 143902 (2008). doi:10.1103/PhysRevLett.100.143902.

[57] M. Holler, A. Zaïr, F. Schapper, T. Auguste, E. Cormier *et al.* 'Ionization effects on spectral signatures of quantum-path interference in high-harmonic generation.' *Optics Express*, **17**, 5716 (2009). doi:10.1364/OE.17.005716.

[58] G. Farkas and C. Tóth. 'Proposal for attosecond light pulse generation using laser induced multiple-harmonic conversion processes in rare gases.' *Physics Letters A*, **168**, 447–450 (1992). doi:10.1016/0375-9601(92)90534-S.

[59] M. Drescher, M. Hentschel, R. Kienberger, G. Tempea, C. Spielmann *et al.* 'X-ray pulses approaching the attosecond frontier.' *Science*, **291**, 1923 –1927 (2001). doi:10.1126/science.1058561.

[60] P. M. Paul, E. S. Toma, P. Breger, G. Mullot, F. Augé *et al.* 'Observation of a train of attosecond pulses from high harmonic generation.' *Science*, **292**, 1689 –1692 (2001). doi:10.1126/science.1059413.

[61] H. Mashiko, S. Gilbertson, C. Li, S. D. Khan, M. M. Shakya *et al.* 'Double optical gating of high-order harmonic generation with carrier-envelope phase stabilized lasers.' *Physical Review Letters*, **100**, 103906 (2008). doi:10.1103/PhysRevLett.100.103906.

[62] F. J. McClung and R. W. Hellwarth. 'Giant optical pulsations from ruby.' *Journal of Applied Physics*, **33**, 828–829 (1962). doi:doi:10.1063/1.1777174.

[63] R. E. Slusher. 'Laser technology.' *Reviews of Modern Physics*, **71**, S471–S479 (1999). doi:10.1103/RevModPhys.71.S471.

[64] R. J. Collins and P. Kisliuk. 'Control of population inversion in pulsed optical masers by feedback modulation.' *Journal of Applied Physics*, **33**, 2009–2011 (1962). doi:doi:10.1063/1.1728883.

[65] D. E. Spence, P. N. Kean and W. Sibbett. '60-fsec pulse generation from a self-mode-locked ti:sapphire laser.' *Optics Letters*, **16**, 42–44 (1991). doi:10.1364/OL.16.000042.

[66] J. Herrmann. 'Theory of kerr-lens mode locking: role of self-focusing and radially varying gain.' *Journal of the Optical Society of America B*, **11**, 498–512 (1994). doi:10.1364/JOSAB.11.000498.

[67] P. F. Moulton. 'Spectroscopic and laser characteristics of Ti:Al2O3.' *Journal of the Optical Society of America B*, **3**, 125–133 (1986). doi:10.1364/JOSAB.3.000125.

[68] R. L. Fork, O. E. Martinez and J. P. Gordon. 'Negative dispersion using pairs of prisms.' *Optics Letters*, **9**, 150–152 (1984). doi:10.1364/OL.9.000150.

[69] E. Treacy. 'Optical pulse compression with diffraction gratings.' *IEEE Journal of Quantum Electronics*, **5**, 454– 458 (1969). doi:10.1109/JQE.1969.1076303.

[70] D. Strickland and G. Mourou. 'Compression of amplified chirped optical pulses.' *Optics Communications*, **56**, 219–221 (1985). doi:10.1016/0030-4018(85)90120-8.

[71] M. Pessot, P. Maine and G. Mourou. '1000 times expansion/compression of optical pulses for chirped pulse amplification.' *Optics Communications*, **62**, 419–421 (1987). doi:10.1016/0030-4018(87)90011-3.

[72] R. Trebino and D. J. Kane. 'Using phase retrieval to measure the intensity and phase of ultrashort pulses: frequency-resolved optical gating.' *Journal of the Optical Society of America A*, **10**, 1101–1111 (1993). doi:10.1364/JOSAA.10.001101.

[73] T. Tsang, M. A. Krumbügel, K. W. DeLong, D. N. Fittinghoff and R. Trebino. 'Frequency-resolved optical-gating measurements of ultrashort pulses using surface third-harmonic generation.' *Optics Letters*, **21**, 1381–1383 (1996). doi:10.1364/OL.21.001381.

[74] G. Stibenz and G. Steinmeyer. 'Interferometric frequency-resolved optical gating.' *Optics Express*, **13**, 2617–2626 (2005). doi:10.1364/OPEX.13.002617.

[75] C. Iaconis and I. Walmsley. 'Spectral phase interferometry for direct electric-field reconstruction of ultrashort optical pulses.' *Optics Letters*, **23**, 792–794 (1998). doi:10.1364/OL.23.000792.

[76] J. M. J. Madey. 'Stimulated emission of bremsstrahlung in a periodic magnetic field.' *Journal of Applied Physics*, **42**, 1906–1913 (1971). doi:doi:10.1063/1.1660466.

[77] D. A. G. Deacon, L. R. Elias, J. M. J. Madey, G. J. Ramian, H. A. Schwettman *et al.* 'First operation of a free-electron laser.' *Physical Review Letters*, **38**, 892–894 (1977). doi:10.1103/PhysRevLett.38.892.

[78] W. Ackermann, G. Asova, V. Ayvazyan, A. Azima, N. Baboi *et al.* 'Operation of a free-electron laser from the extreme ultraviolet to the water window.' *Nature Photonics*, **1**, 336–342 (2007). doi:10.1038/nphoton.2007.76.

[79] P. Emma, R. Akre, ArthurJ., BiontaR., BostedtC. *et al.* 'First lasing and operation of an angstrom-wavelength free-electron laser.' *Nat Photon*, **4**, 641–647 (2010). doi:10.1038/nphoton.2010.176.

[80] D. Pile. 'X-rays: First light from SACLA.' *Nature Photonics*, **5**, 456–457 (2011). doi:10.1038/nphoton.2011.178.

[81] S. Khan. 'Free-electron lasers.' *Journal of Modern Optics*, **55**, 3469–3512 (2008). doi:10.1080/09500340802521175.

[82] S. V. Milton, E. Gluskin, N. D. Arnold, C. Benson, W. Berg *et al.* 'Exponential gain and saturation of a self-amplified spontaneous emission free-electron laser.' *Science*, **292**, 2037 –2041 (2001). doi:10.1126/science.1059955.

[83] G. R. Neil and L. Merminga. 'Technical approaches for high-average-power free-electron lasers.' *Reviews of Modern Physics*, **74**, 685–701 (2002). doi:10.1103/RevModPhys.74.685.

[84] S. Düsterer, P. Radcliffe, C. Bostedt, J. Bozek, A. L. Cavalieri *et al.* 'Femtosecond x-ray pulse length characterization at the linac coherent light source free-electron laser.' *New Journal of Physics*, **13**, 093024 (2011). doi:10.1088/1367-2630/13/9/093024.

[85] T. Brabec. *Strong field laser physics*. Springer, New York (2008). URL `http://site.ebrary.com/id/10252016`.

[86] Y. Ding, Z. Huang and R. D. Ruth. 'Two-bunch self-seeding for narrow-bandwidth hard x-ray free-electron lasers.' *Physical Review Special Topics - Accelerators and Beams*, **13**, 060703 (2010). doi:10.1103/PhysRevSTAB.13.060703.

[87] E. Springate and J. W. Tisch. 'High harmonic generation as a seed source for free electron lasers.' *Journal of Modern Optics*, **58**, 1351–1361 (2011). doi:10.1080/09500340.2011.591505.

[88] J. Amann, W. Berg, V. Blank, F.-J. Decker, Y. Ding *et al.* 'Demonstration of self-seeding in a hard-x-ray free-electron laser.' *Nature Photonics* (2012). doi:10.1038/nphoton.2012.180.

[89] A. Singer, I. A. Vartanyants, M. Kuhlmann, S. Duesterer, R. Treusch *et al.* 'Transverse-coherence properties of the free-electron-laser FLASH at DESY.' *Physical Review Letters*, **101**, 254801 (2008). doi:10.1103/PhysRevLett.101.254801.

[90] I. A. Vartanyants, A. Singer, A. P. Mancuso, O. M. Yefanov, A. Sakdinawat *et al.* 'Coherence properties of individual femtosecond pulses of an x-ray free-electron laser.' *Physical Review Letters*, **107**, 144801 (2011). doi:10.1103/PhysRevLett.107.144801.

[91] R. P. Feynman, R. B. Leighton and M. Sands. *The Feynman Lectures on Physics*, volume 2. Addison-Wesley, sixth edition (1977).

[92] E. Brunetti, R. P. Shanks, G. G. Manahan, M. R. Islam, B. Ersfeld *et al.* 'Low emittance, high brilliance relativistic electron beams from a laser-plasma accelerator.' *Physical Review Letters*, **105**, 215007 (2010). doi:10.1103/PhysRevLett.105.215007.

[93] W. P. Leemans, B. Nagler, A. J. Gonsalves, C. Tóth, K. Nakamura *et al.* 'GeV electron beams from a centimetre-scale accelerator.' *Nature Physics*, **2**, 696–699 (2006). doi:10.1038/nphys418.

[94] J. Arthur, P. Anfinrud, P. Audebert, K. Bane, I. Ben-Zvi *et al.* 'Linac coherent light source (LCLS) conceptual design report.' (2002). URL `http://www.slac.stanford.edu/cgi-wrap/getdoc/slac-r-593.pdf`.

[95] G. Geloni, E. Saldin, E. Schneidmiller and M. Yurkov. 'Scheme for stabilization of output power of an x-ray self-amplified spontaneous emission free-electron laser.' *Physical Review Special Topics - Accelerators and Beams*, **11**, 120701 (2008). doi:10.1103/PhysRevSTAB.11.120701.

[96] T. Limberg and M. Dohlus. 'Bunch compression stability dependence on RF parameters.' In 'Proceedings of the 27th International Free Electron Laser Conference,' page 250. Stanford (2005). URL `http://www.slac.stanford.edu/econf/C0508213/PAPERS/TUOB004.PDF`.

[97] S. P. Hau–Riege, R. M. Bionta, D. D. Ryutov and J. Krzywinski. 'Measurement of x-ray free-electron-laser pulse energies by photoluminescence in nitrogen gas.' *Journal of Applied Physics*, **103**, 053306–053306–9 (2008). doi:doi:10.1063/1.2844478.

[98] M. Richter, A. Gottwald, U. Kroth, A. A. Sorokin, S. V. Bobashev *et al.* 'Measurement of gigawatt radiation pulses from a vacuum and extreme ultraviolet free-electron laser.' *Applied Physics Letters*, **83**, 2970–2972 (2003). doi:doi:10.1063/1.1614417.

[99] M. Richter, S. V. Bobashev, A. A. Sorokin and K. Tiedtke. 'Photon-matter interaction at short wavelengths and ultra-high intensity – gas-phase experiments at FLASH.' *Journal of Physics: Conference Series*, **141**, 012014 (2008). doi:10.1088/1742-6596/141/1/012014.

[100] R. Mitzner, A. A. Sorokin, B. Siemer, S. Roling, M. Rutkowski *et al.* 'Direct autocorrelation of soft-x-ray free-electron-laser pulses by time-resolved two-photon double ionization of he.' *Physical Review A*, **80**, 025402 (2009). doi:10.1103/PhysRevA.80.025402.

[101] R. Moshammer, T. Pfeifer, A. Rudenko, Y. H. Jiang, L. Foucar *et al.* 'Second-order autocorrelation of XUV FEL pulses via time resolved two-photon single ionization of he.' *Optics Express*, **19**, 21698–21706 (2011). doi:10.1364/OE.19.021698.

[102] M. R. Bionta, H. T. Lemke, J. P. Cryan, J. M. Glownia, C. Bostedt *et al.* 'Spectral encoding of x-ray/optical relative delay.' *Optics Express*, **19**, 21855 (2011). doi:10.1364/OE.19.021855.

[103] P. Emma, K. Bane, M. Cornacchia, Z. Huang, H. Schlarb *et al.* 'Femtosecond and subfemtosecond x-ray pulses from a self-amplified spontaneous-Emission–Based free-electron laser.' *Physical Review Letters*, **92** (2004). doi:10.1103/PhysRevLett.92.074801.

[104] E. Gullikson. 'CXRO x-ray interactions with matter.' http://henke.lbl.gov/optical_constants/. URL `http://henke.lbl.gov/optical_constants/`.

[105] Y. Lim, T. Westerwalbesloh, A. Aschentrup, O. Wehmeyer, G. Haindl *et al.* 'Fabrication and characterization of EUV multilayer mirrors optimized for small spectral reflection bandwidth.' *Applied Physics A Materials Science & Processing*, **72**, 121–124 (2001). doi:10.1007/s003390000723.

[106] A. Wonisch, U. Neuhäusler, N. M. Kabachnik, T. Uphues, M. Uiberacker *et al.* 'Design, fabrication, and analysis of chirped multilayer mirrors for reflection of extreme-ultraviolet attosecond pulses.' *Applied Optics*, **45**, 4147–4156 (2006). doi:10.1364/AO.45.004147.

[107] D. Attwood. *Soft X-Rays and Extreme Ultraviolet Radiation: Principles and Applications*. Cambridge University Press (2007).

[108] P. KIRKPATRICK and A. V. BAEZ. 'Formation of optical images by x-rays.' *Journal of the Optical Society of America*, **38**, 766–773 (1948). doi:10.1364/JOSA.38.000766.

[109] T. NAMIOKA. 'Theory of the concave grating.' *Journal of the Optical Society of America*, **49**, 446–460 (1959). doi:10.1364/JOSA.49.000446.

[110] N. Nakano, H. Kuroda, T. Kita and T. Harada. 'Development of a flat-field grazing-incidence XUV spectrometer and its application in picosecond XUV spectroscopy.' *Applied Optics*, **23**, 2386–2392 (1984). doi:10.1364/AO.23.002386.

[111] M. Guilhaus. 'Special feature: Tutorial. principles and instrumentation in time-of-flight mass spectrometry. physical and instrumental concepts.' *Journal of Mass Spectrometry*, **30**, 1519–1532 (1995). doi:10.1002/jms.1190301102.

[112] W. Stephens. 'Proceedings of the american physical society - a pulsed mass spectrometer with time dispersion.' *Physical Review*, **69**, 691 (1946). doi:10.1103/PhysRev.69.674.2.

[113] Boesl, R. Weinkauf and E. W. Schlag. 'Reflectron time-of-flight mass spectrometry and laser excitation for the analysis of neutrals, ionized molecules and secondary fragments.' *International Journal of Mass Spectrometry and Ion Processes*, **112**, 121–166 (1992). doi:10.1016/0168-1176(92)80001-H.

[114] W. C. Wiley and I. H. McLaren. 'Time-of-flight mass spectrometer with improved resolution.' *Review of Scientific Instruments*, **26**, 1150–1157 (1955). doi:10.1063/1.1715212.

[115] A. T. J. B. Eppink and D. H. Parker. 'Velocity map imaging of ions and electrons using electrostatic lenses: Application in photoelectron and photofragment ion imaging of molecular oxygen.' *Review of Scientific Instruments*, **68**, 3477–3484 (1997). doi:doi:10.1063/1.1148310.

[116] R. E. Imhof and F. H. Read. 'A three-aperture electron optical lens for producing an image of variable energy but fixed position.' *Journal of Physics E: Scientific Instruments*, **1**, 859–860 (1968). doi:10.1088/0022-3735/1/8/325.

[117] T. Bergmann, T. P. Martin and H. Schaber. 'High-resolution time-of-flight mass spectrometers: Part i. effects of field distortions in the vicinity of wire meshes.' *Review of Scientific Instruments*, **60**, 347–349 (1989). doi:doi:10.1063/1.1140436.

[118] B. J. Whitaker. *Imaging in Molecular Dynamics: Technology and Applications*. Cambridge University Press (2003).

[119] G. A. Garcia, L. Nahon and I. Powis. 'Two-dimensional charged particle image inversion using a polar basis function expansion.' *Review of Scientific Instruments*, **75**, 4989–4996 (2004). doi:doi:10.1063/1.1807578.

[120] M. J. J. Vrakking. 'An iterative procedure for the inversion of two-dimensional ion/photoelectron imaging experiments.' *Review of Scientific Instruments*, **72**, 4084–4089 (2001). doi:doi:10.1063/1.1406923.

[121] J. M. Hayes. 'Analytical spectroscopy in supersonic expansions.' *Chem. Rev.*, **87**, 745–760 (1987). doi:10.1021/cr00080a004.

[122] F. W. Dunning and R. G. Hulet. *Atomic, molecular, and optical physics. [part B], Atoms and molecules*. Academic Press, San Diego (1996).

[123] C. L. Yaws. 'Yaws' critical property data for chemical engineers and chemists.' (2012). URL `http://www.knovel.com/web/portal/browse/display?_EXT_KNOVEL_DISPLAY_bookid=5083`.

[124] K. J. Ross and B. Sonntag. 'High temperature metal atom beam sources.' *Review of Scientific Instruments*, **66**, 4409–4433 (1995). doi:doi:10.1063/1.1145337.

[125] R. F. M. Lobo and N. T. Silva. 'Neutral c60 effusive source for atomic collisions with fullerene.' *Review of Scientific Instruments*, **72**, 3505–3506 (2001). doi:doi:10.1063/1.1396662.

[126] R. A. Ganeev. 'High-order harmonic generation in a laser plasma: a review of recent achievements.' *Journal of Physics B: Atomic, Molecular and Optical Physics*, **40**, R213–R253 (2007). doi:10.1088/0953-4075/40/22/R01.

[127] C. Hutchison, R. A. Ganeev, T. Witting, F. Frank, W. A. Okell *et al.* 'Stable generation of high-order harmonics of femtosecond laser radiation from laser produced plasma plumes at 1 kHz pulse repetition rate.' *Optics Letters*, **37**, 2064–2066 (2012). doi:10.1364/OL.37.002064.

[128] J. Ladislas Wiza. 'Microchannel plate detectors.' *Nuclear Instruments and Methods*, **162**, 587–601 (1979). doi:10.1016/0029-554X(79)90734-1.

[129] A. Sandhu and X.-M. Tong. 'Femtosecond and attosecond spectroscopy in the XUV regime.' *IEEE Journal of Selected Topics in Quantum Electronics*, **18**, 351 –362 (2012). doi:10.1109/JSTQE.2011.2136332.

[130] H. Muller. 'Reconstruction of attosecond harmonic beating by interference of two-photon transitions.' *Applied Physics B: Lasers and Optics*, **74**, s17–s21 (2002). doi:10.1007/s00340-002-0894-8.

[131] M. Swoboda, J. M. Dahlström, T. Ruchon, P. Johnsson, J. Mauritsson *et al.* 'Intensity dependence of laser-assisted attosecond photoionization spectra.' *Laser Physics*, **19**, 1591–1599 (2009). doi:10.1134/S1054660X09150390.

[132] N. Kouchi, M. Ukai and Y. Hatano. 'Dissociation dynamics of superexcited molecular hydrogen.' *Journal of Physics B: Atomic, Molecular and Optical Physics*, **30**, 2319–2344 (1997). doi:10.1088/0953-4075/30/10/008.

[133] J. D. Bozek, J. E. Furst, T. J. Gay, H. Gould, A. L. D. Kilcoyne *et al.* 'Production of excited atomic hydrogen and deuterium from h 2 and d 2 photodissociation.' *Journal of Physics B: Atomic, Molecular and Optical Physics*, **39**, 4871–4882 (2006). doi:10.1088/0953-4075/39/23/006.

[134] G. Sansone, F. Kelkensberg, J. F. Pérez-Torres, F. Morales, M. F. Kling *et al.* 'Electron localization following attosecond molecular photoionization.' *Nature*, **465**, 763–766 (2010). doi:10.1038/nature09084.

[135] J. Jackson. *Classical electrodynamics*. Wiley, New York, 3rd ed. edition (1999).

[136] P. Kruit and F. H. Read. 'Magnetic field paralleliser for 2π electron-spectrometer and electron-image magnifier.' *Journal of Physics E: Scientific Instruments*, **16**, 313–324 (1983). doi:10.1088/0022-3735/16/4/016.

[137] J. D. Bozek. 'AMO instrumentation for the LCLS x-ray FEL.' *The European Physical Journal Special Topics*, **169**, 129–132 (2009). doi:10.1140/epjst/e2009-00982-y.

[138] L. Young, E. P. Kanter, B. Krässig, Y. Li, A. M. March *et al.* 'Femtosecond electronic response of atoms to ultra-intense x-rays.' *Nature*, **466**, 56–61 (2010). doi:10.1038/nature09177.

[139] J. Bozek. 'The AMO instrument & science drivers.' (2008). URL `http://lcls.slac.stanford.edu/amo/docs/Bozek_Prop_WS_Jun08.ppt`.

[140] O. Hemmers, S. B. Whitfield, P. Glans, H. Wang, D. W. Lindle *et al.* 'High-resolution electron time-of-flight apparatus for the soft x-ray region.' *Review of Scientific Instruments*, **69**, 3809 (1998). doi:doi:10.1063/1.1149183.

[141] C. Cornaggia. 'Ultrafast coulomb explosion imaging of molecules.' *Laser Physics*, **19**, 1660–1670 (2009). doi:10.1134/S1054660X09150122.

[142] Z. Vager, R. Naaman and E. P. Kanter. 'Coulomb explosion imaging of small molecules.' *Science*, **244**, 426–431 (1989).

[143] K. Beckord, J. Becker, U. Werner and H. O. Lutz. 'Note on low-energy proton pairs in collision-induced h 2 dissociation.' *Journal of Physics B: Atomic, Molecular and Optical Physics*, **27**, L585–L589 (1994). doi:10.1088/0953-4075/27/17/004.

[144] K. Codling, L. J. Frasinksi, P. Hatherly and J. R. M. Barr. 'On the major mode of multiphoton multiple ionisation.' *Journal of Physics B: Atomic and Molecular Physics*, **20**, L525–L531 (1987). doi:10.1088/0022-3700/20/16/003.

[145] C. Cornaggia, D. Normand and J. Morellec. 'Role of the molecular electronic configuration in the coulomb fragmentation of n 2 , c 2 h 2 and c 2 h 4 in an intense laser field.' *Journal of Physics B: Atomic, Molecular and Optical Physics*, **25**, L415–L422 (1992). doi:10.1088/0953-4075/25/17/003.

[146] C. Cornaggia, J. Lavancier, D. Normand, J. Morellec, P. Agostini *et al.* 'Multielectron dissociative ionization of diatomic molecules in an intense femtosecond laser field.' *Physical Review A*, **44**, 4499–4505 (1991). doi:10.1103/PhysRevA.44.4499.

[147] C. Cornaggia, M. Schmidt and D. Normand. 'Laser-induced nuclear motions in the coulomb explosion of c_{2}h_{2}^{+} ions.' *Physical Review A*, **51**, 1431–1437 (1995). doi:10.1103/PhysRevA.51.1431.

[148] F. Légaré, K. F. Lee, A. D. Bandrauk, D. M. Villeneuve and P. B. Corkum. 'Laser coulomb explosion imaging for probing ultra-fast molecular dynamics.' *Journal of Physics B: Atomic, Molecular and Optical Physics*, **39**, S503–S513 (2006). doi:10.1088/0953-4075/39/13/S23.

[149] E. Baldit, S. Saugout and C. Cornaggia. 'Coulomb explosion of n_{2} using intense 10- and 40-fs laser pulses.' *Physical Review A*, **71** (2005). doi:10.1103/PhysRevA.71.021403.

[150] A. Hishikawa, A. Iwamae and K. Yamanouchi. 'Ultrafast deformation of the geometrical structure of CO_{2} induced in intense laser fields.' *Physical Review Letters*, **83**, 1127–1130 (1999). doi:10.1103/PhysRevLett.83.1127.

[151] T. A. Carlson, W. E. Hunt and M. O. Krause. 'Relative abundances of ions formed as the result of inner-shell vacancies in atoms.' *Physical Review*, **151**, 41–47 (1966). doi:10.1103/PhysRev.151.41.

[152] Y. Muramatsu, K. Ueda, N. Saito, H. Chiba, M. Lavollée *et al.* 'Direct probe of the bent and linear geometries of the core-excited renner-teller pair states by means of the triple-ion-coincidence momentum imaging technique.' *Physical Review Letters*, **88**, 133002 (2002). doi:10.1103/PhysRevLett.88.133002.

[153] M. Machida, M. Lavollée, J. Randrianjafisoa, G. Laurent, M. Nagoshi *et al.* 'Probe of bending motion following the 1s-1π^* excitation of N2O.' *The Journal of Chemical Physics*, **120**, 3635–3641 (2004). doi:doi:10.1063/1.1641783.

[154] A. De Fanis, N. Saito, M. Machida, K. Okada, H. Chiba *et al.* 'Asymmetric nuclear motion of the f 1s–ionized state in BF_{3} probed by quadruple-ion-coincidence momentum imaging.' *Physical Review A*, **69**, 022506 (2004). doi:10.1103/PhysRevA.69.022506.

[155] D. V. Morgan, R. J. Bartlett and M. Sagurton. 'Single-photon multiple ionization of argon in the k-edge region.' *Physical Review A*, **51**, 2939–2944 (1995). doi:10.1103/PhysRevA.51.2939.

[156] D. V. Morgan, M. Sagurton and R. J. Bartlett. 'Single-photon multiple ionization of neon in the k-edge region.' *Physical Review A*, **55**, 1113–1118 (1997). doi:10.1103/PhysRevA.55.1113.

[157] N. J. Turro, V. Ramamurthy and J. C. Scaiano. *Modern molecular photochemistry of organic molecules*. University Science Books (2010).

[158] W. Fuß, W. E. Schmid and S. A. Trushin. 'Time-resolved dissociative intense-laser field ionization for probing dynamics: Femtosecond photochemical ring opening of 1,3-cyclohexadiene.' *The Journal of Chemical Physics*, **112**, 8347–8362 (2000). doi:doi:10.1063/1.481478.

[159] S. Deb and P. M. Weber. 'The ultrafast pathway of photon-induced electrocyclic ring-opening reactions: The case of 1,3-cyclohexadiene.' *Annual Review of Physical Chemistry*, **62**, 19–39 (2011). doi:10.1146/annurev.physchem.012809.103350.

[160] M. Garavelli, C. S. Page, P. Celani, M. Olivucci, W. E. Schmid *et al.* 'Reaction path of a sub-200 fs photochemical electrocyclic reaction.' *The Journal of Physical Chemistry A*, **105**, 4458–4469 (2001). doi:10.1021/jp010359p.

[161] K. Kosma, S. A. Trushin, W. Fuß and W. E. Schmid. 'Cyclohexadiene ring opening observed with 13 fs resolution: coherent oscillations confirm the reaction path.' *Physical Chemistry Chemical Physics*, **11**, 172–181 (2008). doi:10.1039/B814201G.

[162] N. A. Anderson, S. H. Pullen, L. A. Walker, J. J. Shiang and R. J. Sension. 'Ultrafast polyene dynamics in solution: The conformational relaxation and thermalization of highly excited cis-1,3,5-hexatriene as a function of initial conformation and solvent.' *The Journal of Physical Chemistry A*, **102**, 10588–10598 (1998). doi:10.1021/jp983181o.

[163] S. Lochbrunner, W. Fuss, W. E. Schmid and K.-L. Kompa. 'Electronic relaxation and ground-state dynamics of 1,3-cyclohexadiene and cis-hexatriene in ethanol.' *The Journal of Physical Chemistry A*, **102**, 9334–9344 (1998). doi:10.1021/jp9809179.

[164] S. P. Hau-Riege. 'X-ray atomic scattering factors of low-z ions with a core hole.' *Physical Review A*, **76**, 042511 (2007). doi:10.1103/PhysRevA.76.042511.

[165] L. S. Cederbaum, F. Tarantelli, A. Sgamellotti and J. Schirmer. 'Double vacancies in the core of benzene.' *The Journal of Chemical Physics*, **86**, 2168 (1987). doi:10.1063/1.452756.

[166] J. H. D. Eland, M. Tashiro, P. Linusson, M. Ehara, K. Ueda *et al.* 'Double core hole creation and subsequent auger decay in NH_{3} and CH_{4} molecules.' *Physical Review Letters*, **105**, 213005 (2010). doi:10.1103/PhysRevLett.105.213005.

[167] P. Lablanquie, T. P. Grozdanov, M. Žitnik, S. Carniato, P. Selles *et al.* 'Evidence of single-photon two-site core double ionization of c_{2}h_{2} molecules.' *Physical Review Letters*, **107**, 193004 (2011). doi:10.1103/PhysRevLett.107.193004.

[168] L. Fang, M. Hoener, O. Gessner, F. Tarantelli, S. T. Pratt *et al.* 'Double core-hole production in n_{2}: Beating the auger clock.' *Physical Review Letters*, **105**, 083005 (2010). doi:10.1103/PhysRevLett.105.083005.

[169] P. Salen, P. van der Meulen, H. T. Schmidt, R. D. Thomas, M. Larsson *et al.* 'Experimental verification of the chemical sensitivity of two-site double core-hole states formed by an x-ray free-electron laser.' *Physical Review Letters*, **108**, 153003 (2012). doi:10.1103/PhysRevLett.108.153003.

[170] M. Tashiro, M. Ehara, H. Fukuzawa, K. Ueda, C. Buth *et al.* 'Molecular double core hole electron spectroscopy for chemical analysis.' *The Journal of Chemical Physics*, **132**, 184302–184302–11 (2010). doi:doi:10.1063/1.3408251.

[171] T. Mizuno, T. Yamada, H. Tsuchida, Y. Nakai and A. Itoh. 'Measurement of kinetic energy release in CO fragmentation by charge-changing collisions of fast heavy ions.' *Physical Review A*, **81**, 012704 (2010). doi:10.1103/PhysRevA.81.012704.

[172] I. Noda and Y. Ozaki. *Two-Dimensional Correlation Spectroscopy: Applications in Vibrational and Optical Spectroscopy*. John Wiley & Sons (2005).

[173] J. Eland. 'The dynamics of three-body dissociations of dications studied by the triple coincidence technique PEPIPICO.' *Molecular Physics*, **61**, 725–745 (1987). doi:10.1080/00268978700101421.

[174] M. Stankiewicz, P. A. Hatherly, L. J. Frasinski, K. Codling and D. M. P. Holland. 'The double photoionisation of NH 3 using the triple coincidence (PEPIPICO) technique.' *Journal of Physics B: Atomic, Molecular and Optical Physics*, **22**, 21–31 (1989). doi:10.1088/0953-4075/22/1/006.

[175] J. H. D. Eland, O. Vieuxmaire, T. Kinugawa, P. Lablanquie, R. I. Hall *et al.* 'Complete two-electron spectra in double photoionization: The rare gases ar, kr, and xe.' *Physical Review Letters*, **90**, 053003 (2003). doi:10.1103/PhysRevLett.90.053003.

[176] J. Palaudoux, P. Lablanquie, L. Andric, J. H. D. Eland and F. Penent. 'Multi-coincidence in cascade auger decay processes.' *Journal of Physics: Conference Series*, **141**, 012012 (2008). doi:10.1088/1742-6596/141/1/012012.

[177] L. J. Frasinski, K. Codling and P. A. Hatherly. 'Covariance mapping: A correlation method applied to multiphoton multiple ionization.' *Science*, **246**, 1029–1031 (1989).

[178] L. Frasinski, P. Hatherly and K. Codling. 'Multiphoton multiple ionisation of N2O probed by three-dimensional covariance mapping.' *Physics Letters A*, **156**, 227–232 (1991). doi:10.1016/0375-9601(91)90145-X.

[179] W. Krzanowski. *Principles of multivariate analysis : a user's perspective*. Oxford University Press, Oxford ;;New York, rev. ed. edition (2000).

[180] M. Stankiewicz, L. J. Frasinski, G. M. Cross, P. A. Hatherly, K. Codling *et al.* 'Dissociative ionization of n 2 and CO using intense lasers at 248 and 305 nm.' *Journal of Physics B: Atomic, Molecular and Optical Physics*, **26**, 2619–2626 (1993). doi:10.1088/0953-4075/26/16/017.

[181] P. A. Hatherly, M. Stankiewicz, K. Codling, L. J. Frasinski and G. M. Cross. 'The multielectron dissociative ionization of molecular iodine in intense laser fields.' *Journal of Physics B: Atomic, Molecular and Optical Physics*, **27**, 2993–3003 (1994). doi:10.1088/0953-4075/27/14/032.

[182] K. Codling, C. Cornaggia, L. J. Frasinski, P. A. Hatherly, J. Morellec *et al.* 'Charge-symmetric fragmentation of diatomic molecules in intense picosecond laser fields.' *Journal of Physics B: Atomic, Molecular and Optical Physics*, **24**, L593–L597 (1991). doi:10.1088/0953-4075/24/23/007.

[183] L. J. Frasinski, P. A. Hatherly, K. Codling, M. Larsson, A. Persson *et al.* 'Multielectron dissociative ionization of CO 2 in intense laser fields.' *Journal of Physics B: Atomic, Molecular and Optical Physics*, **27**, L109–L114 (1994). doi:10.1088/0953-4075/27/6/002.

[184] V. R. Bhardwaj, K. Vijayalakshmi and D. Mathur. 'Angle-resolved covariance mapping of spatially-aligned in an intense picosecond laser field.' *Journal of Physics B: Atomic, Molecular and Optical Physics*, **32**, 1087–1095 (1999). doi:10.1088/0953-4075/32/5/004.

[185] W. A. Bryan, J. H. Sanderson, A. El-Zein, W. R. Newell, P. F. Taday *et al.* 'Laser-induced coulomb explosion, geometry modification and reorientation of carbon dioxide.' *Journal of Physics B: Atomic, Molecular and Optical Physics*, **33**, 745–766 (2000). doi:10.1088/0953-4075/33/4/312.

[186] W. A. Bryan, W. R. Newell, J. H. Sanderson and A. J. Langley. 'Observation of multiple ionization pathways for OCS in an intense laser field resolved by three-dimensional covariance mapping and visualized by hierarchical ionization topology.' *Physical Review A*, **74**, 053409 (2006). doi:10.1103/PhysRevA.74.053409.

[187] J. L. Hansen, J. H. Nielsen, C. B. Madsen, A. T. Lindhardt, M. P. Johansson *et al.* 'Control and femtosecond time-resolved imaging of torsion in a chiral molecule.' *The Journal of Chemical Physics*, **136**, 204310–204310–10 (2012). doi:doi:10.1063/1.4719816.

[188] P. Wang and C. R. Vidal. 'Dissociation of multiply ionized carbonyl sulfide due to electron impact.' *The Journal of Chemical Physics*, **118**, 5383–5389 (2003). doi:doi:10.1063/1.1554738.

[189] P. Wang and C. Vidal. 'Electron impact dissociative ionization of carbonyl chlorofluoride.' *International Journal of Mass Spectrometry*, **235**, 207–212 (2004). doi:10.1016/j.ijms.2004.04.016.

[190] P. Wang. 'ELECTRON IMPACT DISSOCIATIVE IONIZATION OF NITROSYL CHLORIDE.' *Modern Physics Letters B*, **26**, 1250065 (2012). doi:10.1142/S0217984912500650.

[191] C. Cornaggia. 'Statistical analysis of fragmentation channels of small multicharged molecular ions.' *Journal of Physics B: Atomic, Molecular and Optical Physics*, **45**, 085602 (2012). doi:10.1088/0953-4075/45/8/085602.

[192] I. Noda. 'Generalized 2-dimensional correlation method applicable to infrared, raman, and other types of spectroscopy.' *Applied Spectroscopy*, **47**, 1329–1336 (1993). doi:10.1366/0003702934067694.

[193] M. E. Sigman and M. R. Williams. 'Covariance mapping in the analysis of ignitable liquids by gas Chromatography/Mass spectrometry.' *Analytical Chemistry*, **78**, 1713–1718 (2006). doi:10.1021/ac058040e.

[194] R. Trainham, J. Tinsley, R. Keegan and W. Quam. 'Covariance spectroscopy applied to nuclear radiation detection.' In L. A. Franks, R. B. James and A. Burger, editors, 'Hard X-Ray, Gamma-Ray, and Neutron Detector Physics Xiii,' volume 8142. Spie-Int Soc Optical Engineering, Bellingham (2011).

[195] L. Frasinski, A. Giles, P. Hatherly, J. Posthumus, M. Thompson *et al.* 'Covariance mapping and triple coincidence techniques applied to multielectron dissociative ionization.' *Journal of Electron Spectroscopy and Related Phenomena*, **79**, 367–371 (1996). doi:10.1016/0368-2048(96)02874-5.

[196] J. Niskanen, P. Norman, H. Aksela and H. Ågren. 'Relativistic contributions to single and double core electron ionization energies of noble gases.' *The Journal of Chemical Physics*, **135**, 054310 (2011). doi:10.1063/1.3621833.

[197] M. Tashiro, M. Ehara and K. Ueda. 'Double core-hole electron spectroscopy for open-shell molecules: theoretical perspective.' *arXiv:1007.0530* (2010).

[198] M. Nakamura, M. Sasanuma, S. Sato, M. Watanabe, H. Yamashita *et al.* 'Absorption structure near the k edge of the nitrogen molecule.' *Physical Review*, **178**, 80–82 (1969). doi:10.1103/PhysRev.178.80.

[199] J. P. Cryan, J. M. Glownia, J. Andreasson, A. Belkacem, N. Berrah *et al.* 'Auger electron angular distribution of double core-hole states in the molecular reference frame.' *Physical Review Letters*, **105**, 083004 (2010). doi:10.1103/PhysRevLett.105.083004.

[200] R. Maurer and R. Watson. 'Dirac-fock energies for multiple k-plus l-shell vacancy states of ions with z = 9 to 18.' *Atomic Data and Nuclear Data Tables*, **34**, 185–199 (1986). doi:10.1016/0092-640X(86)90001-X.

[201] Y. Hikosaka, T. Aoto, P. Lablanquie, F. Penent, E. Shigemasa *et al.* 'Experimental investigation of core-valence double photoionization.' *Physical Review Letters*, **97**, 053003 (2006). doi:10.1103/PhysRevLett.97.053003.

[202] N. Martensson, S. Svensson and U. Gelius. 'Single and double shake-up processes in the ne 1s photoelectron spectrum.' *Journal of Physics B: Atomic and Molecular Physics*, **20**, 6243–6255 (1987). doi:10.1088/0022-3700/20/23/016.

[203] Ž. Šmit, M. Žitnik, L. Avaldi, R. Camilloni, E. Fainelli *et al.* 'Auger hypersatellites in ne atoms induced by electron impact.' *Physical Review A*, **49**, 1480–1483 (1994). doi:10.1103/PhysRevA.49.1480.

[204] B. Kempgens, A. Kivimäki, H. M. Köppe, M. Neeb, A. M. Bradshaw *et al.* 'One-electron versus multielectron effects in the near-threshold c 1s photoionization of acetylene.' *The Journal of Chemical Physics*, **107**, 4219 (1997). doi:10.1063/1.474796.

[205] J. J. Pireaux, S. Svensson, E. Basilier, P.-Å. Malmqvist, U. Gelius *et al.* 'Core-electron relaxation energies and valence-band formation of linear alkanes studied in the gas phase by means of electron spectroscopy.' *Physical Review A*, **14**, 2133–2145 (1976). doi:10.1103/PhysRevA.14.2133.

[206] N. V. Kryzhevoi, R. Santra and L. S. Cederbaum. 'Inner-shell single and double ionization potentials of aminophenol isomers.' *The Journal of Chemical Physics*, **135**, 084302–084302–10 (2011). doi:doi:10.1063/1.3624393.